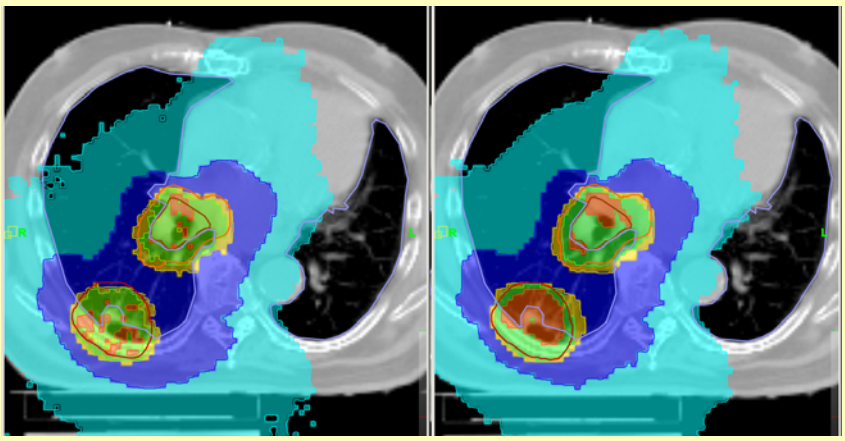
UNIVERSITE CATHOLIQUE DE LOUVAIN
Faculté de médecine
Unité d'Imagerie Moléculaire et de Radiothérapie Expérimentale

Improving confidence for IMRT and helical tomotherapy treatments using accurately benchmarked Monte Carlo simulations

Edmond Sterpin



Thèse présentée en vue de l'obtention du grade de
Docteur en Sciences Biomédicales et Pharmaceutiques

Promoteur : Prof. Stefaan Vynckier

2008



UNIVERSITE CATHOLIQUE DE LOUVAIN
Faculté de médecine
Unité d'Imagerie Moléculaire et de Radiothérapie Expérimentale

Improving confidence for IMRT and helical tomotherapy treatments using accurately benchmarked Monte Carlo simulations

Edmond Sterpin

Thèse présentée en vue de l'obtention du grade de
Docteur en Sciences Biomédicales et Pharmaceutiques

Promoteur : Prof. Stefaan Vynckier

2008

Promoter

Prof. Stefaan Vynckier	Université Catholique de Louvain

Doctoral guidance committee

Prof. Stefaan Vynckier	Université Catholique de Louvain
Prof. Vincent Grégoire	Université Catholique de Louvain
Prof. Youssef El Masri	Université Catholique de Louvain
Dr. Nick Reynaert	Centre Oscar Lambret, Lille

President of the examination committee

Prof. Vincent Grégoire	Université Catholique de Louvain

Examination committee

Prof. Stefaan Vynckier	Université Catholique de Louvain
Prof. Youssef El Masri	Université Catholique de Louvain
Dr. Nick Reynaert	Centre Oscar Lambret, Lille
Prof. Ben J.M. Heijmen	Erasmus MC-Daniel den Hoed Cancer Center
Prof. Francesc Salvat	Universitat de Barcelona
Prof. Dirk Verellen	Vrije Universiteit van Brussel

Table of contents

Table of contents i

Acknowledgements vii

Abstract ix

Résumé xi

List of abbreviations xiii

Chapter 1: Introduction 1

1. Treatment delivery techniques 3
1.1. Types of particles 4
1.2. Multiplying the number of degrees of freedom 7
1.2.1. Intensity-modulated radiation therapy 7
1.3. Imaging and patient positioning devices 11

2. Dose calculation algorithms accuracy 13
2.1. Dose calculation algorithms 15
2.2. Influence of treatment delivery on accuracy 17

3. Objectives of the thesis 18

4. References 22

Chapter 2: Theory 29

1. Absorbed dose and electronic equilibrium 29
1.1. Absorbed dose 29
1.2. Electronic equilibrium 29

2. MC simulations 30
2.1. Generalities on MC simulations 30
2.2. Monte Carlo codes used in medical physics 31
2.3. Photon interactions 32
2.3.1. Photoelectric effect 33
2.3.2. Coherent (Rayleigh) scattering 34
2.3.3. Incoherent (Compton) scattering 34
2.3.4. Electron-positron pair production 34
2.3.5. Attenuation coefficients 35
2.3.6. Atomic relaxation 36
2.4. Electron interactions 36
2.4.1. Elastic scattering 38
2.4.2. Inelastic scattering 38

2.4.3. Bremsstrahlung emission (braking radiation) 39
2.4.4. Positron annihilation 40
2.4.5. Ionization of inner shells 40
2.5. Electron transport mechanics 40
2.5.1. Angular deflections due to soft scattering events 44
2.5.2. Soft energy losses 44
2.6. Expected accuracy of MC simulations in external radiotherapy 45

3. C/S algorithms 47
3.1. General formulation 47

4. References 50

Chapter 3: Publication one 55

Monte Carlo evaluation of the AAA treatment planning algorithm in a heterogeneous multilayer phantom and IMRT clinical treatments for an Elekta SL25 linear accelerator 55

1. INTRODUCTION 56

2. MATERIAL AND METHODS 58
2.1. Linear accelerator 58
2.2. Varian—anisotropic analytical algorithm (AAA) 58
2.3. Phantom measurements 59
2.4. Monte Carlo simulation 61
2.5. IMRT plans 62
2.5.1. Ethmoid tumor 63
2.5.2. Oropharynx tumor 63
2.5.3. Lung tumors 63

3. RESULTS 64
3.1. AAA and MC commissioning 64
3.1.1. Depth dose and profiles 64
3.1.2. Output factors 64
3.2. Phantom measurements 66
3.3. IMRT plans 70
3.3.1. Ethmoid tumor 70
3.3.2. Oropharynx tumor 73
3.3.3. Large lung tumor 74
3.3.4. Small lung tumor 75

4. DISCUSSION 78
4.1. MC 78
4.2. AAA 78
4.2.1. Phantom results 78
4.2.2. IMRT plans 79

5. CONCLUSIONS 80

Chapter 4: Publication 2 *87*

Monte Carlo simulation of the tomotherapy treatment unit in the static mode using MC HAMMER, a Monte Carlo tool dedicated to tomotherapy *87*

1. Introduction **88**

2. Material and methods **89**
2.1. Tomotherapy treatment unit 89
2.2. Measurements 90
2.3. Monte Carlo simulation 91
2.3.1. Geometry definition 91
2.3.2. Particles transport 92
2.3.3. MC HAMMER 92

3. Results and discussion **93**
3.1. Energy and target position tuning 93
3.2. Jaws settings and electron source geometry 96

4. Conclusions **98**

Chapter 5: Publication 3 *101*

Analytical model of the binary multileaf collimator of tomotherapy for Monte Carlo simulations *101*

1. Introduction **102**

2. Material and methods **103**
2.1. Geometry definition 103
2.2. Transfer function (TF) of the MLC 103
2.2.1. Step 1: transform of the phase space file and calculation of the absorption factors 104
2.2.2. Step 2: Accounting for the MLC configuration 104

3. Results and discussion **107**
3.1. Open fields 107
3.2. Two central leaves opened 108
3.3. Tongue and groove 109
3.4. Arbitrary configuration 109
3.5. Fully blocked field 110

4. Conclusions **111**

Chapter 6: Publication 4 *113*

Monte Carlo simulation of helical tomotherapy with PENELOPE *113*

1. Introduction **114**

2. Material and methods 116
2.1. Hi-Art Tomotherapy treatment unit 116
2.2. Measurement setups 116
2.3. Monte Carlo code PENELOPE 117
2.4. Static mode 117
2.5. Analytical model of the binary MLC: the TF method 119
2.6. Simulation of the helical mode: the "TomoPen" model 122
2.6.1. Geometry definition 122
2.6.2. Rotation and translation of the PSFs 122
2.6.3. Accounting for the MLC configurations 123
2.6.4. Calculations of dose distributions 125
2.6.5. Dose calibration of TomoPen 125
2.6.6. Validation of TomoPen 126
2.6.7. Using TomoPen for Delivery Quality Assurance (DQA) plans 126

3. Results 127
3.1. Static mode 127
3.1.1. Open fields 127
3.1.2. MLC geometry validation and fine-tuning of the electron source geometry 128
3.1.2.1. Individual leaf geometry and MLC bank position verification 128
3.1.2.2. T&G 129
3.2. Validation of the TF method 130
3.2.1. T&G effect 131
3.3. Validation of the TomoPen model for commissioning procedures 132
3.3.1. 2.5 cm field on-axis IMRT commissioning procedure 132
3.3.2. 2.5 cm field off-axis IMRT commissioning procedure 133
3.3.3. Application of TomoPen: comparison between C/S and TomoPen for a delivery quality assurance procedure 134

4. Discussion 136

5. Conclusions 137

Chapter 7: Publication 5 143

Monte Carlo evaluation of the convolution/superposition algorithm of Hi-Art™ tomotherapy in heterogeneous phantoms and clinical cases 143

1. Introduction 144

2. Material and methods 145
2.1. Hi-Art™ HT system 145
2.2. Collapsed cone C/S 146
2.3. TomoPen 146
2.4. Phantom experiments 148
2.4.1. Comparison measurements-TomoPen 148

2.4.2. Comparison C/S-TomoPen 150
2.5. Clinical study 150

3. Results 154
3.1. Phantom experiment 154
3.1.1. Comparison TomoPen-measurements 154
3.1.2. Comparison TomoPen-C/S 155
3.2. Clinical studies 157
3.2.1. Head and neck tumors 157
3.2.2. Lung tumors 159
3.2.3. Leg tumor 161
3.3. Discussion 162
3.3.1. Phantom experiments 162
3.3.2. Clinical cases 162

4. Conclusions 163

Chapter 8: Discussion 167

1. Overview of the last studies on the performance of AAA 168
1.1. Phantom studies 168
1.2. Clinical studies 169
1.3. Ability of AAA to model Elekta linacs 171

2. Specific issues of the MC modeling (TomoPen) of the tomotherapy treatment unit 171
2.1. Impact of simplifications in the simulation on accuracy 171
2.2. Dose calibration procedure 173

3. Introducing TomoPen into clinical practice 174
3.1. Considerations on speed 174
3.2. Tuning of TomoPen for other tomotherapy treatment units 176

4. Additional applications of TomoPen 177
4.1. TomoPen for evalutating skin sparing capabilities of the tomotherapy system 178
4.2. TomoPen for Topotherapy 182
4.3. TomoPen as a QA tool 183
4.4. TomoPen for dosimetry 184
4.5. TomoPen for 4D treatment planning 187
4.5.1. TomoPen for intra-fraction motion 187
4.5.2. TomoPen for inter-fraction motion 189

5. Added-value of MC 189

6. References 191

Chapter 9: Conclusions 197

Acknowledgements

First of all, I would like to thank my supervisor Prof. Stefaan Vynckier. I always received his full support and confidence. I benefited from his advice and his wide network of collaborators. I was encouraged to join meetings and congresses all around the world and developed interesting relationships with the scientific community.

The UCL department of radiotherapy, with advanced equipments and strong scientific background, is an excellent treatment centre. I would like to acknowledge Prof. Pierre Scalliet and Prof. Vincent Gregoire for welcoming me in Saint-Luc and helping when I needed it the most.

Of course, nothing could have been possible without the financial support of the FNRS and the Télévie. I express here my sincere gratitude.

During this thesis, I have collaborated with top level scientists working in the Monte Carlo field in medical physics. My first acknowledgements go to Dr. Nick Reynaert for his confidence and advice. I was able to take full advantage of his enormous experience. My initiation in the universe of Monte Carlo simulations could not have been so efficient and interesting without his help. My second acknowledgements go to Prof. Francesc Salvat, from the University of Barcelona from which I could learn more than one could expect from the creator of the PENELOPE code, and perhaps beyond the strict area of science. Gracias por todo.

At the start of my PhD thesis, a tomotherapy machine was installed in Saint-Luc. With the help of Prof. Vynckier and Prof. Gregoire, I could meet Prof. Gustavo Olivera, vice-president of research in Tomotherapy Inc. Thanks for allowing me visiting Tomotherapy Inc. in Madison (Wisconsin) with full support of the company. Also, I would like to acknowledge all the collaborators overseas who worked with Prof. Salvat and me: Prof. Thomas Rockwell Mackie, Sam Jeswani, who shared my passion for Chicago and American rib eye steaks, Bob Cravens, Kenneth Ruchala, Carl Mauer, Eric Schnarr, Michel Moreau, Dan Lucas, Tim Theisen, Paul Reckwerdt, Jan Patrick, Heidi Clarke and, of course, Yul Ouattara for introducing me to the the Tomotherapy soccer team.

I would also like to thank all the physicists and the engineering teammates who gave me great support whenever I need it. For the physics team, I am thankful to Milàn Tomsej, Françoise Vanneste, Nathalie de Patoul, Vinciane Tondeur, Christian Clermont, Joël Martinez, Ahcène Benkemouche and Antoine Delor. I must of course thank the engineers Maxime Coevoet, Gregory Delrue, Vincent Roosen and Simon Vanderbrecht who always helped me and gently welcomed me in their office with such a friendly atmosphere. I also thank my neighbours from the office next door for

their wonderful “Fridays”: Aude Vaandering (thank you so much for having read my thesis), Nicolas Christian, Pierre Castadot, John Lee and Xavier Geets. Special thanks of course to my colleagues in my office who bravely shared the heat of the running computers, Fadi Abboud and Paul Edimo. I also cannot escape from acknowledging my old colleagues and good friends, Martin Morelle, Adil Margoum and Brahim Iaisaouiyan.

Those years on the Saint-Luc campus were not only about work but also very entertaining, especially thanks to Hrag “Esfajani”, Fouzi “Fesutek”, Géraldine, my friends from the badminton and the lab of pharmacotherapy.

Very special thanks to all my family, particularly my mom, dad and sister, Michel, Claire and friends, Joanne, Alan, François for supporting me (I should say “suffering”). Thanks to Luka and “Moltonoos” for the happiness they (will) shine over our lives. Finally, this research experience is nothing compared to the pleasure of sharing each day of my life with Leslie.

Abstract

The radiotherapy community's dream has always been to have available technologies being able to deliver a perfectly accurate high dose to tumor volumes without irradiating surrounding healthy tissues. This dream will never come true, but all the efforts of physicists, physicians and manufacturers must be combined to bring reality as close as possible to this utopia.

Since the beginning of the 60s and the advent of electron linear accelerator mounted on treatment units, the technology in photon therapy has evolved tremendously. Nowadays, the state of art in photon treatments involves intensity-modulated radiotherapy (IMRT) with the help of highly sophisticated imaging devices.

IMRT is a complex technique which requires a good control in the accuracy of all the steps involved in a radiotherapy treatment. Those may be summarized into 3 main categories: the calibration and stability of the treatment unit, the positioning and the quality of the data associated to the patient and the dose calculation process during treatment planning.

To improve the overall uncertainty of a given treatment, research efforts are needed in the three categories. This thesis focuses on the dose calculation process. During the last decades, the complexity and accuracy of dose calculation algorithms increased with the huge improvements in computer technology. Despite this, the vast majority of the algorithms perform important approximations regarding the physics of the particles transport. However, it is possible to design algorithms with minor approximations based on Monte Carlo methods (MC), which faithfully simulate the physical reality and are considered as the most accurate to compute dose in human tissue.

Unfortunately, until recently, the speed of MC simulations was too slow to be compatible with the time constraints associated with clinical routine. But the continuous improvements in computer power combined with the introduction of pertinent simplifications in the MC codes allowed for the introduction of MC into clinical practice, which is already available in several commercial treatment planning systems.

The aim of this thesis was to evaluate the added-value of MC compared to modern analytical algorithms for complex IMRT treatments of tumors surrounded by an important amount of inhomogeneities. Those evaluations were performed for two IMRT delivery techniques: step-and-shoot IMRT and helical tomotherapy. For step-and-shoot IMRT (delivered by an Elekta treatment unit), MC simulations with BEAMnrc were compared to an algorithm released recently by Varian called the Anisotropic Analytical Algorithm (AAA). For helical tomotherapy, a similar study

was performed but for the collapsed-cone convolution/superposition code implemented in the tomotherapy system provided by Tomotherapy Incorporated. During this second study, the MC modeling of tomotherapy based on the MC code PENELOPE was an important aspect since this was the first time that a complete MC model of tomotherapy was designed with all the machine details fully disclosed by the manufacturer. Moreover, the MC model, called TomoPen, was designed for future implementation in the clinical system. Therefore, the speed of the simulation was a critical issue. The simulation strategy adopted in TomoPen, which mainly consisted in symplifying the transport through the multi-leaf collimator, allowed the calculation of dose distributions in a bilateral head-and-neck tumor in around 6 hours on a single 2.5 GHz processor, without losing significant accuracy. Using the cluster delivered with each tomotherapy treatment unit, this simulation time could be reduced by a factor of at least 32.

Generally, a good agreement was achieved between analytical algorithms and MC for the clinical cases selected during this study. However, differences could be observed for critical situations, like small lung or ethmoid tumors. Even though those deviations were not “dramatic”, they clearly demonstrated the potential of introducing MC into clinical routine to improve the overall quality and accuracy of the treatments.

Résumé

Le rêve ultime du radiothérapeute a toujours été d'avoir à disposition des technologies capables de délivrer avec une parfaite précision des doses élevées aux volumes tumoraux sans irradier les tissus sains avoisinants. Ce rêve ne deviendra jamais réalité, mais tous les efforts des physiciens, médecins et industriels doivent être combinés pour que la réalité s'approche le plus possible de cette utopie.

Depuis le début des années 60 et l'avènement des accélérateurs linéaires d'électrons montés sur des unités de traitement, la technologie en thérapie par photons a évolué énormément. Aujourd'hui, les traitements les plus à la pointe incluent la radiothérapie par modulation d'intensité (« Intensity-Modulated Radiation Therapy » ou IMRT) avec l'aide d'outils d'imagerie hautement sophistiqués.

L'IMRT est une technique complexe qui requiert un excellent contrôle de la précision dans toutes les étapes du processus du traitement. Ces étapes peuvent être résumées en trois catégories qui sont 1) l'étalonnage et la stabilité de l'unité de traitement, 2) le positionnement et la qualité des données associées au patient et 3) la précision du calcul de dose effectué lors de la planification du traitement.

Pour améliorer l'incertitude globale d'un traitement donné, des efforts de recherche sont nécessaires dans les trois catégories. Cette thèse se concentre sur le processus de calcul de dose. Durant les dernières décennies, la complexité et la précision des algorithmes de dose ont augmenté fortement grâce aux énormes progrès de l'informatique. Malgré cela, l'immense majorité des algorithmes utilisent des méthodes analytiques impliquant des approximations importantes au niveau de la physique de transport des particules. Il est cependant possible de concevoir des algorithmes qui évitent ces approximations en se basant sur des méthodes dites de Monte Carlo (MC) qui simulent fidèlement la réalité physique et qui sont considérées aujourd'hui comme les plus précises de calcul de la dose dans les tissus humains.

Malheureusement, jusqu'à récemment, la vitesse des simulations MC était trop lente pour être compatible avec les contraintes de temps liées à la routine clinique. Mais les progrès continus en puissance de calcul combinés avec l'introduction de simplifications pertinentes dans les codes MC permettent d'envisager l'introduction d'algorithmes MC en routine clinique, ce qui est déjà le cas pour plusieurs systèmes de planification de traitement commerciaux.

L'objectif de cette thèse était d'évaluer la valeur ajoutée du MC comparé à des algorithmes analytiques modernes pour des traitements IMRT complexes de tumeurs entourées de nombreuses inhomogénéités de densité. Ces évaluations ont été effectuées pour deux techniques de traitement IMRT : « step-and-shoot » et tomothérapie hélicoïdale. Pour l'IMRT « step-and-shoot » délivrée par une unité de

traitement Elekta SL25, des simulations MC avec BEAMnrc ont été comparées avec un algorithme commercialisé récemment par la firme Varian appelé « Anisotropic Analytical Algorithm » (AAA). Pour la tomothérapie, une étude similaire a été accomplie mais pour le code utilisé dans le système fourni par « Tomotherapy Incorporated » et basé sur un algorithme de type convolution/superposition utilisant l'approximation « collapsed-cone ». Durant cette seconde étude, la modélisation MC au moyen du code MC PENELOPE était un aspect très important étant donné que c'est la première fois qu'un code MC complet pour la tomothérapie était construit avec tous les détails techniques de la machine fournis par le constructeur. De plus, le modèle MC, appelé TomoPen, a été conçu en vue d'une introduction future dans le système clinique. La vitesse de la simulation était donc une contrainte importante. La stratégie utilisée pour la simulation et adoptée dans TomoPen consiste principalement à simplifier drastiquement le transport des photons dans le collimateur multilames et permet de calculer des distributions de dose dans une tumeur bilatérale de la sphère tête et cou en à peu près 10 heures sur un processeur de 2 GHz, sans perte de précision significative. En utilisant le groupe d'ordinateurs fourni avec chaque unité de traitement de tomothérapie, ce temps de simulation peut être réduit d'un facteur 32, correspondant au nombre de processeurs.

Durant cette thèse, la correspondance entre algorithmes analytiques et MC était en général satisfaisante pour la majorité des cas cliniques et expérimentaux étudiés. Cependant, des différences ont pu être observées pour des situations critiques, comme des petites tumeurs pulmonaires ou des tumeurs ethmoïdes. Même si ces déviations n'étaient pas « dramatiques », elles ont pu démontrer clairement le potentiel des algorithmes MC dans la pratique clinique afin d'améliorer la qualité globale et la précision des traitements.

List of abbreviations

1D: One-Dimensional
2D: Two-Dimensional
3D: Three-Dimensional
4D: Four-Dimensional
AAA: Analytical Anisotropic Algorithm
AAPM: American Association of Physicists in Medicine
CBCT: Cone-Beam Computed Tomography
CC: Collapsed-Cone
CSDA: Continuous Slowing Down Approximation
CM: Component Module
CP: Clinical Plan
CRT: Conformal RadioTherapy
C/S: Convolution/Superposition
CT: Computed Tomography
CTV: Clinical Target Volume
DQA: Delivery Quality Assurance
DVH: Dose-Volume Histogram
DVO: Dose-Volume Optimizer
EDR: Extended Dose Range
EGS: Electron-Gamma Shower
EPID: Electronic Portal Imaging Device
FWHM: Full Width Half Maximum
GEANT: GEomety ANd Tracking
GS: Gold Standard
GTV: Gross Tumor Volume
HT: Helical Tomotherapy
HU: Hounsfield Units
IAEA: International Atomic Energy Agency
IC: Ion Chamber
ICRU: International Commission on Radiation Units and Measurements
IGRT: Image-Guided Radiation Therapy
IMRT: Intensity-Modulated Radiation Therapy
Iso: Isocenter
Linac: Linear accelerator
MB: Modified Batho
MC: Monte Carlo
MCDE: Monte Carlo Dose Engine
MCNP: Monte Carlo N-Particle
MCTP: Monte Carlo Treatment Planning
MLC: Multi-Leaf Collimator
MS: Measurements
MU: Monitor Unit
NCS: Netherlands Commission on Radiation Dosimetry
NIST: National Institute of Standards and Technology

NRC: National Research council Canada
NTCP: Normal Tissue Complication Probability
PB: Pencil Beam
PDD: Percent Depth Dose
PENELOPE: PENetration and Energy LOss of Positrons and Electrons
PMMA: PolyMethylMethAcrylate
PRESTA: Parameter Reduced Electron Stepping Algorithm
PSF: Phase-Space File
PTV: Planning Target Volume
PVCS: Patient Volume Coordinate System
QA: Quality Assurance
SOBP: Spread-Out Bragg Peak
SSD: Source-Surface Distance
T&G: Tongue and Groove
TCP: Tumor Control Probability
TERMA: Total Energy Released per unit MAss
TF: Transfer Function
TPS : Treatment Planning System
UCL: Université Catholique de Louvain
WP : Water Plan

Chapter 1: Introduction

Current treatments of cancers are usually subdivided into three main categories: surgery, radiotherapy and chemotherapy. Those types of treatments are often combined but, usually, one of these options can be considered as the principal treatment for curing a given pathology. Nowadays, half of the cancers are cured, 22% with surgery, 15% with radiotherapy and 5% with chemotherapy (Kuhn *et al* 2001).

Around 70% of cancers are diagnosed at a stage without distant metastasis (Kuhn *et al* 2001). Therefore, the primary objective of the oncologist is local control of the tumor and radiotherapy is often the best choice to achieve that goal. Since around 30% of treatments fail because of uncontrollable local control (Ching-Li and Voldin 1993), it is clear that improvements in radiotherapy treatments will result in improved statistics of survival.

Radiotherapy can be divided into three main techniques, depending on the type of the radiation source: metabolic radiotherapy, brachytherapy and external radiotherapy. Metabolic radiotherapy uses unsealed sources (which may be injected), while brachyterapy uses sealed source, which may be permanent or extracted. External radiotherapy is the most common technique and is characterized by a source placed outside the patient. Since this work is based on this last technique, only external radiotherapy will be explored in the introduction.

Radiotherapy treatments consist in delivering lethal doses to tumor volumes while sparing at maximum healthy tissue. When radiations interact with patient tissues, they cause direct or indirect ionizations which may damage the DNA in the cells' nuclei. Depending on the importance of the damage, cells retain a certain ability to repair DNA. However, the recovering tools of tumor cells are often less efficient than those of healthy cells and, therefore, tumors exhibit a higher sensitivity to radiations than healthy tissues. The differential behavior between tumor cells and healthy cells facing irradiation is a prerequisite in the efficiency of a radiotherapy treatment.

To quantify the sensitivity of both tumor and healthy tissues versus radiation, two important notions are defined in radiotherapy, which are the probability of tumor control (*TCP*) and the probability of normal tissue complication (*NTCP*). Both are given as a function of the absorbed dose. Generally, *TCP* and *NTCP* curves have a sigmoid shape as shown in Figure 1. 1(a). The probability of uncomplicated tumor is defined as $P_{UTC} = TCP(1 - NTCP)$ and has a clock-like shape (Figure 1. 1(b)).

Obviously, the prescribed dose should be chosen to maximize P_{UTC} and the maximum value of P_{UTC} will be higher if *TCP* and *NTCP* curves are far from each other. Moreover, by avoiding healthy tissue during treatment, one could possibly keep *TCP* and *NTCP* wide apart (*i.e.* a high maximum value of P_{UTC}).

TCP and *NTCP*-dose curves have a steep slope (inherent to the sigmoid shape). Therefore, the absorbed dose must be determined with the highest accuracy achievable since an error in the dose may lead to a dramatic change in *TCP* and even more in *NTCP* (Fraass *et al* 2003, Papanikolaou *et al* 2004). For instance, an error of 5% in the dose may result in 10-20 % change of the *TCP* (Fraass *et al* 2003). Therefore, dose deposition accuracy is crucial to deliver an optimal treatment.

According to the general context of external radiotherapy described above, the needs in research and development for dosimetry could be divided into two categories:

1. Improving the techniques of treatment delivery to increase the maximum value of $P_{UTC.}$ For instance, this includes the development of ballistic of treatment and/or the possibility of using more appropriate types of particles.

2. Improving the accuracy of the delivered dose.

During research and development efforts, the two categories are often tightly bounded, since bringing new technology to the radiotherapy community immediately requires new developments regarding accuracy, and, *vice versa*, requirements in accuracy bring new technology. It is worth mentioning that research is also needed in areas other than dosimetry. Those areas include development of imaging devices and analysis for improved diagnosis and tumor delineation. Moreover, the radiobiological impact of radiation depends strongly on the type of particle and the fractionation plan chosen to treat a tumor. This last point is crucial since it allows delivering a total dose to the tumor in several fractions in such a way that tumor damage is maximized whereas healthy tissue recovering is kept at an acceptable level. Since the patient can recover between two fractions, the total dose given to the tumor can be much higher than if it was delivered in a single fraction.

This introduction first focuses on the scientific rationale for improving treatment delivery techniques and accuracy to provide an overview of the context of this thesis before defining its main objectives.

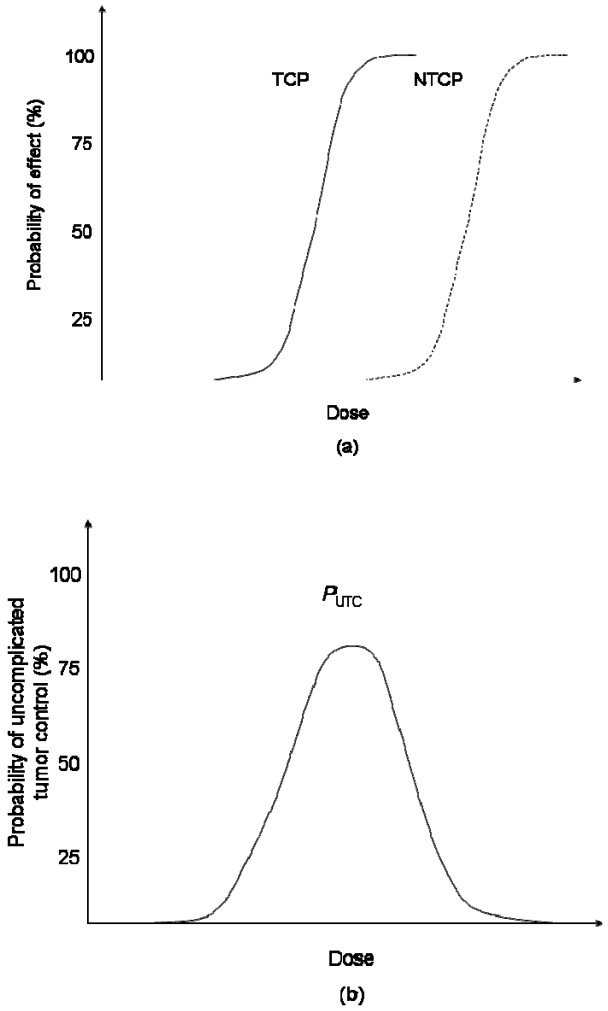


Figure 1. 1. Schematic representation of probability of tumor control (TCP) and probability of normal tissue complication (NTCP) (a) and probability of uncomplicated tumor control (P_{UTC}) (b).

1. Treatment delivery techniques

One of the main objectives of research and developments in radiotherapy, *i.e.* improve local control and/or sparing healthy tissues, may be achieved through three major means

1. Making a wide set of different types of particle available with appropriate properties regarding the dose deposition process and/or the radiobiological effect.

2. Multiplying the number of degrees of freedom to deliver the beam.

3. Improving imaging and patient positioning devices to enhance tumor tracking and reduce target volumes.

1.1. Types of particles

Radiotherapy treatments began soon after the discovery of the X-rays by Röntgen (1895) and the radium by Curie (1898), when physicians observed the tumor shrinkage when exposed to radiations (Wambersie 2002). The type of external beams used until the 1950's were restricted to X-rays with energies of order of a few hundreds of keV. At those energies, it is not possible to cure tumors located deeper than a few centimeters without causing unacceptable damage to surrounding healthy tissues. Brachytherapy was already available by using Radium gamma rays, however, it was also limited to accessible and small tumors. Radium was also used in external radiotherapy by assembling important quantities of radium. Those radium sources were used for deeper tumors, but due to the low specific activity of radium, huge treatments times (>1 hour) were necessary, which compromised the precision of the treatment.

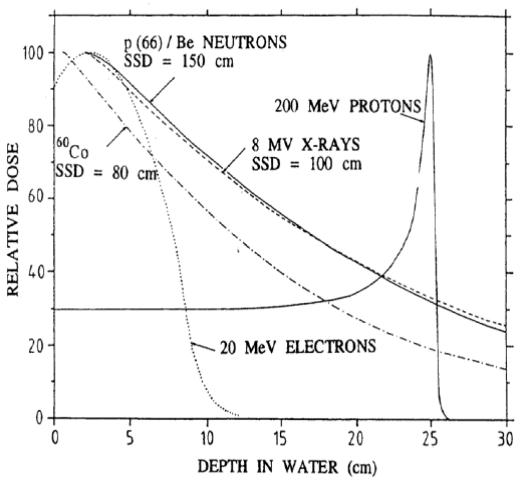
In the 1950's, electrons linear accelerator and treatment devices with cobalt sources become available, tremendously speeding up the progress in the quality of treatments with respect to the ballistic. In cobalt treatment facilities, the gamma photons emitted by the cobalt (energies of 1.1 and 1.3 MeV) are used. In linear accelerator treatment devices ("linac"), which is, by far, the most used technology today, both photon and electron beams are produced. Photon beams are produced indirectly from the accelerated electrons by the bremsstrahlung effect of the electrons striking a high-density target. The dose-deposition of photons beam in matter is characterized by an exponential attenuation and the inverse square law of the distance with respect to the photon source after a steep rising in the first centimeters (see curve (a) in Figure 1. 2). This last phenomenon, known as the build-up effect, is due to the distance needed to reach equilibrium of the secondary electrons generated by the photons. On the other hand with electrons beams, the dose deposited is maximum and relatively constant for depths within the average range of the electrons, which is

determined by their initial energy (curve (b) in Figure 1. 2). For depths close to the range of the electrons, the dose decreases rapidly until it reaches a residual dose due to the bremsstrahlung photons generated by the electrons.

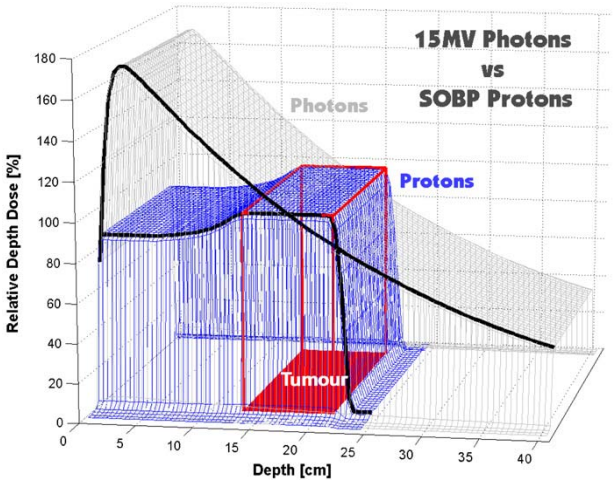
Introduced since a few decades (Smith 2006), protons beams are characterized by a much different variation of the dose with the depth than photons and electrons. Their potential interest to treat tumors was first suggested by Wilson (1946). The dose is small and constant for depth within the range of the protons and increases sharply for depths close to the range of the protons. This very narrow high-dose region is called the Bragg-peak, but may be broadened (SOBP "Spread Out Bragg Peak") by modulating the energy of the beam and distributing different Bragg-peaks over a precise distance (*i.e.* the tumor size). On the other hand, accelerating protons to the required energy for treatment is, for the moment, only possible utilizing large accelerators (*i.e.* cyclotrons or synchrotrons) which are much more expensive than electron linear accelerators.

The treatment beams described above are characterized by a different dose deposition process but have a very similar radiobiological effect. The radiobiological effect of the beams depends strongly on the type of particle used and their associated energy transfer per unit length, known as the linear-energy-transfer (LET). However, certain tumors may exhibit a higher sensitivity to certain types of radiations than healthy tissue for identical absorbed doses, depending on the linear-energy-transfer (LET). Neutrons (high LET) have a similar dose deposition process than photons (low LET) (Figure 1. 2 (a)), but have a differential radiobiological effect on certain types of tumors. Advantages of protons (dose-deposition process, (Figure 1. 2 (a) and (b)) and neutrons (high LET) can also be combined using heavy ions beams (alpha particles, carbon …). Even though treatment facilities using neutrons and heavy ions do exist, the cost and the complexity of those techniques prevent the large spread of this promising technology.

In the following sections and chapters, the contents will be restricted to photon beams, since only those were considered in this PhD thesis. It is, however, worth mentioning that the concepts developed in the two following sections 1.2 and 1.3 are generally applicable to all types of beams.



(a)



(b)

Figure 1. 2. Depth dose distribution of various types of beams. In figure (a) the proton beam is monoenergetic. In figure (b) (Smith 2006) the energies of the protons are modulated to produce a dose plateau to cover the tumor (the Spread Out Bragg Peak (SOBP)).

1.2. Multiplying the number of degrees of freedom

Computed tomography (CT) scanners were commercially available around 1972 (Webb 1993), opening the field of 3D imaging. Previously, target volumes and organs at risk could only be estimated from planar radiographic images of the patient lying in the treatment position (called the "simulation" process). During simulation, the various beam incidences, possibly coplanar, were chosen and planar radiographs acquired for each beam angle. The estimation of the dose delivered to the patient was based on severe approximations regarding the geometry and composition of the patient.

It took time before the clear potential of using 3D images was fully exploited. The main restriction was insufficient computer power to calculate 3D dose distributions in a reasonable amount of time and the unavailability of 3D treatment planning system. Limitations in the technology of treatment machines also restricted the possibilities of using many beam angles and with arbitrary field shapes.

With the fast improvements in computer technology observed in the last decades, accurate 3D conformal radiotherapy (3D-CRT) could be implemented. In this technique, the radiation oncologist draws directly the 3D volumes to be treated and the organs at risk of interest on the CT scan. The physicist's objective is to find the best angles and beam shapes to "conform" the dose to the target volume while diminishing the dose delivered to the organs at risk (Figure 1. 4 (b)). Beams with almost arbitrary shapes can be delivered using blocks or multileaf collimators (MLC, Figure 1.). 3D-CRT enables dose escalation within the tumor volume, which increases the probability of local control (Thames *et al* 1992, Hanks *et al* 1998, Hanks *et al* 1999, Mohan *et al* 1999). Moreover, diminishing the dose to organs at risk does have a clinical outcome, as with the parotids in head and neck tumors where evidence shows a correlation between the salivary function and the mean dose to the parotids (Eisbruch *et al* 1999)

Despite its wide possibilities, 3D-CRT fails to deliver concave dose distributions, which may be required in 30% of the clinical cases (Webb *et al* 2000). For instance, concave dose distributions are needed when the spinal cord is surrounded by tumor tissue in head and neck tumors. Such distributions cannot be achieved without intensity-modulated beams (Webb *et al* 2000).

1.2.1. Intensity-modulated radiation therapy

Intensity-modulated radiation therapy (IMRT) is a form of 3D-CRT (Webb 2000). The interest of IMRT was first illustrated by Brahme *et al* (1982), while the

concepts of modern IMRT were described by Brahme *et al* in 1988. IMRT consists in modulating the fluence of each beam incidence to achieve better sparing of healthy tissue and improved conformity to target volumes (Bortfeld 2006). The modulated fluence is obtained through an optimization process where the physicist defines constraints on the dose-volume histograms[1] (DVH) of target volumes and critical structures and the TPS defines the fluence maps to satisfy the user requirements (Webb 1989). This process is called inverse treatment planning unlike forward treatment planning where the user defines himself the properties of each beam (weight, wedges …), such as classic 3D-CRT. Using this technique, the resulting dose distribution may present concavities using this technique (Figure 1. 4 (c)). Evidences of potential positive clinical outcome of IMRT compared to conventional conformal techniques are reviewed in Guerrero and Nutting (2004a and 2004b).

To obtain physically irregular fluence maps, MultiLeaf Collimators (MLC) are widely used. Various techniques exist. In step-and-shoot IMRT (De Neve *et al* 1999), beams are modulated by the superposition of static fields with different MLC configurations. In dynamic IMRT, modulation is obtained by continuously moving the leaves (Burman *et al* 1997, Boyer *et al* 2000a and 2000b). These two techniques use fixed angles to deliver the beam. IMRT can also be delivered through rotational deliveries. With conventional linacs and MLCs, the technique is called intensity-modulated arc therapy (IMAT, Yu 1995), with multiple arcs, or volumetric arc therapy (VMAT) (Otto 2008), with one single arc. With the addition of the appropriate devices, conventional linacs may also be used to deliver serial (or sequential) tomotherapy (Carol *et al* 1993, Carol 1995). In this technique, a narrow rotation of a intensity modulated beam is used with the treatment couch immobilized. When the rotation is done, the treatment couch is translated by the appropriate distance, according to the slice widths. Another relatively new technique is helical tomotherapy (HT) (Mackie *et al* 1993, Mackie 2006) where modulation is obtained by the simultaneous movement of the couch, the gantry and a binary MLC. This technique allows for an increase in the number of degrees of freedom to achieve improved target conformation and better sparing of healthy tissue (Beavis 2004).

To determine whether the quality of the treatment plan improves or not with the use of one technique to another, dose-volume histograms (DVH) are often compared. Figure 1. 5 illustrates the differences between a 3D-CRT plan and a

[1] Introduced by Goetin and Verhey in Shipley *et al* (1979), a dose-volume histogram (DVH) may be defined as the volume of tissue one organ or region of interest receiving a given dose. Generally, cumulative histograms are used in clinics, even though differential histograms may sometimes provide important information.

tomotherapy (a form of IMRT) plan for two organs at risk of primary importance in head and neck tumors. Evidently, the left parotid is less irradiated in the tomotherapy plan, and this may result in a positive clinical outcome with an improved parotid function after treatment (Sultanem *et al* 2000, Hsiung *et al* 2006)



Figure 1. 3. Illustration of the MLC of the Elekta SL25.

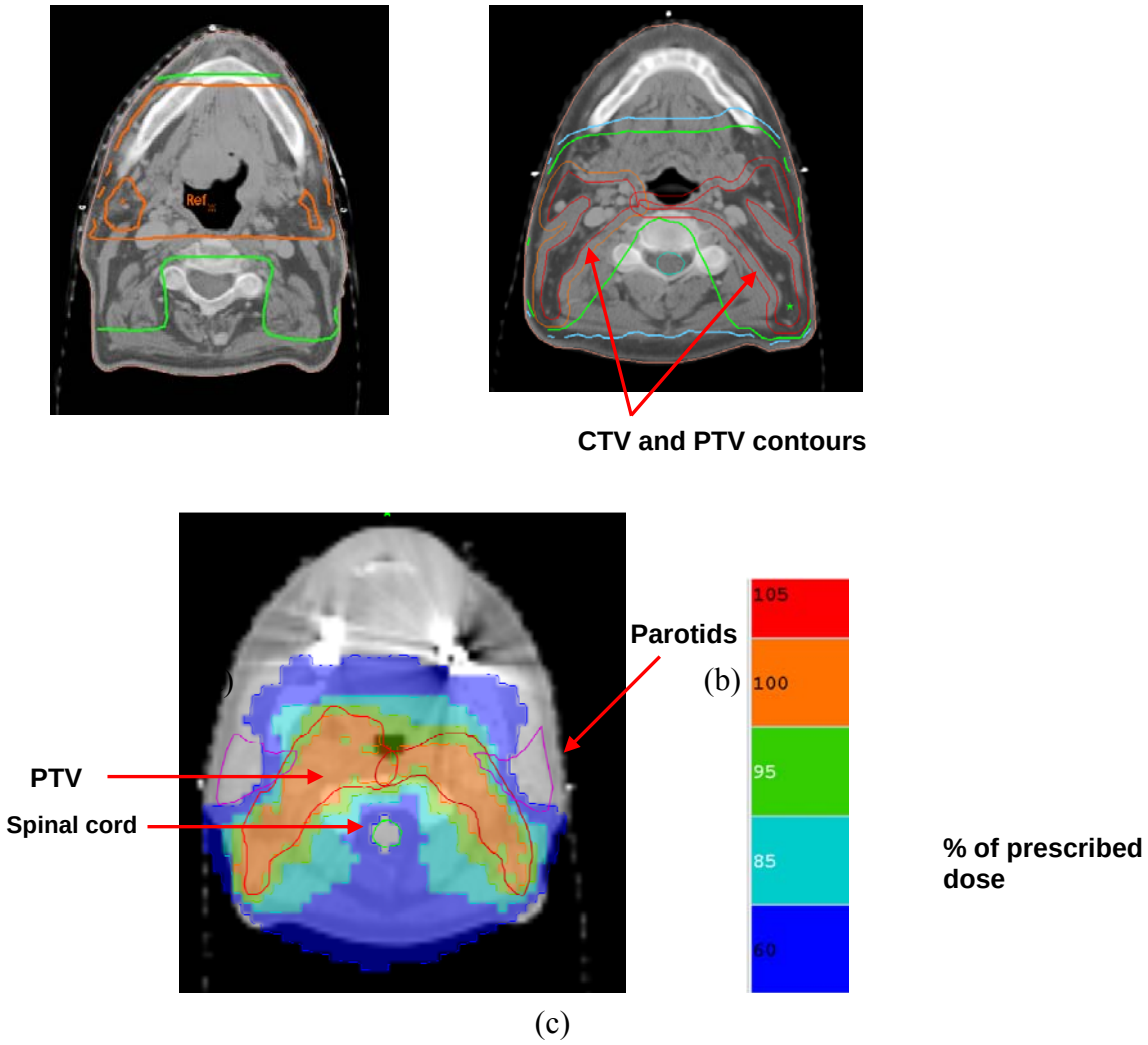


Figure 1. 4. Comparison of isodose distributions for three treatment techniques: "classic" (a), 3D-CRT (b) and intensity modulated (c) radiotherapy.

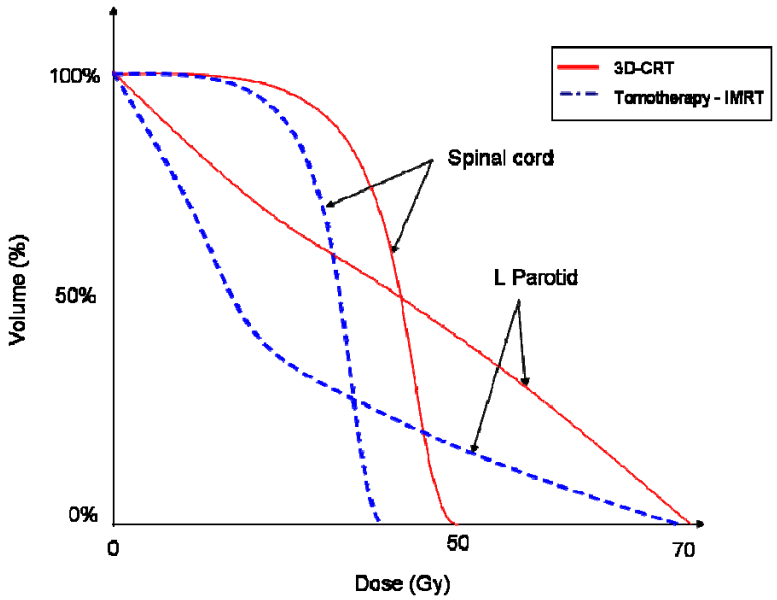


Figure 1. 5. Comparison of DVH between a tumor treated by 3D-CRT and tomotherapy (IMRT) for two organs at risk: the spinal cord and the left parotid.

1.3. Imaging and patient positioning devices

In CRT and subsequent treatment techniques, different target volumes are defined following the recommendations of ICRU reports No. 50 and 62 (International Commission of Radiations Units and Measurements). From the gross tumor volume (GTV), which is the macroscopic extension of the tumor, a clinical target volume (CTV) is constructed by adding a margin accounting for the microscopic spread of the tumor. This extension is based on biological and not geometrical considerations. The internal target volume (ITV) consists in the CTV plus a margin which accounts for the variations in the size and fluctuations in positions of the CTV in the patient reference frame which are, for instance, due to breathing or rectal contents (International Atomic Energy Agency (IAEA) 2005). The planning target volume (PTV), which is the target volume during treatment planning, includes the CTV with a geometrical margin which accounts for the internal movement of the tumor and setup errors. Those volumes are illustrated graphically in Figure 1. 6.

Evidently, larger margins lead to larger irradiated volumes and higher doses to healthy tissues. Moreover, a precise knowledge of the position of the tumor at each stage of the treatment may help avoiding a miss of the target. Therefore, high level imaging technology is essential to improve the overall quality of the treatment.

Ideally, three types of movements of the patient need to be corrected for during treatment:

1. setup error (the patient is not positioned exactly at the same position for each treatment fraction)

2. inter-fraction motion (tumor movement due to changes in the anatomy of the patient between the fractions (for instance, tumor shrinkage))

3. intra-fraction motion (tumor movement during a treatment fraction mostly due to the respiration)

In the beginning, orthogonal radiographic films were acquired using the irradiation device (Cobalt or linac) to ensure that the patient was correctly positioned for each treatment fraction. Of course, the process of developing the film is time consuming. Nowadays, films are being replaced by electronic portal imagers (EPID) placed on the arm of the linacs. Film development is, therefore, no longer required and the correction process of setup errors is faster and more reliable. Moreover, EPID can be used for dosimetry verification (Conte *et al* 1997, Kroonwijk *et al* 1997).

EPID technologies are well adapted to account for intra-fraction movement, with the possible use of markers or additional planar imaging devices. On the other hand, although it is possible to perform some inter-fraction correction using EPID technology, most of the imaging systems are used to correct for the setup error only. More advanced technologies exist to correct for inter fraction motion, among which the Cone-Beam CT (CBCT) mounted on a linac (Jaffray and Wong 1997, Jaffray *et al* 1999) or the MVCT (Megavoltage Computed Tomography) mode of the Hi-Art system of Tomotherapy (Ruchala 1999, Ruchala *et al* 2000a, Ruchala *et al* 2000b). Treatment accounting for patient motion is usually called IGRT (image-guided radiation therapy) or adaptive radiation therapy depending on whether they account for inter- and/or intra-fraction motion.

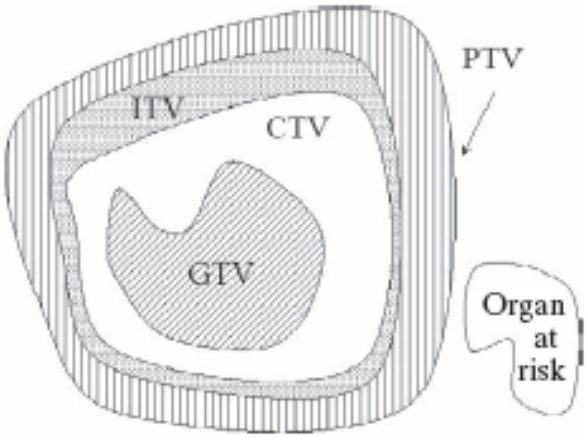


Figure 1. 6. Definition of the volumes of interest as defined in the ICRU reports 52 and 62 (figure from IAEA (2005)).

2. Dose calculation algorithms accuracy

As already mentioned, high accuracy is required due to the steep slope of *TCP*- and *NTCP*- dose relationships (Figure 1. 1). In the process of a radiotherapy treatment, many operations are involved, each one introducing a certain amount of uncertainty in the global uncertainty of the treatment, as shown in Table 1. 1 (Ahnesjö and Aspradakis 1999). Many authors tried to estimate the effect of uncertainty on cure and/or occurrence of side effects. Boyer and Schultheiss (1988) concluded that an improvement of 1% in accuracy resulted in a 2% increase of cure. Clinical effects were also reported for dose errors of 7% (Papanikolaou *et al* 2004).

Nowadays, a 5% global uncertainty is considered as a reasonable goal to achieve (Mijnheer *et al* 1987, ICRU 1976). With combined efforts in research and development, the overall uncertainty could be reduced to 2.5%, as claimed in the AAPM report 85 (Papanikolaou *et al* 2004).

Source of uncertainty	Present technique (%)	Future development (%)
Absorbed dose determination at the calibration point	2.0	1.0
Additional uncertainty for other points	1.1	0.5
Monitor stability	1.0	0.5
Beam flatness	1.5	0.8
Patient data uncertainties	1.5	1.0
Beam and patient set-up	2.5	1.6
Overall excluding dose calculation	**4.1**	**2.4**
Dose calculation	1.0 2.0 3.0 4.0 5.0	0.5 1.0 2.0 3.0 4.0
Resulting overall uncertainty	**4.2 4.6 5.1 5.7 6.5**	**2.4 2.6 3.1 3.8 4.7**

Table 1. 1. Uncertainties attached to the various processes involved in a treatment. The first column gives the values of uncertainties generally achieved while the second column provides the future accuracy goals for each process. The contribution of dose calculation uncertainty is isolated by computing the overall uncertainty first without the influence of dose calculation and afterwards with several values of the dose calculation uncertainty.

2.1. Dose calculation algorithms

The main objective of a dose calculation algorithm implemented into a treatment planning system (TPS) is to provide accurate and reliable dose distributions in a calculation time compatible with the constraints of clinical routine.

In Table 1. 1, the influence of the uncertainty of dose calculation on the overall uncertainty is clearly illustrated. If an overall uncertainty of 5% is the objective, a 3% uncertainty on the dose calculation accuracy may be accepted (Fraass *et al* 2003). On the other hand, if all the other sources of uncertainties are brought to their minimum value after intensive research and development, dose calculation accuracy must also be diminished. For a global uncertainty inferior to 3%, a dose calculation uncertainty of 2% may be considered as the maximum (Fraass *et al* 2003).

In addition to those requirements in accuracy, calculation speed is a critical aspect in clinical practice. Indeed, during direct or inverse treatment planning, dose needs to be computed several times to allow the user (physicist or physician) to verify whether the dose distribution meets the clinical requirements in the target volume and the organs at risk. Since several treatment plans have to be prepared dayly in a typical treatment center, the dose calculation process should not take more than a minute or a few minutes so that the user does not need to spend too much time waiting for the dose calculation results.

The first dose calculation algorithms were very simple. In fact, at the very beginning, monitor units were calculated by hand. In such a case, the patient was assumed to be a cubic water phantom and the monitor units were interpolated from tables obtained from extensive measurements. With the improvements in computer technology, more elaborate dose calculation algorithms were introduced. Most of them were based on the convolution/superposition (C/S) approach, (pencil-beam (PB) C/S, for instance). The specific anatomy of the patients (shape and variation in densities) as well as complex field shapes started to be taken into account (Wong and Purdy 1989). C/S algorithms are generally based on the same idea, which consists in convolving an intensity-function with an energy deposition kernel for all the interacting sites in the considered medium. The dose at a given point is obtained by the superposition of the contribution of each interacting site to this considered point. The intensity-function accounts for photon attenuation, beam shape and modulation whereas the energy deposition kernel describes the energy distribution deposited by secondary particles released from a photon interaction site. Several types of C/S algorithms exist, with different approximations. More details on those algorithms may be found in chapter 2, 3 and 7 as well as in Ahnesjö and Aspradakis (1999).

The first PB algorithms were not able to predict for modifications in secondary electron transport due to inhomogeneities. Simultaneously with the computing power, this drawback favored an increase in the complexity of those algorithms with the years, which are now able to handle approximately modifications in secondary electron transport (Ahnesjö *et al* 1989, Fogliata *et al* 2007).

Throughout the last 50 years, Monte Carlo (MC) simulations gained more and more importance in medical physics (Rogers 2006). Monte Carlo techniques are based on the use of random number generators to sample the physical formulas for radiation transport and deliver reliable "average" values of interest (like the dose, see chapter two for more details). Because available MC methods required until recently too much computation time, the use of MC simulations was restricted to research and verification purposes or to define basic data for analytical algorithms (like the energy deposition kernels, as explained in the next chapter). With the improvements in computing power, TPS using MC techniques to calculate dose distributions appeared recently (Cygler *et al* 2004, Heath *et al* 2004, Hartman Siantar *et al* 2001, Reynaert *et al* 2007). In those MC-based algorithms, approximations in physics are often performed to enhance speed, with a minimal cost in accuracy.

The development of dose calculation algorithms with the improvements in computing power with time is summarized in Figure 1. 7. Since MC is based on basic physical principles, it is generally assumed as the most accurate tool to compute dose in tissue (Verhaegen and Seuntjens 2002) and considered nowadays as the final limit of complexity one can consider for radiotherapy applications (at least with photons and electrons). The type "a", type "b" classification was proposed by Fogliata *et al* (2007) and Knöös *et al* (2006) according to whether a given algorithm completely disregards (type "a") or not (type "b") the modifications of secondary electron transport due to the presence of inhomogeneities. It is generally straightforward to classify the algorithms according to this definition. Since it is difficult to give here an exhaustive list of all the algorithms used in clinic or research, we only provide this classification for the algorithms used during this thesis, which are:

1. Single PB convolution with Modified Batho (MB) heterogeneity correction (Varian) → type "a".

2. Anisotropic Analytical Algorithm (AAA) (Varian) → type "b".

3. C/S with the collapsed-cone approximation (Tomotherapy Inc.) → type "b".

4. MC simulations → type "b".

The results shown in chapter 3 of this thesis or in Fogliata *et al* (2007) provide a clear illustration of the performances one can expect from a type "b" versus a type "a" algorithm. Details on each algorithm may be found in the following chapters.

The first developments in calculation algorithms resulted in a clinically significant improvement in accuracy. However, modern dose calculation algorithms have already a good accuracy and it is not obvious that having algorithms based on principles closer to the physical reality will result in a clinically significant gain in accuracy compared to the other sources of uncertainties listed in Table 1. 1.

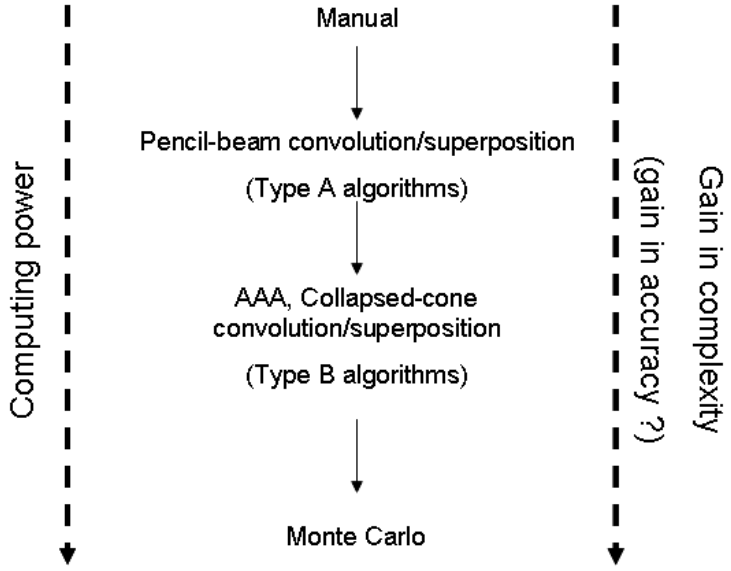


Figure 1. 7. Algorithms used in medical physics in increasing order of complexity and computing power requirements.

2.2. Influence of treatment delivery on accuracy

The inherent approximations in the physics of transport performed in analytical algorithms may influence their accuracy depending on the complexity of the treatment. Therefore, requirements in uncertainty for those algorithms are generally less severe for complex treatments, as shown in Table 1. 2 (adapted from Van Dyk *et*

al 1993 and taken from Ahnesjö and Aspradakis 1999). This is certainly the case for IMRT, which may be considered as the most complex technique clinically available today for photon beams. It requires completely different approaches in dose calculation and dosimetry than conventional and 3D-CRT in order to ensure an acceptable accuracy (Liu *et al* 2001, Siebers *et al* 2002, Bouchard and Seuntjens 2004).

	Central axis (except build-up)	High dose region Low dose gradient	Large dose gradient	Low dose region Low dose gradient
Homogeneous water slab – simple fields	2%	3%	4 mm	3% (~50%)
Stack of tissue slabs – simple fields	3%	3%	4 mm	3% (~50%)
Anthropomorphic phantoms – complex beams		4%	4mm	3% (~50%)

Table 1. 2. Dose and positional accuracy criteria for dose calculations for various configurations and regions of interest. Percentages are given relative to the calibration value, excepted in brackets where the percentages are relative to local values. Positional tolerances are defined as the distances between measured dose points and the nearest points in a calculated distribution which contain the same dose values (Ahnesjö and Aspradakis 1999, van't Veld 1997, Harms *et al* 1998)

3. Objectives of the thesis

To make the arguments more precise, let us extract the main points of section 2:

1. If research in measurements, linac manufacturing and patient positioning lead to a decrease of their uncertainties to the minimum values, then dose calculation accuracy must also be improved and the calculation uncertainty kept below 2% (Table 1. 1).

2. The accuracy of analytical algorithms may depend on the complexity of the treatment (Table 1. 2) due to the approximations performed regarding the physics of transport. Moreover, modifications in secondary electron transport in inhomogeneities are only, at most, partially taken into account. This reduces, *a priori*, the confidence one may have in analytical algorithms.

To meet a 2% calculation uncertainty goal and limit the dependence of uncertainty on treatment delivery complexity, algorithms based on MC simulations are often proposed (Fraass *et al* 2003, Reynaert *et al* 2007). Considering the fact that, in MC, each particle is tracked through the geometry of the treatment head and the patient, MC based algorithms are expected to be more accurate than other types of algorithms, especially in inhomogeneities (lung, air cavities) and for complex treatments (IMRT) (Rogers *et al* 1995, Reynaert *et al* 2007).

The diagram shown in Figure 1. 8 gives an overview of the general scope of this thesis. According to the literature cited throughout section 2, the basic hypothesis is that the combined effect of complex treatments (IMRT) and the presence of inhomogeneities may maximize the differences between MC and analytical algorithms.

Therefore, the main objective of this thesis was to compare MC with modern (type "b") analytical dose calculation algorithms already used in clinic in IMRT treatments. The added-value of MC could then be evaluated to determine whether MC should be introduced into clinical practice or not to reduce significantly the global uncertainty on the delivered dose. If no significant differences could be observed between MC and analytical algorithms for complex cases, then introducing MC into clinic would become harder to justify since no differences should be expected for simpler cases neither.

This study was done for the two IMRT delivery techniques proposed in our institution: step-and-shoot IMRT with an Elekta SL25 linear accelerator and helical tomotherapy. For tomotherapy, moreover, the modeling part was also an important objective of this thesis since it is the first time that a complete MC simulation of the Hi-Art^{TM} machine was performed with all the technical details fully disclosed by the manufacturer.

Phantom and clinical studies comparing MC and various types of algorithms already exist in the literature, most of them regrouped in two excellent reviews (Reynaert *et al* 2007, Chetty *et al* 2008). However, both reviews insist on the need for additional clinical examples to determine whether introducing Monte Carlo Treatment Planning (MCTP) into clinical practice does significantly improve accuracy. This PhD

thesis answers to this wish (at least partially) and will make an effort to give a significant contribution to the debate between pro- and con- MCTP (Mohan *et al* 2001).

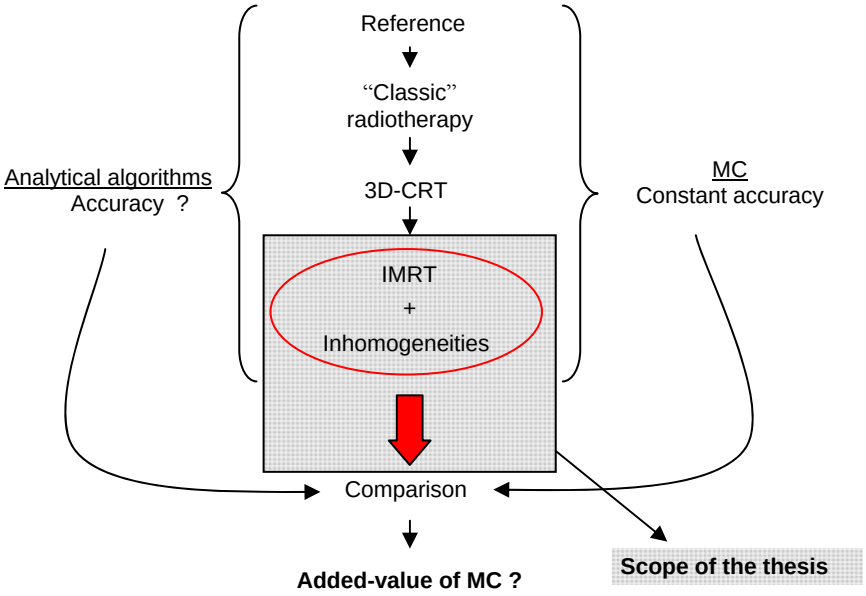


Figure 1. 8. Treatment delivery techniques with photons in increasing order of complexity. Where MC accuracy should exhibit negligible influence with treatment setup, accuracy of analytical algorithms is more a matter of concern. The thesis focuses on the *a priori* most challenging clinical situations for analytical algorithms, which are IMRT treatments for tumors surrounded by a great amount of inhomogeneities.

The next chapter will provide a brief theoretical background of the various notions used in this thesis. More specifically, the physics of the different dose calculation algorithms will be explored, with more details given for the physics of MC simulations.

The following chapters present the papers published during the thesis. These are organized around three main subjects of which an overview is given in Table 1. 3. The first subject (chapter 3) concerns the MC modeling of the Elekta SL25 linac in the step-and-shoot IMRT mode for the 6MV photon beam. As an application, the model was used to evaluate the accuracy of the new algorithm released by Varian, AAA. The first part of the evaluation was based on a comparison between MC, AAA and

measurements in inhomogeneous phantoms using small fields. Clinical IMRT treatments calculated both with MC and AAA were thereafter compared to estimate the clinical impact of the approximations in the physics of transport. The modeling and experiments are detailed in Sterpin *et al* (2007a). Several papers were published on the evaluation of the performance of AAA (Van Esch *et al* 2006, Fogliata *et al* 2006 and 2007, Bragg and Conway 2006, Knöös *et al* 2006), but none of them included IMRT clinical plans in their study, which was the main purpose of Sterpin *et al* (2007a).

The second subject concerned the modeling of the Hi-Art^{TM} HT machine, which was realized in a strong collaboration with Tomotherapy Inc. In the first paper, the speed of the simulation was a secondary issue. This was not the case for the HT machine, since the objective of the collaboration was to build a model fast enough to make future implementation of the MC model in the Hi-Art^{TM} system possible. Of course, the gain in speed could not be obtained at a price of a loss in accuracy. Because of the requirements in simulation speed combined with the fact that it was the first complete MC simulation of HT, three papers were necessary to fully describe the MC model (Sterpin *et al* 2007b, Sterpin *et al* 2008a and Sterpin *et al* 2008b)

The first paper (chapter 4) describes the simulation of the static mode and the tuning of the MC model of the treatment head. The second paper (chapter 5) describes a fast simulation strategy of the MLC. The MLC is the only part of the treatment head that needs to be actually simulated during a treatment, since the other parts remain fixed (with respect to the electron source) and can be simulated once and for all. Therefore, large gains in simulation speed may be obtained by simplifying the transport through the MLC. The last paper (chapter 6) summarizes the two first papers but extensively describes the MC model of the helical mode called TomoPen.

The last paper (Sterpin *et al* 2008c, chapter 7), submitted but not yet accepted, followed a similar approach as in Sterpin *et al* (2007a) but for the HT machine using the TomoPen model. Again, it was the first time that a MC evaluation of the accuracy of the dose calculation algorithm delivered with the HT system was performed.

Chapter #	Title	Year	Contents
3	Monte Carlo simulation of the AAA treatment planning algorithm in a heterogeneous multilayer phantom and IMRT clinical treatments for an Elekta SL25 linear accelerator	2007a	MC modeling of the Elekta SL25 with BEAM/EGSnrc in the 6MV mode for IMRT. Evaluation of the Varian-AAA algorithm in phantoms and clinical cases
4	Monte Carlo simulation of the Tomotherapy treatment unit in the static mode using MC HAMMER, a Monte Carlo tool dedicated to Tomotherapy	2007b	Description of the fast MC model of helical tomotherapy
5	Analytical model of the binary multileaf collimator of Tomotherapy for Monte Carlo simulations	2008a	
6	Monte Carlo simulation of helical Tomotherapy with PENELOPE	2008b	
7	Monte Carlo evaluation of the C/S algorithm of Hi-Art^{TM} tomotherapy in heterogeneous phantoms and clinical cases	2008c	Evaluation of the accuracy of the TPS of tomotherapy in phantoms and clinical cases

Table 1. 3. Overview of the papers published during the thesis.

4. References

Ahnesjö A 1989 Collapsed cone convolution of radiant energy for photon dose calculation in heterogeneous media *Med. Phys.* **16** 577–92

Ahnesjö A and Aspradakis M M 1999 Dose calculations for external photon beams in radiotherapy *Phys. Med. Biol.* **44** R99-155

Beavis A W 2004 Is tomotherapy the future of IMRT *Br. J. Radiol.* **77** 285-95

Boyer A L and Schultheiss T 1988 Effects of dosimetric and clinical uncertainty on complication-free local tumor control *Radiother. Oncol.* **11** 65-71

Brahme A, Roos J E and Lax I 1982 Solution of an integral equation encountered in rotation therapy *Phys. Med. Biol.* **27** 1221-9

Brahme A 1988 Optimistion of stationary and moving beam radiation therapy techniques *Radiother. Oncol.* **12** 129-40

Bortfeld T 2006 IMRT: a review and preview *Phys. Med. Biol.* **51** R363-79

Bouchard H and Seuntjens J 2004 Ionization chamber-based reference dosimetry of intensity modulated radiation beams *Med. Phys.* **31** 2454-65

Boyer A, Xing L, Luxton G and Ma C-M 2000a DMLC IMRT is sufficient for all clinical purposes *Proc. 13th INt. Conf. on the Use of computers in Radiation Therapy (Heidelberg, May 2000)* ed W Schlegel and T Brotefeld (Heigelberg: Springer) pp 7-9

Boyer A, Xing L, Luxton G and Ma C-M 2000b DMLC IMRT by dynamic MLC *Proc. 13th INt. Conf. on the Use of computers in Radiation Therapy (Heidelberg, May 2000)* ed W Schlegel and T Brotefeld (Heigelberg: Springer) pp 160-3

Bragg C M and Conway J 2006 Dosimetric verification of the anisotropic analytical algorithm for radiotherapy treatment planning *Radiother. Oncol.* **81** 315-23

Burman C, Chui C S, Kutcher G, Leibel S, Zelefsky M, LoSasso T, Spirou S, Wu Q W, Yang J, Stein J, Mohan R, Fuks Z and Ling C C 1997 Planning, delivery, and quality assurance of intensity-modulated radiotherapy using dynamic multileaf collimator: a strategy for large-scale implementation for the treatment of carcinoma of the prostate *Int. J. Radiat. Oncol. Biol. Phys.* **39** 863-73

Carol M P *et al* 1993 An automatic 3D treatment planning and implementation system for optimized conformal therapy. *Three-Dimensional Treatment Planning* ed P Minet (Geneva: WHO) pp 173-87

Carol M P 1995 A system for planning and rotational delivery of intensity-modulated fields *Int. J. Imaging Syst. Tech.* **6** 56-61

Chetty I J, Curran B, Cygler J E, DeMarco J J, Ezzell G, Faddegon B A, Kawrakow I, Keall P J, Liu H, Ma C M, Rogers D W O, Seuntjens J, Sheikh-Bagheri D and Siebers J V 2007 Report of the AAPM Task Group No. 105: Issues associated with clinical implementation of Monte Carlo-based photon and electron external beam treatment planning *Med. Phys.* **34** 4818-53

Ching-Li H an Volodin V 1993 Opening statement *Three-Dimensional Treatment Planning (Proc. EAR Conf. (WHO, Geneva, 1992))* ed P Minet (Geneva:Minet) pp xix-xxi Clinical delivery of intensity modulated conformal radiotherapy for relapsed or second-primary head and neck cancer using a multileaf collimator with dynamic control *Radioth. Oncol.* **50** 301-14

Conte L, Stucchi P, Mordacchini C, Bianchi C, Monciardini M, Novario R, Cassani E, Mantovani R, Antognoni P and Tordiglione M 1997 The use of an electronic portal imaging device for exit dosimetry *Proc. 12th Int. Conf. on the Use of Computers in*

Radiation Therapy (Salt Lake City, Utah, May 1997) ed D D Leavitt and G Starkschall (Madison, WI: Medical Physics Publishing) pp 279-81

Cygler J E, Daskalov G M, chang G H and ding G X 2004 Evaluation of the first Monte Carlo dose calculation engine for electrorn beam treatment planning *Med. Phys.* **31** 142-53

De Neve W, De Gersem W, Derycke S, De Meerleer G, Moerman M, Bate M T, Van Duyse B, Vakaet L, De Deene Y, Mersseman B and De Wagter C 1999 Clinical delivery of intensity modulated conformal radiotherapy for relapsed or second-primary head and neck cancer using a multileaf collimator with dynamic control *Radiother. Oncol.* **50** 301-14

Eisbruch A, Tenhaken RK, Kim HM et al. Dose, volume and relationships in parotid salivary glands following conformal and intensity-modulated irradiation of head and neck cancer. Int J Radiat Oncol Biol Phys 1999;45:577-587

Fogliata A, Nicolini G, Vanetti G, Clivio A and Cozzi L 2006 Dosimetric validation of the anisotropic analytical algorithm for photon dose calculation: fundamental characterization in water *Phys. Med. Biol.* **51** 1421-38

Fogliata A, Vanetti E, Albers D, Brink C, Clivio A, Knöös T, Nicolini G and Cozzi L 2007 On the dosimetric behaviour of photon dose calculation algorithms in the presence of simple geometric heterogeneities: comparison with Monte Carlo *Phys. Med. Biol.* **52** 1363-85

Fraass B A, Smathers J and Deye J 2003 Summary and recommendations of a National Cancer Institute workshop on issues limiting the clinical use of Monte Carlo dose calculation algorithms for megavoltage external beam radiation therapy *Med. Phys.* **30** 3206-16

Guerrero U M T and Nutting C M 2004a Clinical use of intensity modulated radiotherapy part I *Br. J. Radiol.* **77** 88-96

Guerrero U M T and Nutting C M 2004b Clinical use of intensity modulated radiotherapy part II *Br. J. Radiol.* **77** 177-82

Hanks G E, Hanlon A L, Schultheiss T E, Pinover W H, Movsas B, Epstein B E, and Hunt M A 1998 Dose escalation with 3D conformal treatment: Five year outcomes, treatment optimization, and future directions *Int. J. Radiat. Oncol., Biol., Phys.* **41**501–10

Hanks G E, Hanlon A L, Pinover W H, Horwitz E M and Schultheiss T E 1999 Survival advantage for prostate cancer patients treated with high-dose three-dimensional conformal radiotherapy *Cancer J. Sci. Am.* **5** 152-8

ICRU 1976 Determination of absorbed dose in a patient irradiated by beams of x or gamma rays in radiotherapy procedures *ICRU Publication* 24 (Bethesda, MD: International Commission on Radiation Units and Measurements)

Harms W B, Low D A, Wong J W and Purdy J A 1998 A software tool for the quantitative evaluation of 3D dose calculation algorithms *Med. Phys.* **25** 1830-36

Hartmann Siantar C L *et al* 2001 Description and dosimetric verification of the PEREGRINE Monte Carlo dose calculation system for photon beams incident on a water phantom *Med. Phys.* **28** 1322-37

Heath E, Seuntjens J and Sheik-Bagheri D 2004 Dosimetric evaluation of the clinical implementation of the first commercial IMRT Monte Carlo treatment planning system at 6 MV *Med. Phys.* **31** 2771-9

Hsiung C-Y, Ting H-M, Huang H-Y, Lee C-H, Huang E-Y and Hsu H-C 2006 Parotid-sparing intensity modulated radiotherapy for nasopharyngeal carcinoma: preserved parotid function after IMRT on quantitative salivary scintigraphy and comparison with historical data after conventional radiotherapy *Int. J. Radiat. Oncol. Biol. Phys.* **66** 451-61

IAEA 2005 *Radiation Oncology Physics: a handbook for teachers and students* IAEA Vienna

ICRU 1993 Prescriping, recording and reporting photon beam therapy *ICRU Publication* 50 (Bethesda, MD: International Commission on Radiation Units and Measurements)

ICRU 1999 Prescriping, recording and reporting photon beam therapy (Supplement to ICRU publication 50) *ICRU Publication* 62 (Bethesda, MD: International Commission on Radiation Units and Measurements)

Jaffray D A and Wong J W 1997 Exploring 'target of the day' strategies for a medical linear accelerator with conebeam-CT scanning capability *Proc. 12th Int. conf. on the Uose of Computers in Radiatino Therapy (Salt Lake City, Utah, May 1997)* ed D D Leavitt and G Starkschall (Madison, WI: Medical Physics Publishing) pp 172-5

Jaffray D A, Drake D G, Moreau M, Martinez A A and Wong J W 1999 A radiographic and tomographic imaging system integrated into a medical linear accelerator for localisation of bone and sof-tissue targets *Int. J. Radiat. Oncol. Biol. Phys.* **45** 773-89

Knöös T, Wieslander E, Cozzi L, Briunk C, Fogliata A, Albers D, Nyström and Lassen S 2006 Comparison of dose calculation algorithms for treatment planning in external photon beam therapy for clinical situations *Phys. Med. Biol.* **51** 5785-807

Kroonwijk M, Pasma K L, Quint S, visser A G and Hijmen B J M 1997 Development and clinical implementation of in-vivo dosimetry using an electronic portal imaging device *Proc. 12th Int. conf. on the Use of Computers in Radiation Therapy (Salt Lake*

City, Utah, May 1997) ed D D Leavitt and G Starkschall (Madison, WI: Medical Physics Publishing) pp 276-8

Kuhn Gerard 2001 Towards IMRT treatments in head and neck tumors: implementation and dosimetric verificationof a new treatment technique *University College London* 2001

Liu H H, Verhaegen F and Dong L 2001 A method of simulating dynamic multileaf collimators using Monte Carlo techniques for intensity-modulated radiation therapy *Phys. Med. Biol.* **46** 2283-98

Mackie T R, Holmes T W, Swerdloff S, Reckwerdt P J, Deasy J O, Yang J, Paliwal B R and Kinsella T J 1993 Tomotherapy: a new concept in delivery of dynamic conformal radiotherapy *Med. Phys.* **20** 1709-19

Mackie T R 2006 History of Tomotherapy *Phys. Med. Biol.* **51** R427-53

Mijnheer B J, Battermann J J and Wambersie A 1987 What degree of accuracy is required and can be achieved in photon and neutron therapy? *Radiother. Oncol.* **8** 237-52

Mohan R, Cardinale R and Hagen M 1999 Comments on 'Further improvements in dose distributions are unlikely to affect cure rates' [1999 *Med. Phys.* **26** 1007-9] *Med. Phys.* **26** 2701-3

Mohan R, Antolak J and Hendee W R 2001 Monte Carlo techniques should replace analytical methods for estimating dose distributions in radiotherapy treatment planning *Med. Phys.* **28** 123-6

Otto K 2008 Volumetric modulated arc therapy: IMRT in a single gantry arc *Med. Phys.* **35** 310-7

Papanikolaou N, Battista J, Boyer A, Kappas C, Klein N, Mackie T R, Sharpe M and Van Dyk J 2004 Tissue inhomogeneity corrections for megavoltage photon beams. AAPM report No 85, task group No 65 of the radiation therapy committee of the American association of physisicts in medicin. Madison: medical physics publishingReynaert N, van der Marck S C, Schaart D R, Van der Zee W, Van Vliet-Vroegindeweij, Tomsej M, Jansen J, Heijmen B, Coghe M, De Wagter C 2007 Monte Carlo treatment planning for photon and electron beams *Radiation Phys. and Chem.* **76** 643-86

Rogers D W O 2006 Fifty years of Monte Carlo simulations for medical physics *Phys. Med. Biol.* **51** R287-301

Rogers D W O, Faddegon B A, Ding G X, Ma C M, We J and Mackie T R 1995 BEAM: a Monte Carlo code to simulate radiotherapy treatment units *Med. Phys.* **22** 503-24

Ruchala K 1999 Megavoltage CT for Tomotherapy verification *PhD Thesis* University of Wisconsin, Madison, WI

Ruchala K J, Olivera G H, Schloesser E A, Hinderer R and Mackie T R 2000a Calibration of a tomotherapeutic MVCT system *Phys. Med. Biol.* **45** N27-N36

Ruchala K J, Olivera G H, Kapatoes J M, Schloesser E A, Reckwerdt P J and Mackie T R 2000b Megavoltage CT image reconstruction during tomotherapy treatments *Phys. Med. Biol.* **45** 3545-62

Shipley W U, Tepper J E, Prout G R, Verhey L J, Mendiondo O A, Goitein M, Koehler A M and Suit H D 1979 Proton radiation as boost therapy for localized prostatic carcinoma *JAMA* **241** 1912–5

Siebers J V, Keall P J, Kim J O and Mohan R 2002 A method for photon beam Monte Carlo multileaf collimator particle transport *Phys. Med. Biol.* **47** 3225-32

Smith A R 2006 Proton Therapy *Phys. Med. Biol.* **51** R491-504

Sterpin E, Tomsej M, Reynaert N, De Smedt B and Vynckier S 2007a Monte Carlo simulation of the AAA treatment planning algorithm in a heterogeneous multiplayer phantom and IMRT clinical treatments for an Elekta SL25 linear accelerator *Med. Phys.* **34** 1665-77

Sterpin E, Tomsej M, Cravens B, Salvat F, Ruchala K, Olivera G H and S Vynckier 2007b Monte Carlo simulation of the Tomotherapy treatment unit in the static mode using MC HAMMER, a Monte Carlo tool dedicated to Tomotherapy *JPCS* **74** 021019

Sterpin E, Salvat F, Olivera G H and Vynckier S 2008a Analytical model of the binary multileaf collimator of Tomotherapy for Monte Carlo simulations *J. Phys.: Conf. Ser.* **102** 012022

Sterpin E, Salvat F, Cravens R, Ruchala K, Olivera G H and Vynckier S 2008b Monte Carlo simulation of helical Tomotherapy with PENELOPE *Phys. Med. Biol.* **53** 2161-80

Sterpin E and Vynckier S 2008c Monte Carlo evaluation of the convolution/superposition algorithm of Hi-Art^{TM} tomotherapy in heterogeneous phantoms and clinical cases *submitted to Med. Phys.*

Sultanem K, Shu H K, Xia P, Akazawa C, Quivey J M, Verhey L J and Fu K K 2000 Three dimensional intensity-modulated radiotherapy for nasopharyngeal carcinoma: the University of California-San Francisco experience *Int. J. Radiat. Oncol. Biol. Phys.* **48** 711-22

Thames H D, Schultheiss T E, Hendry J H, Tucker S L, Dubray B M and Brock W A 1992 Can modest escalations of dose be detected as increased tumor control *Int. J. Radiat. Oncol. Biol. Phys.* **22** 241-6

Van Dyk J, Barnett R B, Cygler J E and Shragge P C 1993 Commissioning and quality assurance of treatment planning computers *Int. J. Radiat. Oncol. Biol. Phys.* **26** 261–73

Van Esch A, Tillikainen L, Pyykkonen J, Tenhunen M, Helminen H, Siljamäki S, Alakuijala J, Paiusco M, Iori M, Huyskens D P 2006 Testing of the analytical anisotropic algorithm for photon dose calculation *Med. Phys.* **33** 4130-48

van't Veld A A 1997 Analysis of accuracy in dose and position in calculations of a treatment planning system for blocked photon fields *Radiother. Oncol.* **45** 245–51

Wambersie A 2002 Du radium aux accélérateurs linéaires et aux ions lourds *50 ans de médecine à l'UCL* (Editions Racine)

Webb S 1993 *The physics of Three-Dimensional Radiation Therapy: Conformal Radiotherapy, Radiosurgery and Treatment Planning* (Bristol: Institue of Physics Publishing)

Webb S 1989 Optimization of conformal radiotherapy dose distributions by simulated annealing *Phys. Med. Biol.* **34** 1349-70

Webb S 2000 *Intensity Modulated Radiation Therapy* (Bristol: Institute of Physics Publishing)

Wong J W and Purdy J A 1989 On methods of inhomogeneity corrections for photon transport *Med. Phys.* **17** 807-14

Yu C X, 1995 Intensity-modulated arc therapy with dynamic multileaf collimation: an alternative to tomotherapy *Phys. Med. Biol.* **40** 1435-49

Chapter 2: Theory

1. Absorbed dose and electronic equilibrium

1.1. Absorbed dose

The absorbed dose is the quotient between the energy $\Delta\varepsilon$ imparted by ionizing radiation to mass Δm in a small volume ΔV:

$$D = \Delta\varepsilon / \Delta m \qquad \textbf{(1)}$$

The energy imparted $\Delta\varepsilon$ is the sum of energies (including the rest energy of massive particles) of all particles entering the volume minus the energy of all particles leaving the volume. The dose is a local function of position. It is worth mentioning that the considered volume cannot be infinitesimal and must have therefore a certain volume such that statistical fluctuations of the energy loss process of charged particles are negligible in the considered volume (Attix *et al* 1968).

1.2. Electronic equilibrium

If the number of electrons entering the volume V is exactly equal to the number of electrons that leave the volume V, then the situation is called charged particle equilibrium. Electronic equilibrium allows for drastic simplifications in secondary electron transport since secondary electron dose distributions remain essentially constant in the irradiated volume where electron equilibrium holds and secondary electrons generated by photon interactions may be considered to deposit their energy locally in a first approximation.

Under conditions of electronic disequilibrium, the behavior of the secondary electrons may have a strong influence on the dose. At an interface between low-density and high-density media, underdosage may occur in the high density region since the electrons leaving the volume are not replaced by electrons coming from the low-density region because of the reduced number of photons interactions in the low-density region. The most famous example in clinic is that, when a photon beam enters a patient, the dose is reduced in the first centimeters (the so-called “build-up” region illustrated in Figure 2. 1 (left picture)) and allows for skin sparing in photon beams.

This electronic disequilibrium is mainly due to a deficit of secondary electrons in the direction of the photon beam. A similar effect may also be observed due to lateral electronic disequilibrium. In water, this occurs if half the field width is smaller than the mean lateral component of the range of secondary electron in water (De Vlamynck *et al* 1999). Since the lateral range is inversely proportional to the density, in a rough approximation, conditions for lateral electronic disequilibrium are very likely to be encountered in low density tissues (such as lungs), especially for small fields or a superposition of small fields, like, for instance, IMRT. Moreover, in low density media, the penumbra at the beam edges is less sharp because of a dosimetric blurring introduced by the increased range of the electrons. Those two effects, dose drop and dosimetric blurring are both illustrated in Figure 2. 1 on the left and right side, respectively.

2. MC simulations

2.1. Generalities on MC simulations

Giving a generic definition of MC simulations is not a trivial task due to the wide variety of applications, from the determination of the number π to the resolution of complex integrals. In all the applications of the Monte Carlo method, a stochastic model is built in which the expected value of a random number is equivalent to a physical value. This expected value is estimated by the average of many independents samplings representing the random number introduced above. For the constructions of the series of independent samplings, other random variables are used according to the distributions of the random variable to estimate. Since the delivered value is an average, it is also associated with a standard deviation.

In our particular case of radiation transport, a MC method consists of generating a large number of random particle histories, that is, sequences of free flights, interaction events (with occasional generation of energetic secondary particles). The location and the result of each interaction (namely, angular deflection, energy loss and secondary particle production) are determined from probability distributions dictated by the physics of the interactions, which is dictated by the so-called differential cross-sections. Quantitative values of interest are then obtained by averaging over a large number of simulated histories. In our case, of course, the principal quantity to be determined is the dose distribution.

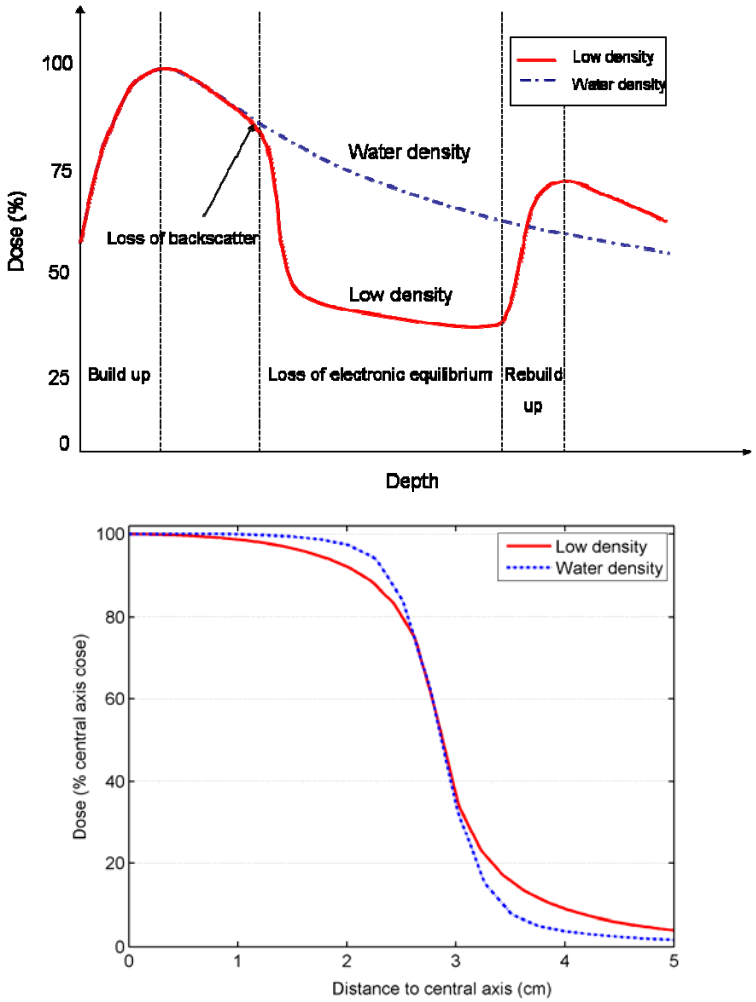


Figure 2. 1. Effect of electronic disequilibrium on dose distributions. The upper plot shows the effect of the lateral electronic disequilibrium on depth dose distributions. The lower plot illustrates the penumbra widening effect in a lateral profile.

2.2. Monte Carlo codes used in medical physics

In radiation transport, a number of MC codes exist, but some of them are more adapted to the problems encountered in radiotherapy. The most known are PENELOPE (Salvat *et al* 2006), EGSnrc (Kawrakow 2000a, Kawrakow and Rogers 2000) (based on the popular EGS4 (Nelson *et al* (1985)), MCNP (Biresmeister 2000,

Waters 2002) and GEANT (Agostinelli *et al* 2003). PENELOPE and EGSnrc are restricted to electron/positron and photon transport, whereas MCNP and GEANT may simulate many other particles, like neutrons or protons. PENELOPE and EGSnrc are therefore focused on the particles of interest in medical physics. EGSnrc has been benchmarked extensively and a very good accuracy for external radiotherapy applications was proven even in extreme situations (Kawrakow 2000b, Verhaegen 2002). PENELOPE also demonstrated its capabilities for radiotherapy applications (Sempau *et al* 2003, Sempau *et al* 2006, Al-dweri *et al* 2005), and was benchmarked by other MC codes (Ye *et al* 2005, Mazurier *et al* 2001, Siegbahn *et al* 2003). In various publications (Jeraj *et al* 2002, Schaart *et al* 2002, Reynaert *et al* 2002, Carrier *et al* 2004, Rodrigues *et al* 2004, Torres *et al* 2004, Poon and Verhaegen 2005, Poon *et al* 2005), MCNP and GEANT have shown less accuracy and/or more sensitivity to transport parameters than PENELOPE and EGSnrc, which renders those codes less suitable for MCTP. Nonetheless, MCNP and GEANT developers release new versions with improvements which will help those codes playing a more important role in the radiotherapy field. It has also to be mentioned that other particles than electrons/positrons or photons may be produced in photon beams. Indeed, at high nominal energies (18MV or higher), the production of neutrons and protons in the treatment head may have a significant contribution to the dose to the patient (Chibani and Ma 2003). MCNP and GEANT can handle those particles, which may be an advantage for some specific effects.

In this work, PENELOPE and EGSnrc are only used. Many aspects of the underlying physics of PENELOPE and EGS are essentially the same, especially for photon transport. However, for some issues related to electron transport, their approaches differ significantly. PENELOPE is delivered with a detailed manual (Salvat *et al* 2006) which provides not only instructions to perform simulations but also relatively detailed information on the Monte Carlo algorithm itself and the underlying physics. Moreover, it is the most used code in this PhD thesis. Therefore, we will focus on the physics of PENELOPE in the following sections whereas the physics of EGSnrc will be explored only when the differences with PENELOPE may have some impact on the simulations.

2.3. Photon interactions

In the following sections, only the dominant interactions occurring at energies encountered in external radiotherapy are described (roughly, from 100 keV to around 30 MeV).

- Photoelectric absorption
- Coherent scattering (Rayleigh)
- Incoherent scattering (Compton)
- Electron-positron pair production

The interactions processes are illustrated in Figure 2. 2. As mentioned above, photonuclear absorption and subsequent neutron and/or proton emission are disregarded, which does not introduce substantial errors for most of the applications (Hubbell *et al* 1980).

Cross-sections of compounds or mixtures are always calculated from cross-sections of atoms using the additivity approximation, *i.e.*, the molecular cross section for a process is approximated by the sum of the atomic cross sections of all the atoms in the molecule. This approximation is assumed to be valid for the radiotherapy applications (Salvat *et al* 2006).

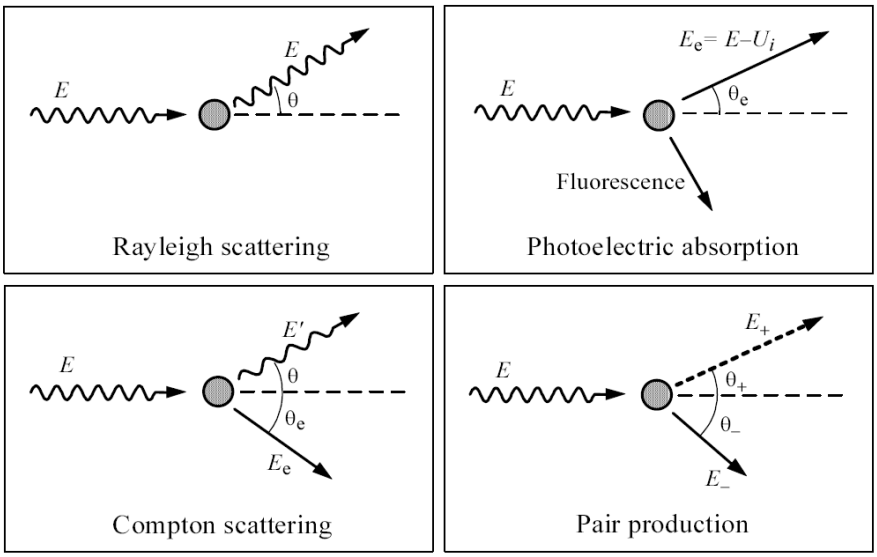


Figure 2. 2. Basic interactions of photons with matter (from Salvat *et al* 2006).

2.3.1. Photoelectric effect

In the photoelectric effect, a photon of energy E is absorbed by an atom which ejects an electron. In PENELOPE, only single-photon absorption is accounted for. This hypothesis is valid for low-density photon beams, which is the case in

radiotherapy. The cross sections are extracted from the LLNL Evaluated Photon Data Library (EPDL, Cullen *et al* 1997). Above 1 keV, they are accurate within a few percent (Cullen *et al* 1997). For compounds and mixtures, the cross sections are calculated using the additivity rule. The simulation of the photoelectric effect consists in selecting the element where the interaction occurs, selecting the shell of the element which is ionized and then determining the direction of the emitted photoelectron.

2.3.2. Coherent (Rayleigh) scattering

In this process, photons are scattered without losing energy. The differential cross-section given by Born (1969) is not perfectly adequate for energies close to the K absorption edge. However, at those energies, the photoelectric effect is much more dominant than the coherent scattering, and therefore the accuracy of the cross-section used in PENELOPE is sufficient for the simulations.

2.3.3. Incoherent (Compton) scattering

In the Compton effect, a photon is scattered by weakly bounded electron. The scattered photon transfers part of its energy to the electron (incoherent scattering). Different approaches can be used to simulate Compton scattering. A rough approximation is to consider the target electrons free and at rest. Under this approximation, the differential cross-section is given by the well known Klein-Nishina formula. In reality, however, electrons are bounded and not at rest (Doppler broadening). In PENELOPE, the differential cross-section accounts for the binding energies and the Doppler broadening, which gives significant differences compared to Klein-Nishina cross section, especially for low energies (effect of binding) and large (Doppler broadening) transferred energies.

2.3.4. Electron-positron pair production

When a photon is absorbed in the vicinity of a massive particle, a nucleus or an electron, it can be absorbed and electron-positron pairs are then created. When the interaction occurs in the field of a nucleus, the phenomenon is called pair production. This can occur only if the energy of the photon is higher than twice the rest energy of the electron (511 keV). When the interaction occurs in the vicinity of an electron, appreciable kinetic energy is transferred to the target electron, and the phenomenon is

called triplet production. The threshold energy, assuming the target electron is at rest, is 4 times the rest energy of the electron. The differential cross-section used in PENELOPE is based on the high-energy theory of Bethe and Heitler, which corresponds to the ultra-relativistic Born approximation (Motz *et al* 1969, Tsai 1974).

PENELOPE uses the Bethe-Heitler formula only to select the kinetic energy of the produced pair. The mean free paths for pair production are rather obtained from interpolation of a table generated by XCOM (Berger and Hubbel, 1987). It is also worth mentioning that even though triplet production is accounted for in the total cross sections, the events are simulated as if they were pairs. This does not introduce significant errors, since the recoil electron has a mean free path much smaller than that of the incident photon.

2.3.5. Attenuation coefficients

Photons perpendicular to a semi-infinite material of thickness x will have a probability to face no interaction with the material given by

$$p(x) = e^{-\mu x} \qquad \textbf{(2)}$$

where μ is the attenuation coefficient which can be expressed as

$$\frac{\mu}{\rho} = \frac{N_A}{A_M}(\sigma_{ph} + \sigma_{Ra} + \sigma_{Co} + \sigma_{pp}) \qquad \textbf{(3)}$$

N_A and A_M are the Avogadro number and the molar mass, respectively. σ_{ph}, σ_{Ra}, σ_{Co} and σ_{pp} are the photoelectric, Rayleigh, Compton and pair-production total cross-sections, respectively. Two examples of the variation of the attenuation coefficient with the energy of the incident photon are illustrated in Figure 2. 3. From this figure, it may be observed that the dominant interaction process in patients (mostly water) for the main energies encountered in this work (100 keV to 6 MeV) is evidently the Compton interaction.

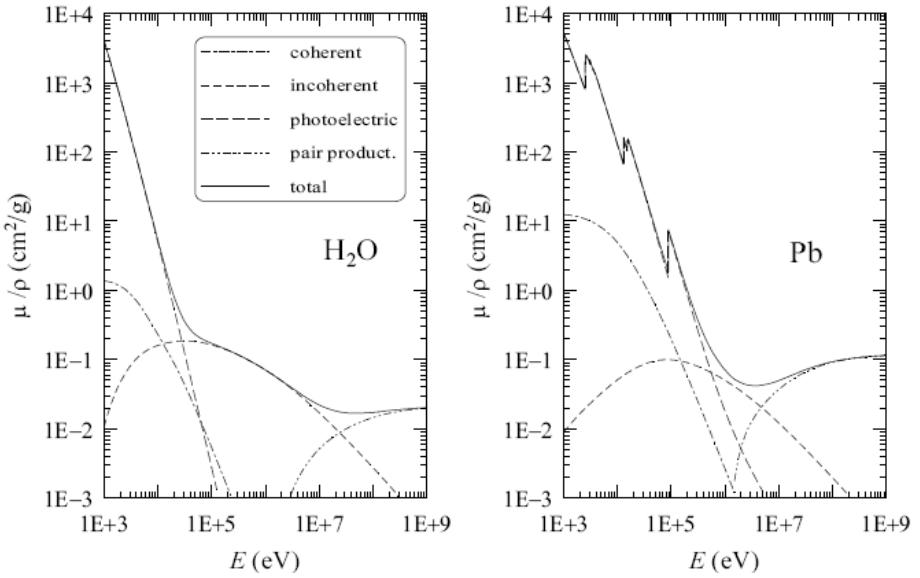


Figure 2. 3. Total attenuation coefficient with the contribution of each individual type of interactions for photons in two materials, water (left) and lead (right) (from Salvat *et al* 2006).

2.3.6. Atomic relaxation

Atoms are primarily ionized by photon interactions and by electron or positron impact. Excited ions with a vacancy in an inner shell relax to their ground state through a sequence of radiative and non-radiative transitions. In a radiative transition, the vacancy is filled by an electron from an outer shell and an x-ray with characteristic energy is emitted. In a non-radiative transition (*i.e.* with no emission of photons), the vacancy is filled by an outer electron and the excess energy is released through emission of an electron from a shell that is farther out (Auger electron). Each non-radiative transition generates an additional vacancy that, in turn, migrates outwards. The production of vacancies in inner shells and their subsequent relaxation through x-ray and Auger electron emissions are simulated in detail in PENELOPE. More details are given in the manual.

2.4. Electron interactions

Electrons and positrons interact with matter through 4 processes:

- Elastic scattering.

- Inelastic scattering.
- Bremsstrahlung emission.
- Electron-positron annihilation.

Those processes are schematically described in Figure 2. 4. As with the photons, differential cross-sections of compounds and mixtures are calculated from the atomic cross-sections using the additivity rule. It is also worth mentioning that the cross-sections must be sampled fast to run simulations in acceptable times. In PENELOPE, the cross-sections enable a fast sampling without losing significant accuracy for most of the simulations purposes. To ensure reliable simulation results, the cross-section must have a physically reasonable shape and only reproduce a few integrals of the exact cross-sections (Liljequist, 1987; Fernandez-Varea 1993), which is the case in PENELOPE, especially if the cross sections are aimed to determine multiple scattering distributions (section 2.5).

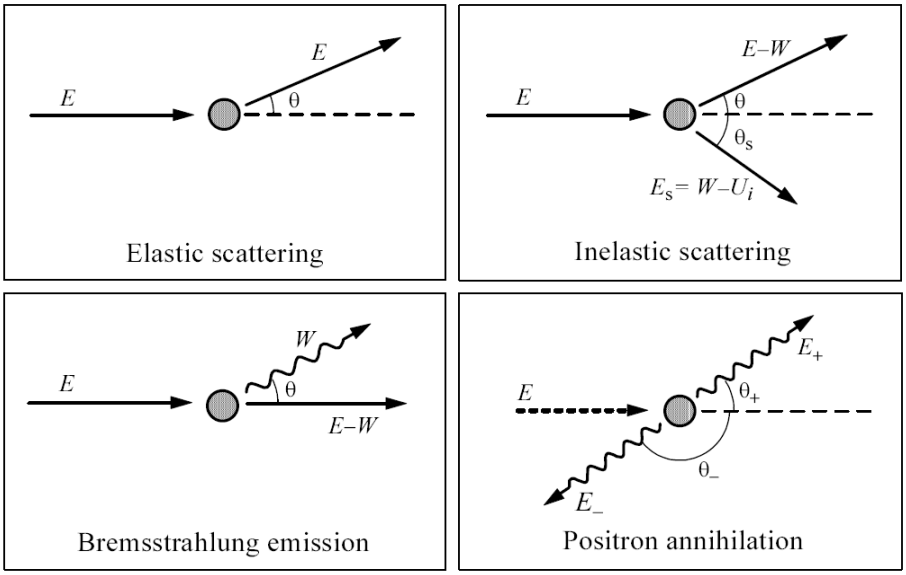


Figure 2. 4. Basic interactions of electrons and positrons with matter (from Salvat *et al* 2006).

2.4.1. Elastic scattering

By definition, an elastic collision leaves the target atom in its original state. In the case of electrons[2], elastic scattering is responsible of the large deviations of the trajectory of electrons. In PENELOPE, the cross-sections for elastic-scattering are calculated from numerical partial-wave cross sections for free neutral atoms. Those numerical partial-wave cross sections are pre-calculated using the program ELSEPA (Elastic Scattering of Electrons and Positrons in Atoms) (Salvat *et al* 2005), which accounts for relativistic effects. ELSEPA calculates cross-sections under the static field approximation, which provides very accurate result for energies above 10 keV. For lower energies, the static-field approximation is less realistic and introduces significant errors for energies below 1 keV. Therefore, the lower limit of validity of PENELOPE for accurate elastic scattering simulation is 1 keV. The additivity rule is also responsible for significant deviations of the cross-sections from reality for energies below a few keV. Considering the energy range of the simulations performed in this thesis, those limitations of PENELOPE will have a negligible influence on the validity of the results.

2.4.2. Inelastic scattering

Inelastic scattering is the main process of energy loss. It is convenient to separate the inelastic collisions of electrons/positrons with matter into two main categories according to the interactions parameters r and b which are the radius of the atom and the impact parameter, respectively (see Figure 2. 5)

- Distant collisions ($b >> r$): those collisions involve small transfer of energy but are the most frequent and contribute to around half of the energy loss
- Close collisions ($b \approx r$): electron/positron may transfer a large amount of energy to the target atom (more specifically, the atomic electrons)

[2] In the following sections and paragraphs, we will mention positrons only if they have a different behaviour in matter than electrons.

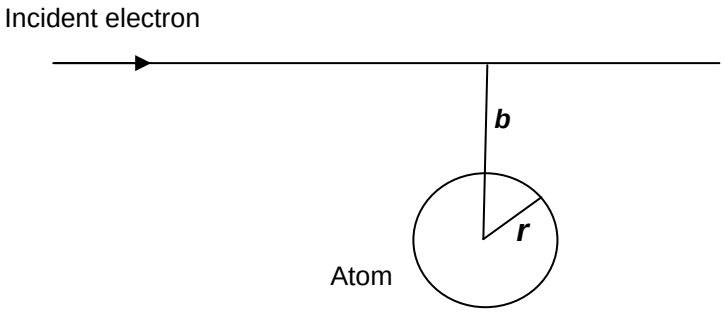


Figure 2. 5. Definition of interactions parameters of electrons. *r* is the radius of the target atom, *b* is the impact parameter.

The starting point is the cross-section of inelastic collision, differential in the energy loss and the energy recoil, obtained from the first Born approximation and accounting for the theory of condensed materials as written in Fano (1963). This total cross-section can be separated into three contributions: the distant contribution of exchange of virtual photon and the distant and close contributions of interactions in the instantaneous longitudinal Coulomb field. The distant contribution of exchange of virtual photon is given in Salvat and Fernandez (1992), whereas the contribution of distant interaction in the Coulomb field is deduced from the general theory, as exposed in detail in the PENELOPE manual. For close collisions, cross-sections must account for some specific effects. For electrons, Moller corrected the cross-section for the indistinguishability of the target and the projectile electrons (Moller 1932). For the positrons, the competition between inelastic scattering and electron-positron annihilation mechanisms must be accounted for directly in the expression of the cross-section (Bhabba 1936).

Finally, it has to be mentioned that the resulting stopping-powers are in very good agreement with the ICRU37 stopping power tables for energies above 10 keV.

2.4.3. Bremsstrahlung emission (braking radiation)

Electrons/positrons accelerating in the electrostatic field of atoms emit bremsstrahlung (braking radiation). In PENELOPE, the energy spectrum of emitted photons is given by the Bethe-Heitler formula, obtained within the Born approximation. The angular distribution of the emitted photons is inspired from semi-empirical analytical formulae derived by Kirkpatrick and Wiedmann (1945), further modified by Statham (1976). Through a parameterization involving two energy-

dependent parameters, the "exact" angular distribution from Kissel *et al* (1983) is reproduced with very good accuracy.

2.4.4. Positron annihilation

In this process, a positron of energy E can annihilate with the electrons of the medium, with an emission of two photons. Assuming the atomic electrons at rest, the two photons share the kinetic energy of the positron and the rest energies of the electron and the positron. PENELOPE uses the differential cross-section given by Heitler (1954) in the centre-of-mass system further modified by Nelson *et al* (1985) to express the differential cross-section in the laboratory frame.

2.4.5. Ionization of inner shells

The theory presented in sections 2.4.2 does not give realistic values of the cross sections for ionization of inner shells. Hence, it is not appropriate to simulate inner-shell ionization by electron and positron impact and the subsequent emission of fluorescent radiation, *i.e.* Auger electrons and characteristic x-rays. Consequently, inner-shell ionization is considered in PENELOPE as an independent interaction process that has no effect on the state of the projectile. Accordingly, in the simulation of inelastic collisions the projectile is assumed to cause only the ejection of knock-on electrons (delta rays); in these collisions the target atom is considered to remain unaltered to avoid double counting of ionizations. Thus, to determine the location of ionizing events and the atomic shell that is ionized, we only need to consider cross sections for ionization of individual inner shells, which can be obtained from elaborate theoretical models. The relaxation of the vacancies produced by inner-shell ionizations is simulated as described in 2.3.6. This kind of simulation scheme is trivial to implement, but it may cause artifacts (in the form of small negative doses) in space regions where the simulated dose distributions have large relative statistical uncertainties. The reason is that simulated Auger electrons and x-rays remove energy from their site (volume bin) of birth, in quantities that may exceed the actual energy deposited by the projectile.

2.5. Electron transport mechanics

The notions developed in sections 2.3 and 2.4 allow for a detailed Monte Carlo simulation of all the particles, interaction by interaction. Although this is

possible for photons in reasonable calculation time, electrons suffer so many interactions along their path that simulating each interaction will result in a prohibitive calculation time, especially for the energies considered in radiotherapy (up to 30 MeV).

Therefore, another strategy must be adopted. In PENELOPE, soft interactions with small deviations and small energy losses are regrouped into one single interaction whereas hard collisions are still simulated in detail. The distinction between soft or hard interactions is performed in the code by using appropriate cutoff values for each interaction. Owing to the fact that for high-energy electrons the differential cross sections for the various interaction processes decrease rapidly with the polar scattering angle and the energy loss, cutoff values can be selected such that the mean number of hard events per electron track is sufficiently small to permit their detailed simulation. In general, this is accomplished by using relatively small cutoff values, so that each soft interaction has only a slight effect on the simulated track. The global effect of the (usually many) soft interactions that take place between each pair of consecutive hard events can then be simulated accurately by using a multiple scattering approach. Hard events occur much less frequently than soft events, but they have severe effects on the track evolution (*i.e.* they cause large angular deflections and lateral displacements or considerable energy losses), which can only be properly reproduced by detailed simulation. The computer time needed to simulate each track diminishes rapidly when the cutoff values for the angular deflection and the energy loss are increased. Mixed simulation algorithms are usually very stable under variations of the adopted cutoff values, whenever these are kept below some reasonable limits.

Because of this mixed simulation scheme, PENELOPE belongs to so-called "class II" algorithms. In "class I" algorithms, all the interactions are regrouped, and the production of secondary electrons is not correlated with the transport of the primary electron. Finally, some algorithms may be "class II" for certain types of interactions, and "class I" for other types of interactions. This is the case of EGSnrc, which is "class II" for inelastic and bremsstrahlung collisions as well as positron annihilation, but is fundamentally a "class I" algorithm for elastic collisions[3]. The main advantages of "class II" algorithms is to enable an improved simulation of spatial distribution, proper crossing of interfaces and reduce the dependence of the results with the parameters defined by the user.

[3] However, one option in EGSnrc allows for turning to single elastic scattering mode to cross interfaces between two media. But, strictly speaking, EGSnrc does not implement the mixed simulation of the elastic scattering.

In PENELOPE, the probability distribution of the step length *s* between two consecutive hard events, in absence of soft energy-loss events, is given by:

$$p(s) = \Sigma_h \exp(-\Sigma_h s) \quad \textbf{(4)}$$

with

$$\Sigma_h = N\left[\sigma_{el}^{(h)} + \sigma_{in}^{(h)} + \sigma_{br}^{(h)}\left(+\sigma_{an}^{(h)}\right) + \sigma_{si}\right] = \left[\lambda_T^{(h)}\right]^{-1} \quad \textbf{(5)}$$

where "el"=elastic, "in"=inelastic, "br"=bremsstrahlung, "an"=annihilation in case of positrons and "si"=ionization of inner shells. (h) refers to the fact that the cross-sections are restricted to hard events. $\lambda_T^{(h)}$ is the total mean free path between two consecutive hard events. Finally, *N* is the number of molecules per unit volume. In PENELOPE, deviation of the projectile between two hard events is due mainly to elastic scattering with a small contribution of soft inelastic scattering which is accounted for in PENELOPE, whereas energy loss is for all the other soft-collisions (which are included in the restricted stopping power for soft collisions). Of course, when a hard event occurs, the interaction is simulated in detail according to the cross-sections of the processes described in 2.4 and, more extensively, in the manual of PENELOPE.

In each hard event, one and only one interaction (i="el", "in", "br", "an" or "si") occurs with probability:

$$p_i = \sigma_i^{(h)} / \sigma_T^{(h)} \quad \textbf{(6)}$$

where $\sigma_T^{(h)}$ refers to the total cross section. When soft energy-losses are considered, the probability distribution function of the distance *s* travelled by the particle to the following hard interaction is not given by equation **(6)** because the mean free path $\lambda_T^{(h)}$ varies with energy and may change appreciably along a single step. The simplest way to cope with this problem is to limit the length of the step to make sure that the average energy loss is much smaller than the kinetic energy *E* at the beginning of the step, and consider that $\lambda_T^{(h)}(E)$ remains essentially constant along the step. Then, the mean energy loss in a step is given by:

$$\left\langle \Delta E \right\rangle = \lambda_T^{(h)} S(E) \qquad \textbf{(7)}$$

where

$$S(E) = S_{in}(E) + S_{br}(E) \qquad \textbf{(8)}$$

is the total stopping power. Since the mean free path between consecutive hard events of any kind is shorter than the mean free path between hard elastic events, the energy loss per step can be limited by re-defining the hard mean free path. If we wish to tolerate average fractional energy losses $\Delta E / E$ along a step of the order of C_2 (a small value, say, 0.05, controlled by the user), we simply take

$$\lambda_{el}^{h}(E) = \max\left\{ \lambda_{el}(E), \min\left[C_1 \lambda_{el,1}(E), C_2 \frac{E}{S(E)} \right] \right\} \qquad \textbf{(9)}$$

where $\lambda_{el}(E)$ is the elastic transport mean free path, $\lambda_{el}^{h}(E)$ is the elastic mean free path between two hard events, $\lambda_{el,1}(E)$ is the first transport mean free path[4] and C_1 allows the user to control the mean free path for hard elastic events, in other words, the angular deflection between two hard elastic events. C_2 may be used to control the energy loss per step. Equation **(9)** effectively limits the average energy loss per step at the expense of increasing the frequency of hard elastic events. The parameters C_1 and C_2 determine the computer time needed to simulate each track. Depending on the energy and the values of C_1 and C_2, the distance between two hard events will be limited either by maximal elastic mean free path (C_1, $\lambda_{el}(E)$), which limits angular deflection, or the maximum average fractional energy loss per step (C_2). If C_1 and C_2 equal zero, then the track length is limited only by the elastic mean free path[5]. The values of C_1 and C_2 are limited (<0.2) to keep enough details in the simulation. As shown in Salvat *et al* (2006), the stability of the PENLOPE code is such that the accuracy of the simulation results is not altered by varying the simulation parameters.

[4] Which is the first moment of the multiple-scattering distribution.
[5] The simulation becomes then purely detailed since the average deflection between two hard elastic events (C_1) equals zero (therefore, only hard elastic events are simulated)

We do not enter here in further details, which can be found in the PENELOPE manual for the interested readers.

2.5.1. Angular deflections due to soft scattering events

The general equations of the spatial distribution of the diffused electron are given by Lewis (1950). More practically, the angular deviation and lateral displacements are simulated in PENELOPE using the random-hinge method, in which an artificial soft scattering event takes place at a random distance τ sampled in the interval $(0, s)$ (see Figure 2. 6). The associated algorithm can be formulated as follows:

1. The electron first moves a random distance τ, which is sampled uniformly in the interval $(0; s)$, in the initial direction.

2. Then a single artifcial soft scattering event (a hinge) takes place, in which the electron changes its direction of movement according to the multiple scattering distribution.

3. Finally, the electron moves a distance $s - \tau$ in the new direction.

This method has the advantage that it provides a direct solution to the problem of crossing interfaces between different regions. Indeed, by stopping the particle at the interface and simulating the hinge only if the particle did not cross the interface yet, we ensure that the direction of movement is correct in average. It has also to be mentioned that the random-hinge method and the fact that PENELOPE is a full “class II” algorithm, allow for escaping from computer intensive computations of the minimum distance between the simulated particle and the interfaces surrounding it, which is needed in EGSnrc, for instance.

2.5.2. Soft energy losses

In EGSnrc, soft energy losses due to inelastic collisions and bremsstrahlung are accounted for in the continuous slowing down approximation (CSDA). In this approximation, a projectile of a given energy and traveling a certain distance will lose always the same amount of energy given by the restricted stopping powers. This approach neglects energy straggling (the energy lost by the particle is a random variable, not a fixed value as in the CSDA approximation). This implies that the cutoff energy for hard inelastic/radiative events should be small so that the importance of soft

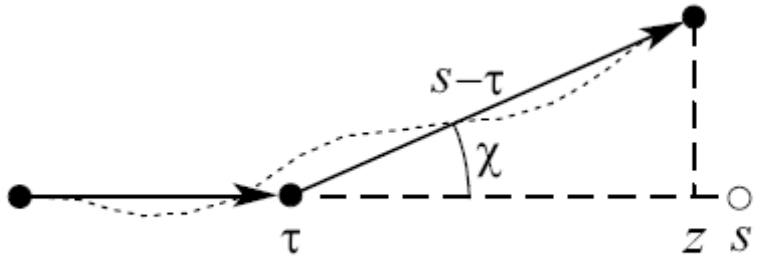


Figure 2. 6. Simulation of the global effect of "soft" collision events between two consecutive "hard" collision events by the random-hinge method (from Salvat *et al* 2006).

collisions in the stopping power is small. Of course, the smallest the cutoff values, the more hard events need to be simulated in detail. In PENELOPE, energy straggling is introduced through an energy loss distribution reproducing on average the energy-loss value given in the CSDA range and with a variance reproducing the energy straggling effects.

2.6. Expected accuracy of MC simulations in external radiotherapy

MC simulations are expected to provide the dose distributions with highest accuracy to meet the requirements mentioned in Chapter 1, sections 2 and 3. Of course, the global uncertainty of a MC treatment plan will never be zero, because sources of uncertainties remain (Reynaert *et al* 2007):

- Statistical uncertainty
- Uncertainties in the beam model
- Uncertainties in the conversion of the CT scan values into material and density
- Uncertainties in the physical model and the cross section libraries

The first point is under control of the user. It can virtually approach zero by simulating enough histories. However, diminishing the statistical uncertainty to very small values (for instance less than 0.1%) may be too much time consuming,

especially if the aim of the MC model is to be used in a MC-based treatment planning system. Indeed, statistical uncertainties are proportional to the reciprocal of the square root of simulation time. Hence to reduce the uncertainty by a factor of 10, we must increase the time by a factor of 100.

The quality of the beam model is difficult to estimate. It is however accepted that the MC model should match reference measurements within 1% (1 σ). The uncertainty in the conversion of the CT scan is even more difficult to estimate, but several authors insist on how much care must be taken when performing CT scan conversion to density and material composition (Vanderstraeten *et al* 2007, Verhaegen and Devic 2005).

Finally, the uncertainties due to the inherent approximations in the mechanics of transport and cross sections of the Monte Carlo codes must be estimated. Generally, the authors assume they are small enough to be negligible (Fraass *et al* 2003). In the scope of this PhD thesis, we also assume this hypothesis, because:

- Most of the potential limitations of the codes occur for energies lower than 10 keV, which is the lowest cutoff energy in almost all of our simulations (therefore, particles with energies lower than 10 keV have their energy deposited locally, without explicit transport)
- The main process of interaction of the photons with matter in the considered energy range is the Compton effect, which is appropriately modeled in PENELOPE (Brusa *et al* 1996)
- Possible remaining errors are probably compensated during the tuning process of the beam model

This last point is more controversial. It has to be mentioned that the main objective of the tuning process of a MC model is first to reproduce *measurements* in reference conditions but not the *reality*. Indeed, during the tuning process, the electron source energy and geometry distribution of the MC model are found after a trial-error process until calculated dose distributions match measurements in reference conditions. The fact that measurements and calculations are in agreement does not mean that the hypothesis made on the energetic and geometric distributions of the electron source reproduce exactly the physical reality.

3. C/S algorithms

All the non-MC algorithms studied in this PhD thesis are "kernel-based" algorithms. Details and references for each algorithm may be found in the papers Sterpin *et al* 2007 (for AAA) and Sterpin *et al* 2008 (for tomotherapy).

In the previous section, it was shown that MC methods sample directly physical relationships to deliver average values of interest. C/S algorithms use a completely different approach by solving integrals representing approximately the macroscopic physical reality in a deterministic manner.

3.1. General formulation

C/S algorithms are fundamentally based on the general equation (Ahnesjö and Aspradakis 1999) :

$$D(\mathbf{r}) = \iiint_V T(\mathbf{s})h(\mathbf{r}-\mathbf{s})d^3s \qquad \textbf{(10)}$$

where T is the TERMA (Total Energy Released per unit MAss), h is the energy deposition kernel, $\mathbf{r}$ is the position where the dose is calculated and $\mathbf{s}$ defines the position of all irradiating sites contributing to the dose at $\mathbf{r}$. The TERMA represents the energy released in the media (here the patient) through the attenuation of the primary photons. The energy deposition kernel represents the average dose distribution around a primary interaction site of a photon in an infinite and homogeneous media. It is worth mentioning that in recent algorithms, the kernels are determined by Monte Carlo simulations, whereas they were previously determined from measurements. An illustration of the effect of the convolution of the TERMA with the energy deposition kernel is illustrated in Figure 2. 7.

Equation **(10)** is valid for a monoenergetic parallel beam with an arbitrary fluence (which means that the kernels are spatially invariant). This situation never occurs in clinic because:

- Beams are polyenergetic and divergent
- Patients are heterogeneous and finite

Several groups worked on how to introduce the effect of polyenergetic and divergent beams in **(10)**. Their work is summarized in the review of Ahnesjö and

Aspradakis (1999). Inhomogeneties are usually accounted for using the density scaling technique. The validity of the density scaling technique was investigated by Mohan *et al* (1986) and Woo and Cunningham (1990).

The finite extent of the patient may have a significant influence, especially when tumors are located close to the skin. In such case, C/S algorithms may overestimate the dose close to the interface because they do not account for the missing backscatter (Mohan *et al* 1986).

When energy spectra and heterogeneity effects are introduced in **(10)**, the convolution integral becomes complex and must be calculated for all the points in the volume of interest, which requires N^7 multiplications and summation, where N is the number of dose calculation points (or voxels). Despite the major improvements in computer technology, such a high complexity would result in prohibitive calculation time.

One popular approach is to use pencil-kernels, which can be viewed as point-kernels pre-integrated over the depth dimension (Figure 2. 8). The motivation of such an approach is to save computation time without losing the ability to account for beam modulation and field shapes. However, in most of the pencil-beam algorithms, only broad beam heterogeneity corrections are applied which will only account for changes in attenuation but not in electron transport, like the power-law method of Batho (Batho 1964) or the equivalent tissue air ratio method (ETAR) (Sontag and Cunningham 1978a and 1978b). The limitations of algorithms with heterogeneity corrections based on broad beam data were extensively studied elsewhere (El-Khatib and Battista 1984, Thomas 1991, Knöös *et al* 1995, Vanderstraeten *et al* 2006, Carrasco *et al* 2004, Jones and Das 2005).

One of the algorithms studied during this thesis is still based on the pencil-beam approximation (AAA). However, there is large freedom to apply the density scaling technique of the kernels in all the directions (chapter 3, Van Esch *et al* 2007, Fogliata *et al* 2008) which enables the possibility to handle modifications of electron transport due to inhomogeneities (more specifically, loss of electronic equilibrium effects). Therefore, AAA belongs certainly to advanced algorithms (type "b") and may be excluded from the category of classic PB algorithms.

Nowadays, it is generally assumed that the C/S algorithms offering the best accuracy are based on the collapsed-cone (CC) approximation. In this approximation, angular discretization of the kernels is performed (Ahnesjö 1989). The convolution of the TERMA with the angular discretized kernel implies that all the energy released into coaxial cones of equal solid angles from volume elements on the cone axis is rectilinearly transported, attenuated and deposited in volume elements on that axis. The superiority of CC algorithms over pencil-beam algorithms (except AAA) has been

clearly demonstrated through many studies (Fogliata *et al* 2007, Knöös *et al* 2006, Vanderstraeten *et al* 2006, Carrasco *et al* 2004, Jones and Das 2005).

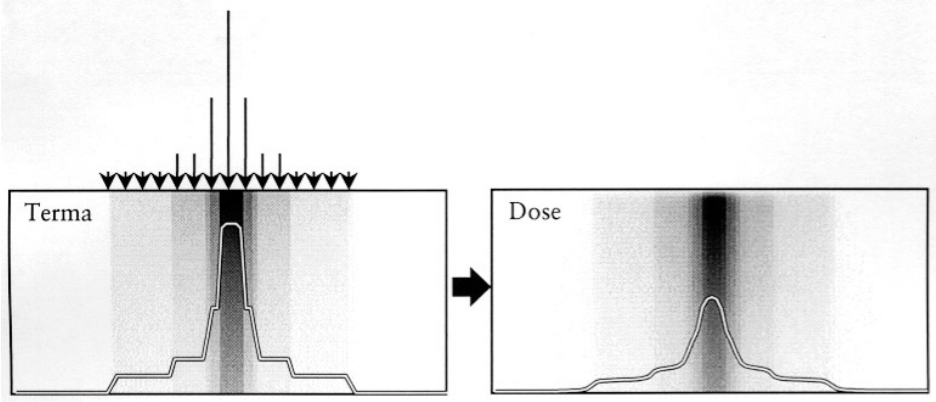


Figure 2. 7. Result of the convolution of the TERMA with the energy deposition kernel (Ahnesjö and Aspradakis 1999).

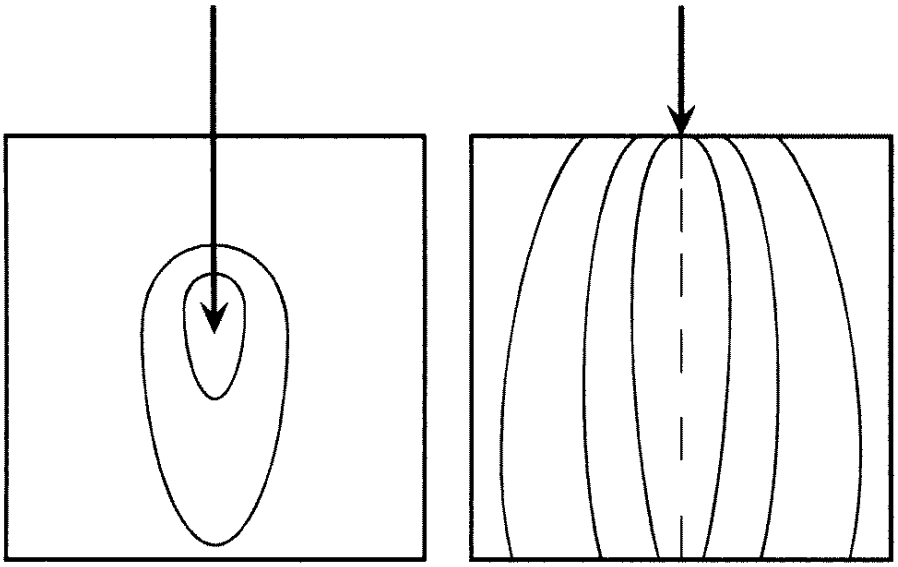


Figure 2. 8. Geometric representation of dose deposition for point kernels (left) and pencil kernels (right) (Ahnesjö and Aspradakis 1999).

4. References

Agostinelli S, Allison J, Amako K *et al* 2003 GEANT4 – a simulation toolkit *Nucl. Instr. Meth. Phys. Res. A* **506** 250-303

Ahnesjö A and Aspradakis M M 1999 Dose calculations for external photon beams in radiotherapy *Phys. Med. Biol.* **44** R99-155

Al-Dweri F M O, Rojas E L and Lallena A M 2005 Effects of bone- and air-tissue inhomogeneities on the dose distributions of the Leksell Gamma Knife calculated with PENELOPE *Phys. Med. Biol.* **50** 5665-78

Attix F H, Roesch W C and Tochilin E 1968 *Radiation Dosimetry* Second Edition Volume 1 (Academic Press)

Batho H F 1964 Lung corrections in cobalt 60 bezam therapy *J. Can. Assoc. Radiol.* **15** 79-83

Berger M J and Hubbel J H 1987 *XCOM: Photon cross sections on a personal computer* Report NBSIR 87-3597, National Bureau of Standards, Gaithersburg, MD

Born M 1969 *Atomic Physics* Blackie and Son, London

Briesmeister J F 2000 *MCNPTM: A general Monte Carlo N-particle transport code, version 4C* Technical report no LA-13709-M, Los Alamos National Laboratory

Brusa D, Stuts G, Rivero J A, Fernandez-Varea J M and Salvat F 1996 Fast Sampling algorithm for the simulation of photon Compton scattering *Nucl. Instrum. Meth. A* **379**, 167-75

Carrasco P, Jornet N, Duch M A, Weber L, Ginjaume M, Eudaldo T, Jurado, D, Ruiz A and Ribas M 2004 Comparison of dose calculation algorithms in phantoms with lung equivalent heterogeneities under conditions of lateral electronic disequilibrium *Med. Phys.* **31** 2899-911

Carrier J-F, Archembault L and Beaulieu L 2004 Validation of GEANT4, an object-oriented Monte Carlo toolkit for simulaiotns in medical physics *Med. Phys.* **31** 484-92

Chibani O and Ma C M 2003 Photonuclear dose calculations for high-energy photon beams from Siemens and Varian Linacs *Med. Phys.* **30** 1990-2000

Cullen D E, Hubbel J H and Kissel L 1997 EPDL97 The evaluated data library, '97 version *Report UCRL-50400* **6** (Lawrece Livermore National Laboratory, Livermore, CA

De Vlamynck K, Palmans H, Verhaegen F, De Wagter C, De Neve W and Thierens H 1999 Dose measurements compared with Monte Carlo simulations of narrow 6MV multileaf collimator shaped photon beams Med. Phys. **26** 1874-82

El-Khatib E and Battista J J 1984 Improved lung dose calculation using tissue-maximum ratios in the Batho correction *Med. Phys.* **11** 279–86

Fano U 1963 Penetration of protons, alpha particles and mesons *Ann. Rev. Nucl. Sci.* **13** 1-66

Fernandez-Varea J M, Mayol R, Baro J and Salvat F 1993 On the theory and simulation of multiple elastic scattering of electrons *Nucl. Instrum. Meth. B* **73** 447-73

Fogliata A, Nicolini G, Vanetti G, Clivio A and Cozzi L 2006 Dosimetric validation of the anisotropic analytical algorithm for photon dose calculation: fundamental characterization in water *Phys. Med. Biol.* **51** 1421-38

Heitler W 1954 *The quantum theory of Radiation* (Oxford Univ. Press, London)

Jeraj R, Keall P J and Ostwald P M 1999 Comparisons between MCNP, EGS4 and experiment for clinical electron beams *Phys. Med. Biol.* **44** 705-17

Kawrakow I and Rogers D W O 2000 *The EGSnrc code system: Monte Carlo simulation of electron and photon transport* NRCC Report PIRS-701 Ottawa: National Research Council of Canada

Kawrakow I 2000a Accurate condensed history Monte Carlo simulation of electron transport: I. EGSnrc, the new
EGS4 version *Med. Phys.* **27** 485–98

Kawrakow I 2000b Accurate condensed history Monte Carlo simulation of electron transport. II. Application to ion chamber response simulations *Med. Phys.* **27** 499-513

Kirkpatrick P and Wiedmann L 1945 Theoretical continuous X-ray energy and polarization *Phys. Rev.* **67** 321-39

Kissel L, Quarles C A and Pratt R H 1983 Shape functions for atomic-field bremsstrahlung from electrons of kinetic energy 1-500 keV on selected neutral atoms $1 \leq Z \leq 92$ *At. Data Nucl. Data Tables* **28** 381-460

Knöös T, Ahnesjö A, Nilsson P and Weber L 1995 Limitations of a pencil beam approach to photon dose caculations in lung tissue *Phys. Med. Biol.* **40** 1411-20

Jones A O and Das I J 2005 Comparison of inhomogeneity correction algorithms in small photon fields *Med. Phys.* **32** 766-76

Lewis H W 1950 Multiple scattering in an infinite medium *Phys. Rev.* **78** 526-29

Liljequist D 1987 Critical path length for the similarity of elastic multiple scattering processes *J. Appl. Phys.* **62** 333-41

Mazurier J, Gouriou J, Chauvenet B and Barthe J 2001 Calculation of perturbation factors for some reference dosimeters in high-energy photon beams with the Monte Carlo code PENELOPE *Phys. Med. Biol.* **46** 1707-17

Mohan R, Chui C and Lidofsky L 1986 Differential pencil beam dose computation model for photons *Med. Phys.* **13** 64–73

Moller C 1932 Zur Theorie des Durchgangs schneller elektronen durch materie *Ann. Physik* **14** 531-85

Motz J W, Olsen H A and Kock H W 1969 Pair production by photons *Rev. Mod. Phys.* **41** 581-639

Nelson W R, Hirayama H and Rogers D W O 1985 The EGS4 code system *Report SLAC-265* (Stanford linear accelerator center, Stanford, CA)

Poon E and Verhaegen F 2005 Accuracy of photon and electron physics in GEANT4 for radiotherapy applications *Med. Phys.* **32** 1696-711

Poon E, Verhaegen F and Seuntjens J 2005 Consistency test of the electron transport algorithm in the GEANT4 Monte Carlo code *Phys. Med. Biol.* **50** 681-94

Reynaert N, van der Marck S C, Schaart D R, Van der Zee W, Van Vliet-Vroegindeweij, Tomsej M, Jansen J, Heijmen B, Coghe M, De Wagter C 2007 Monte Carlo treatment planning for photon and electron beams *Radiation Phys. and Chem.* **76** 643-86

Reynaert N, Palmans H, Thierens H and Jeraj R 2002 Parameter dependence of the MCNP electron transport in determining dose distributions *Med. Phys.* **29** 2446-54

Rodrigues P, Trindade A, Peralta L, Alvees C, Chaves A and Lopes M C 2004 Application of GEANT4 radiation transport toolkit to calculations in anthropomorphic phantoms *Applied Radiation and Isotopes* **61** 1451-61

Salvat F and Fernandez-Varea J M 1992 Semiempirical cross sections for the simulation of the energy loss of electrons and positrons in matter *Nucl. Instrum. Meth. B* **63** 255-69

Salvat F, Jablonski A and Powell C J 2005 ELSEPA-Dirac partial-wave calculation of elastgic scattering of electrons and positrons in matter *Comput. Phys. Commun.* **165** 157-90

Salvat F, Fernandez-Varea J M, and Sempau J 2006 *PENELOPE-2006: A Code System for Monte Carlo Simulation of Electron and Photon Transport* OECD Nuclear Energy Agency, Issy-les-Moulineaux, France

Schaart D R, Jansen J T M, Zoetelief J and de Leege P F A 2002 A comparison of MCNP4C electron transport with ITS 3.0 and experiment at incident energies between 100 keV and 20 MeV: influence of voxel size, substeps and energy indexing algorithm *Phys. Med. Biol.* **47** 1459-84

Sempau J, Sanchez-Reyes A, Salvat F, Oulad ben Tahar H, Jiang S B and Fernandez-Varea J M 2001 Monte Carlo simulation of electron beams from an accelerator head using PENELOPE *Phys. Med. Biol.* **46** 1163-86

Sempau J, Fernandez-Varea J M, Acosta E and Salvat F 2003 Experimental benchmarks of the Monte Carlo code PENELOPE *Nucl. Instrum. Methods Phys.* **B 207**, 107–23

Sempau J and Andreo P 2006 Configuration of the electron transport algorithm of PENELOPE to simulate ion chambers *Phys. Med. Biol.* **51** 3533-48

Siegbahn E A, Nilsson B, Fernandez-Varea J and Andreo P 2003 Caluclation of electron fluenc correction factors using the Monte Carlo code PENELOPE *Phys. Med. Biol.* **48** 1263-75

Sontag M R and Cunningham J R 1978a Clinical application of a CT based treatment planning system *Comput. Tomogr.* **2** 117-30

Sontag M R and Cunningham J R 1978b The equivalent tissue-air ratio method for making absorbed dose in a heterogeneous medium *Radiology* **129** 787-94

Statham P J 1976 The generation, absorption and ansisotropy of thick-target bremsstrahlung and the implications for quantitative energy dispersive analysis *X-Ray Spectrom.* **5** 154-68

Sterpin E, Tomsej M, Reynaert N, De Smedt B and Vynckier S 2007 Monte Carlo simulation of the AAA treatment planning algorithm in a heterogeneous multiplayer phantom and IMRT clinical treatments for an Elekta SL25 linear accelerator *Med. Phys.* **34** 1665-77

Sterpin E and Vynckier S 2008 Monte Carlo evaluation of the convolution/superposition algorithm of Hi-Art^{TM} tomotherapy in heterogeneous phantoms and clinical cases *submitted to Med. Phys.*

Thomas S J 1991 A modified power-law formula for inhomogeneity corrections in beams of high-energy x-rays *Med. Phys.* **18** 719–23

Torres J, Buades M J, Almansa J F, Guerrer R and Lallena A M 2004 Dosimetry characterization of ^{32}P intravascular brachytherapy sourc wires using Monte Carlo codes PENELOPE and GEANT4 *Med. Phys.* **31** 296-304

Tsai Y S 1974 Pair production and bremsstrahlung of charged leptons *Rev. Mod. Phys.* **46** 815-51

Ulmer W, Pyyry J and Kaissl W 2005 A 3D photon superposition/convolution algorithm and its foundation on results of Monte Carlo calculations *Phys. Med. Biol.* **50** 1767-90

Vanderstraeten B, Reynaert N, Paelinck L, Madani I, De Wagter C, De Gersem W, and De Neve W 2006 Accuracy fo patient dose calculation for lung IMRT: A comparison of Monte Carlo, convolution/superposition, and pencil beam computations *Med. Phys.* **33** 3149-57

Vanderstraeten B, Chin P W, Fix M, Leal A, Mora G, Reynaert N, Seco J, Soukup M, Spezi E, De Neve W and Thierens H 2007 Conversion of CT numbers into tissue parmeters for Monte Carlo dose calculations: a multi-centre study *Phys. Med. Biol.* **52** 539-62

Van Esch A, Tillikainen L, Pyykkonen J, Tenhunen M, Helminen H, Siljamaki S, Alakuijala J, Paiusco M, Iori M and Huskens D P 2007 Testing of the analytical anisotropic algorithm *Med. Phys.* **33** 4130-48

Verhaegen F 2002 Evaluation of the EGSnrc Monte Carlo code for interface dosimetry near high-Z media exposed to kilovolt and ^{60}Co photons *Phys. Med. Biol.* **47** 1691-705

Verhaegen F and Devic S 2005 Sensitivity study for CT image use in Monte Carlo treatment planning *Phys. Med. Biol.* **50** 937-46

Waters L S 2002 *MCNPX user's manual version 2.4.0.* Report no LA-CP-02-408 Los Alamos National Laboratory

Wilson R R 1946 Radiological use of fast protons *Radiology* **47** 487

Woo M K and Cunningham J R 1990 The validity of the density scaling method in primary electron transport for photon and electron beams *Med. Phys.* **17** 187-94

Ye S J, Brezovich I A, Pareek P and Naqvi N A 2004 Benchmark of PENELOPE codes for low-energy photon transport : dose comparisons with MCNP4 and EGS4 *Phys. Med. Biol.* **49** 387-97

Chapter 3: Publication one

Monte Carlo evaluation of the AAA treatment planning algorithm in a heterogeneous multilayer phantom and IMRT clinical treatments for an Elekta SL25 linear accelerator

E. Sterpin[a], M. Tomsej[a], B. De Smedt[b], N. Reynaert[b] and S. Vynckier[a]

[a] Department of Radiotherapy, St-Luc University Hospital,

10 av. Hippocrate, 1200 Brussels, Belgium

[b] Department of Medical Physics, Ghent University,

Proeftuinstraat 86, 9000 Ghent, Belgium

Med. Phys. **34** 1665-77 (2007)

Abstract

The Anisotropic Analytical Algorithm (AAA) is a new pencil beam C/S algorithm proposed by Varian for photon dose calculations. The configuration of AAA depends on linear accelerator design and specifications. The purpose of this study was to investigate the accuracy of AAA for an Elekta SL25 linear accelerator for small fields and intensity modulated radiation therapy (IMRT) treatments in inhomogeneous media. The accuracy of AAA was evaluated in two studies. First, AAA was compared both with Monte Carlo (MC) and the measurements in an inhomogeneous phantom simulating lung equivalent tissues and bone ribs. The algorithm was tested under

lateral electronic disequilibrium conditions, using small fields (2x2 cm2). Good agreement was generally achieved for depth dose and profiles, with deviations generally below 3% in lung inhomogeneities and below 5% at interfaces. However, the effects of attenuation and scattering close to the bone ribs were not fully taken into account by AAA, and small inhomogeneities may lead to planning errors. Second, AAA and MC were compared for IMRT plans in clinical conditions, *i.e.*, dose calculations in a computed tomography scan of a patient. One ethmoid tumor, one oropharynx and two lung tumors are presented in this paper. Small differences were found between the dose volume histograms. For instance, a 1.7% difference for the mean planning target volume dose was obtained for the ethmoid case. Since better agreement was achieved for the same plans but in homogeneous conditions, these differences must be attributed to the handling of inhomogeneities by AAA. Therefore, inherent assumptions of the algorithm, principally the assumption of independent depth and lateral directions in the scaling of the kernels, were slightly influencing AAA's validity in inhomogeneities. However, AAA showed a good accuracy overall and a great ability to handle small fields in inhomogeneous media compared to other pencil beam convolution algorithms.

© 2007 American Association of Physicists in Medicine.

1. INTRODUCTION

The main advantage of intensity modulated radiation therapy (IMRT), compared to three-dimensional conformal therapy, is an increased conformity to the target, and a better sparing of the normal adjacent tissues and/or organs at risk. Complex dose distributions are achieved using irregular fluence maps obtained through the optimization process. Considering the step and shoot technique, the irregular fluence is delivered by a superposition of several segments of beams.

However, for photon dose calculations, problems related to loss of lateral electronic equilibrium appear when small fields are used. IMRT therefore requires faithful modeling of both small fields and the effect of low densities in lung and head and neck cases because of the presence of lung tissues, air cavities and air-tissue interfaces.

Accuracy and quality assurance of the commercial treatment planning systems in these conditions still concern the scientific community.[1–5] Today, most of the commercial treatment planning systems use correction-based algorithms, which do not take into account loss of lateral electronic equilibrium, and this may lead to

significant errors.[3,4,6] Current Varian Eclipse algorithms (single pencil beam convolution) are generally based on the modified Batho power law for inhomogeneity correction. Limitations of this technique have been studied previously.[7]

Major improvements have been achieved in convolution/superposition algorithms, which are generally based on Monte Carlo (MC) generated kernels for energy deposition by an interacting photon in an infinite homogeneous medium. Convolution/superposition algorithms with collapsed cone approximation have shown good accuracy in inhomogeneous media4,[8,9] even though deviations were reported at interfaces and, less significantly, in low density media. Another popular approach is to use pencil beam kernels instead of point scatter kernel. Pencil beam limitations in inhomogeneous media were extensively studied elsewhere[10] although accurate results were reported for conformal radiotherapy to head and neck tumors, even in the presence of large air cavities.[11]

Monte Carlo simulations are widely accepted as the most accurate tool to model radiation transport in linear accelerator geometries and to calculate dose distribution in tissues.[12] Since electron transport and linear accelerator geometry can, in principle, be accurately taken into account, the validity of Monte Carlo simulations is not limited by the complexity of treatments (IMRT, small fields) and the presence of inhomogeneities.

The aim of this work was to study the accuracy of a new pencil beam convolution algorithm: the Analytical Anistropic Algorithm (AAA) implemented in Varian Eclipse for IMRT purposes. Its accuracy in homogeneous phantoms[13,14] and inhomogeneous phantoms[14] has already been studied for Varian linear accelerators by other groups. AAA was also tested in clinical situations (for conformal radiotherapy) in a recent paper.[15] However, this algorithm has not yet been configured and studied for Elekta linear accelerators; special attention was therefore needed for the commissioning of the algorithm, since configuration of AAA depends on manufacturer specifications, concerning, for instance, the material of the flattening filter.

The work was divided into three parts. First, the Elekta SL25 linear accelerator was modeled with BEAMnrc[16] and compared to measurements in water. Second, accuracy of both Monte Carlo simulation and AAA was studied with respect to measurements in an inhomogeneous phantom. Finally, dose distributions were calculated using Monte Carlo and AAA for lung and head and neck patients treated with the IMRT technique. Dose volume histograms (DVHs) obtained by both techniques were compared for different volumes. Complexity increased with every step, giving more importance to the Monte Carlo simulations as a reference calculation tool, since accurate measurements become difficult in non-reference conditions and

are almost impossible in patients. This methodology enabled the authors to test AAA's validity from the simplest conditions to complex clinical treatments, without compromising the understanding of possible disagreements in each part of the study.

2. MATERIAL AND METHODS

2.1. Linear accelerator

An Elekta SL25 linear accelerator with two photon energies (6 and 25 MV) was used; only the 6 MV beam was used for this study. The multileaf collimator has rounded leaf ends and focused leaf sides and the projected thickness of the leaves at the isocenter plane is 1 cm. The backup jaws also have rounded leaf ends and have a field opening corresponding to the most retracted leaves.

The Elekta SL25 is equipped with a backscatter plate, preventing particles backscattered by the collimating devices from reaching the monitor chamber, ensuring the independence of the monitor chamber signal of the field shapes.

2.2. Varian—anisotropic analytical algorithm (AAA)

AAA is a three-dimensional pencil beam convolution/superposition algorithm, originally designed by Ulmer[17–19] and Kaissl. The development was continued by the research group of Varian Medical Systems, Helsinki. A sum of six radial exponential functions is now being used to model the lateral scatter kernels instead of the originally proposed three Gaussians. The use of exponential functions reduces boundary artifacts between tissues of different densities and enables faster dose distribution calculations.

The particle source is divided into three subsources, each of them having its particular Monte Carlo derived model: the primary source, the scattered extra-focal photons (primary collimator and flattening filter[20]) and the electrons and photons created in the beam-limiting devices and in the air (photon and electron contamination source). The initial photon spectrum just below the target is taken from the Eclipse database and was pre-calculated by Monte Carlo simulation using BEAM.[16] Modification of the spectrum through the flattening filter (beam hardening) is modeled by attenuating the initial spectrum by a radially varying amount of the flattening filter material. The beam is divided into fanlines (beamlets) and the convolutions are performed, for each beamlet comprised in the clinical beam, using kernels and an intensity function. The final dose distribution is obtained by a superposition of the

dose contribution of each individual beamlet. The kernels are calculated using a sum of six depth dependent weighted exponentials, defining the lateral scattering in order to fit Monte Carlo derived pencil beam scatter kernels. Inhomogeneities are taken into account by lateral density scaling of the photon scatter kernel, depth dependent correction factors, and also a "history correction convolution," introduced in the depth direction to model changes of electronic fluence conditions at interfaces. Finally, the polyenergetic photon scatter kernel is obtained through a weighted sum of monoenergetic Monte Carlo derived kernels calculated using EGSnrc in water.

All the calculations performed by AAA were compared to the results obtained with the single pencil beam convolution and the Modified Batho (MB) power law heterogeneity correction, which is still used in most of the Eclipse stations worldwide. The resolution of the calculation grid was equal to 2.5 mm for AAA and MB calculations.

AAA configuration depends on the physical properties of the linear accelerator (flattening filter material…) and, therefore, some extra work was needed to configure AAA. The commissioning has been completed by comparing AAA calculations against measurements in water in reference conditions (water phantom, SSD=95 cm, square fields). Output factors were calculated and compared to measurements and MC simulations for square fields (2x2 cm^2–40x40 cm^2) and for rectangular fields (2x5 cm^2, 3x5 cm^2, 2x10 cm^2 and 3x10 cm^2) on-axis, 5 and 10 cm off-axis to determine if AAA can accurately calculate output factors for IMRT field configurations. For fields larger than 10x10 cm^2, output factors were measured using a IBA-Wellhöfer CC13 (0.13 cm3 active volume) ionization chamber, whereas for smaller fields we used an IBA-Wellhöfer NAC micro-ionization chamber, which has an active volume of 0.007 cm3.

2.3. Phantom measurements

The phantom used in the present study consisted of several slabs (see Fig. 1). A 2.9 cm polystyrene slab was introduced to provide electronic equilibrium. The next slab (L1) consisted of cork, simulating lung tissue. Then came a poly-methylmethacrylate (PMMA) slab (muscle tissue equivalent) with cylindrical Teflon inserts (simulating ribs), a polyethylene slab (adipose tissue), and again a cork layer (L2) and a PMMA slab in order to minimize the influence of the treatment.

Depth dose and lateral dose profile measurements were performed for three field sizes (2x2 cm^2, 6x6 cm^2 and 10x10 cm^2) using Kodak EDR-2 films placed individually at several positions perpendicular to the beam axis. The origin of the

coordinates was placed at the isocenter, localized in the middle of the PMMA region and between two cylindrical ribs. The number of monitor units generally equaled 200. For the 2x2 cm^2 field (see below), 300 monitor units were used in order to compensate for the lower doses associated with the smaller field size. Conversion of optical density to dose was based on a calibration curve established for the 6 MV beam. The dose range chosen in this experiment, from 0 to 3 Gy, guaranteed that measurements were performed in the linear region of the film.

Films were used in this work because of their resolution. The energy dependence of the films may, however, introduce dosimetric errors. For uniform fields, where good accuracy was expected inside the field (within 1%),[21] dose may be overestimated outside the field because of the relative over response of the film to low energies,[22,23] even though this effect has been shown to be negligible with EDR-2 films or less significant than, for instance, with XV2 films.[21,24,25] Moreover, film response is depth dependent because of the relatively increased scattered radiation with depth, but, this phenomenon does not introduce significant deviations (up to 2–3% at large depths (15 cm)) for the field sizes used in the experiment, as already demonstrated in other papers.[21,26] The expected accuracy inside the field was therefore estimated better than 3%.

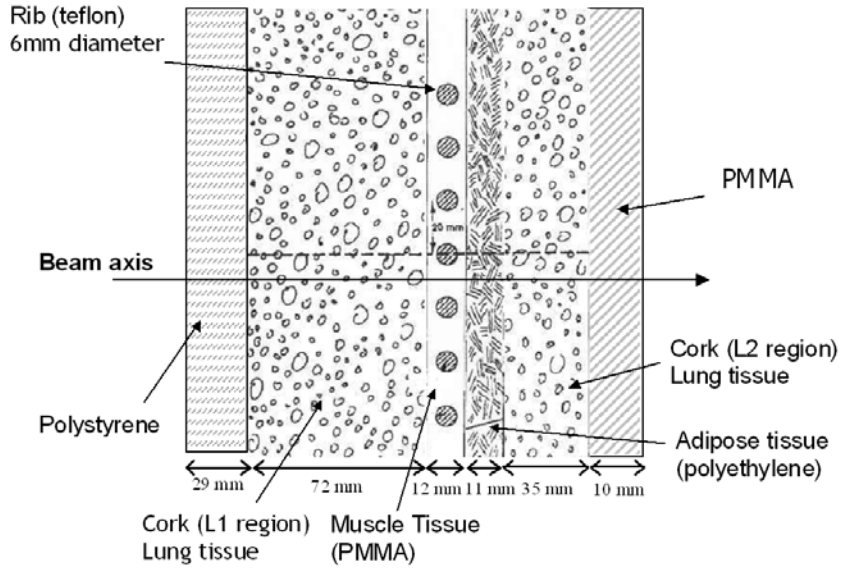


Fig. 1. Experimental phantom composed by a succession of slabs of different materials, respectively along the beam axis: polystyrene, cork (lung equivalent, L1), PMMA (muscle tissue equivalent), polyethylene (adipose tissue equivalent), cork (L2) and one slab of PMMA.

2.4. Monte Carlo simulation

BEAMnrc[16] was used to model our linear accelerator, whereas electron transport was performed by EGSnrc,[27] which is based on the popular EGS4. All the component modules (CMs) were defined according to manufacturer specifications and precise modeling of the multileaf collimator was included using the detailed CM MLCE.[28] Accurate simulation of the MLC was required. As a variance reduction technique, directional bremsstrahlung splitting was applied for photon production inside the target. Electron transport was performed by the algorithm PRESTA II. In EGSnrc, electrons and photons were simulated until their total energy reached ECUT and PCUT, respectively. Their remaining energy was then deposited locally. ECUT and PCUT equaled, respectively, 0.521 and 0.01 MeV and no range rejection was applied. The resulting phase space at the exit plane was used as an input for the DOSXYZnrc[29] code, which calculates the dose distributions in a phantom. ECUT and PCUT where chosen as above. Voxel sizes were 0.5x0.5x0.5 cm3 in low gradient regions, whereas the voxel size was reduced, in high gradient regions, in the direction corresponding to the gradient in order to achieve good resolution (1 mm). The number of histories was such that the standard deviation was below 0.5% at maximum dose and particles were recycled less than twice. Generally, matching between measurements and our MC model was considered to be achieved when local dose differences were below 2% of maximum dose and, in dose gradients, when shifts were below 1 mm. As part of the commissioning process of the MC calculations, the energy has been tuned by matching calculated and measured profiles using a PFD3G Wellhöfer silicon diode at SSD=95 cm and depth=5 cm for a 30x30 cm^2 field. Profiles were chosen because of their larger sensitivity to energy variations of the electrons striking the target compared to the central axis depth dose. Depth dose distributions measured by an ionization chamber Wellhöfer CC13 down to 3x3 cm^2 fields were also compared to MC simulations. The electron source geometry was modeled to match measured and calculated profiles for small fields (1x1 cm^2, 2x2 cm^2, and 3x3 cm^2) along the cross plane axis.

The inhomogeneous phantom was scanned and introduced in DOSXYZnrc using CTCREATE. For phantom calculations, ECUT=0.521 MeV, PCUT=0.01 MeV. Range rejection was applied with ESAVE=1 MeV, to speed up our simulation, voxel sizes were 0.2x0.2x0.2 cm3 and standard deviation was kept below 0.5 % at dose maximum.

For patient cases, calculations were performed by the Monte Carlo dose engine MCDE[30] with our Monte Carlo model. MCDE was based on the BEAMnrc/EGSnrc package and enabled the calculations in a computed tomography (CT) set using DICOM input files generated by Eclipse. For each voxel, mass density was derived from CT number, using a continuous calibration curve. This allowed six different materials to be associated with the CT number for each voxel: air, lung, adipose tissue, muscle, cartilage and cortical bone.

MCDE was also calibrated for the calculation of absolute doses for a given number of monitor units. The normalization factor to convert Gy/particle to absolute dose was calculated for a 10x10 cm^2 field in a water phantom, SSD=95 cm at 5 cm depth.

After the simulation run, MCDE provides a DICOM file with the Monte Carlo calculated dose grid which can be introduced in Eclipse. Finally, DVHs calculated with AAA and MCDE plans were compared at the Eclipse station. MCDE had already been used in other studies involving a comparison between MC and convolution/superposition algorithms for IMRT treatments.[31–33] Monte Carlo simulations calculate the dose to medium, whereas dose to water was obtained from treatment planning systems. Dose conversion was performed following the general rules provided by Siebers *et al.*,[34] *i.e.*, $D_w=D_{med}s_{w,med}$ and $s_{w,med}$ depending only on the nominal energy and the medium.

2.5. IMRT plans

In this study, four IMRT plans were planned: one ethmoid tumor, one oropharynx tumor, one large and one small lung tumor. These cases were selected because they tested the algorithm to its limits, due to the use of IMRT fields in highly inhomogeneous media with large and small planning target volumes (PTVs). For all the plans, the mean dose to the PTV equaled the prescribed dose (when AAA was used) and the optimization was performed by the dose volume optimizer (DVO) provided by Eclipse. The optimized fluences were then converted to delivered fluences using multiple static segments by the leaf motion calculator. AAA, MB, and MC then calculated the dose distribution according to these delivered fluences with the same number of monitor units per segment for each algorithm. Optimization options were set to reach a “reasonable” level of modulation. Generally, the number of segments per beam was between 10 and 20. This methodology, combined with the fact that DVHs

were compared on the same treatment planning system (TPS), guaranteed that only the performances of the dose calculation algorithms themselves were compared.

2.5.1. Ethmoid tumor

The ethmoid tumor was an advanced adenocarcinoma. The dose prescription was 70 Gy. The treatment was planned using seven noncoplanar IMRT fields optimized by the dose volume optimizer (DVO) provided by Eclipse. The constraints were set in such a way that the dose to the critical structures was minimized without compromising PTV coverage and dose homogeneity in the PTV. Many air cavities surrounded by bones were situated into the PTV, providing a challenging case for the AAA algorithm. Air cavities were removed manually from the PTV contour (PTV-air) for DVH calculation in order to avoid deviations introduced by poor statistics of MC calculations in air.[35]

2.5.2. Oropharynx tumor

The study concerning the tumor of the oropharynx included two volumes: one large bilateral volume (PTV 50 Gy), which included the tumor and additional regions where a prophylactic dose of 50 Gy was given (50 Gy plan). The tumor was an advanced squamous cell carcinoma with invaded lymph nodes (T4 N2b M0) of the oropharynx. A second PTV (PTV 70 Gy) was defined in order to give an additional dose of 20 Gy to the tumor (70 Gy plan). The same methodology was applied as for the ethmoid tumor. In the upper part of the PTV, many air cavities were present, which were removed from the PTV contour for DVH calculation.

2.5.3. Lung tumors

Two lung tumors were studied, with the same dose prescription of 60 Gy. The first case was a relatively large tumor (5.5 cm) while the second one had a smaller diameter (~2 cm, PTV extension equal to 2 cm) and was located close to the chest wall. These two sizes were chosen to study the accuracy for small and large tumors sizes (*i.e.*, field sizes) since the phantom results have shown great dependence on field size.

3. RESULTS

3.1. AAA and MC commissioning

3.1.1. Depth dose and profiles

AAA configuration led to results fulfilling the acceptability criteria proposed by Venselaar, Welleweerd, and Mijnheer,[1] (2% deviation on-axis, 3 % off-axis, and 2 mm in high dose gradients) for depth dose and profiles. Agreement was generally within 1%/1 mm except for the 2x2 cm^2 field depth dose.

MC simulations generally fitted to measurements within 2%/1 mm, as shown in Figs. 2(a) and 2(b) for an electron source with a Gaussian spectral distribution. The average energy and the full width at half maximum (FWHM) equaled, respectively, 5.7 and 1 MeV. This last value was chosen according to manufacturer specifications and was similar to what can be found elsewhere for Elekta linear accelerators.[36] A circular Gaussian distribution was also chosen for the electron source geometric distribution with FWHM=2.5 mm to reproduce dose profiles for all the field sizes down to 1x1 cm^2 with deviations smaller than 1 ml, as illustrated in Fig. 2(c) for a 2x2 cm^2 field. For information, AAA results are also drawn in Figs. 2(a)–2(c). Agreement was similar to MC simulations except for the 2x2 cm^2 field where a small deviation (1 mm) can be observed.

3.1.2. Output factors

Measured and calculated output factors for squared fields are presented in Fig. 3. For AAA, agreement with measurements was generally within 1% for all the field sizes, whereas it was better than 0.5% for MC. On-axis and off-axis output factors are also compared in Table 1 for small rectangular fields. Good agreement was obtained for AAA and MC with deviations generally within 1% with few values within 1.4%, demonstrating the capacity of both systems to calculate accurately output factors for small fields. However, for 5x2 and 10x2 cm^2 fields, differences up to 2% between AAA and MC could occur.

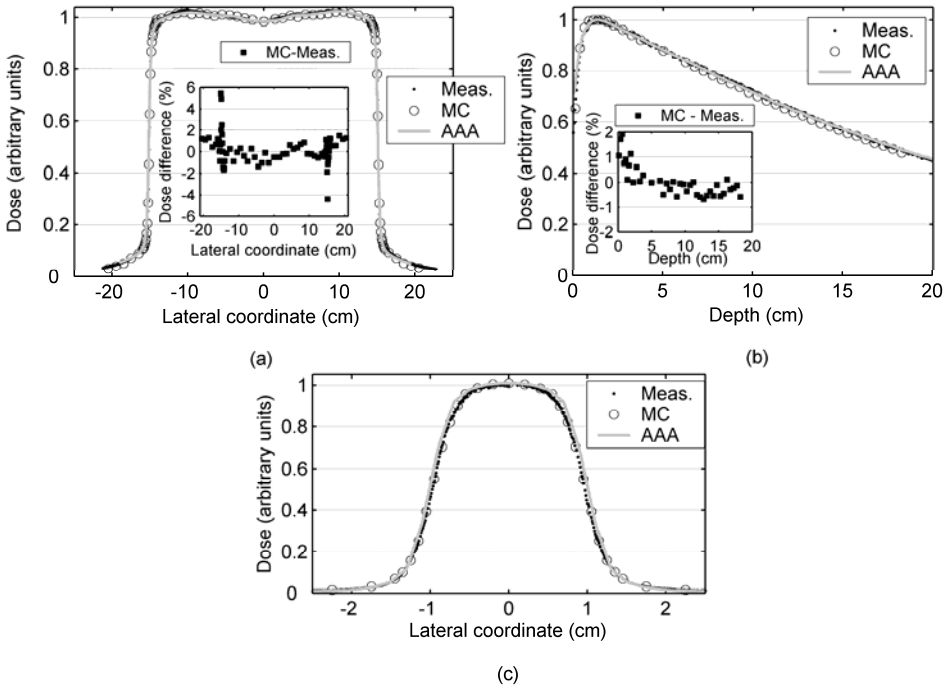


Fig. 2. Comparison of measured (solid points) and calculated (MC, open circles; AAA, gray line) lateral profiles for a 30x30 cm² field (a), depth dose distributions for a 30x30 cm² field (b) and lateral profiles for a 2x2 cm² field (c). Insets represent differences between MC and measurements. Measurements and calculations were performed in a water phantom (SSD = 95 cm). Profiles were measured and calculated at 5 cm depth.

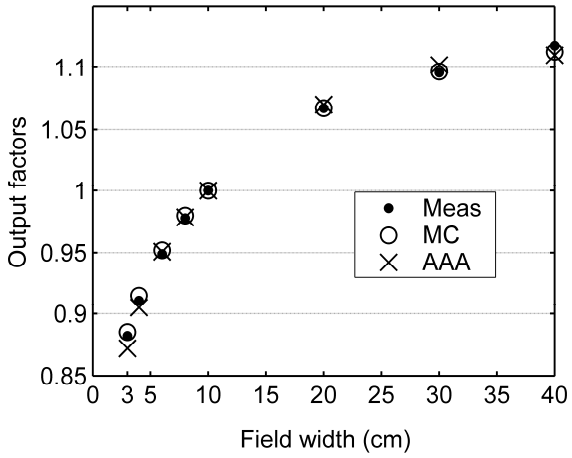


Fig. 3. Comparison of measured (points) and calculated (MC, open circles; AAA, crosses) output factors.

Field (cm^2)	Offset (cm)	Meas.	AAA	Meas.–AAA (%)	MC	Meas.–MC (%)
5x2	0	0.863	0.868	-0.5	0.873	-1.0
	5	0.896	0.888	0.8	0.905	-0.9
	10	0.937	0.924	1.3	0.927	0.1
5x3	0	0.895	0.898	-0.3	0.898	-0.3
	5	0.933	0.924	0.9	0.928	0.5
	10	0.972	0.962	1.0	0.974	-0.2
10x2	0	0.873	0.879	-0.6	0.882	-0.9
	5	0.906	0.898	0.8	0.915	-0.9
	10	0.946	0.934	1.2	0.955	-0.9
10x3	0	0.912	0.911	0.1	0.912	0.0
	5	0.946	0.937	0.9	0.942	0.4
	10	0.990	0.976	1.4	0.978	1.2

Table 1. On-axis and off-axis output factors measured (Meas.) with a micro ionization chamber and calculated with AAA and MC.

3.2. Phantom measurements

Depth dose measurements were performed for 2x2, 6x6 and 10x10 cm^2 fields. Figures 4(a)–4(c) show a comparison between measured, MC, AAA and MB calculated depth dose curves. All the depth doses were normalized at the depth of maximum dose and the origin of the depth axis (axial coordinate) was placed at the isocenter. Conversion of dose to medium to dose to water was performed for measurements and the Monte Carlo data since AAA provides dose to water, even though conversion factors were close to 1 (below 1% difference, except inside cylinder ribs). Good agreement was achieved between Monte Carlo calculations and measurements, for all field sizes, with deviations smaller than 2%/1 mm, as the acceptance criteria. For the 2x2 cm^2 field, AAA showed an overall good agreement in the L1 region, proving that the algorithm was accounting for loss of lateral electronic equilibrium contrary to single pencil beam convolution with MB heterogeneity correction. Deviations were smaller than 3% but they reached 5% close to the L1-PMMA interface. Good agreement was also achieved in the PMMA layer, with deviations smaller than 3%. The disagreement for MB correction was expected and already demonstrated in other papers.3 For the 6x6 cm^2 field size AAA slightly underestimated the dose in the lung regions (2–4%), whereas AAA overestimated the dose (3% maximum difference) in the muscle equivalent region as illustrated in Fig. 4(b). The agreement was still acceptable, but not significantly better than MB. Figure 4(c) shows a 10x10 cm^2 depth dose where good agreement was generally obtained for

all the algorithms (differences smaller than 2%). Central axis depth dose curves measured and calculated with MC and AAA are also compared to 2 cm off-axis depth dose in Fig. 4(d). Despite an underestimation of dose in lung equivalent regions (up to 4%), this figure clearly demonstrates that AAA was correcting for inhomogeneities in all directions.

Figure 5 compares 2x2 cm^2 (a), 6x6 cm^2 (b) and 10x10 cm^2 (c) dose profiles acquired in the middle of L1. Good agreement was achieved between MC and the measured profiles (deviations smaller than 2%/1 mm) even for the 2x2 cm^2 field except outside the field. AAA showed good agreement for the 6x6 and 10x10 cm^2 profiles, because of the lateral density scaling of the kernels, while MB underestimated the beam penumbra and overestimated the dose near the beam edges (up to 7–8% of central dose difference for the 6x6 cm^2 field). For the 2x2 cm^3 field, AAA's accuracy was decreasing, the beam penumbra was underestimated. This error could, however, not be caused by the inhomogeneity correction as AAA underestimated the penumbras for the 2x2 cm^2 field in water (see Fig. 2(c)). Finally, profiles were measured just below the muscle tissue equivalent slab (Figs. 6(a) and 6(b)). These figures clearly illustrate the differential attenuation due to the ribs pattern. For MC calculations, good agreement was generally achieved. Differences were typically of the order of 2% of maximum dose and within 1 mm in the dose dips. These deviations were compatible with the expected accuracy of MC calculations (2% /1 mm) and measurements (3%). However, neither AAA nor MB took into account the extra attenuation due to ribs, providing an almost flat profile. These results might lead to planning errors for small bone inhomogeneities such as those studied here.

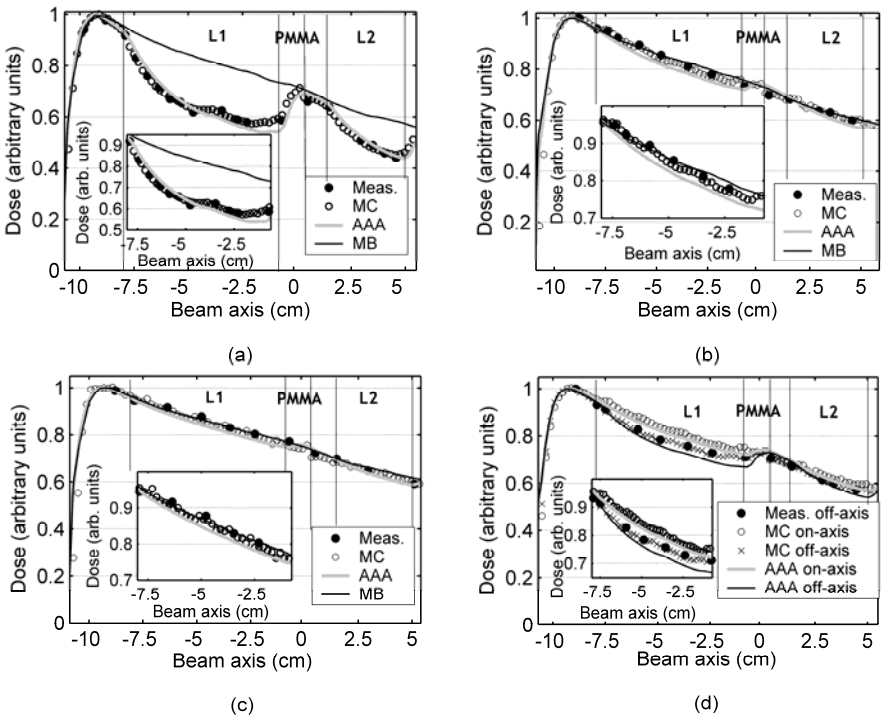


Fig. 4. PDDs comparison, for 2x2 cm² (a), 6x6 cm² (b) and 10x10 cm² (c) 6 MV fields in the lung phantom, between measured (Meas., solid circles) and calculated by Monte Carlo (MC, open circles), AAA (gray line) and modified Batho heterogeneity correction (MB, black line). Figure (d) shows an on-axis and 2 cm off-axis PDDs comparison for a 6x6 cm² field between measured (Meas. solid circles), MC (on-axis, open circles, off-axis, crosses) and AAA (on-axis, gray line , off-axis, black line). The insets are the same plots with a better resolution for the analysis of the L1 region.

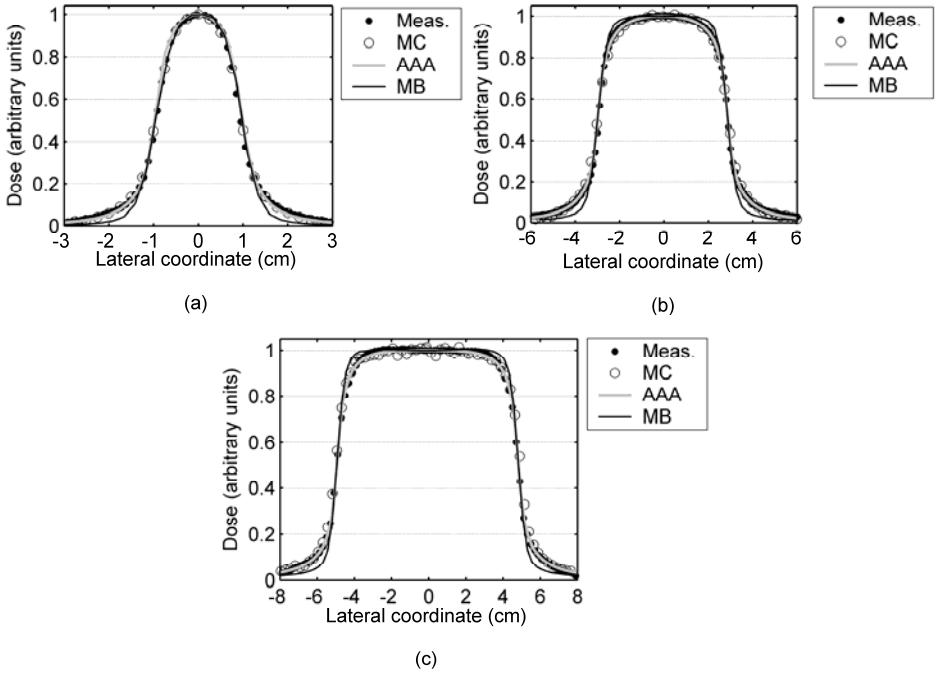


Fig. 5. Lateral dose profile comparison, for 2x2 cm² (a), 6x6 cm² (b) and 10x10 cm² (c) 6 MV fields acquired in the middle of the first lung equivalent region (L1), between measured (points) and calculated by Monte Carlo (open circles), AAA (gray line) and modified Batho heterogeneity correction (MB, black line)

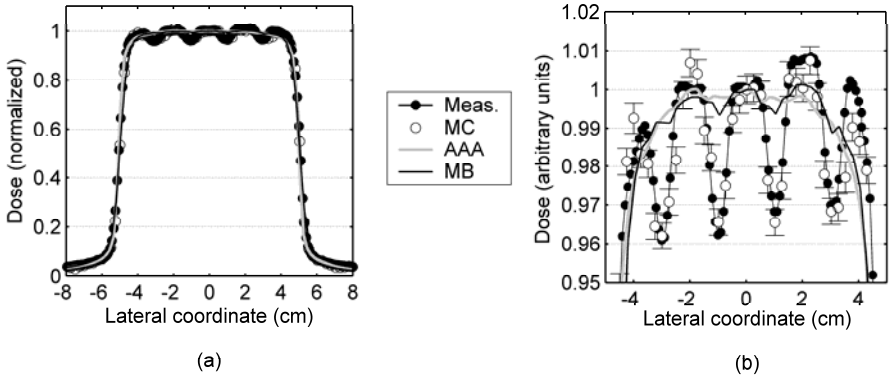


Fig. 6. Lateral dose profiles comparison for a 10x10 cm² field. The profile was measured (solid-points line) and calculated (MC, open circles; AAA, gray line; MB, black line) below the cylinder ribs pattern. The (b) profile is a zoom of the (a) profile where statistical uncertainty (1σ) is shown.

3.3. IMRT plans

Clinical case studies are presented in this section. In order to limit the number of figures, DVHs are shown for the ethmoid and the small lung tumors only. For the same cases, individual dose profiles were compared since DVH could hide possible deviations between algorithms in terms of isodose distribution. Additional calculations were performed with all the hounsfield units turned to zero (density of water) within the skin contour, which allows eliminating differences in particle transport inside the patient. Therefore, the possible remaining discrepancy will be likely due to differences between the algorithms in beam modeling aspects. The plans calculated with the original hounsfield units will be referred as the clinical plan (CP). WP (water plan) indicates that the hounsfield units were turned to zero. As for the DVHs, the results for the two calculation modes (CP and WP) are only shown for the ethmoid and the small lung tumor cases.

Values characterizing DVHs are reported in tables for all the cases. The values were chosen according to the dose constraints applied during the optimization process and according to their importance for the clinical evaluation of the plan. For instance, the dose received by 2% of the volume (D_2) was the only critical parameter for serial organs at risk, such as the spinal cord. The lung volumes receiving 20 and 25 Gy (V20Gy and V25Gy) were minimized for the lung cases (parallel organs at risk).

3.3.1. Ethmoid tumor

In Fig. 7(a), the DVHs calculated by AAA, MC and the older Eclipse algorithm (MB) are compared for the PTV without air and for the optical chiasm, while DVHs for the optical nerves are compared in Fig. 7(b). Good agreement was generally achieved between all the curves except for the left optical nerve where MB was significantly overestimating the dose.

As it can be seen in Table 2, very good agreement was obtained between AAA and MC in the WP case for the PTV without air (PTV-air). The mean dose difference was equal to 0.9 Gy (1.3%) and the standard deviations were comparable.

For the CP, however, dose received by 95% of the volume of the PTV-air (D_{95}) was overestimated in AAA (1.4%). Moreover, the mean dose difference was about 1.2 Gy (1.7%) and the dose received by 2% of the volume was equal to 74.2 Gy for AAA, whereas it reached 76.6 Gy for MC (3.4%). For critical structures, differences were below 2% of the dose constraint (D_2 below 60 Gy for the three structures shown (except for the optical chiasm where the mean dose difference was,

respectively, equal to 2.6 Gy (4%) and 2.3 Gy (3.8%). Similar observations could be made concerning MB compared to MC (except for the right optical nerve (6.4 Gy difference for D_2).

It is difficult to draw definitive conclusions regarding DVHs on small structures such as optical nerves, since small errors on isodose distributions may lead to significant deviations.

However, in routine practice, radiation oncologists may actually account for these DVHs to evaluate the quality of a treatment plan, and it is therefore interesting to include these structures in the comparison.

Figure 8(a) shows a comparison between the isodose curves calculated with AAA and MC with the dose profiles associated with the lines drawn on the picture. Generally, isodose curves were very similar outside the PTV but were difficult to analyze inside the PTV due to the presence of air cavities. For the dose profiles illustrated in Figs. 8(b) and 8(c), an overall good agreement was achieved, with differences generally smaller than 2% of the prescribed dose, except in air regions of the PTV (up to 12%) and dose gradients (up to 5%). The order of magnitude of the deviations in the individual profiles was compatible with the differences between the DVHs.

		AAA-	MC-CP	MB-CP	AAA-WP	MC-WP	MB-WP
PTV – air	Mean (Gy)	70.2	71.4	70.4	70.7	71.6	70.0
	STD (Gy)	2.0	2.8	2.8	1.9	2.2	2.0
	D_{95} (Gy)	67.6	66.6	67.3	68.0	68.7	67
	D_2 (Gy)	74.2	76.6	74.0	74.6	76.0	74.0
Optic chiasm	D_2 (Gy)	49.2	47.6	48.2	49.0	47.6	47.9
Left optic nerve	D_2 (Gy)	58.6	59.4	58.9	58.9	58.8	58.2
Right optic nerve	D_2 (Gy)	57.9	59.4	53.0	58.2	59.0	58.0

Table 2. Ethmoid tumor study. Comparison of the DVHs' characteristic values (mean, standard deviation (STD), dose delivered to 95% of the volume (D_{95}) and to 2% of the volume (D_2)) between AAA, MC and MB for the plan in clinical conditions (CP) and the plan with CT hounsfield units all set to zero (WP)

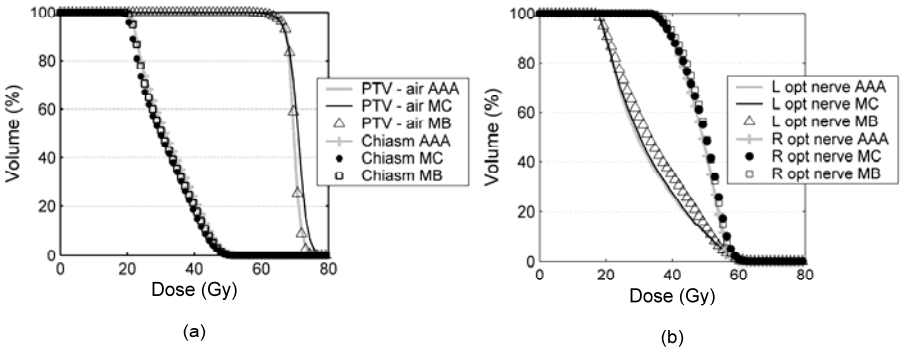
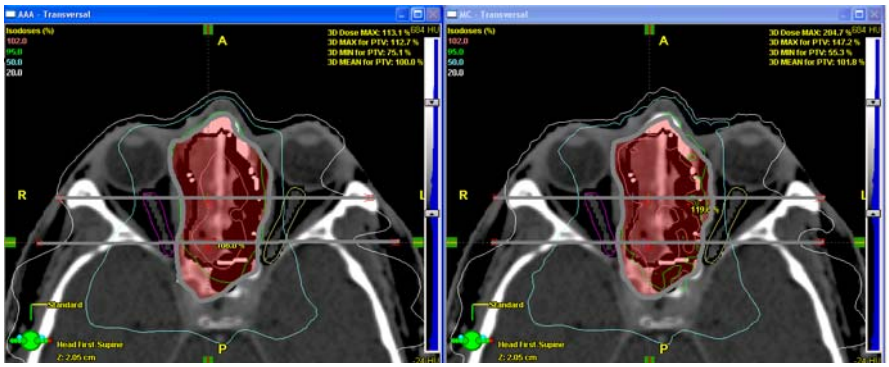


Fig. 7. Ethmoid tumor in clinical conditions study. DVH comparison between AAA, MC and MB for the PTV without air cavities and for the optic chiasm (a) and the left and right optic nerves (b)



(a)

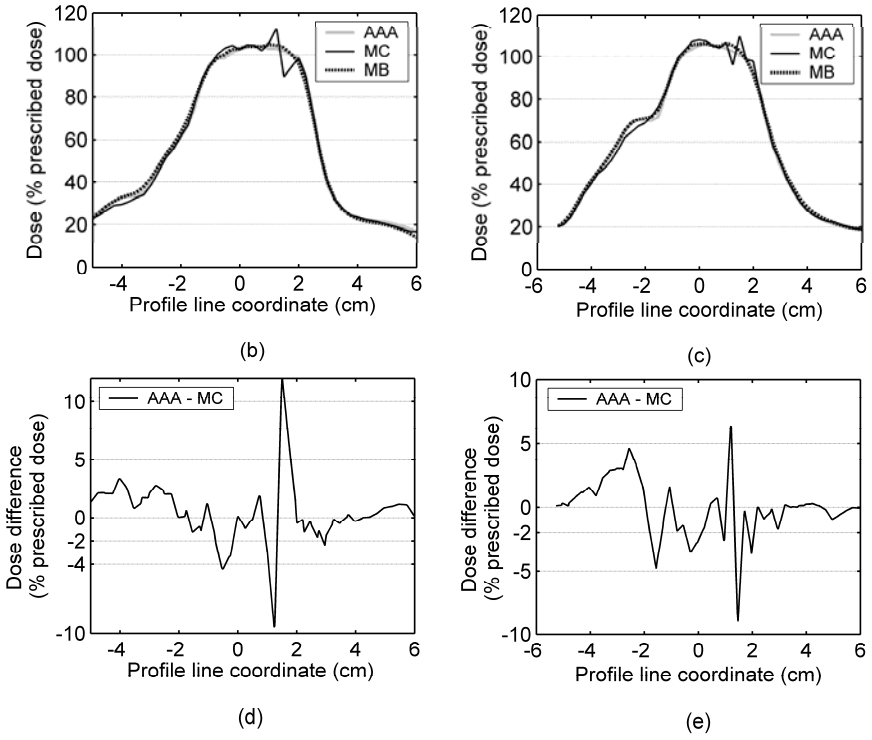


Fig. 8. Ethmoid plan calculated with AAA (left) and MC (right) (a). PTV contour is represented by the thick contour. Profiles were acquired along the thick lines, one at the isocenter and the other 1.5 cm more posterior. Figures (b), (c) show dose profile comparison between AAA (gray line), MC (black line) and MB (dotted line), respectively, at the isocenter and 1.5 cm more posterior. Figures (c) and (d) represent dose differences between AAA and MC for the profiles in figures (b) and (c) respectively.

3.3.2. Oropharynx tumor

In this case, results are shown in Table 3 for the bilateral plan (50 Gy) and the total plan (70 Gy) for the PTV. For the critical structures, results are shown only for the total plan (70 Gy). AAA and MB results were similar, and the same conclusions could be drawn for both of them. Very good agreement was achieved for the PTV 50 Gy and PTV 70 Gy.

Between AAA and MC, the maximum dose difference was around 1.8 % of the prescribed dose (50 Gy) for D_2 and the "PTV 50 Gy," whereas the estimation of the PTV coverage (D_{95}) was similar.

For the critical structures, good agreement was also achieved. For the spinal cord, the difference between AAA and MC was around 2% of the dose constraint (50 Gy) for D_2. Concerning the contra-lateral parotid, the mean dose difference between AAA and MC was 4.2% of the dose constraint (26 Gy).

		AAA	MC	MB
PTV – air 50 Gy	Mean (Gy)	50.0	50.6	50.1
	STD (Gy)	1.2	1.6	1.3
	D_{95} (Gy)	48.0	48.1	47.5
	D_2 (Gy)	52.5	53.4	52.4
PTV – air 70 Gy	Mean (Gy)	70.0	70.9	70.2
	STD (Gy)	1.6	2.0	1.5
	D_{95} (Gy)	67.4	67.5	67.2
	D_2 (Gy)	73.3	74.3	73.0
Spinal cord (70 Gy)	D_2 (Gy)	39.5	40.5	39.5
Homolateral parotid (Gy)	Mean (Gy)	61.1	60.4	60.2
Controlateral parotid (Gy)	Mean (Gy)	25.9	27.0	25.4

Table 3. Oropharynx tumor study. Comparison of DVHs' characteristic values (mean dose, standard deviation (STD), dose delivered to 95% of the volume (D_{95}) and to 2% of the volume (D_2)) for the bilateral plan (50 Gy) and the total plan (70 Gy) between AAA, MC and MB.

3.3.3. Large lung tumor

Table 4 summarizes numerical values characterizing the DVHs. Good agreement was obtained between the DVHs (not shown). The DVH of the PTV was steeper for AAA since standard deviations were equal to 1.5 and 2.1 Gy, respectively, for AAA and MC. The mean dose difference between AAA and MC equaled 2% of the prescribed dose. As in the ethmoid case, AAA underestimated the high dose regions since D_2 was equal to 64.3 Gy, while MC provided 66.3 Gy (3.3% difference). The agreement was similar for MB compared to MC, except for the PTV coverage, with a deviation of 1.2 Gy for D_{95} (2%).

		AAA	MC	MB
PTV	Mean (Gy)	60.0	61.3	60.5
	STD (Gy)	1.5	2.1	1.2
	D_{95} (Gy)	57.3	57.6	59.8
	D_2 (Gy)	64.3	66.3	64.1
Spinal cord	D_2 (Gy)	25	24.8	23.8
Left lung	V_{20Gy} (%)	0.0	0.0	0.0
	V_{25Gy} (%)	0.0	0.0	0.0
Right lung	V_{20Gy} (%)	66.0	66.4	65.6
	V_{25Gy} (%)	62.0	62.5	61.0

Table 4. Large lung tumor. Comparison of DVHs' characteristics (mean, standard deviation (STD), dose delivered to 95% of the volume (D_{95}), to 2% of the volume (D_2) and volume receiving 20 and 25 Gy (V_{20Gy} and V_{25Gy})) between AAA, MC and MB.

3.3.4. Small lung tumor

Results are summarized in Table 5. Figure 9 shows the DVHs of the PTV. For WP, the mean dose difference between MC and AAA was about 2.1%. For CP, the deviation of the mean dose was more substantial with a difference of 3.3%. For D_{95}, the difference was also significant (2.5%). Good agreement was achieved for the standard deviation with 0.3 Gy difference only. This result indicates that the shape of the DVH was similar between AAA and MC as it can be seen in Fig. 9. It is also worth mentioning that MB predicted a DVH that was too steep, with 1.4 Gy difference between MC and MB, and significantly overestimated D_{95} (4.8%).

In order to understand the origin of these discrepancies between AAA and MC, individual dose profiles were also compared. It was observed that AAA and MC always yielded profiles with the same shape, but that the dose was, on average, 3% underestimated by AAA in each profile. This is illustrated in Fig. 10, where profiles were acquired in the direction drawn in Fig. 10(a) for each algorithm and were then compared in Figs. 10(b) and 10(c). As mentioned above, the dose was, on average, 3.2% smaller with AAA, whereas local differences could reach 6%. These observations were consistent with results obtained in Table 5.

		AAA-CP	MC-CP	MB-CP	AAA-WP	MC-WP	MB-WP
PTV	Mean	60.0	62.0	62.3	61.3	62.6	61.4
	STD (Gy)	2.6	2.9	1.4	1.8	1.9	2.0
	D_{95} (Gy)	55.3	56.8	59.7	57.8	58.5	57.7
	D_2 (Gy)	63.4	66.5	64.2	63.4	65.3	63.2
Left lung	V_{20Gy} (%)	0.0	0.0	0.0	0.0	0.0	0.0
	V_{25Gy} (%)	0.0	0.0	0.0	0.0	0.0	0.0
Right	V_{20Gy} (%)	7.5	8.1	8.6	6.9	7.3	6.9
	V_{25Gy} (%)	5.3	5.7	5.8	5.2	5.3	5.2

Table 5. Small lung tumor study. Comparison of DVHs' characteristic values (mean, standard deviation (STD), dose delivered to 95% of the volume (D_{95}), to 2% of the volume (D_2) and volume receiving 20 and 25 Gy (V_{20Gy} and V_{25Gy})) between AAA and MC for the plan in clinical conditions (CP) and the plan with CT hounsfield units all set to zero (WP).

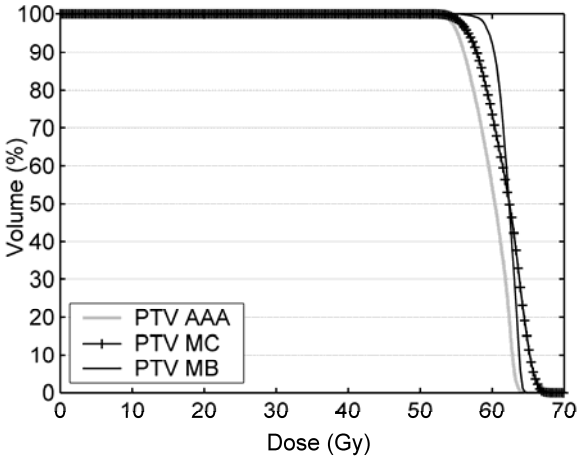
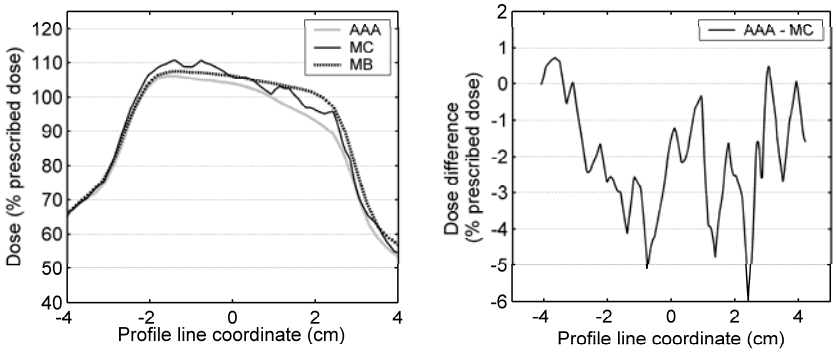


Fig. 9. Small lung tumor study. DVH comparison between AAA, MC and MB for the PTV in clinical conditions (CP).



(a)



(b) (c)

Fig. 10. Isodose curve comparison between plan calculated by AAA (left) and MC (right) (a). The profiles were acquired along the thick lines and compared between AAA (gray line), MC (black line) and MB (dotted line) (b). Figure (c) shows the difference between AAA and MC profiles.

4. DISCUSSION

4.1. MC

All MC calculations of our study were in very good agreement with the measured data, providing proof of the accuracy of our model. Differences between MC and measurement were almost always below 2% of the maximum dose – 1 mm shifting in high dose gradients regions. These were our acceptance criteria for the MC modeling. These results were, of course, a prerequisite before considering MC as reference tool for other studies.

4.2. AAA

4.2.1. Phantom results

AAA's accuracy was generally good for a fast pencil beam convolution/superposition algorithm. However, small differences could be observed, particularly just upstream from the L1 PMMA interface for the 2x2 cm^2 field and also for larger field sizes (6x6 cm^2), where AAA slightly overestimated (2–4%) the dose drop in the lung regions and the "re-build-up" effect. Similar discrepancies were found by other authors[14] in comparable situations in low density materials. In the paper of Van Esch *et al.*, a 7% deviation was found though for the smallest field studies (3x3 cm^2). These discrepancies were attributed, as in the present paper, to the basic assumption o f independent lateral and depth directions in kernel scaling. However, in our study, AAA provided clear improvements compared to MB in L1 for the 2x2 cm^2 field, where MB overestimated the dose up the 19%, whereas the magnitude of the deviations from measurements of AAA and MB were comparable in the other paper (7%). These different conclusions may be attributed to different phantom designs, linear accelerator modeling (Varian or Elekta) or measurement modalities. It should be mentioned that, in our study, measurements validity was confirmed by MC calculations and *vice versa*.

Lateral density scaling of the kernels was performed accurately, as demonstrated in Fig. 5, even though small disagreements arose for the 2x2 cm^2 field. Despite these encouraging results, AAA could not account for the "bone" cylinder pattern accurately (Fig. 6). In this case, the algorithm should take into account two phenomena: the attenuation of the photon fluence as well as the modification of scatter and electronic fluence just below the bone pattern. Since the cylinders have a density

of 1.6 g/cm^3, the attenuation of the photon fluence should be of the order of 1%, which cannot explain the 3% attenuation measured and calculated by MC in Fig. 6. Therefore, small inhomogeneities may not be taken into account correctly because of the basic assumption of independent lateral and depth directions in the density scaling process.

These observations lead to the conclusion that the use of kernels scaled along the depth and lateral directions provides clear improvements compared to other pencil beam based algorithms for large inhomogeneities whatever the field size. However, pencil beam and independent depth and lateral scaling approximations of the kernels may still involve significant inaccuracies due to modification of the electronic fluence provided by small inhomogeneities.

4.2.2. IMRT plans

In the first case concerning the ethmoid tumor, good agreement was achieved, with differences generally below 2% of the prescribed dose, even though significant differences could be noted, especially for the DVH of the PTV in the high dose regions.

In the study of the oropharynx tumor, good correspondence was obtained for all the plans. MB was expected to be accurate in this case, since the tumor volume was relatively large, with inhomogeneities only in a small fraction of the PTV. AAA, MC and MB were, indeed, all in agreement, proving that AAA was able to handle cases correctly, when these are *a priori* less critical for algorithm's accuracy.

Concerning AAA, the same conclusions could be drawn for the large lung tumor case. AAA, however, slightly underestimated the mean dose (2% of the prescribed dose) and the high doses (4%). However, as shown in Table 4, MB overestimated the PTV coverage compared to AAA, as could be expected from the phantom study, as seen in Figs. 5(b) and 5(c).

Study concerning the small lung tumor showed significant differences (3.3%) with respect to the mean dose between AAA and MC. Since deviations were also found for WP (2.1% for the mean dose) the discrepancy was more likely due to differences in beam modeling between AAA and MC, which is crucial in IMRT, rather than the effect of the inhomogeneities. However, the extra underestimation of the mean dose to the PTV compared to the plan with hounsfield units turned to zero may originate from overestimation of loss of lateral electronic equilibrium, as stated in the phantom study.

Except for this problem with the mean dose, AAA appears to provide significant improvements compared to MB as shown in Table 5, where MB predicts too steep a DVH and overestimates substantially D_{95} (4.8%). Since small fields were used and significant amounts of lung tissue were encompassed by the PTV, penumbra widening and loss of lateral electronic equilibrium effects actually occur in a high percentage of the PTV, leading to an important overestimation by MB of the dose in the lung tissues within the PTV.

This last study, achieved in extreme conditions, *i.e.*, small tumor (2 cm diameter), inhomogeneous media (lung tissue) and irregular fields, demonstrates the need for highly accurate algorithms in case of lung tumors. The magnitude of the deviations observed in this paper is consistent with other studies,[15] reporting, for example, in lung tumor study, a 2.2 % difference between AAA and MC for the mean dose to PTV. However, the comparison is rather difficult since the aim of our study was to systematically analyze AAA performance for IMRT treatment using one specific linear accelerator (Elekta), one beam energy (X6) and with minimized sources of additional uncertainties (same TPS used for all the operations except for the dose calculation).

Finally, it should be mentioned that calculation time was similar between AAA and MB (around 1–2 min on a single CPU for a IMRT plan), whereas MC calculations were finished after several hours (with calculations performed on a cluster[30]).

5. CONCLUSIONS

The phantom study demonstrated the potential of the AAA algorithm to account accurately for inhomogeneities even in conditions of severe lateral electronic disequilibrium. The only significant differences were found below the ribs, where AAA did not fully account for the effect of the cylinders on the dose distribution. According to our studies, AAA's validity is not limited by field size for 6 MV regular beams in lung tissue. It provides an important improvement compared to MB or other correction-based calculation algorithms.

In the IMRT study, different cases were studied in different conditions, in order to study a range of treatments where improvements in dose calculation accuracy with AAA could be expected compared to older Eclipse algorithms. Except for the oropharynx tumor study, significant differences were found for all the other plans, especially in the small lung tumor case. In both lung tumors, all the differences could be discussed and predicted on the basis of the phantom study.

Even though large differences were found between AAA and MB, these differences were smaller when AAA was compared to MC calculations. Since better agreement was achieved for the same plans in homogeneous conditions, the presence of inhomogeneities slightly influences AAA's accuracy and might be inherent to the pencil beam kernel approximation and independent depth and lateral scaling of the kernels. Despite these small discrepancies, AAA demonstrated in both studies its better agreement compared to the previous Eclipse algorithm (MB), certainly for lung tumors. AAA configuration for Elekta linear accelerators appears to be feasible.

These studies also show the capacity of MC simulations to perform quality assurance and evaluation of commercial treatment planning systems, since the algorithms can be tested closer to their limits of validity and in clinical conditions. An accurate and complete modeling of the linear accelerator is, however, required in order to use MC results as the benchmark in nonstandard conditions (IMRT) or conditions not easily accessible to measurements (*i.e.*, patients). Finally, the deviations shown in this paper for the clinical cases demonstrate the potential and the importance of introducing MC calculations into treatment planning procedures, providing that computation time is reasonably small for routine practice.

Acknowledgements

The authors wish to thank Martin Sabel, Laura Tillikainen and other involved people from Varian Medical Systems for providing us with the AAA system and their advice. The authors are particularly grateful to Maxime Coevoet and Adil Margoum for their help during this work. This work was supported by a grant from the Belgian "Fonds National pour la Recherche Scientifique" (F.N.R.S., Grant No. FC 73512).

References

1. J. Venselaar, H. Welleweerd, and B. Mijnheer, "Tolerances for the accuracy of photon beam dose calculations of treatment planning systems," Radiother. Oncol. 60, 191–201 (2001).
2. B. Fraas, K. Doppke, M. Hunt, G. Kutcher, G. Starkschall, R. Stern, and J. Van Dyke, "AAPM Radiation therapy committee Task Group 53. Quality assurance for clinical radiotherapy treatment planning," Med. Phys. 25, 1773–1829 (1998).
3. P. Carrasco, N. Jornet, M. A. Duch, L. Weber, M. Ginjaume, T. Eudaldo, D. Jurado, A. Ruiz, and M. Ribas, "Comparison of dose calculational

gorithms in phantoms with lung equivalent heterogeneities under conditions of lateral electronic disequilibrium," Med. Phys. 31, 2899–2911 (2004).

4. A. O. Jones and I. J. Das, "Comparison of inhomogeneity correction algorithms in small photon fields," Med. Phys. 32, 766–776 (2005).
5. M. R. Arnfield, C. H. Siantar, J. Siebers, P. Garmon, L. Cox, and R. Mohan, "The impact of electron transport on the accuracy of computed dose," Med. Phys. 27, 1266–1274 (2000).
6. C. Martens, N. Reynaert, C. De Wagter, P. Nilsson, M. Coghe, H. Palmans, H. Thierens, and W. De Neve, "Underdosage of the upper-airway mucosa for small fields as used in intensity-modulated radiation therapy: A comparison between radiochromic film measurements, Monte Carlo simulations, and collapsed cone convolutions," Med. Phys. 29, 1528– 1535 (2002).
7. J. W. Wong and R. M. Henkelman, "Reconsideration of the power-law (Batho) equation for inhomogeneity corrections," Med. Phys. 9, 4, 521–530 (1982).
8. A. Ahnesjö, "Collapsed cone convolution of radiant energy for photon dose calculation in heterogeneous media," Med. Phys. 16, 577–592 (1989).
9. M. M. Aspradakis, R. H. Morrison, N. D. Richmond, and A. Steele, "Experimental verification of convolution/superposition photondose calculations for radiotherapy treatment planning," Phys. Med. Biol. 48, 2873–2893 (2003).
10. T. Knöös, A. Ahnesjö, P. Nilsson, and L. Weber, "Limitations of a pencilbeam approach to photon dose calculations in lung tissue," Phys. Med. Biol. 40, 1411–1420 (1995).
11. L. Wang, E. Yorke, and C.-S. Chui, "Monte Carlo evaluation of tissue inhomogeneity effects in the treatment of the head and neck," Int. J. Radiat. Oncol., Biol., Phys. 50, 1339–1349 (2001).
12. F. Verhaegen and J. Seuntjens, "Monte Carlo modeling of external radiotherapy photon beams," Phys. Med. Biol. 48, R107–R164 (2003).
13. A. Fogliata, G. Nicolini, E. Vanetti, A. Clivio, and L. Cozzi, "Dosimetric validation of the Anisotropic analytical algorithm for photon dose calculation: Fundamental characterization in water," Phys. Med. Biol. 51, 1421–1438 (2006).

14. A. Van Esch, L. Tillikainen, J. Pyykkonen, M. Tenhunen, H. Helminen, S. Sijamäki, J. Alakuijala, M. Paiusco, M. Iori, and D. P. Husykens, "Testing of the analytical anisotropic algorithm for photon dose calculation," Med. Phys. 33, 4130–4148 (2006).
15. T. Knöös, E. Wieslander, L. Cozzi, C. Brink, A. Fogliata, D. Albers, H. Nyström, and S. Lassen, "Comparison of dose calculation algorithms for treatment planning in external photon beam therapy for clinical situations," Phys. Med. Biol. 51, 5785–5807 (2006).
16. D. W. Rogers, B. A. Faddegon, X. Ding, C. M. Ma, and J. We, "BEAM: A Monte Carlo code to simulate radiotherapy treatments units," Med. Phys. 22, 503–524 (1995).
17. W. Ulmer, J. Pyyry, and W. Kaissl, "The inverse problem of a Gaussian convolution and its application to the finite size of the measurement chambers/detectors in photon and proton dosimetry," Phys. Med. Biol. 48, 707–727 (2003).
18. W. Ulmer, J. Pyyry, and W. Kaissl, "A 3D photon superposition/convolution algorithm and its foundation on results of Monte Carlo calculations," Phys. Med. Biol. 50, 1767–1790 (2005).
19. W. Ulmer and D. Harder, "A triple Gaussian pencil beam model for photon beam treatment planning," Magnetism 5, 25–30 (1995).
20. H. Helen Liu, T. R. Mackie, and E. C. McCullough, "A dual sourcephoton beam model used in convolution/superposition dose calculations for clinical megavoltage x-ray beams," Med. Phys. 24, 1960–1974 (1997).
21. X. R. Zhu, P. A. Jursinic, D. F. Grimm, F. Lopez, J. J. Rownd, and M. T. Gillin, "Evaluation of Kodak EDR2 film for dose verification of intensity modulated radiation therapy delivered by a static multileaf collimator," Med. Phys. 29, 1687–1692 (2002).
22. A. Palm, A. S. Kirov, and T. LoSasso, "Predicting energy response of radiographic film in a 6 MV x-ray beam using Monte Carlo calculated fluence spectra and absorbed dose," Med. Phys. 31, 3168–3178 (2004).
23. I. J. Yeo, A. Beiki-Ardakani, Y. Cho, M. Heydarian, T. Zhang, and M. Islam, "EDR2 film dosimetry for IMRT verification using low-energy photon filters," Med. Phys. 31, 1960–1963 (2004).
24. N. Dogan, L. B. Leybovich, and A. Sethi, "Comparative evaluation of Kodak EDR2 and XV2 films for verification of intensity modulated radiation therapy," Phys. Med. Biol. 47, 4121–4130 (2002).

25. I. J. Chetty and P. M. Charland, "Investigation of Kodak extended-dose range (EDR) film for megavoltage photon beam dosimetry," Phys. Med. Biol. 47, 3629–3641 (2002).
26. A. J. Olch, "Dosimetric performance of an enhanced dose range radiographic film for intensity-modulated radiation therapy quality assurance," Med. Phys. 29, 2159–2168 (2002).
27. I. Kawrakow, "Accurate condensed history Monte Carlo simulation of electron transport. I. EGSnrc, the new EGS4 version," Med. Phys. 27, 485–498 (2000).
28. J. Van de Walle, C. Martens, N. Reynaert, H. Palmans, M. Coge, W. De Neve, C. De Wagter, and H. Thierens, "Monte Carlo model of the Elekta Sliplus accelerator: Validation of a new MLC component module in BEAM for a 6MV beam," Phys. Med. Biol. 48, 371–385 (2003).
29. B. R. B. Walters and D. W. O. Rogers, "DOSXYZnrc Users Manual," National Research Council of Canada, Ottawa, NRCC Report No. PIRS-794 revA (2004).
30. N. Reynaert, B. De Smedt, M. Coghe, L. Paelinck, B. Van Duyse, W. De Gersem, C. De Wagter, W. De Neve, and H. Thierens, "MCDE: A new Monte Carlo dose engine for IMRT with an efficient scoring method," Phys. Med. Biol. 49, N235–N241 (2004).
31. L. Paelinck, B. De Smedt, N. Reynaert, M. Coghe, W. De Gersem, C. De Wagter, B. Vanderstraeten, H. Thierens, and W. De Neve, "Comparison of dose-volume histograms of IMRT treatment plans for ethmoid sinus cancer computed by advanced treatment planning systems including Monte Carlo," Radiother. Oncol. 81, 250–256 (2006).
32. N. Reynaert, M. Coghe, B. De Smedt, L. Paelinck, B. Vanderstraeten, W. De Gersem, B. Van Duyse, C. De Wagter, W. De Neve, and H. Thierens, "The importance of accurate linear accelerator head modelling for IMRT Monte Carlo calculations," Phys. Med. Biol. 50, 831–846 (2005).
33. B. Vanderstraeten, N. Reynaert, L. Paelinck, I. Madani, C. De Wagter, W. De Gersem, W. De Neve, and H. Thierens, "Accuracy of patient dose calculation for lung IMRT: A comparison of Monte Carlo, convolution/ superposition, and pencil beam computations," Med. Phys. 33, 3149–3158 (2006).
34. J. V. Siebers, P. J. Keall, A. E. Nahum, and R. Mohan, "Converting absorbed dose to medium to absorbed dose to water for Monte Carlo

based photon beam dose calculations," Phys. Med. Biol. 45, 983–995 (2000).

35. C. Boudreau, E. Heath, J. Seuntjens, O. Ballivy, and W. Parker, "IMRT head and neck treatment planning with a commercially available Monte Carlo based planning system," Phys. Med. Biol. 50, 879–890 (2005).
36. D. Sheikh-Bagheri and D. W. O. Rogers, "Monte Carlo calculation of nine megavoltage photon beam spectra using the BEAM code," Med. Phys. 29, 391–402 (2002).

Chapter 4: Publication 2

Monte Carlo simulation of the tomotherapy treatment unit in the static mode using MC HAMMER, a Monte Carlo tool dedicated to tomotherapy

E. Sterpin[a], M. Tomsej[a], B. Cravens[b], F. Salvat[c], K. Ruchala[b], G. H. Olivera[b], and S. Vynckier[a]

[a] Department of Radiotherapy, St-Luc University Hospital, 10 av. Hippocrate, 1200 Brussels, Belgium

[b] Tomotherapy Inc., 1240 Deming Way, Madison, Wisconsin 52717

[c] Facultat de Fisica (ECM), Universitat de Barcelona, Societat Catalan de Fisica (IEC), Diagonal 647, 08028 Barcelona, Spain

J. Phys.: Conf. Ser. **74** 021019 (2007)

Abstract.

Helical tomotherapy (HT) is designed to deliver highly modulated IMRT treatments. The concept of HT provides new challenges in MC simulation, because simultaneous movement of the gantry, the couch and the multi-leaf collimator (MLC) must be simulated accurately. However, before accounting for gantry, couch movement and multileaf collimator configurations, high accuracy must be achieved while simulating open static fields (1x40, 2.5x40 and 5 x 40 cm²). This is performed using MC HAMMER, which is a graphical user interface allowing MC simulation using PENELOPE for various configurations of HT. Since the geometry of the different elements and materials involved in the beam generation are precisely known

and defined, the only parameters that need to be tuned on are therefore electron source spot size and electron energy. Beyond the build up region, good agreement (2%/1mm) is achieved for all the field sizes between measurements (ion chamber) and simulations with an electron source energy set to 5.5 MeV. The electron source spot size is modelled as a gaussian distribution with full width half maximum equal to 1.4 mm. This value was chosen to match measured and calculated penumbras in the longitudinal direction.

1. Introduction

Intensity Modulated Radiation Therapy (IMRT) allows better sparing of the healthy tissue while increasing dose conformity and homogeneity to the target [1]-[3]. Helical Tomotherapy (HT) is designed to deliver highly modulated IMRT treatments, yielding significant reduction of dose to critical tissues without compromising target coverage. The irregular fluence is obtained through the optimization process results of the simultaneous movement of the gantry, table and multileaf collimator. The resulting dose distribution is calculated with the treatment planning system developed by Tomotherapy and based on a collapsed cone convolution algorithm [4], [5].

This algorithm has shown great accuracy for simple configurations in inhomogeneous media [6], but the scientific community is still concerned when small fields or a superposition of small fields, *i.e.* IMRT fields, are used especially in low density inhomogeneities [7] - [10]. Convolution/superposition algorithms are known to be more accurate than older correction-based algorithms, even though deviations were reported at interfaces and in low density regions [8], [11], [12]

Monte Carlo (MC) simulation is considered as the most accurate method to calculate dose distributions in tissue [13]. Moreover, the validity of MC simulation is not limited by the complexity of the treatment, provided that the treatment delivery is simulated in a realistic manner. Therefore, the precise modeling of HT is necessary to evaluate the convolution/superposition algorithm accuracy in complex situations.

HT modeling is divided into three parts. Firstly, the elements of the treatment head involved in the beam generation and broad beam collimations devices (jaws) must be accurately and completely modeled. Secondly, the multileaf collimator (MLC) geometry has to be defined precisely. Finally, the helical mode need to be simulated by calculating, translating and rotating the phase spaces delivered statically according to the pitch setup and the MLC configuration at each time of the treatment. When all these steps are accomplished, dose distribution inside patients for clinically delivered treatments may be calculated and then compared with the convolution/superposition

algorithm. The code used for the simulations PENELOPE [14] which allows the user to determine any geometry configuration provided that all the bodies of the geometry are delimited by quadric surfaces. PENELOPE incorporates elaborate physical models which have been used for radiotherapy applications [15] and benchmarked experimentally [16] and with other MC codes [17]. A dedicated graphical user interface, called MC HAMMER, for HT simulations was developed.

This paper covers the first part of the simulation, *i.e.* static fields. The model was commissioned by comparing calculated and measured data in reference conditions. Of course, the highest accuracy must be achieved, since the resulting phase spaces will be used as an input when the helical mode will be turned on. A previous paper was already published on the Monte Carlo modeling of HT [18], principally on radiation characteristics aspects. However, the present work included a more detailed model of HT treatment planning for future MC treatment planning purposes. It was also based on the last HT system and uses PENELOPE code instead of MCNP.

2. Material and methods

2.1. Tomotherapy treatment unit

HT delivers intensity modulated radiotherapy. The treatment head is composed by a linear accelerator tube (SIEMENS), beam formation elements (target, beam hardener), collimating devices (jaws and primary collimator) and a binary MLC to provide modulation. The head can rotate continuously and simultaneously with the translation of the treatment table (helical delivery), in the manner of a CT scanner. HT can operate in two modes. In the treatment mode, the nominal energy is equal to 6 MV. HT has also the ability to acquire CT scan images with the patient in the treatment position, with a nominal energy reduced to 3.5 MV in that case.

When all the leaves are open, the position of the jaws can be set to define three field sizes, 40x1, 40x2.5 and 40x5 cm² at the isocenter (SSD = 85 cm). Lower field sizes permit higher longitudinal modulation of the dose distribution but at the cost of higher treatment times. Due to the absence of a flattening filter, the transverse profile has a typical cone shape.

The binary MLC equipping the system is composed by 64 movable leaves with a projected nominal thickness at the isocenter of 6.25 mm. Apart from those leaves, there are two additional stationary leaves at each extremity of the MLC that affect the beam collimation, even when a static open field is delivered.

2.2. Measurements

Most of the measurements were performed in a water tank, with a SSD set to 85 cm. The dimensions of the water tank were 60x27x27 cm^3, where 60 cm refers to the lateral dimension. The detector was an Extradin A1SL ion chamber (Standard Imaging). . The collecting volume and its diameter equaled 0.056 cm^3 and 4.1 mm. Profiles were measured at several depths (1.5 cm, 5 cm and 10 cm). Lateral profiles refer to profiles measured in the direction where the field size is equal to 40 cm. In the longitudinal direction, the field width is determined by the jaws and may have three values (5 cm, 2.5 cm, and 1 cm). The simulations were compared to a "gold standard" (GS) which was obtained by acquiring profiles and depth dose distribution from several Tomotherapy units, with the Extradin A1SL ion chamber. All the data were then averaged to provide only one depth dose and one set of profiles. Currently, each new released unit is tuned in order to match the GS within 1%/1mm for depth dose and lateral profiles and within 1% of full width half maximum (FWHM) for longitudinal profiles of open fields. Basic measurements of the HT unit of our institution, e.g. depth dose curves and open fields' profiles, are in agreement with the GS within the same limits. Therefore, the parameters of the MC simulation could be used for both the GS and the HT unit of our institution with the same level of accuracy. It is worthwhile to mention that the choice of the detector was made implicitly, since one of the purposes of the MC simulation is to match the GS.

Some ion chamber designs may be not adequate to measure accurately the dose in the build up region [19]. Even though MC simulations should reproduce as close as possible commissioning data (*i.e.* the GS, measured with an ion chamber), additional measurements in Solid Water™ were performed using EDR-2 films placed at several depths, perpendicular to the beam axis, to study the build up region. Films were placed each 2 mm from 0.1 to 1.5 cm depth, and each 5 mm from 1.5 to 5 cm depth. EDR-2 films were chosen because of their better resolution and because several studies show that EDR-2 films yield generally accurate results with deviations generally within 2% , for perpendicular [20] and parallel [21], [22] depth dose measurements. High depths (>10 cm) and large fields may lead to substantial deviations because of the potential over-response of the film to scattered photons with lower energies [20], [21].

2.3. Monte Carlo simulation

2.3.1. Geometry definition

Through the PENGEOM subroutine package, PENELOPE provides great freedom to the user to define easily complex geometries, allowing an exact reproduction of some unique features of HT, like the jaw collimation system. Since the geometry and the materials were known in detail and PENELOPE was able to reproduce it faithfully, no modifications of the geometry should have been introduced further during the tuning and the commissioning processes of the model. Furthermore, the program GVIEW provided with the PENELOPE package enabled the verification of the geometry as it was defined in the MC simulation, as illustrated in figure 1.

However, there remained a small uncertainty in the geometry, which was the exact position of the target along the beam axis. When the machine is assembled, the target is mounted up into the linear accelerator, shifting systematically a little the target from its original position, which explains the uncertainty. The order of magnitude of this displacement with respect to the original position is around a few millimeters. The lateral profile width is very sensitive to the position of the target, whereas it is relatively insensitive to the other parameters. Therefore, the position could be accurately determined by matching calculated and measured lateral profile width during a standard iterative process. The last parameters for MC tuning were the energy and the geometric distribution of the electron source. The energy was determined matching cone profiles and percent depth doses (pdd) for the largest field (5 cm). The cone profile shape has a high sensitivity to the electron energy since it depends on the angular distribution of the photons emitted by the target, which is a function of electron energy. The electron source spot size was determined by comparing calculated and measured penumbras. During all these steps, the acceptance criteria are, beyond the build up region, local dose differences below 2% of dose maximum for all the points, and, in high dose gradients, differences in millimeters had to be similar as the criteria used for the matching of a given Tomotherapy treatment unit with the GS.

Even though the MLC was not included in the simulations presented in this paper, some modeling of the MLC was necessary to account for the two external stationary leaves. The region occupied by the MLC in the treatment head is shown in figure 1.

Dose distributions were calculated in a water phantom, with a voxel size of 2x2x2 mm^3. However, some averaging was allowed, depending on which profile was acquired. For depth dose calculations, the voxel size was increased up to 1 cm in the

transverse direction. For profiles shown in this paper, the voxel size was increased up to 6 mm in the depth direction and 6 mm in the direction perpendicular to the direction of the profile considered The number of simulated histories was such that the statistical uncertainty is smaller than 1% (one sigma) of maximum dose for all the voxels.

Two phase-space scoring planes were used in our simulations, one below the jaws and the other one below the lead plate, as depicted in figure 1. In this paper, the dose calculations were then always performed from the phase space file representing the particle fluence at the second plane

2.3.2. Particles transport

The transport of particles is simulated by PENELOPE (an acronym for PENetration and Energy LOss of Positrons and Electrons). While photons are tracked using the conventional detailed method (*i.e.*, interaction by interaction), electrons and positrons are simulated using a mixed (class II) scheme. Firstly, hard collisions are simulated individually from the corresponding differential cross sections. Soft interactions between consecutive hard collisions are, however, simulated globally as a single "artificial" event using multiple-scattering approximations. The simulation is controlled by four user-defined parameters: C_1, C_2, W_{cc} and W_{cr}. The parameter C_1 determines the mean free path for hard elastic events; C_2 sets the upper limit for the average fractional energy loss in a single step. The parameters W_{cc} and W_{cr} are energy-loss cutoff values that separate soft and hard events, for inelastic collisions and bremsstrahlung emission, respectively. Thus, inelastic collisions (bremsstrahlung events) with energy loss larger than W_{cc} (W_{cr}) are simulated individually. In the present simulations we adopted the following set of simulation parameters: $C_1 = C_2 =$ 0.05 and $W_{cc} = W_{cr} =$ 10 keV. These values are somewhat conservative for a routine simulation, but here it was wise to sacrifice simulation speed to ensure reliability of the whole tuning process.

2.3.3. MC HAMMER

MC HAMMER is a graphical interface that allows the user to change easily some parameters of the simulation, like the energy, the geometric distribution of the source, the jaws settings … The geometry definition can be visualized in two or three dimensions. Once the parameters of the simulation were defined, phase space files could be calculated and analyzed. In its current version, the interface was configured for static mode and phase space calculations only. Dose calculations were therefore

performed using the user code "penmain" in the PENELOPE distribution. The interface permits to run the simulation on a single CPU where MC HAMMER is installed (standalone job) or on a cluster. In our case, a cluster with 16 computers was used.

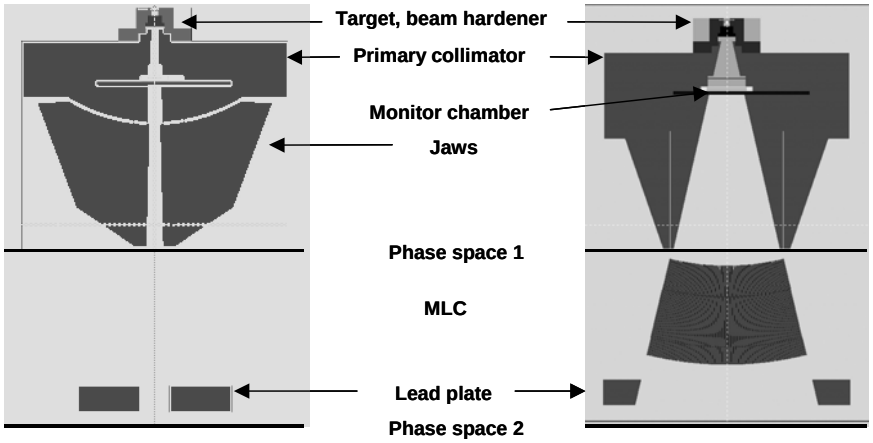


Figure 1 Geometry of the Tomotherapy treatment head as defined in the MC simulation. The images represent two sections of the head geometry for the open field configuration, in the longitudinal direction (left), and in the lateral direction (right picture) where the MLC is also illustrated. On the left picture, it can be seen that the design of the jaws specific to Tomotherapy is reproduced in the simulation. The thick lines represent the phase-space planes used in the simulations.

3. Results and discussion

3.1. Energy and target position tuning

The target position was assumed to be correctly determined when the calculated cone profile width agreed with the measured one within 1 mm, as illustrated in the inset in figure 2. When the target is not displaced, the lateral profile width is 5 mm overestimated, which is not the case when the target is shifted 2.5 mm further from the isocenter. Therefore, the distance from source to isocenter is 85.25 cm in our simulation. However, in the rest of the paper, the values of the SSD are given according to the nominal value of the SSD (source to isocenter distance of 85 cm)

The energy was first determined by comparing transverse profiles. When the energy increases, bremsstrahlung photons are preferentially emitted forward at higher energies and, therefore, the ratio between the dose on the central axis and a dose at a

given point off-axis is increased (the lateral profile is more "pointed"). The best agreement (within 1%/1mm) was obtained for a monoenergetic electron source with an energy equal to 5.5 MeV, as illustrated in figure 2, where measured and calculated profiles are normalized on the central axis. The energy spread of the electron source was a rather insensitive parameter, as stated already by other authors for conventional linear accelerators [13], [23]. For the sake of clarity, MC points were drawn each cm only, except at the edges of the profiles. In figure 3 (a) measurements performed with ion chamber are compared with MC calculations. It is worthwhile to mention that the depth dose curves were scaled such that measurements and MC were equal at 2 cm depth. Outside the build up region, good agreement was obtained with deviations smaller than 1%. In the build-up region, ion chamber measurements deviated substantially from MC results. To resolve this discrepancy, which could have originated from a non adapted ion chamber design for measurements in the build up region, EDR-2 films measurements in Solid Water™ were compared to MC simulations in the same medium. Results are shown in figure 3 (b) where good agreement was obtained between EDR-2 measurements and MC with deviations smaller than 1%/1mm. As the GS, measurements were normalized at depth of maximum dose (1.5 cm) and MC was normalized in the same manner as in figure 3 (a).

The resulting photon energy spectrum of the second phase space file was shown in figure 4. The maximum energy was of course 5.5 MeV, while the average energy equaled 1.4 MeV. Moreover, the peak due to electron-positron annihilation is clearly visible (511 keV peak). The emerging beam consisted mainly of photons, with a negligible contribution of charged particles (electrons and positrons). Indeed, the ratio between the maximum (energy) fluence of charged particles and the maximum fluence of photons (excluding the annihilation peak) was around 0.25%.

Good agreement was also obtained for other field sizes, but, for conciseness, these results are not shown in this paper but will be included in a forthcoming publication.

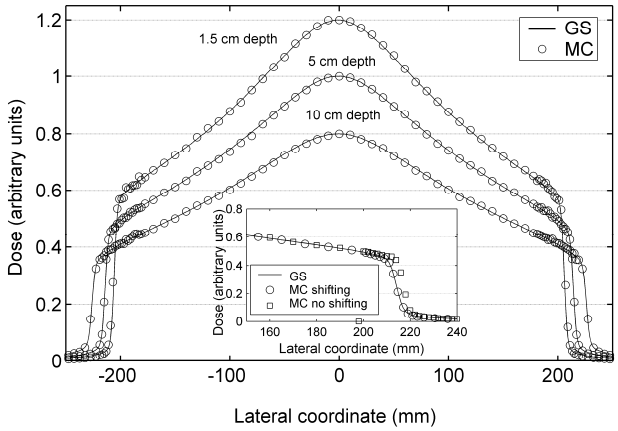


Figure 2. Lateral profiles comparison between Monte Carlo simulation (MC, open circles) and the gold standard (GS, solid line) for a 40x5cm² field. The profiles are acquired in a water phantom at 1.5, 5 and 10 cm depth and SSD = 85 cm. In the insets, measured (GS, solid line) and calculated profiles (MC) at 5 cm depth, SSD = 85 cm are compared for different positions of the target in the simulation (with tuned displacement, open circles, without displacement, open squares)

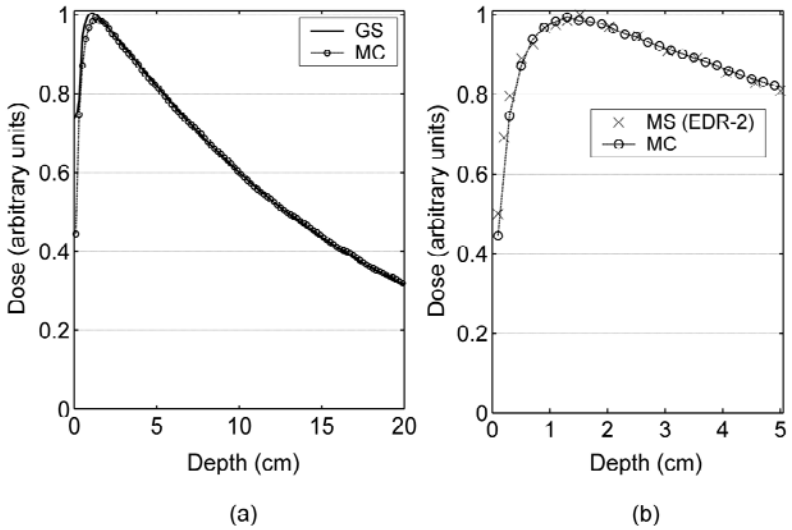


Figure 3. 40 x 5 cm² field depth dose comparison between MC simulations (open circles) and measurements (GS, solid line; EDR-2, crosses). MC calculations is firstly (a) compared to ion chamber measurements (MS, solid line) in a water phantom (SSD = 85 cm) and secondly (b) to EDR-2 film measurements in Solid Water™ (crosses) (SSD=85 cm). In each figure, MC simulations are performed according to the experimental conditions (water phantom or Solid Water™ phantom).

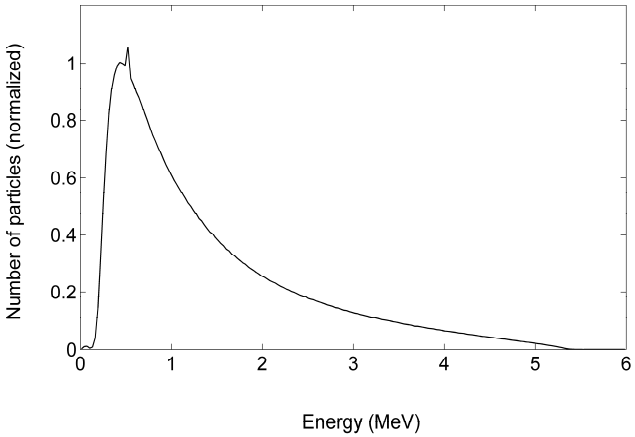


Figure 4. Total spectrum of the second phase space file. The maximum energy is equal to 5.5 MeV and the average energy is around 1.4 MeV.

3.2. Jaws settings and electron source geometry

In the simulation, the position of the jaws must be accurately defined according to the GS in the longitudinal direction for the three field sizes. This position was determined comparing the FWHM at a given depth (5 cm). The results are shown in figure 5. The calculated and measured FWHMs agreed within 1% of FWHM.

The penumbra depends on the electron source spot size and the active volume of the detector shape used in the measurements. It can be quantitatively defined as the distance between 80% and 20% of the dose at the central axis. The active volume of the ion chamber has a diameter of 4 mm. To reproduce partially the averaging effect of the chamber, each point in the MC curve represents the average of a given number of neighboring voxels, which corresponds to an active volume of 8 mm^3 times the number of such voxels since the original voxel size is 8mm^3. Of course, this is an approximation, since the ion chamber is cylindrical whereas the voxels are cubic. To illustrate the effect of both electron source spot size and voxel size, figure 6 shows the calculated dose profile for a point source, and with a gaussian distribution (FWHM = 1.4 mm) with voxel sizes of 2, 4 and 6 mm in the longitudinal direction. As expected, increasing voxel size and electron source distribution lead to a larger penumbra and a smoother fall-off. The best agreement was achieved for FWHM = 1.4 mm and a voxel size of 4 mm in the longitudinal direction, which corresponds to the diameter of the ion chamber, as clearly shown in figure 6.

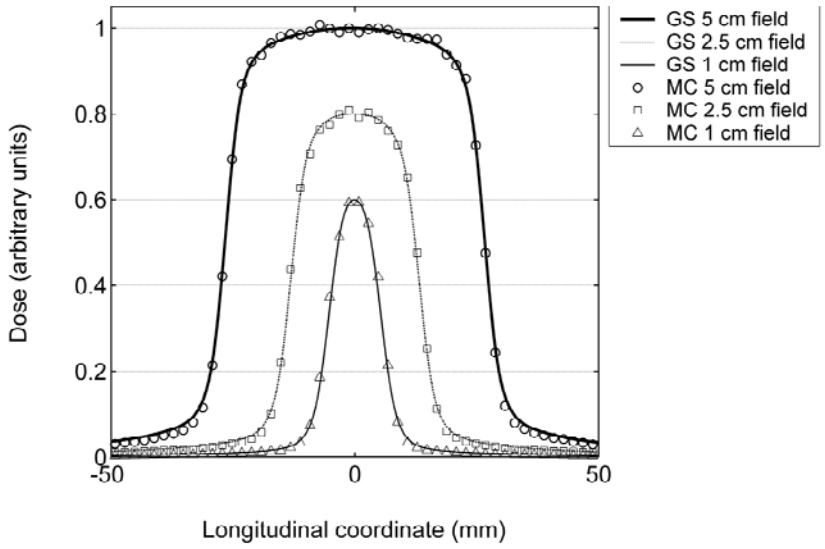


Figure 5. Comparison between measured (GS) and calculated (MC) longitudinal profiles, for the three static field sizes available in the tomotherapy treatment unit (5cm, 2.5 cm, 1 cm). The profiles are acquired at SSD = 85 cm and 5 cm depth. The electron source (E=5.5 MeV) has a gaussian geometric spread with FWHM = 1.4 mm.

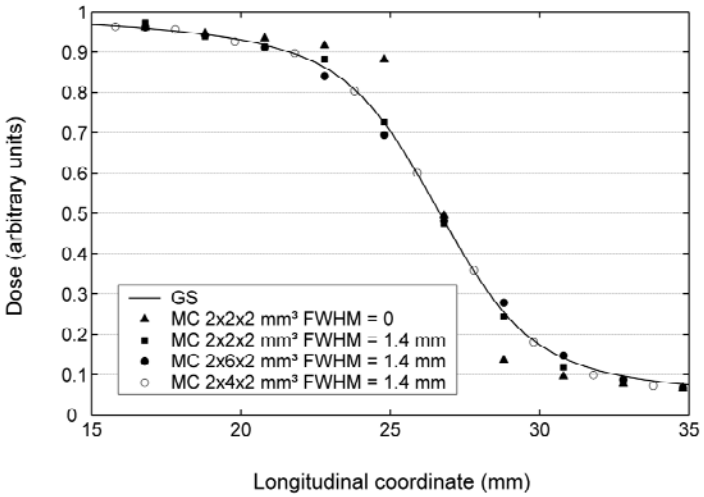


Figure 6. Comparison between calculated (MC) and measured (GS) penumbras (longitudinal profile), for the 40x5 cm² field. The profiles were acquired at 5 cm depth, SSD = 85 cm. The effects of both the electron source spot size and the voxel size are illustrated.

4. Conclusions

PENELOPE is well suited to model the unique features of HT because of the freedom let to the user to define new geometries. Thanks to the detailed definition of the geometry, only three parameters needed to be determined: the energy, the spot size of electron source and the target position. The typical cone profile shape, due to the absence of flattening filter, was found to be sensitive to the energy of the primary electron beam and the target position. Percent depth dose and longitudinal profiles were also calculated in water phantom and compared to measurements. Good agreement was achieved with deviations below 1 mm and 2% of dose maximum.

Collimation by the jaws was also simulated accurately for all the field sizes. Particles can be stored in a phase space placed below the jaws, thus yielding to a significant reduction of computation time, since calculations through the beam formation elements and the jaws are not necessary anymore. Therefore, the phase space files for the three field sizes can now be used for more complex configurations using the MLC, these simulations have already been validated but not shown here for conciseness.

Acknowledgements

This work was supported by a grant from the Belgian 'Fonds National pour la Recherche Scientifique' (F.N.R.S., grant number FC 73512)

References

[1] Sultanem K, Shu HK, Xia P, Akazawa C, Quivey J M, Verhey L J and Fu K K 2000 Three-dimensional intensity-modulated radiotherapy in the treatment of nasopharyngeal carcinoma: the University of California-San Francisco experience *Int. J. Radiat. Oncol. Biol. Phys.* **48** 711-22

[2] Hsiung C-Y, T H-M, Huang H-Y, Lee C-H, Huang E-Y and Hsu H-C 2006 Parotid-sparing internsity-modulated radiotherapy for nasopharyngeal carcinoma: preserved parotid function after IMRT on quantitative salivary scitnigraphy and comparison with historical data after conventinal radiotherapy *Int. J. Radiat. Oncol. Biol. Phys.* **66** 451-61

[3] Luxton G, Hancock S K and Boyer A L 2004 Dosimetry and radiobiologic model comparison of IMRT and 3D conformal radiotherapy in treatment of carcinoma of the prostate *Int. J. Radiat. Oncol. Biol. Phys.* **59** 267-84

[4] Mackie T R, Olivera G H, Reckwerdt P J and Shepard D M 2000 Convolution/superposition photon dose algorithm *General Practice of Radiation Oncology Physics in the 21st Century, ed A Shiu and D Mellenberg (College Park, MD: American association of Physicists in Medicine)* 39-56

[5] Mackie T R, Reckwerdt P J, Olivera G H, Shepard D and Zachman J, 2001a The convolution algorithm in IMRT *In 3-D Conformal and Intensity Modulated Radiation Therapy, ed J Purdy, W III Grant, J Palta, B Butler and C Perez (Madison, WI: Advanced Medical Publishing)* 179-90
[6] Lu W, Olivera G H, Chen ML, Rechwerdt P J and Mackie T R, 2005 Accurate convolution/superposition for multi-resolution dose calculation using cumulative tabulated kernels *Phys. Med. Biol.* **50** 655-80
[7] Carrasco P, Jornet N, Duch M A, Weber L, Ginjaume M, Eudaldo T, Jurado D, Ruiz A and Ribas M, 2004 Comparison of dose calculation algorithms in phantoms with lung equivalent heterogeneities under conditions of lateral electronic disequilibrium *Med. Phys.* **31** 2899-911
[8] Jones A O and Das I J, 2005 Comparison of inhomogeneity correction algorithms in small photon fields *Med. Phys.* **32** 766-76
[9] Arnfield M R, Siantar C H, Siebers J, Garmon P, Cox L and Mohan R, 2000 The impact of electron transport on the accuracy of computed dose *Med. Phys.* **27** 1266-74
[10] Martens C, Reynaert N, De Wagter C, Nilsson P, Coghe M, Palmans H, Thierens H and De Neve W, 2002 Underdosage of the upper-airway mucosa for small fields as used in intensity-modulated radiation therapy : a comparison between radiochromic film measurements, Monte Carlo simulations, and collapsed cone convolutions *Med. Phys*. **29** 1528-35
[11] Ahnesjö A, 1989 Collapsed cone convolution of radiant energy for photon dose calculation in heterogeneous media *Med. Phys.* **16** 577-92
[12] Aspradakis M M, Morrison R H, Richmond N D and Steele A, 2003 Experimental verification of convolution/superposition photon dose calculations for radiotherapy treatment planning *Phys. Med. Biol.* **48** 2873-93
[13] Verhaegen F and Seuntjens J, 2003 Monte Carlo modeling of external radiotherapy photon beams *Phys. Med. Biol.* **48** R107-64
[14] Salvat F, Fernandez-Varea J M, and Sempau J 2006 *PENELOPE-2006: A Code System for Monte Carlo Simulation of Electron and Photon Transport* OECD Nuclear Energy Agency, Issy-les-Moulineaux, France
[15] Sempau J, Fernandez-Varea J M, Acosta E and Salvat F 2003 Experimental benchmarks of the Monte Carlo code PENELOPE *Nucl. Instrum. Methods Phys.* **B 207**, 107–23
[16] Sempau J, Sanchez-Reyes A, Salvat F, Oulad ben Tahar H, Jiang S B and Fernandez-Varea J M, 2001 Monte Carlo simulation of electron beams from an accelerator head using PENELOPE *Phys. Med. Biol.* **46** 1163-86
[17] Ye S J, Brezovich I A, Pareek P and Naqvi N A, 2004 Benchmark of PENELOPE codes for low-energy photon transport : dose comparisons with MCNP4 and EGS4 *Phys. Med. Biol.* **49** 387-97
[18] Jeraj R, Mackie T R, Balog J, Olivera G, Pearson D, Kapatoes J, Ruchala K and Reckwerdt P, 2004 Radiation characteristics of helical tomotherapy *Med. Phys*. **31** 396-404
[19] Abdel-Rahman W, Seuntjens J P, Verhaegen F, Deblois F and Podgorsak E B, 2005 Validation of Monte Carlo calculated surface doses for megavoltage photon beams *Med. Phys.* **32 (1)** 286-98
[20] Zhu X R, Jursinic P A, Grimm D F, Lopez F, Rownd J J and Gillin M T, 2002

Evaluation of Kodak EDR-2 film for dose verification of intensity modulated radiation therapy delivered by a static multileaf collimator *Med. Phys.* **29 (8)** 1687-92
[21] Olch A J, 2002 Dosimetric performance of an enhanced dose range radiographic film for intensity-modulated radiation therapy quality assurance *Med. Phys.* **29 (9)** 2159-68
[22] Dogan N, Leybovich L B and Sethi A 2002 Comparative evaluation of Kodak EDR2 and XV2 films for verification of intensity modulated radiation therapy *Phys Med Biol* **47** 4121-30
[23] Sheikh-Bagheri and Rogers D W O 2002 Monte Carlo calculation of nine megavoltage photon beam spectra using the BEAM code *Med. Phys.* **29** 391-402

Chapter 5: Publication 3

Analytical model of the binary multileaf collimator of tomotherapy for Monte Carlo simulations

E Sterpin[a], F Salvat[b], G H Olivera[c,d] and S Vynckier[a]

[a] Department of Radiotherapy, St-Luc University Hospital, 10 av. Hippocrate, 1200 Brussels, Belgium

[b] Facultat de Fisica (ECM), Universitat de Barcelona, Diagonal 647, 08028 Barcelona, Spain

[c] Tomotherapy Inc., 1240 Deming Way, Madison WI USA

d Department of Medical Physics University of Wisconsin-Madison, Madison WI USA

J. Phys.: Conf. Ser. **102** 012022 (2008)

Abstract.

Helical Tomotherapy (HT) delivers intensity-modulated radiotherapy by the means of many configurations of the binary multi-leaf collimator (MLC). The aim of the present study was to devise a method, which we call the "transfer function" (TF) method, to perform the transport of particles through the MLC much faster than the time consuming Monte Carlo (MC) simulation and with no significant loss of accuracy. The TF method consists of calculating, for each photon in the phase-space file, the attenuation factor for each leaf (up to three) that the photon passes, assuming straight propagation through closed leaves, and storing these factors in a modified phase-space file. To account for the transport through the MLC in a given

configuration, the weight of a photon is simply multiplied by the attenuation factors of the leaves that are intersected by the photon ray and are closed. The TF method was combined with the PENELOPE MC code, and validated with measurements for the three static field sizes available (40x5, 40x2.5 and 40x1 cm²) and for some MLC patterns. The TF method allows a large reduction in computation time, without introducing appreciable deviations from the result of full MC simulations.

1. Introduction

Helical Tomotherapy (HT) delivers intensity-modulated radiation therapy (IMRT) by the means of the simultaneous movement of the couch, the gantry and the binary multi-leaf collimator (MLC). It is generally recognized that Monte Carlo (MC) simulations provide the most accurate for dose distributions in tissue [1]. For the aforesaid treatment delivery procedures, no fast and reliable Monte Carlo (MC) modeling has been devised to date, although an extensive literature exists on MC modeling of conventional linear accelerators[2], including dynamic accessories [3]-[6]

The treatment head of HT was previously modeled using PENELOPE and commissioned with measurements [1]-[8]. The MLC is the only device in the treatment head which is moving during irradiation and which needs to be actually simulated for each individual treatment. Therefore, the transport of particles through the MLC is a critical issue regarding the speed of the simulation through the treatment head. Since the leaves are often closed during a typical treatment procedure, straight MC simulations would spend much time tracking particles through the MLC geometry that, in many cases, have a very small probability of reaching the phantom surface.

To increase the calculation efficiency for forthcoming simulations of the helical mode, we have devised a generic analytical method, called the "transfer function" (TF) method, to transport photons through the MLC, without any significant loss of accuracy as compared with the full MC simulations. The MLC geometry was described in all detail to define the TF method, but strong approximations had to be introduced regarding the transport of photons. The accuracy of the TF method was tested by comparing dose distributions in a water phantom obtained from full MC simulations and from simulations using the TF method, for various configurations of the MLC.

Other authors already introduced approximations with a similar approach in their MC model to enable faster simulations of the MLC [3]-[6] but our model differs significantly, principally because neither modification nor approximation of the

geometry of the MLC were needed, owing to the capabilities of PENELOPE and to the fact that the MLC is binary.

2. Material and methods

2.1. Geometry definition

The binary MLC of HT is composed by 64 leaves with a projected nominal thickness of 6.25 mm at the isocenter. The MLC is called "binary" because each leaf can have only two states: fully closed or wide open. Accurate MC simulations with PENELOPE of HT in the static mode were previously performed and commissioned with measurements 0. Since the geometry and materials were fully disclosed by the manufacturer, the treatment head was reproduced in detail in the simulation, using the PENGEOM subroutine package. It was found that for a monoenergetic electron source with an energy of 5.5 MeV and a spatial Gaussian distribution with FHWM = 1.4 mm, calculations and measurements agreed to within 2% and 1mm for the three static open fields available with HT (40x5, 40x2.5 and 40x1 cm²). The three resulting phase space files, one for each field size and recorded at a plane perpendicular to the beam and just below the jaws, could then be used for describing the transport through the MLC and stored for future developments. Moreover, the MLC geometry definition was verified for different configurations and good agreement was obtained with measurements, similar to the degree of agreement found in the commissioning. Finally, it was also observed that electron contamination in the beam was negligible, a fact that is important for the considerations that follow.

Since the full MC model reproduced accurately the measurements, results obtained from full MC simulations are regarded as reference data in the present study.

2.2. Transfer function (TF) of the MLC

The TF method is set in two steps. In the first step, the phase space file is transformed by adding calculated attenuation factors for the complete MLC geometry with all the leaves closed. The second step created a new phase space file where the MLC configuration was taken into account. This phase space file was then used for dose calculations in a water phantom.

2.2.1. Step 1: transform of the phase space file and calculation of the absorption factors

This transformation was performed by using a modified version of PENELOPE where the photons are transported along their initial direction without interacting (simple ray-tracing) through the MLC geometry with all the leaves closed and the other static parts of the MC geometry present below the phase space file (lead plate below the MLC 0). For each photon, an attenuation coefficient (μ) is calculated by PENELOPE according to the energy of the particle and the material of the MLC (tungsten). PENELOPE also calculates the raylength (t_i where i is the label of the leaf) of the photon in each leaf it passes. If the photon crosses more than three leaves, the photon is disregarded (not included in the transformed phase-space file). Moreover, contaminant electrons are removed and not included in the new phase-space file. Accounting for all the photons who might cross more than three leaves would have required 64 attenuation factors and the 64 associated leaves labels, which would have resulted in a huge phase space file and a slower simulation. Since less than 0.1% of the photons cross more than three leaves, it is likely that neglecting them will not lead to significant deviations from the straight MC method.

Therefore, for each photon kept, three pairs of numbers are added at each line of the transformed phase space file. Each pair consists of the label (i) of a crossed leaf and the associated attenuation coefficient, $\exp(-\mu t_i)$. Figure 1 illustrates this procedure for the leaves 20 to 24. This first step needs to be performed only once for a given phase space file.

2.2.2. Step 2: Accounting for the MLC configuration

A new phase space file, in a plane placed just below the MLC, is generated. Each photon is assumed to move straight ahead through the MLC and its position coordinates are replaced by those of the intersection between the straight trajectory and the lower phase-space plane. It is now straightforward to account for an arbitrary MLC configuration. Let us assume that the state of each leaf (open or close) is known. It suffices to read, for each particle, the labels and the associated attenuation coefficients and toggle to one the attenuation coefficients corresponding to open leaves (no attenuation in that case). The weight of the photon is then multiplied by the adapted attenuation coefficients and the corrected weight is written into the new phase space file for future dose calculation. It is clear that the simulation time through the MLC itself is virtually zero (it requires to read 6 six variables and perform a

multiplication) if one wants to calculate dose distributions in water or in a CT structure.

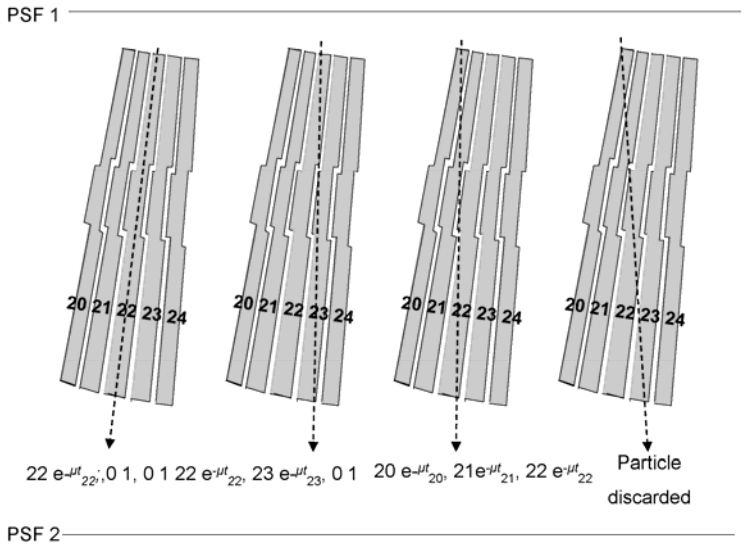


Figure 1. Schematic representation of the ray-tracing technique performed by the ray-tracing code with PENGEOM, for the leaves 20 to 24. Photons are transported along linear trajectories through the MLC geometry. When the trajectory crosses leaf number *i*, the ray-length within this leaf (t_i) is calculated and an attenuation coefficient is determined according to the energy of the particle and the material of the MLC. This is performed when one (a), two (b) or three (c) leaves are crossed, and all the determined attenuation coefficients are incorporated into the phase space file (PSF) with their associated leaf label. When more than three leaves are crossed (d), the photon is discarded.

In many aspects, the method described above is similar to the one described by Siebers *et al* (2002) and even more to the Chen *et al* (2000)'s method. However, the TF method uses the exact geometry of the MLC, which is not the case in Siebers *et al* (2002) even though the potential errors introduced are minimal. Moreover, and this is the major difference, the TF method takes full advantage of the "binary" property of the MLC, which simplifies greatly the problem:

- Attenuation coefficient (μ) may be precalculated
- Pathlengths are exact (no interpolation required as in Chen *et al* (2000)) and must be calculated only once, for only one configuration

of the MLC (all leaves closed) in order to provide enough information for all the possible configurations of the MLC

- Transport through the MLC is performed only once, which avoid any additional geometric operation

Evidently, with this process we have introduced several approximations. First, the generality of the phase-space files is partially lost since contaminant electrons and widely divergent photons are discarded. Second, the scattering of photons and the production of secondary particles within closed leaves are ignored. First-Compton scattering is taken into account in Siebers *et al* (2002), but it was decided to neglect this phenomenon, mainly to improve speed and the simplicity, and evaluating afterwards the potential deviations from the straight MC method introduced.

The impact of the different approximations on the accuracy must be determined through comparisons of dose distributions in a water phantom obtained from full MC simulations and from simulations using the TF method, for different MLC configurations.

After calculating the phase-space file below the MLC, either with the full MC or the TF method, the dose distributions were calculated using the user code "penmain" from the PENELOPE distribution. The surface of the phantom was placed at the isocenter (source surface distance (SSD) of 85 cm). In all calculations, the dose was tallied using voxels of 2x2x2 mm^3. The number of histories was such that the statistical uncertainty of the generated dose distributions was smaller than 1.5% (3σ) for the maximum dose voxel when the full MC method was employed for the open fields. The correct statistical uncertainty could only be determined in that case, since statistical information is partially lost when the TF method is used. Indeed, realistic estimations of the uncertainty is based on an efficient history by history method attributed to Salvat and described by Sempau *et al* [9]. Since some particles are discarded in the TF method, it is not possible to link each photon to each primary electron striking the target, which is required to perform a proper estimation of the uncertainty. One can still evaluate the statistics in a first approximation by considering that each photon is issued from a primary electron, but this will result in an underestimation of the uncertainty. Dose distributions calculated with "penmain" are expressed in units of eV/g per primary electron striking on the target. In the present work, the results obtained with the two methods are expressed in this unit, in order to enable a "fair" comparison without introducing artificial corrections due to inappropriate normalizations.

3. Results and discussion

3.1. Open fields

To check whether the transformed phase-space files retain information from the original MC phase-space files, dose distributions calculated from the full MC and the TF method corresponding to open fields (40x5, 40x2.5 and 40x1 cm²) were compared. The corresponding dose profiles were found to be in close agreement (within statistical uncertainty, not shown) for all the field sizes, as expected, since the vast majority of the photons were kept in the transformed phase-space files (more than 99.9% for a given open field). Some concern may arise regarding the depth dose distributions, because all the contaminant electrons are disregarded in the TF method. This approximation may lead to significant deviations in the build up region where electrons deposit most of their energy. However, good agreement was also observed (within statistical uncertainty) for all the open fields, as shown in the insets of figure 2 for a 40x5 cm² (a) and a 40x2.5 cm² (b) fields; for the sake of visibility, points are drawn each cm only after the build up region. This result is consistent with the fact that contamination is negligible for HT.

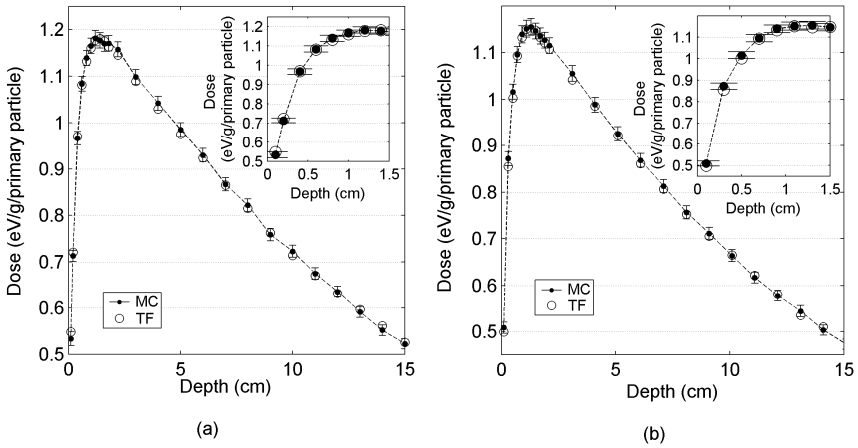


Figure 2. Comparison of depth-dose distributions obtained from the MC (dashed line, solid points) and the TF (open circles) methods for a 40x5 cm² field (a) and a 40x2.5 cm² field (b). Insets show a zoom on the build-up region. The depth-dose curves were calculated at SSD=85 cm. Errors bars (3σ) are plotted in the MC profiles.

3.2. Two central leaves opened

Transverse profiles and depth-dose distributions calculated with the full MC and the TF method for the two central leaves open were also analyzed. Transverse profiles are compared in figure 3. The agreement is seen to be very good, with deviations within statistical error bars (1.2 % (3σ) at maximum dose). Similar agreement is obtained for the depth-dose distributions (not shown). The agreement for doses above 10% of maximum dose is confirmed by the plot of the ratio between MC and TF, displayed as an inset in figure 3. However, for low doses, the difference can reach 50 % of the local dose (<0.6% of maximum dose) 2 cm off-axis, which is likely due to the non-simulation of the scattering by the MLC. But this occurs for very low doses and is expected to have negligible impact in clinical situations. Therefore, the phenomena that are not properly accounted for in the TF method (such as scattering and secondary particle production in the MLC) have an overall negligible effect on the dose distributions.

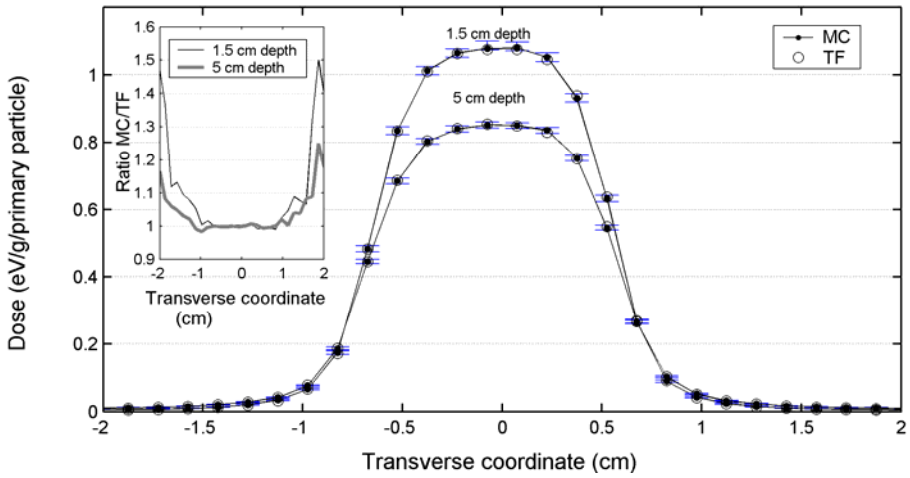


Figure 3. Comparison of transverse profiles resulting from the full MC (solid line, solid points) and the TF methods (open circles) for the 40x2.5 cm² static field with the two central leaves open. The profiles were calculated at SSD = 85 cm and for 1.5 cm and 5 cm depths. Errors bars (3σ) are plotted in the MC profiles. The inset shows the ratio between the full MC and the TF methods for the two depths (1.5 cm thin black line, 5 cm thick grey line).

3.3. Tongue and groove

To analyze the tongue and groove effect over the entire field, dose profiles obtained with even and odd leaves opened were added and compared for the two techniques, as illustrated in figure 4 for a reduced part of the profiles (to improve visibility of the results obtained with the two simulation modalities). The agreement is seen to be acceptable, with deviations within the statistical uncertainty of the MC results.

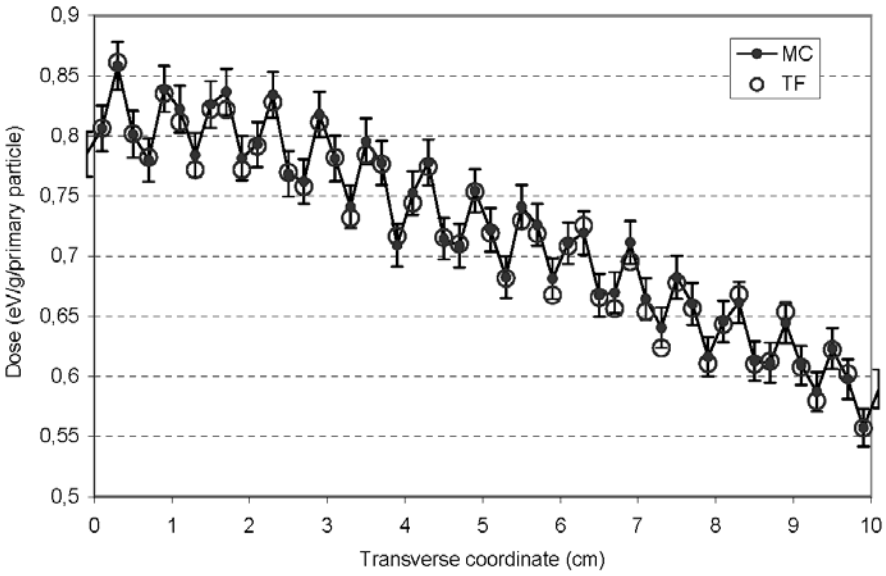


Figure 4. Comparison of transverse profiles calculated with the MC (solid line, solid points) and the TF methods (open circles) over 10-cm interval of the 40x2.5 cm² field with even leaves and odd leaves opened sequentially. The profiles were calculated in a water phantom at 5 cm depth and SSD = 85 cm.

3.4. Arbitrary configuration

The TF method is also able to reproduce, with similar accuracy, the dose distributions corresponding to other configurations of the MLC. Consequently, its accuracy is independent of the number of leaves that are simultaneously opened, as shown in figure 5, where deviations are again within the statistical uncertainty of the MC data.

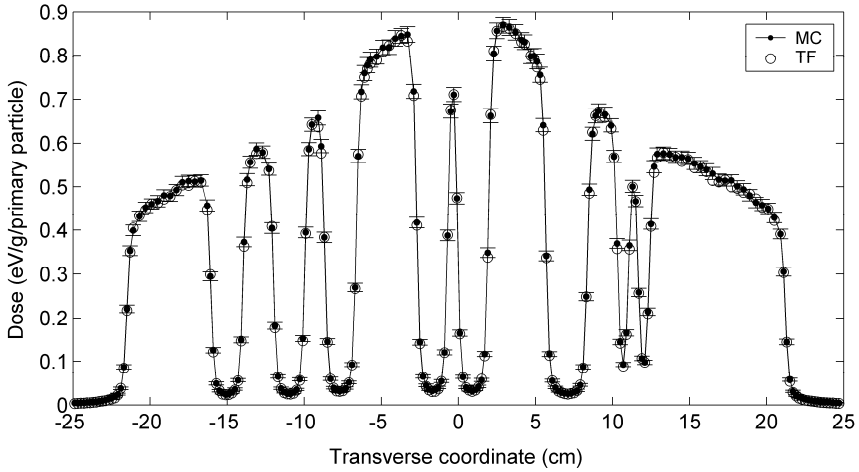


Figure 5. Comparison of transverse profiles generated by the MC (solid line, solid points) and the TF methods (open circles) for a complicated configuration of the MLC and the 40x2.5 cm² static field. The profiles were calculated at SSD = 85 cm and 5 cm depth. Errors bars (3σ) are plotted in the MC profiles.

3.5. Fully blocked field

This test enabled the evaluation of the possible deviations introduced by the TF method in predicting attenuation and scattering by the MLC. Inter-leaf and intra-leaf leakage estimated from results of simulations with full MC and the TF method were compared. Again, overall good agreement was obtained, with deviations almost within statistical uncertainty of the MC result (figure 6), even though they are likely due to the neglected scattering in the TF method. It is also worth mentioning that the leakage for the MLC of HT is very small, with an interleaf leakage of around 0.2% of the dose of the corresponding open field at the same point and an intra-leaf leakage of around 0.1%.

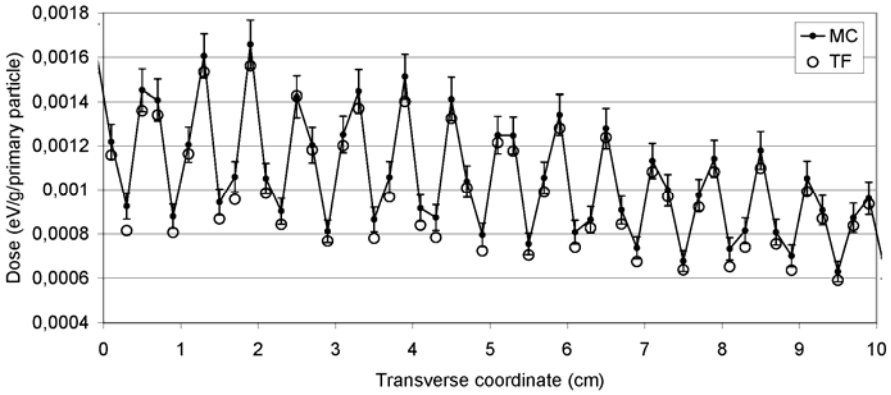


Figure 6. Comparison of transverse profiles calculated with the MC (solid line, solid points) and the TF methods (open circles) over 10-cm interval of the 40x2.5 cm² field with all the leaves closed. The profiles were calculated in a water phantom at 5 cm depth and SSD = 85 cm.

4. Conclusions

The TF method was described and simulation results using this method were compared to results from corresponding full MC simulations for different configurations of the MLC. The tongue and groove effect is accurately accounted for and the leakage is also simulated correctly by the TF method. No significant deviations between the two methods were observed, even though the TF methods does yield a huge gain in computation time, since the transport through the MLC is now almost instantaneous. For instance, for one single leaf opened, the simulation of transport through the MLC is, roughly, more than 500 times faster than a full MC simulation and 60 times faster than a MC simulation with no electron transport. Therefore, the ray-tracing technique described in this study is fast, reliable and well adapted to the HT MLC design and can therefore be used for future helical calculations without any significant loss of accuracy.

Acknowledgements

This work was supported by a grant from the Belgian 'Fonds National pour la Recherche Scientifique' (F.N.R.S., grant number FC 73512)

References

[1] Reynaert N, van der Marck S C, Schaart D R, Van der Zee W, Van Vliet-Vroegindeweij, Tomsej M, Jansen J, Heijmen B, Coghe M, De Wagter C 2007 Monte Carlo treatment planning for photon and electron beams *Radiation Phys. and Chem.* **76** 643-86

[2] Verhaegen F and Seuntjens J, 2003 Monte Carlo modeling of external radiotherapy photon beams *Phys. Med. Biol.* **48** R107-64
[3] Deng J, Pawlicki T, Chen Y, Li J, Jiang S B and Ma C M 2001 The MLC tongue-and-groove effect on IMRT dose distributions *Phys. Med. Biol.* **46** 1039-60
[4] Keall P J, Siebers J V, Arnfield M, Kim J O and Mohan R 2001 Monte Carlo dose calculations for dynamic IMRT treatments *Phys. Med. Biol*. **46** 929-41
[5] Siebers J V, Keall P J, Kim J O, Mahoan R, 2002 A method for photon beam Monte Carlo multileaf collimator particle transport *Phys. Med. Biol.* **47** 3225-32
[6] Chen Y, Boyer A L and Ma C M 2000 Calculation of x-ray transmission through a multileaf collimator *Med. Phys.* **27** 1717-26
[7] Sterpin E, Tomsej M, Cravens B, Salvat C, Ruchala K, Olivera G H and S Vynckier 2007 Monte Carlo simulation of the Tomotherapy treatment unit in the static mode using MC HAMMER, a Monte Carlo tool dedicated to Tomotherapy *JPCS* **74** 021019
[8] Salvat F, Fernandez-Varea J M, and Sempau J 2006 *PENELOPE-2006: A Code System for Monte Carlo Simulation of Electron and Photon Transport* OECD Nuclear Energy Agency, Issy-les-Moulineaux, France
[9] Sempau J, WildermannS J and Bielajew A F 2000 DPM, a fast, accurate Monte Carlo code optimized for photon and electron radiotherapy treatment planning dose calculations *Phys. Med. Biol.* **45** 2263-91

Chapter 6: Publication 4

Monte Carlo simulation of helical tomotherapy with PENELOPE

E Sterpin[a], F Salvat[b], R Cravens[c], K Ruchala[c], G H Olivera[c,d] and S Vynckier[a]

[a] Université Catholique de Louvain, Department of Radiotherapy, St-Luc University Hospital, 10 av. Hippocrate, 1200 Brussels, Belgium

[b] Facultat de Fisica (ECM), Universitat de Barcelona, Diagonal 647, 08028 Barcelona, Spain

[c] Tomotherapy Inc., 1240 Deming Way, Madison, WI USA

[d] Department of Medical Physics University of Wisconsin-Madison, Madison WI USA

Phys. Med. Biol. **53** 2161-2180 (2008)

Abstract.

Helical Tomotherapy (HT) delivers intensity-modulated radiation therapy (IMRT) using the simultaneous movement of the couch, the gantry and the binary multileaf collimator (MLC), a procedure that differs from conventional dynamic or step-and-shoot IMRT. A Monte Carlo (MC) simulation of HT in the helical mode requires therefore a new approach. Using validated phases-space files (PSF) obtained through the MC simulation of the static mode with PENELOPE, an analytical model of the binary MLC, called the "transfer function" (TF), was first devised to perform the transport of particles through the MLC much faster than time consuming MC simulation and with no significant loss of accuracy. Second, a new tool, called TomoPen, was designed to simulate the helical mode by rotating and translating the initial coordinates and directions of the particles in the PSF according to the instantaneous position of the machine, transporting the particles through the MLC (in the instantaneous configuration defined by the sinogram), and computing the dose

distribution in the CT structure using PENELOPE. Good agreement with measurements and with the treatment planning system of Tomotherapy was obtained, with deviations generally well within 2%/1mm, for the simulation of the helical mode for two commissioning procedures and a clinical plan calculated and measured in homogeneous conditions.

1. Introduction

Intensity-modulated radiation therapy (IMRT) has been used in clinical practice for more than one decade (Webb 2004). In comparison with three-dimensional conformal therapy, IMRT allows for improved conformation of target volumes as well as better sparing of normal adjacent tissues (Sultanem *et al* 2000, Hsiung *et al* 2006, Luxton *et al* 2004). Helical Tomotherapy (HT) is a sophisticated form of IMRT in which highly modulated treatments are delivered by taking advantage of the combined movements of the couch, the gantry and the multileaf collimator (MLC) (Mackie *et al* 1993).

In IMRT treatments, many irregular beams are used simultaneously, a situation that may lead to substantial errors in the dose distributions evaluated from correction-based algorithms and from convolution/superposition algorithms, specially in inhomogeneities (Keall *et al* 2001, Deng *et al* 2001, Vanderstraeten *et al* 2006, Martens *et al* 2002, Sterpin *et al* 2007a, Madani *et al* 2007, Paelinck *et al* 2006, Fogliata *et al* 2007, Carrasco *et al* 2004, Jones and Das 2005, Arnfield *et al* 2000). Monte Carlo (MC) simulations are accepted as the most accurate tools to calculate dose distributions in tissues (Verhaegen and Seuntjens 2003, Reynaert *et al* 2007). MC models for IMRT with conventional treatment units have been proposed by different authors (Deng *et al* 2000, Deng *et al* 2001, Chen *et al* 1999, Siebers *et al* 2002, Liu *et al* 2001, Keall *et al* 2001, Reynaert *et al* 2004, Heath *et al* 2004). Simulations of a HT prototype in static mode were published by Jeraj *et al* (2004 and 2005). More recently, Sterpin *et al* (2007b) reported MC studies of the Hi-Art^{TM} system, but limited again to the static operation mode.

In the present article we describe the first complete MC simulation of the Hi-Art^{TM} machine operating in the helical mode with technical information fully disclosed by the manufacturer (Tomotherapy Inc., Madison WI, USA). The simulations were performed by using the general-purpose MC code system PENELOPE (Salvat *et al* 2006). This code simulates coupled electron-photon transport in arbitrary materials and in a wide energy range, from a few hundred eV up to 1 GeV. The reliability of the physical interaction models and the tracking algorithms implemented in PENELOPE

has been demonstrated by Sempau *et al* (2003) through an extensive set of benchmark comparisons of simulation results with experimental data. PENELOPE has been used for different applications in radiotherapy (Sempau *et al* 2001, Al-Dweri *et al* 2005) and other fields (Sempau and Andreo 2006); it has also been benchmarked with other MC codes (Ye *et al* 2004, Mazurier *et al* 2001, Siegbahn *et al* 2003).

The simulation of the Hi-Art^{TM} HT machine consisted of several stages. First of all, the geometry of the machine was coded according to the PENGEOM format and syntax, including a very detailed description of the MLC and of all other mechanical parts that may influence the final radiation beam. The physical parameters of the machine (energy and spatial distribution of the primary electron beam) were determined by fitting measured spatial dose distributions in a homogeneous water phantom for various static configurations of the machine, including the three field sizes available (40x5, 40x2.5 and 40x1 cm²) and different configurations of the binary MLC.

The transport of the radiation beam through the MLC is the most difficult aspect of IMRT simulations (Verhaegen and Seuntjens 2003) because of the complicated geometry of the MLC. Moreover, the MLC is the only part of the accelerator head that is moving during irradiation and that needs to be actually simulated for each individual treatment. Therefore, the transport of particles through the MLC is a critical issue regarding the speed of transport simulation through the treatment head. The MLC of the Hi-Art^{TM} machine is binary, *i.e.*, each leaf can only be fully open or completely closed. This peculiarity allows for large simplifications in the description of the transport through the MLC, which may be accurately accounted for by means of a purely analytical "transfer function" (TF). The accuracy of the TF method was verified by comparing dose distributions in a water phantom obtained from MC calculations with detailed simulation of the transport of particles through the MLC and from simulations using the TF.

A main program, called "TomoPen", was written to perform the simulation of helical treatments. This program calculates three-dimensional dose distributions in patient specific CT geometries, it translates and rotates the phase-space files (PSFs) to follow the movement of the head relative to the CT volume and, at the same time, it uses the TF method to account for the instantaneous configuration of the MLC as defined by the sinogram. The validity of the models and methods presented here was verified by comparing measurements and simulations for commissioning procedures and a patient plan.

2. Material and methods

2.1. Hi-Art Tomotherapy treatment unit

The treatment head is composed of a linear accelerator tube, beam formation elements (target, beam hardener), collimating devices (jaws and primary collimator) and a binary MLC to provide modulation. The head can rotate continuously and simultaneously with the translation of the treatment table (helical delivery), in the manner of a CT scanner. The HT machine can operate in two modes. In the treatment mode, the nominal energy equals 6 MV. HT has also the ability to acquire CT scan images with the patient in the treatment position, in which case the beam energy is reduced to a nominal value of 3.5 MV.

When all the leaves of the MLC are open, the position of the jaws can be set to define three field sizes, 40x1, 40x2.5 and 40x5 cm² at the isocenter (source-to-surface distance (SSD) = 85 cm). The binary MLC equipping the system is composed of 64 movable leaves with a projected nominal thickness at the isocenter of 6.25 mm. Apart from those leaves, there are two additional stationary leaves at each extremity of the MLC that affect the beam collimation, even when a static open field is delivered.

Helical delivery is mechanically controlled by the pitch, the sinogram and the gantry rotation period (Mackie *et al* 1993, Kapatoes *et al* 2001a and Kapatoes *et al* 2001b). The pitch is defined as the fraction of field width travelled per gantry rotation. The sinogram provides the fraction of time during which each leaf is fully open for a sequence of discrete positions of the gantry, which are called “projections”.

2.2. Measurement setups

Depending on the mode of radiation delivery (static or helical), the measurements were performed on a water phantom, a solid-water rectangular phantom or the “cheese phantom” provided by Tomotherapy Inc. A description of the cheese phantom may be found in Thomas et al (2005). Two detectors were used for the experiments presented in this paper. The first was an Extradin A1SL ion chamber (Standard Imaging), similar to the one used during the commissioning and for configuration measurements of the treatment planning system (TPS). The collecting volume and its diameter equal 0.056 cm³ and 4.1 mm, respectively. If the wall (A150 material) is included, the diameter reaches 6.25 mm.

When improved spatial resolution was required, Kodak EDR-2 films were used in Solid Water^{TM} based phantoms. Several studies showed that EDR-2 films

generally yield accurate results with deviations mostly within 2% for dose profiles (Zhu et al 2002, Olch 2002).

2.3. Monte Carlo code PENELOPE

The transport of particles is simulated by PENELOPE (an acronym for PENetration and Energy Loss of Positrons and Electrons). PENELOPE includes a flexible geometry package named PENGEOM, which automatically tracks particles through complex material structures consisting of homogeneous bodies limited by quadric surfaces (constructive quadric geometry). The code system also allows the user to apply various variance reduction techniques (splitting, Russian roulette, interaction forcing) to improve the efficiency of the simulations.

While photons are tracked using the conventional detailed method (*i.e.*, interaction by interaction), electrons and positrons are simulated using a mixed (class II) scheme, that is, hard collisions are simulated individually from the corresponding differential cross sections while the global effect of the soft interactions between consecutive hard collisions is simulated as a single "artificial" event using multiple-scattering approximations. The simulation is controlled by seven user-defined parameters: E_{ABS} (1), E_{ABS} (2), E_{ABS} (3), C_1, C_2, W_{cc} and W_{cr}. The three first parameters are the absorption energies of, respectively, electrons, photons and positrons. When the energy of a given particle becomes lower than its corresponding E_{ABS}, the simulation is discontinued and the residual energy of the particle is locally deposited. The parameter C_1 determines the mean free path for hard elastic events; C_2 sets the upper limit for the average fractional energy loss in a single step. The parameters W_{cc} and W_{cr} are energy-loss cut-off values that separate soft and hard events, for inelastic collisions and bremsstrahlung emission, respectively. Thus, inelastic collisions (bremsstrahlung events) with energy loss larger than W_{cc} (W_{cr}) are simulated individually. For the various simulations presented in this paper, we adopted the following set of simulation parameters: E_{ABS} (1) = E_{ABS} (3) = 100 keV, E_{ABS} (2) = 10 keV, $C_1 = C_2 = 0.05$ and $W_{cc} = W_{cr} = 10$ keV. These values are somewhat conservative for routine simulations, but in this case it is wise to sacrifice simulation speed to ensure reliability of the whole tuning process.

2.4. Static mode

The definition of the geometry was performed according to detailed technical drawings fully disclosed by Tomotherapy Inc. Figure 1 displays central sections of the HT head model along the longitudinal and transverse directions, as indicated on the

schematic representation of a patient lying on the treatment couch. The MLC was modeled by defining the geometry of one leaf (tongue and groove (T&G), leaf-end sides), from which all the other leaves were generated using the "clone" operation of the PENGEOM routines. The MLC geometry was validated by comparing simulation results (with a voxel size of 2x2x2 mm^3) with measurements for two different configurations in a Solid Water™ rectangular phantom. First, calculations and measurements were performed for the MLC with all the even leaves open, and, similarly, with odd leaves open. This allows for the verification of the geometry, the thickness and the spacing of each leaf It also permitted to determine if fine corrections on the leaf bank, such as a rotation or a displacement, should be applied. The effects of the T&G and the electron source spot size may be further analyzed by comparing measurements and calculations for the two central leaves open sequentially and simultaneously.

As shown in figure 1, two scoring planes were used in our simulation, the first one below the jaws and the second one below the lead plate. The dose calculations reported below were always performed from precalculated PSFs at the second plane, below the lead plate. When the calculated dose distributions for open fields matched the measured ones, the simulation could run again and the particles were stored in a PSF at the first plane, below the jaws. The three resulting PSFs, one for each field size, can be used as an input for any other configuration of the MLC. In this way, the transport of particles through the upper part of the treatment head had to be performed only once. The number of particles in the PSFs was high enough (more than a one hundred million) to ensure that the particles would not have to be recycled too many times (less than five)[6].

[6] A particle in a phase-space file is recycled when it is used several times in the same dose calculation process. The uncertainty on the resulting dose distribution must be calculated with caution to account for the fact that phase-space particles and, hence, primary particles, are simulated several times. More details in Walters *et al* (2002) and Sempau *et al* (2001)

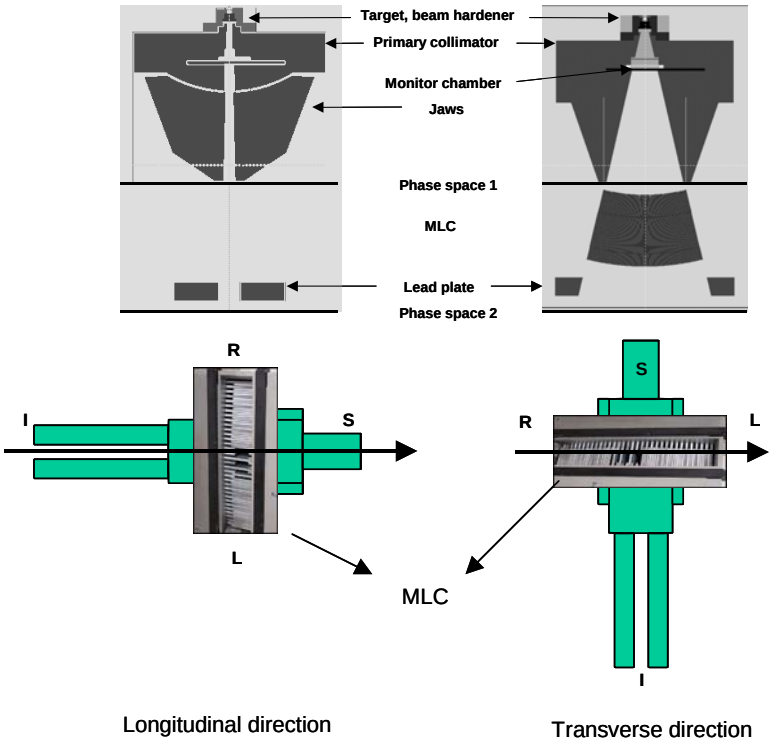


Figure 1. Geometry of the tomotherapy treatment head as defined in the MC simulation. The upper part of the figure shows two sections of the geometry for an open field: one along the longitudinal direction (left picture), where the nominal field width is limited by the movable jaws (5 cm, 2.5 cm or 1 cm), and one along the transverse direction (right picture), where the nominal field width is fixed at 40 cm. The thick horizontal lines represent planes where PSFs respect to the treatment head as indicated by the MLC. The transverse direction goes from right (R) to left (L) whereas the longitudinal direction goes from the inferior part (I) to the superior part (S) of the schematic patient.

2.5. Analytical model of the binary MLC: the TF method

To increase the calculation efficiency for the simulation of the helical mode, we have devised a specific analytical procedure, called the TF method, to describe the transport of photons through the MLC. Although this method involves quite drastic approximations, it does not imply any significant loss of accuracy as compared with the full MC simulation. In the TF method, the MLC geometry is described in all detail, approximations are introduced regarding only the transport of photons.

Other authors have introduced similar approximations in their MC models to enable faster simulation of photon transport through the MLC (Laub *et al* 2000, Pawlicki and Ma 2001, Ma *et al* 1999, Ma *et al* 2000a, Keall *et al* 2001, Siebers *et al* 2002, Deng *et al* 2001, Chen *et al* 2000). In Siebers *et al* (2002), for instance, the average transmission for each particle through the MLC geometry is calculated according to the energy of the particle and the thickness of material traversed. First order Compton scatter from the MLC is also evaluated. However, the exact geometry of the MLC is not used, even though corrections are introduced to minimize potential errors. The philosophy of our model is closer to the one described in the paper of Chen *et al* (2000) since it calculates path-lengths according to the exact geometry of the MLC and transmission probabilities based on the energy of the particle in the PSF. The model depicted below differs, however, significantly, principally because it takes full advantage of the fact that the MLC is binary.

The TF method consists of two steps. First, the photons are transported along linear trajectories through the MLC geometry, and their position coordinates are replaced by those of the intersection between the straight trajectory and the lower PSF plane. When the trajectory crosses leaf number i, the ray-length within this leaf (t_i (cm)) is calculated and an attenuation coefficient (μ) is determined by PENELOPE according to the energy of the particle and the material of the MLC; the attenuation factor exp ($-\mu t_i$) is assigned to each crossed leaf. If a photon crosses at most three leaves, the leaf labels and the corresponding attenuation factors are incorporated into the PSF. If the photon crosses more than three leaves, the photon is disregarded (not included in the transformed PSF). These concepts are illustrated in figure 2. It has to be mentioned that contaminant electrons are removed and not included in the new PSF. The second step of the TF method describes the collimating effect of the MLC for a given configuration through the following modification of the photon weights. If a leaf is open, the associated attenuation factor is replaced by unity. The weight of the transmitted photon is obtained by multiplying its initial weight (before entering the MLC) by the attenuation factors of the crossed leaves.

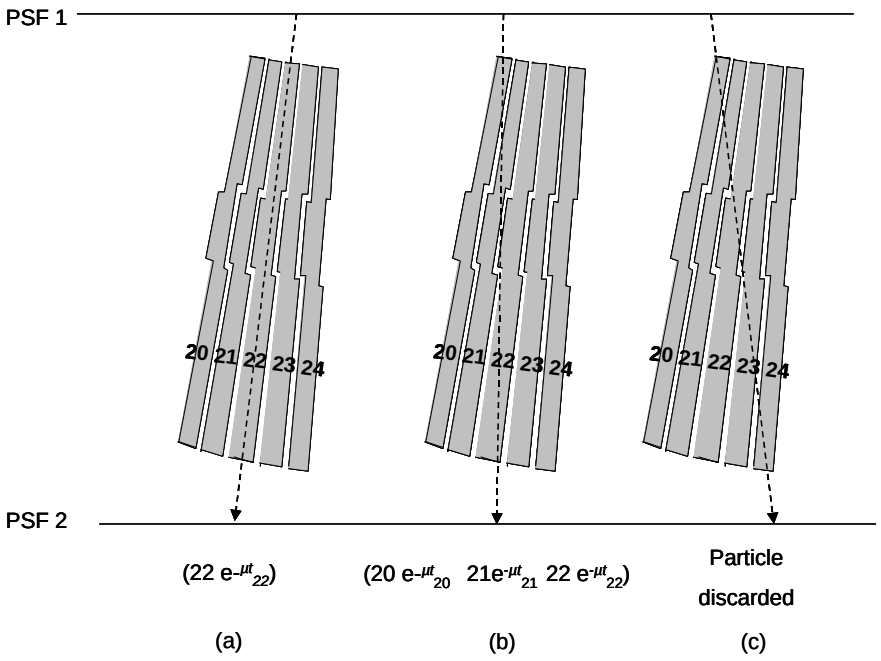


Figure 2. Schematic representation of the ray-tracing technique used to describe the transmission through the MLC, for the leaves 20 to 24. Photons are transported along linear trajectories through the MLC geometry using the PENGEOM routines. When the trajectory crosses leaf number *i*, the ray-length within this leaf (t_i) is calculated and an attenuation coefficient is determined according to the energy of the particle and the material of the MLC. This is performed when one (a), two or three (b) leaves are crossed, and the determined attenuation factors are incorporated into the PSF with their associated leaf label. When more than three leaves are crossed (c), the photon is discarded.

The TF method described above evidently introduces several approximations. First, the PSFs are partially altered, because contaminant electrons and widely divergent photons are discarded. Second, the scattering of photons and the production of secondary particles within closed leaves are ignored. The impact of those approximations on the accuracy must be determined through comparisons of dose distributions in a water phantom obtained from full MC simulations (with a voxel size of 2x2x2 mm^3) and from simulations using the TF method, for different MLC configurations.

Correct statistical uncertainties could only be determined when the full MC simulation through the MLC was employed, since statistical information is partially lost when the TF method is used.

2.6. Simulation of the helical mode: the "TomoPen" model

With the PSFs calculated in the simulation of the static mode (section 2.4) and the analytical method (section 2.5), a fast simulation of the helical mode may now be implemented. During this study, we only considered homogeneous cylindrical phantoms, made with Solid Water^{TM}.

2.6.1. Geometry definition

The first step consists of converting the density matrix of the CT scan of the cylindrical phantom used in the TPS of HT in a format readable by PENELOPE. This creates a file where a density (in g/cm³) and a material (air or Solid WaterTM) is associated to each voxel position defined by three coordinates in the Patient Volume Coordinate System (PVCS) reference frame used in both PENELOPE and the HT TPS as shown in figure 3. In this reference frame, the z-axis corresponds to the axis of the couch from superior to inferior, the x-axis the lateral direction (left-right) and the y-axis the posterior-anterior direction. The instantaneous rotation angle of the gantry is also represented in figure 3 and defined by the variable ξ. Therefore, the instantaneous position of the exit plane of the treatment head, *i.e.* the second phase-space plane in figure 3, can be expressed in PVCS using the 4 variables (x, y, z, ξ), where x, y, and z are the coordinates of the photons in the PSF for ξ=0.

2.6.2. Rotation and translation of the PSFs

Knowing the number of projections per rotation and the angle of the gantry at the beginning of the treatment, the rotation angle ξ is trivially deduced for each projection in the sinogram. The TomoPen model simulates an almost continuous rotation by dividing each projection into several sub projections (11 in the cases shown) and the sinogram values are interpolated accordingly. The x and y coordinates of the simulated particles can then be modified accordingly. The instantaneous position of the simulated particles along the z-axis in PVCS is calculated from the z-coordinate defining the position of the first projection and the translation of the couch defined by the pitch, the field width, ξ and the number of subprojections within each projection.

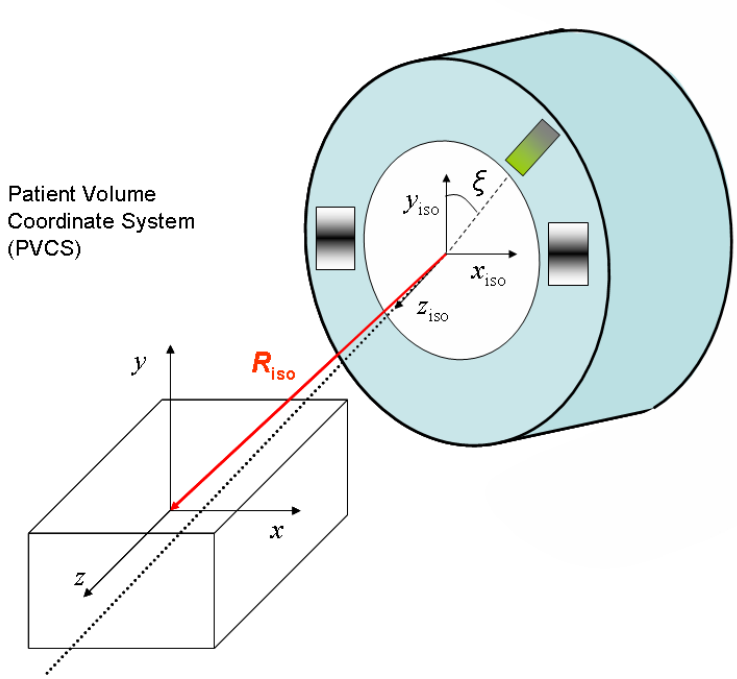


Figure 3. Geometry adopted in the simulation of the helical mode. (x_{iso}, y_{iso} ,z_{iso}) is the reference frame with the origin placed at the isocenter of HT. The coordinates of the voxels of the density matrix derived from the CT scan are defined in the HT TPS and the TomoPen simulation in the Patient Volume Coordinate System (PVCS) with an origin placed at the vertex of the density matrix. The variable ξ is the instantaneous rotation angle of the gantry, which is defined in the HT TPS and the MC simulation as in the figure.

2.6.3. Accounting for the MLC configurations

Since the opening times in the sinogram are defined for each leaf, it is convenient to model the MLC on a per leaf basis. Therefore, the PSF with the attenuation factors was split into 64 new PSFs according to the first leaf that is hit by the photon trajectory. In this way, a PSF is attached to each leaf. This approach enabled the possibility of using different strategies. The roughest one consists of simulating only photons in the PSFs corresponding to open leaves. This crude approach induces a small loss in accuracy only for fields with a few leaves open. A more accurate method is obtained by tracking the photons from the PSFs of the open leaves and the closed leaves with at least one adjacent leaf open. We found that this strategy yields simulated dose distributions with the same accuracy as those obtained with the original TF technique described by Sterpin et al (2007). Of course, this

statement is not true for the leakage, which is completely neglected for a fully blocked field.

Sterpin *et al* (2007c) found that inter-leaf and intra-leaf leakages are of order of 0.2% and 0.1%, respectively, of the dose delivered by the corresponding open field. This is consistent with the value predicted in Balog *et al* (1999) (around 0.3%). This value is significantly lower than with conventional linear accelerators, where the leakage is of order of 1.5%-2% (Arnfield *et al* 2000, LoSasso *et al* 1998, Kim *et al* 2001, Siebers *et al* 2002, Van de Walle *et al* 2003). Several authors insist on the importance of simulating accurately radiation leakage, especially for IMRT since the number of monitor units is substantially increased compared to conformal radiotherapy, which may lead to a significant contribution of the MLC leakage to the total dose (up to 10%) (Keall *et al* 2001, Siebers *et al* 2002, Chen *et al* 2000). However, due to the around ten times lower value of the leakage for the HT MLC for a static field, the maximum deviation introduced by neglecting the leakage should be smaller than 1.5% for highly modulated beams (Balog *et al* 1999), even though the efficiency of HT is lower than conventional IMRT. Therefore, it appears that the huge gain in computation time observed by neglecting leakage will not introduce unacceptable deviations. Despite all, it is worth noticing that the method described in this paper for the helical mode can be generalized to a model where the leakage is accounted for with minor modifications, but with a significant increase in computation time.

The dose calculations are performed by using the 64 PSFs obtained through the process described above. Let TWL_i denote the total weight of all the particles in the PSF associated to the i-th leaf (which may intuitively considered as the "intensity" of each leaf). Note that, for the helical mode, it is essential to ensure that the total weight of the particles simulated for each active leaf does correspond to the time that leaf is active. A leaf is considered as active either if it is open or if it is adjacent to an open leaf. To keep proper control of the weights, we consider the relative total weight of each leaf, $RW_i = TWL_i / TWL_{MAX}$, where TWL_{MAX} is the largest total weight among the 64 PSFs, *i.e.* the total weight of the most intensive leaf. If the i-th leaf is open during a whole projection, we simulate photons from its PSF up to a total weight equal to RW_i TW, where TW is an input parameter, whose value is normally much less than unity. The parameter TW determines the number of particles that are simulated per projection, *i.e.* the statistics. Since a leaf is active not only when open but also when an adjacent leaf is open, we need to follow the instantaneous configuration of the MLC in the course of each projection. This is accomplished by considering the fraction of time (FT_i) while the leaf has been open in the course of each projection; this value is

defined as the total weight of particles already simulated during the current projection divided by $RW_i\ TW$.

During each projection, the instantaneous configuration of the MLC is described, in accordance with the sinogram values, by using the following rules:

- The total weight of photons simulated for the *i*-th leaf is equal to $r\ RW_i\ TW$, where r is the maximum of the sinogram values for the considered leaf and the two adjacent ones.
- During the simulation of each leaf i, the instantaneous configuration of the MLC is set by comparing the sinogram values with FT_i. If the sinogram value for the leaf j is larger than FT_i, the leaf j is open, otherwise it is closed.

2.6.4. Calculations of dose distributions

After applying the TF weight correction described above, the photons that emerge from the MLC enter the CT structure. The simulation of radiation transport within the volume of the CT scan is performed by means of the user-code PENCT, which generates random electron-photon showers in CT geometries using PENELOPE, with the same settings as in section 2.3.

2.6.5. Dose calibration of TomoPen

Due to the simulation schemes adopted in this study, which are substantially different from straight MC simulations, the TomoPen results are given in arbitrary units instead of the more familiar Gy/primary particle simulated. To convert them into Gy units, the on-axis commissioning procedure was chosen. The procedure delivers a nearly homogeneous dose over a volume with dimensions of several centimeters (see section 3.3.1). The calibration of TomoPen consisted of scaling the MC calculated dose D_{MC} so as to match the dose $D_{C/S}$ given by the convolution/superposition (C/S) calculation. Specifically, a scaling factor M is introduced such that $D_{C/S} = D_{MC}\ M$ for a particular point within the homogeneous region. The M factor depends on TW, the number of projections per second, and a value characterizing the output of the machine, the dose rate, R. We can thus write

$$D_{MC}(\text{Gy}) = D_{C/S}(\text{Gy}) = D_{MC}(\text{arbitrary units})\frac{T_{Gantry}R}{N_{Proj}TW}C$$

where T_{Gantry} is the gantry revolution period, N_{Proj} is the number of projections per rotation and C is a constant factor that has to be determined only once for each field size, which is defined by the positions of the jaws (in the present case, 2.5 cm). The quantity $R\ T_{Gantry} / N_{proj}$ is proportional to the number of monitor units delivered during one projection. This calibration procedure has the main advantage that small output variations due to small differences (less than 1 mm) of the longitudinal field-widths compare to the nominal values (1, 2.5 and 5 cm) are directly accounted for in the normalization factor.

2.6.6. Validation of TomoPen

The model was validated and calibrated using two commissioning procedures for the 2.5 cm field. The MC calculations were performed in the cheese phantom (Thomas *et al* 2005) and compared to C/S calculations delivered by the TPS of HT and measurements with the Extradin A1SL ion-chamber and EDR-2 films. In both calculations modalities, the voxel size is fixed by the grid resolution used in the TPS, which is about 3.5x3.5x2 mm³ where 2 mm is the voxel width in the longitudinal direction. Ion chamber measurements were performed in the transverse direction at several discrete positions in the cheese phantom whereas an EDR-2 film was placed perpendicular to the beam at its vertical position.

The same comparisons were made for the other field sizes with very similar results, but, since the simulation scheme is identical for all the field sizes, only the results obtained with the 2.5 cm field are presented below, because this is the field size most frequently used in the clinical practice of our radiotherapy department, in Saint-Luc.

2.6.7. Using TomoPen for Delivery Quality Assurance (DQA) plans

To illustrate the capabilities of the TomoPen model in clinical situations, C/S and TomoPen results were compared for a DQA of a treatment plan of a patient treated in our institution for a bilateral head and neck tumor. The plan was already validated prior to treatment with measurements performed by an ion chamber for point's measurements and EDR-2 films for dose distributions following basically the same guidelines as presented in Thomas *et al* (2005).

3. Results

3.1. Static mode

The main parameters that needed to be tuned for MC simulation are the energy of the primary electron beam and the spatial distribution of the electron source. In Sterpin *et al* (2007b), the procedure followed for tuning the beam energy was described. Moreover, a first estimation of the spatial distribution of the electron source was found by fitting calculated and measured penumbras in the longitudinal direction as explained in Sterpin *et al* (2007b).

A finer tuning was however performed for the present study for some specific configurations of the MLC for which the resulting transverse profiles are more sensitive to the spot size.

3.1.1. Open fields

The results obtained for open fields were presented by Sterpin *et al* (2007b). However, some important results are illustrated here to emphasize on the quality of the data obtained for the static mode, which is a prerequisite for simulating the helical mode. Figures 4(a) and 4(b) display transverse profiles and depth dose distributions for the 40x5 cm² field using the HT unit of our department obtained from our MC simulations and measured (MS) with an ion chamber in a water phantom. The phantom was placed at a SSD of 85 cm. For transverse profiles, both the MC simulation results and the measured data are normalized on the central axis and scaled at 120, 100 and 80 % for the depths 1.5, 5 and 10 cm, respectively. For the depth dose distribution, MC is normalized such that MC and MS are equal at 2 cm depth. Generally, good agreement (within 1%/1mm) was achieved between ion-chamber measurements and the MC results for a monoenergetic electron source with energy equal to 5.5 MeV. In the build up region, there is a significant deviation, up to 40% in the first millimeters, which was attributed to the ion chamber design, as discussed in Sterpin et al (2007b). Measured and calculated longitudinal profiles are also compared for the three field sizes available with HT in figure 4 (c). The dose distributions are normalized on the central axis and scaled at 100, 80 and 60 % for the 5, the 2.5 and the 1 cm field, respectively. The positions of the jaws were set so that calculated and measured FWHM agreed within 1%.

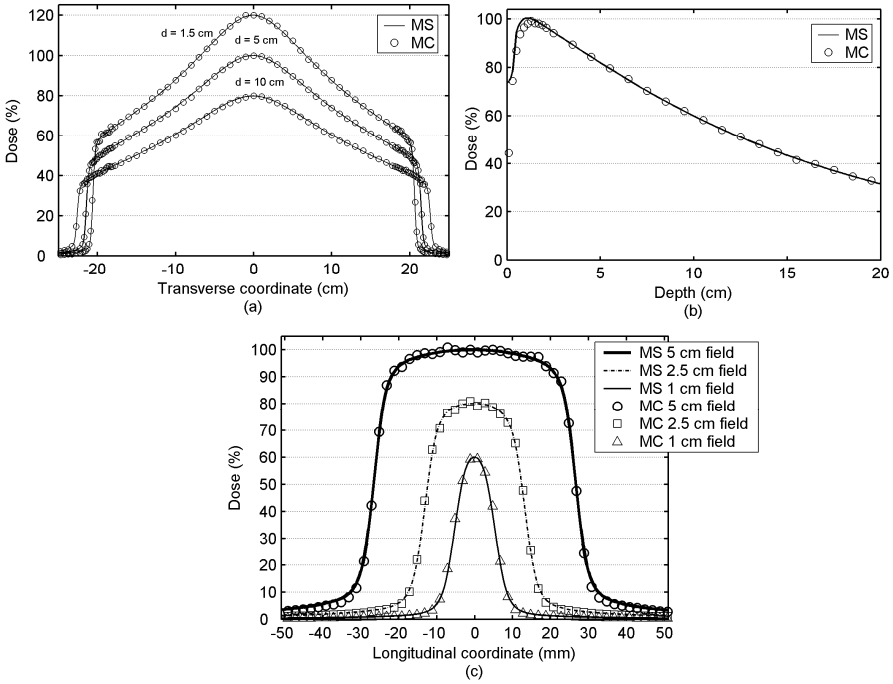


Figure 4. Transverse profiles (a) at three depths (d=1.5 cm, d=5 cm and d=10 cm) and depth dose distributions (b) comparison between measurements (MS) and Monte Carlo (MC) results for the 40x5 cm² field. Comparison of MS and MC longitudinal profiles at 5 cm depth (c) for the three static field sizes available in the Tomotherapy treatment unit (40x5 cm², 40x2.5 cm², 40x1 cm²). All the profiles and depth dose were acquired in a water phantom with SSD = 85 cm.

3.1.2. MLC geometry validation and fine-tuning of the electron source geometry

3.1.2.1. Individual leaf geometry and MLC bank position verification

A comparison of measurements (MS) with an ion chamber and MC results is displayed in figure 5 (a) and (b). MC data are normalized so that the maximum point in the profile, corresponding to the most central leaf, is made equal to the measurement at the same position. Moreover, the MS curve is shifted of 0.5 mm in order to align the profiles yielded by the most central leaf. This shift allows compensating for the uncertainty in experimental setup and possible small misalignment (<0.2mm) of the MLC of our HT unit. When this correction is applied, good agreement is achieved, with differences smaller than 0.5 mm.

.

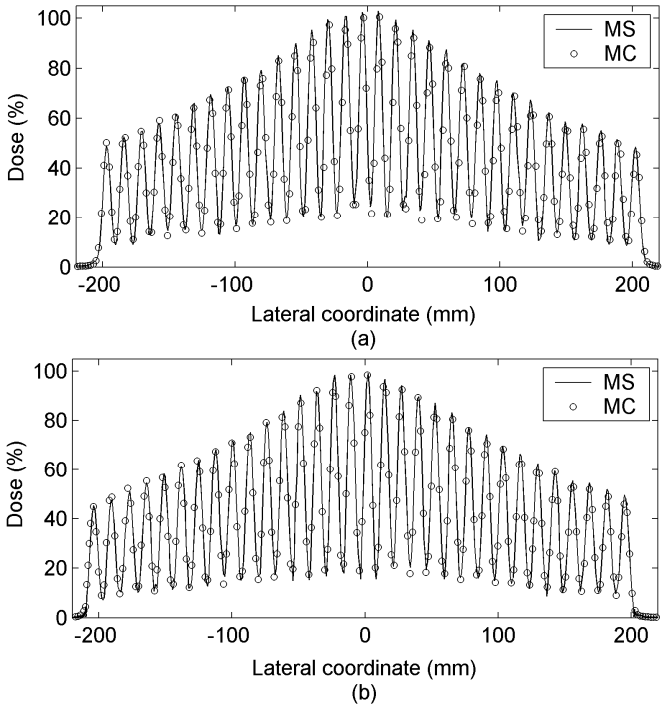


Figure 5. Transverse profiles obtained from MC simulation (open circles) and from measurements (MS, solid line) for the 2.5 cm field, with even leaves open (a) and odd leaves open (b). The profiles were acquired in a water phantom at 1.5 cm depth and SSD = 85 cm.

3.1.2.2. T&G

Sequential and simultaneous opening of the two central leaves yield the dose distributions shown in figure 6. MC dose profiles are shown for electron sources with FWHM = 1.4 mm, which corresponds to the value obtained in Sterpin *et al* (2007b) and with FWHM = 0, to illustrate the effect of the spot size on the dose distributions. The measured and calculated data are normalized according to the maximum of the profile with two leaves opened simultaneously.

For the profile with FWHM = 1.4 mm, good agreement is achieved between MC and measurements with differences smaller than 2 %/1mm. This result validates the chosen electron source distribution, that is, a gaussian distribution with FWHM = 1.4 mm. In the T&G characteristic dip region, the dose is reduced by 17.5 % when

leaves are opened sequentially. This reduction can be mostly explained by the presence of the T&G mechanism, as already noted by other authors (Balog *et al* 2003).

The electron source spot size has a significant effect on the dose distribution. First of all, as expected, the fall off of the profiles is steeper when FWHM = 0. Moreover, dose reduction at the "horns" of the profile (for leaves open sequentially) is much less pronounced for FWHM = 0. Indeed, at the centre of each leaf opening, the dose reduction is of order of 6% for a FWHM = 1.4 mm whereas it reaches only 1.5% when FWHM = 0. Finally, the magnitude of the dip in the T&G region is higher when FWHM = 0, with a dose reduction of 25.4 %.

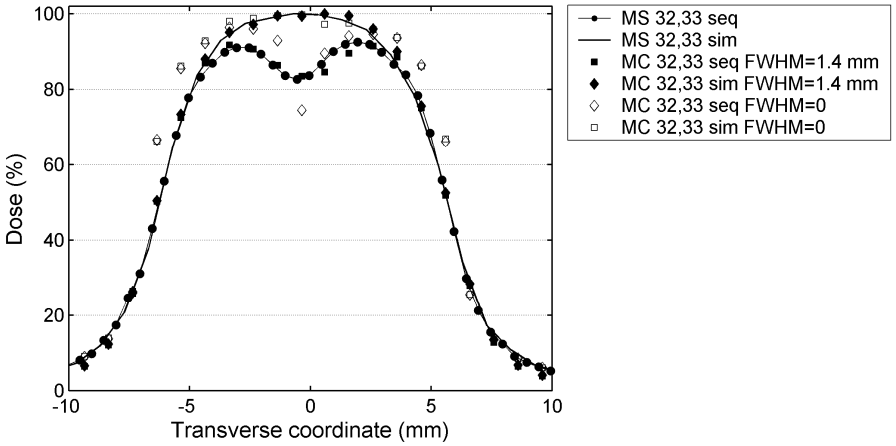


Figure 6. Dose distributions simulated and measured with EDR-2 films (SSD = 85 cm, depth = 1.5 cm). The two central leaves (32 and 33) are opened sequentially ("seq") and simultaneously ("sim") in both measurements (MS) and calculations (MC). Simulation results for a point source (FWHM = 0) and for a source with a gaussian distribution (FWHM = 1.4mm) are displayed. The comparison illustrates the effects of the T&G and the electron source spot size.

3.2. Validation of the TF method

It was observed in Sterpin *et al* (2007c) that the transformed PSFs obtained had enough generality with the TF method to reproduce full MC simulations of static open fields. Even in the build up region, including the phantom surface, where removed contaminant electrons could have introduced significant deviations, very good agreement was achieved, well within statistical uncertainty (1.5% (3 σ) at maximum dose). Good agreement (within statistical uncertainty) was also obtained for an arbitrary configuration using different opening of the leaves and for a fully blocked field. To illustrate the capabilities of the TF method, one result is, however, shown in

this paper, involving a challenging MLC configuration for the TF method. As in the section 3.1.2, the voxel size chosen is 2x2x2 mm³.

3.2.1. T&G effect

To analyze the T&G effect over the entire field, dose profiles were generated for two configurations of the MLC: 1) all even leaves open and all odd leaves closed and 2) all even leaves closed and odd leaves open. The simulations of each of these configurations were performed by using both full MC simulation and the TF method. The results from each simulation procedure for these two configurations were added to obtain the dose distributions, a portion of the calculated transverse profiles shown in figure 7. The agreement is seen to be acceptable, with deviations within the statistical uncertainty of the MC results.

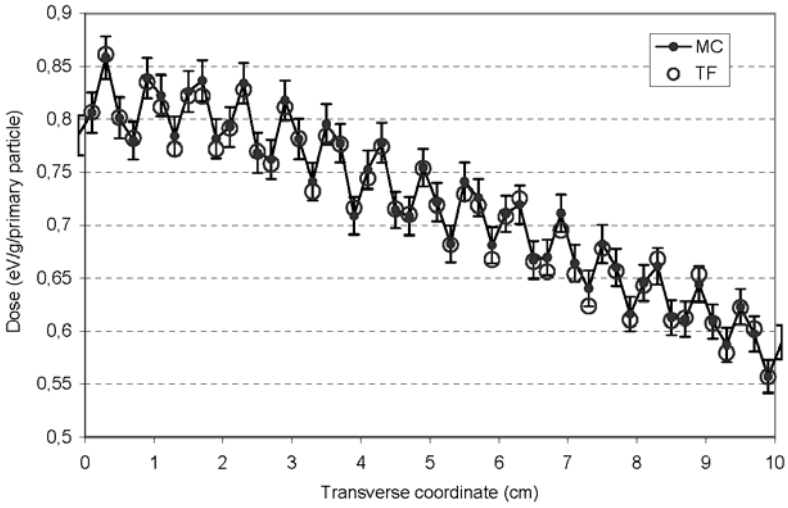


Figure 7. Comparison of transverse profiles calculated with the MC (solid line, solid points) and the TF methods (open circles) over 10-cm interval of the 40x2.5 cm² field with even leaves and odd leaves opened sequentially. The profiles were calculated in a water phantom at 5 cm depth and SSD = 85 cm.

3.3. Validation of the TomoPen model for commissioning procedures

3.3.1. 2.5 cm field on-axis IMRT commissioning procedure

Figure 8 displays images of the dose distributions obtained from C/S calculations and from TomoPen simulations for the considered commissioning procedure. Dose profiles along the transverse and the longitudinal axes are compared. Good agreement is obtained between the two calculation modalities and the measurements, as shown in figure 9, with deviations generally well within 2%/1mm. The very close agreement in the longitudinal direction as seen in figure 9 (b) proves that the movement of the couch is simulated accurately. It is worth mentioning that no geometrical shift of the TomoPen data was necessary to match the C/S results and measurements.

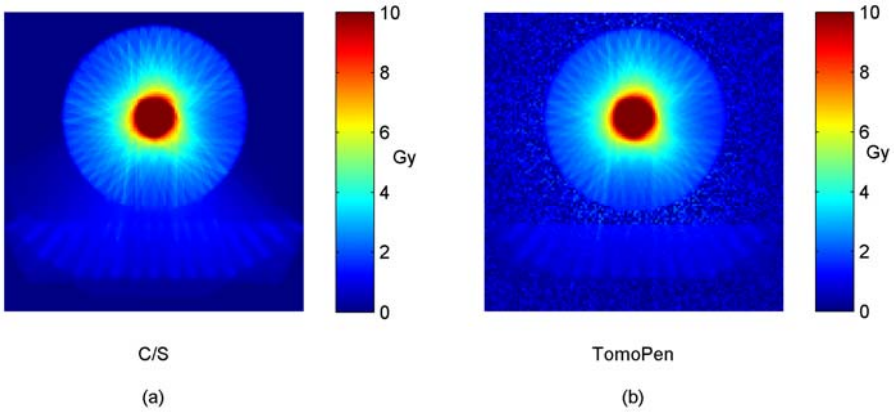
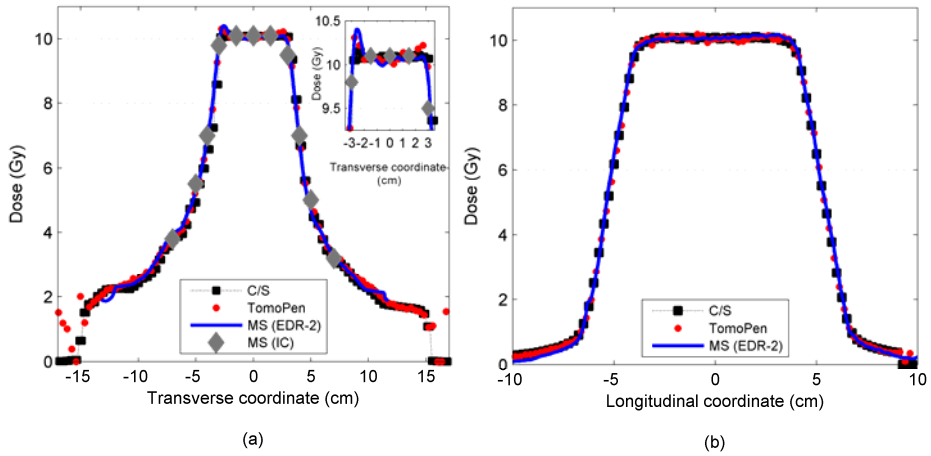


Figure 8. Dose distribution calculated by C/S (a) and TomoPen (b) for the on-axis commissioning procedure.

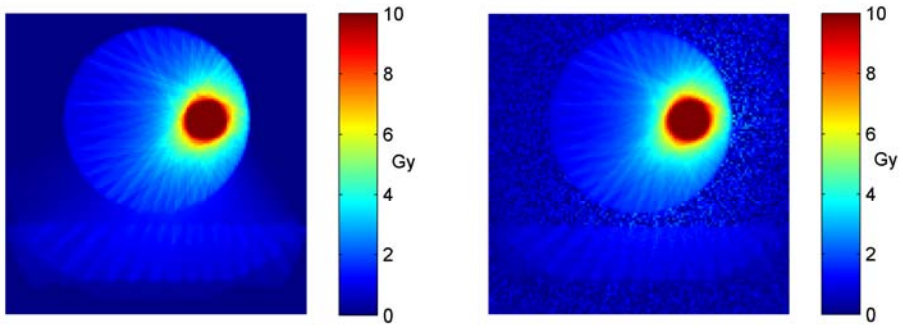


(a) (b)

Figure 9. Comparison of dose profiles in the transverse (a) and longitudinal (b) directions generated by C/S (solid squared-dashed line), TomoPen (solid points) and measured with EDR-2 films (solid line) for the on-axis commissioning procedure in the cheese phantom using the 40x2.5 cm² field. Ion chamber measurements (IC, solid points) are also shown for the transverse profile.

3.3.2. 2.5 cm field off-axis IMRT commissioning procedure

This procedure delivers similar dose distribution as the on-axis procedure, but shifted around 8.5 cm in the transverse direction (see figure 10). In figure 11, very good agreement is achieved between calculated and measured profiles for all the modalities, with deviations generally within 2 %/1 mm.



(a) (b)

Figure 10. Dose map calculated by C/S (a) and TomoPen (b) for the off-axis commissioning procedure.

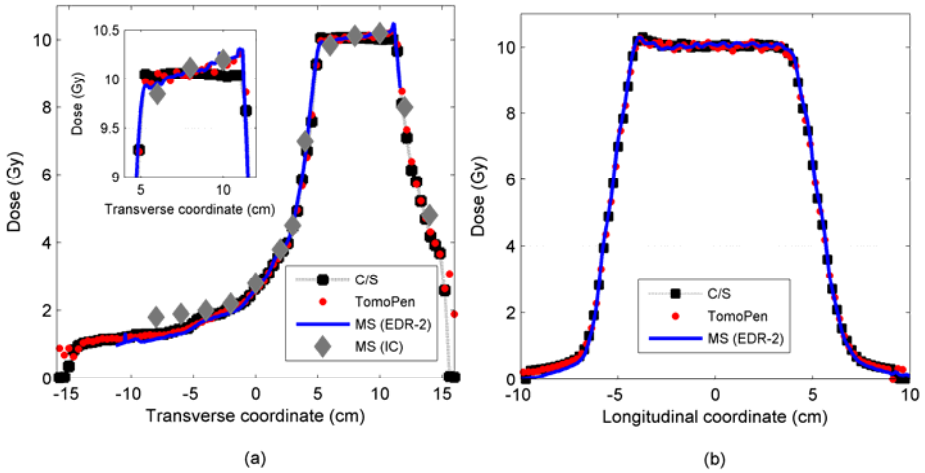


Figure 11. Comparison of dose profiles in the transverse (a) and longitudinal (b) directions generated by C/S (solid squared-dashed line), TomoPen (solid points) and measured with EDR-2 films (solid line) for the off-axis commissioning procedure in the cheese phantom using the 40x2.5 cm² field. Ion chamber measurements (IC, solid points) are also shown for the transverse profile.

3.3.3. Application of TomoPen: comparison between C/S and TomoPen for a delivery quality assurance procedure

C/S and TomoPen dose distributions were compared using profiles acquired in regions were the dose is homogeneous, (figure 12 (a)), and in regions of strong dose gradients, figure 12 (a) and (b). The dose profiles calculated by C/S and TomoPen along the lines shown in the images (a) and (b) are compared in the plots (c)-(f). Good agreement was found between C/S and TomoPen, with deviations generally within 2%/1mm, even in the presence of strong gradients, as shown in figure 12 (d)-(f).

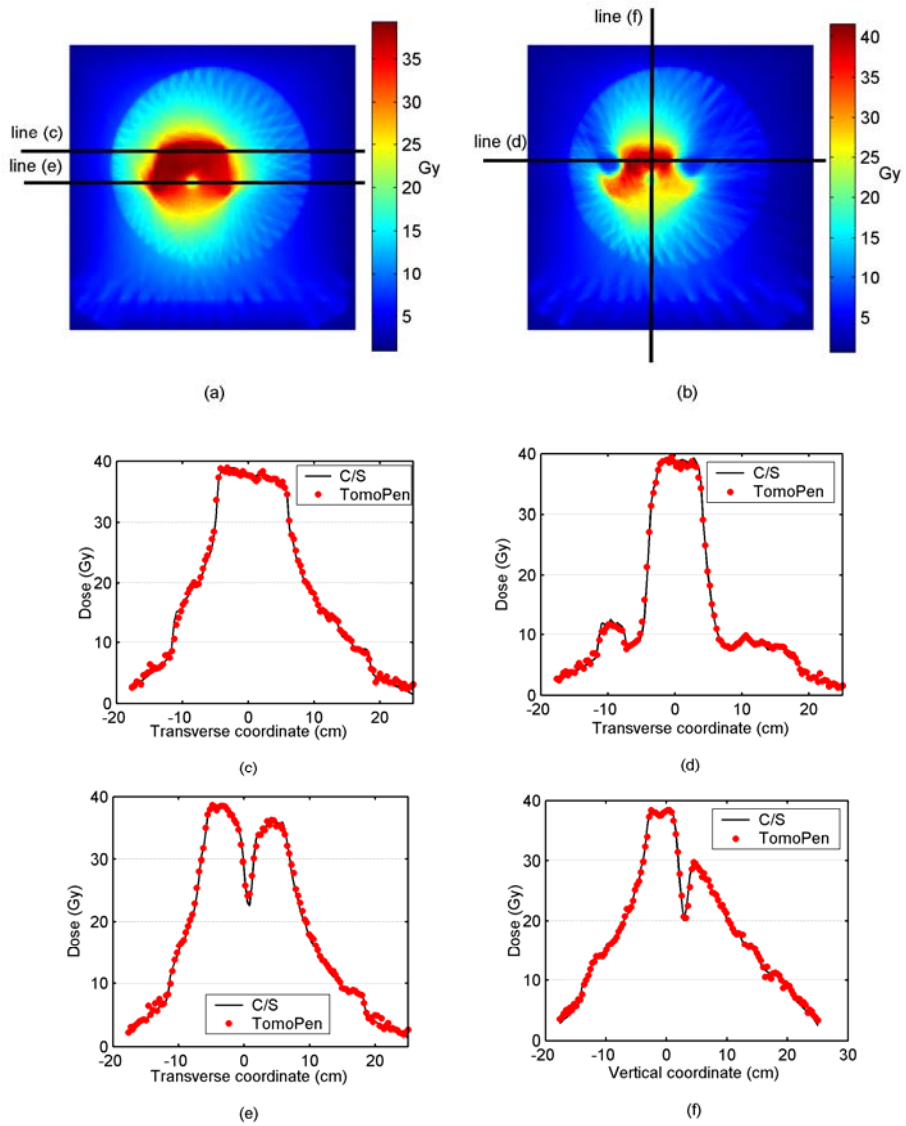


Figure 12. Comparison of dose profiles for a DQA plan calculated with C/S (line) and with TomoPen (points), at positions along the straight lines shown in the dose maps (a) and (b).

4. Discussion

The present study and the preliminary analysis of Sterpin *et al* (2007b) demonstrate that open static fields are accurately simulated and, consequently, that the generated PSFs can be used for all the other applications. The MLC model was also shown to be realistic and it was tested for two configurations. In the first test illustrated in figure 5, it was observed that each individual leaf was correctly modeled. Since the agreement held for all the leaves, whatever the position in the profile was, it can also be concluded that no global correction (*i.e.* tilt, shift or rotation) is needed for the leaf bank, and that the cloning of the central leaf was also performed accurately. Moreover, our model is capable to reproduce measured T&G effect with a good agreement, as shown in figure 6, proving that both the T&G mechanism and the electron source spot size were correctly modeled in the simulation.

The TF method described in this paper and in Sterpin *et al* (2007c) is able to perform a very fast simulation of the MLC without any significant loss of accuracy despite the strong approximations performed in the TF method for a wide set of MLC configurations in the static mode. Therefore, the phenomena that are not properly accounted for such as contamination and widely divergent photons as well as scattering and secondary particle production in the MLC have a negligible effect on the dose distributions. They are expected to have also a negligible clinical impact since the MLC configurations in the helical mode are, on average, much less challenging that the ones presented here and in Sterpin *et al* (2007c)

In the helical mode, good agreement was obtained for the two commissioning procedures, as shown in figures 8-12, where C/S is expected to have also good agreement because of the homogeneous phantom and the relative simplicity of the procedure. Similar agreement was achieved between measurements and both calculation modalities, as illustrated in figure 12 for a DQA of a clinical case, proving that TomoPen can be used for calculations in different clinical situations. The TomoPen model of the helical mode is close to the reality, but has potential limitations, principally because it assumes that each leaf of the MLC can only have two states (open or close), which is not exactly true. To evaluate those limitations, an additional study, beyond the scope of this paper, should be performed for cases where the imperfect binary property of the MLC may have a visible effect, which can be quantified. However, this limitation should introduce minor dosimetric effects according to Kapatoes *et al* (2001b) and since the time to open/close a leaf is small (20ms).

Good agreement with measurements was also achieved with C/S for the clinical example shown in this paper. Therefore, to evaluate the added-value of TomoPen compared to C/S, other comparisons should be performed for treatment cases where deviations are more likely to occur because of the presence inhomogeneities and/or when beam modeling might play a significant role due to the complexity of the treatment. However, this is, again, beyond the scope of the present study, which is restricted to the modeling of HT, and will be the subject of a forthcoming paper.

5. Conclusions

We have shown that PENELOPE is well suited to model the unique features of HT. Because of the detailed definition of the geometry, only two parameters had to be determined to model the static mode: the primary electron energy and the electron source spot size. The widest open field was used during the tuning process. Good agreement between simulation and experiment was obtained, with deviations below 1 mm and 2% of the maximum dose, for an electron source energy of 5.5 MeV and a electron source distribution with FWHM=1.4mm. Calculations also reproduced experimental measurements for different configurations of the MLC. The definition of the geometry of each individual leaf and T&G effects were verified during these experiments, as well as the leaf bank's properties.

The simulation of the helical mode has been described in detail, as well as the approximations introduced. Good agreement was obtained between measurements, C/S and TomoPen for the two commissioning procedures considered, proving that the mechanics of a helical treatment is well accounted for in the simulation. Typical calculation times were of the order of 10 hours on a single processor (2 GHz). The calculation time is now mainly due to the MC simulation inside the CT geometry, since the time spent to transport the photons through the MLC is made negligibly small because of the TF technique. Using a less conservative approach for the dose calculation in CT geometries, the computation time might be reduced by more than one order of magnitude. Further speed-up can be obtained by running the code on a computer cluster.

The TomoPen tool presented here is also able to calculate DQA plans and may be used as a complementary tool in routine DQA programs. Future development and testing will enable this tool to be used also for the effects of inhomogeneities on dose distributions and other dosimetry applications of a MC based TPS.

Acknowledgements

This work was supported by a Grant from the Belgian "Fonds National pour la Recherche Scientifique" (FC 73512). The authors wish to thank Carl Mauer, Eric Schnarr and Sam Jeswani from Tomotherapy Inc. for their precious help. Francesc Salvat gratefully acknowledges financial support from the Spanish Ministerio de Educación y Ciencia (project no.\ FPA2006-12066).

References

Al-Dweri F M O, Rojas E L and Lallena A M 2005 Effects of bone- and air-tissue inhomogeneities on the dose distributions of the Leksell Gamma Knife calculated with PENELOPE *Phys. Med. Biol.* **50** 5665-78

Arnfield M R, Siebers, J V, Kim J O, Wu Q, Keall P J and Mohan R 2000 A method for determining multileaf collimator transmission and scatter for dynamic intensity modulated radiotherapy *Med. Phys.* **27** 2231-41

Balog J P, Mackie T R, Wenman D L, Glass M, Fang G and Pearson D 1999 Multileaf collimator interleaf transmission *Med. Phys.* **26** 176-86

Balog J P, Mackie T R, Reckwerdt P, Glass M and Angelos L 2003 Characterization of the output for helical delivery of intensity modulated slit beams *Med. Phys*. **26** 55-64

Carrasco P, Jornet N, Duch M A, Weber L, Ginjaume M, Eudaldo T, Jurado, D, Ruiz A and Ribas M 2004 Comparison of dose calculation algorithms in phantoms with lung equivalent heterogeneities under conditions of lateral electronic disequilibrium *Med. Phys*. **31** 2899-911

Chen Y, Boyer A L and Ma C M 2000 Calculation of x-ray transmission through a multileaf collimator *Med. Phys*. **27** 1717-26

Deng J, Jiang S B, Kapur A, Li J, Pawlicki T and Ma C M 2000 Photon beam characterization and modeling for Monte Carlo treatment planning *Phys. Med. Biol.* **45** 411-27

Deng J, Pawlicki T, Chen Y, Li j, Jiang S B and Ma C M 2001 The MLC tongue-and-groove effect on IMRT dose distributions *Med. Phys.* **46** 1039-60

Fogliata A, Vanetti E, Albers D, Brink C, Clivio A, Knöös T, Nicolini G and Cozzi L 2007 On the dosimetric behaviour of photon dose calculation algorithms in the presence of simple geometric heterogeneities: comparison with Monte Carlo *Phys. Med. Biol.* **52** 1363-85

Heath E, Seuntjens J and Sheikh-Bagheri D 2004 Dosimetric evaluation of the clinical implementation of the first commercial IMRT Monte Carlo treatment planning system at 6MV *Med. Phys.* **31** 2771-9

Hsiung C-Y, T H-M, Huang H-Y, Lee C-H, Huang E-Y and Hsu H-C 2006 Parotid-sparing internsity-modulated radiotherapy for nasopharyngeal carcinoma: preserved parotid function after IMRT on quantitative salivary scintigraphy and comparison with historical data after conventinal radiotherapy *Int. J. Radiat. Oncol. Biol. Phys.* **66** 451-61

Jeraj R, Mackie T R, Balog J, Olivera G, Pearson D, Kapatoes J, Ruchala K and Reckwerdt P 2004 Radiation characteristics of helical tomotherapy *Med. Phys*. **31** 396-404

Jeraj R, Mackie T R, Balog J and Olivera G 2005 Dose calibration of nonconventional treatment systems applied to helical tomotherapy *Med. Phys.* **32** 570-7

Jones A O and Das I J 2005 Comparison of inhomogeneity correction algorithms in small photon fields *Med. Phys.* **32** 766-76

Kapatoes J M, Olivera G H, Balog J P, Keller H, Reckwerdt P J and Mackie T R 2001a On the accuracy and effectiveness of dose reconstruction for tomotherapy *Phys. Med. Biol.* **46** 943-66

Kapatoes J M, Olivera G H, Ruchala K J and Mackie T R 2001b On the verification of the incident energy fluence in tomotherapy IMRT *Phys. Med. Biol.* **46** 2953-65

Keall P J, Siebers J V, Arnfield M, Kim J O and Mohan R 2001 Monte Carlo dose calculations for dynamic IMRT treatments *Phys. Med. Biol.* **46** 929-41

Kim J O, Siebers J V, Keall P J, Arnfield M R and Mohan R 2001 A Monte Carlo study of radiation transport through multileaf collimators *Med. Phys.* **28** 2497-506

Laub w, Alber M, Birkner M and Nusslin F 2000 Monte Carlo dose computation for IMRT optimization *Phys. Med. Biol.* **45** 1741-54

Liu H H, Verhaegen F and Dong L 2001 A method of simulating dynamic multileaf collimators using Monte Carlo techniques for intensity-modulated radiation therapy *Phys. Med. Biol.* **46** 2283-98

LoSasso T, Chui C-S and Ling C C 1998 Physical and dosimetric aspects of a multileaf collimation system used in the dynamic mode for implementing intensity modulated radiotherapy *Med. Phys.* **25** 1919-27

Luxton G, Hancock S K and Boyer A L 2004 Dosimetry and radiobiologic model comparison of IMRT and 3D conformal radiotherapy in treatment of carcinoma of the prostate *Int. J. Radiat. Oncol. Biol. Phys.* **59** 267-84

Ma C M, Mok E, Kapur A, Pawlicki T, Findley D, Brain S, Forster K and Boyer A L 1999 Clinical implementation of a Monte Carlo treatment planning system *Med. Phys.* **26** 2133-43

Ma C M, Pawlicki T, Jiang S B, Li J S, Deng J, Mok E, Kapur A, Xing L, Ma L and Boyer A L 2000 Monte Carlo verification of IMRT dose distributions from a commercial treatment planning optimization system *Phys. Med. Biol.* **45** 2483-95

Mackie T R, Holmes T W, Swerdloff S, Reckwerdt P J, Deasy J O, Yang J, Paliwal B R and Kinsella T J 1993 Tomotherapy: a new concept in the delivery of dynamic conformal radiotherapy *Med. Phys.* **20** 1709-19

Madani I, Vanderstraeten B, Bral S, Coghe M, De Gersem W, De Wagter C, Thierens H and De Neve W 2007 Comparison of 6MV and 18MV photons for IMRT treatment of lung cancer *Radiother. Oncol.* **82** 63-9

Martens C, Reynaert N, De Wagter C, Nilsson P, Coghe M, Palmans H, Thierens H andDe Neve W 2002 Underdosage of the upper-airway mucosa for small fields as used in intensity-modulated radiation therapy: A comparison between radiochromic films measurements, Monte Carlo simulations, and collapsed cone convolution calculations *Med. Phys.* **29** 1528-35

Mazurier J, Gouriou J, Chauvenet B and Barthe J 2001 Calculation of perturbation factors for some reference dosimeters in high-energy photon beams with the Monte Carlo code PENELOPE *Phys. Med. Biol.* **46** 1707-17

Olch A J 2002 Dosimetric performance of an enhanced dose range radiographic film for intensity-modulated radiation therapy quality assurance *Med. Phys.* **29** 2159-68

Paelinck L, De Smedt B, Reynaert N, Coghe M, De Gersem W, De Wagter C, Vanderstraeten B, Thierens H and De Neve W 2006 Comparison of dose-volume histograms of IMRT treatment plans for ethmoid sinus cancer computed by advanced treatment planning systems including Monte Carlo *Radiother. Oncol.* **81** 250-6

Pawlicki T and Ma C M 2001 Monte Carlo simulation for MLC-based intensity-modulated radiotherapy *Med. Dosim.* **26** 157-68

Reynaert N, van der Marck S C, Schaart D R, Van der Zee W, Van Vliet-Vroegindeweij, Tomsej M, Jansen J, Heijmen B, Coghe M, De Wagter C 2007 Monte Carlo treatment planning for photon and electron beams *Radiation Phys. and Chem.* **76** 643-86

Salvat F, Fernandez-Varea J M, and Sempau J 2006 *PENELOPE-2006: A Code System for Monte Carlo Simulation of Electron and Photon Transport* OECD Nuclear Energy Agency, Issy-les-Moulineaux, France

Sempau J, Sanchez-Reyes A, Salvat F, Oulad ben Tahar H, Jiang S B and Fernandez-Varea J M 2001 Monte Carlo simulation of electron beams from an accelerator head using PENELOPE *Phys. Med. Biol.* **46** 1163-86

Sempau J, Fernandez-Varea J M, Acosta E and Salvat F 2003 Experimental benchmarks of the Monte Carlo code PENELOPE *Nucl. Instrum. Methods Phys.* **B 207**, 107–23

Sempau J and Andreo P 2006 Configuration of the electron transport algorithm of PENELOPE to simulate ion chambers *Phys. Med. Biol.* **51** 3533-48

Siebers J V, Keall P J, Kim J O and Mohan R 2002 A method for photon beam Monte Carlo multileaf collimator particle transport *Phys. Med. Biol.* **47** 3225-32

Siegbahn E A, Nilsson B, Fernandez-Varea J M and Andreo P 2003 Calculation of electron fluence correction factors using the Monte Carlo code PENELOPE *Phys. Med. Biol.* **48** 1263-75

Sterpin E, Tomsej M, Reynaert N, De Smedt B and Vynckier S 2007a Monte Carlo simulation of the AAA treatment planning algorithm in a heterogeneous multiplayer phantom and IMRT clinical treatments for an Elekta SL25 linear accelerator *Med. Phys*. **34** 1665-77

Sterpin E, Tomsej M, Cravens B, Salvat F, Ruchala K, Olivera G H and S Vynckier 2007b Monte Carlo simulation of the Tomotherapy treatment unit in the static mode using MC HAMMER, a Monte Carlo tool dedicated to Tomotherapy *JPCS* **74** 021019

Sterpin E, Salvat F, Olivera G H and Vynckier S 2007c Analytical model of the binary multileaf collimator of Tomotherapy for Monte Carlo simulations *JPCS* (accepted for publication)

Sultanem K, Shu HK, Xia P, Akazawa C, Quivey J M, Verhey L J and Fu K K 2000 Three-dimensional intensity-modulated radiotherapy in the treatment of nasopharyngeal carcinoma: the University of California-San Francisco experience *Int. J. Radiat. Oncol. Biol. Phys.* **48** 711-22

Thomas S D, Mackenzied M, Field G C, Syme A M and Fallone B G 2005 Patient specific treatment verifications for helical tomotherapy treatment plans *Med. Phys.* **32** 3793-800

Vanderstraeten B, Reynaert N, Paelinck L, Madani I, De Wagter C, De Gersem W, and De Neve W 2006 Accuracy fo patient doe calculation for lung IMRT: A comparison of Monte Carlo, convolution/superposition, and pencil beam computations *Med. Phys.* **33** 3149-57

Van de Walle J, Martens C, Reynaert N, Palmans H, Coghe M, De Neve W, De Wagter C and Thierens H 2003 Monte Carlo model of the ELEKTA Sliplus accelerator: validation of a new MLC component module in BEAM for a 6MV beam *Phys. Med. Biol.* **48** 371-85

Verhaegen F and Seuntjens J 2003 Monte Carlo modeling of external radiotherapy photon beams *Phys. Med. Biol.* **48** R107-64

Walters B R B, Kawrakow I and D W O Rogers 2002 History by history statistical estimators in the BEAM code system *Med. Phys.* **29** 2745-52

Webb S 2004 *Contemporary IMRT—Developing Physics and Clinical Implementation* (Bristol: Institute of Physics Publishing)

Ye S J, Brezovich I A, Pareek P and Naqvi N A 2004 Benchmark of PENELOPE codes for low-energy photon transport : dose comparisons with MCNP4 and EGS4 *Phys. Med. Biol.* **49** 387-97

Zhu X R, Jursinic P A, Grimm D F, Lopez F, Rownd J J and Gillin M T 2002 Evaluation of Kodak EDR-2 film for dose verification of intensity modulated radiation therapy delivered by a static multileaf collimator *Med. Phys.* **29 (8)** 1687-92

Chapter 7: Publication 5

Monte Carlo evaluation of the convolution/superposition algorithm of Hi-Art™ tomotherapy in heterogeneous phantoms and clinical cases

E. Sterpin[a], F. Salvat[b], G. Olivera[c,d] and S. Vynckier[a]

[a] Université Catholique de Louvain, Department of Radiotherapy, St-Luc University Hospital, 10 av. Hippocrate, 1200 Brussels, Belgium

[b] Facultat de Fisica (ECM), Universitat de Barcelona, Diagonal 647, 08028 Barcelona, Spain

[c] Tomotherapy Inc., 1240 Deming Way, Madison, WI USA

[d] Department of Medical Physics University of Wisconsin-Madison, Madison WI USA

Abstract.

The reliability of the convolution/superposition (C/S) algorithm of the Hi-Art™ Tomotherapy system is evaluated by using the Monte Carlo model TomoPen, which has been already validated for homogeneous phantoms. The study was performed in three stages. First, measurements with EBT Gafchromic film for a 1.25x2.5 cm² field in a heterogeneous phantom consisting of two slabs of polystyrene separated with Styrofoam were compared with simulation results from TomoPen. The

excellent agreement found in this comparison justifies the use of TomoPen as the reference for the remaining parts of this work. Second, to allow analysis and interpretation of the results in clinical cases, dose distributions calculated with TomoPen and C/S were compared for a similar phantom geometry, with multiple slabs of various densities. Even in conditions of lack of lateral electronic equilibrium, overall good agreement was obtained between C/S and TomoPen results, with deviations within 3 %/2 mm, showing that the C/S algorithm accounts for modifications in secondary electron transport due to the presence of a low-density media. Finally, calculations were performed with TomoPen and C/S of dose distributions in various clinical cases, from large bilateral head and neck tumors to small lung tumors with diameter < 3 cm. To ensure a "fair" comparison, identical dose calculation grid and dose-volume histogram calculator were used. Very good agreement was obtained for most of the cases, with no significant differences between the DVHs obtained from both calculations. However, deviations were found for the small lung tumors, of up to 4% for the dose received by 95% of the target volume. Therefore, the approximations in the C/S algorithm slightly influence accuracy in small lung tumors even though the C/S algorithm of the Tomotherapy system shows very good overall behavior.

1. Introduction

The Hi-Art™ helical tomotherapy (HT) system was introduced more than half a decade ago. It is designed to deliver highly intensity-modulated radiation therapy (IMRT) by means of the simultaneous movement of the treatment couch, the gantry and the multi-leaf collimator (MLC)[1-2]. This configuration enables delivering highly conformal dose coverage of target volumes, while reducing the dose to organs at risk[3].

In the HT system, the calculation of dose is performed by using a convolution/superposition algorithm (C/S) based on the collapsed-cone approach[4-6]. Such an algorithm implements various approximations in the physics of radiation transport that allow reducing the calculation time to levels that are acceptable for clinical practice. Although collapsed-cone-based C/S algorithms represent major improvements in comparison with older pencil-beam algorithms[10], these approximations may introduce appreciable distortions of the dose distributions, especially in the case of small fields or superpositions of small fields (such as those found in IMRT) irradiating low-density media[6]-[8].

On the other hand, Monte Carlo (MC) simulation algorithms model radiation transport through a detailed description of the physics of the interactions of radiation

and is therefore accepted as the most accurate methodology to compute dose distributions in tissues[11-13]. Because of their ability to describe radiation transport in complex geometries, MC algorithms can readily account for the details of the patient morphology, including the effects of strong inhomogeneities. The advantages of introducing MC dose calculation algorithms have been analyzed in multiple publications[12-13].

The aim of the present article is to evaluate the accuracy of the C/S algorithm provided with HT systems for various clinical cases. Our study is based on the MC model TomoPen of HT, which was previously validated in homogeneous phantoms[14-0]. Several studies with comparisons between MC and analytical algorithms in phantoms and clinical cases[6]-10,14, 17-23 have already been published, but none of them addressed the C/S algorithm of Tomotherapy Inc.

In order to predict, understand and interpret the deviations between the dose distributions calculated with the C/S algorithm and TomoPen, we first assessed the reliability of the latter for beams with regular geometries in heterogeneous phantoms. This was performed by comparing results from measurements performed with EBT Gafchromic™ films in heterogeneous phantoms with regular field geometries with simulation results from TomoPen. After showing that the MC results agree satisfactorily with experiment, we proceeded to compare results from TomoPen and C/S for inhomogenous phantoms. Finally, dose distributions calculated with TomoPen and C/S for a number of clinical cases, from large bilateral head and neck tumors to small lung tumors with diameter < 3 cm, were compared.

2. Material and methods

2.1. Hi-Art™ HT system

IMRT treatments with HT are delivered using a fan beam with simultaneous movement of the gantry and the treatment couch, in an architecture similar to that of a CT scan, together with continuous modulation with the binary MLC[1,2]. The linear accelerator tube delivers two nominal energies, 6 MV and 3.5 MV, for the treatment mode and the imaging mode, respectively. In current HT systems, the fan beam can have three sizes: 40x1, 40x2.5 and 40x5 cm². Faster treatments are obtained with the 40x5 cm² field, whereas higher longitudinal modulation is achieved using the 40x1 cm² field.

2.2. Collapsed cone C/S

The HT C/S algorithm is based on the convolution of a TERMA (Total Energy Released by unit MAss) function with an energy deposition kernel. The TERMA calculation accounts mainly of the beam modeling and models the primary photons that interact with the material. The dose distribution is obtained after the convolution of the TERMA with energy deposition kernels. In the full volume C/S algorithm, energy deposition kernels are described in three dimensions ("point kernels"). Calculating the convolution integral for each point of the volume using a point kernel is extremely time consuming and, therefore, full volume C/S is not used in clinical practice. One popular approach is to integrate the point kernel over the depth dimension to obtain "pencil" kernels. Pencil-beam based algorithms are popular and still widely used in radiotherapy. However, they suffer from a significant lack of accuracy in inhomogeneities[6]-10, even though improvements have been introduced in the recent pencil-beam AAA algorithm[10,14].

The C/S algorithm of the HT system is based on the collapsed-cone approximation[6]. In this approximation, the energy released into coaxial cones of equal solid angles from volume elements on the cone axis is rectilinearly transported, attenuated and deposited in volume elements on that axis[4-5]. Kernel density scaling is applied to account for inhomogeneities, and the validity of this method was already evaluated elsewhere[25]. Currently, C/S algorithms based on the collapsed-cone approximation are considered as the most accurate after MC-based algorithms, as shown extensively in the literature[6]-10,22.

2.3. TomoPen

The TomoPen MC model of HT has been described in detail previously[14-16] and, therefore, only a brief account is given here. The validation of the model was performed through three successive steps. First, measured static open fields (commissioning data) were reproduced accurately by MC simulations with the PENELOPE code[26]. Thereafter, using precalculated phase-space files at planes below the movable jaws, a fast technique for simulating the collimation through the MLC was devised. This technique, which we call the Transfer Function method (TF), is much faster than a straight MC simulation of the transport through the MLC, reducing the computation time to a negligible value[15]. In a few words, it consists in pre-calculating, for each photon in the phase-space files obtained for the static mode, the effective attenuation through the leaves using exponential attenuation and a simple

ray-tracing algorithm that allows for the various possible configurations of the MLC. It was observed by Sterpin *et al* (2008a) that no significant differences could be found between TF method and the full simulation through the MLC, despite the strong approximations made regarding the transport of photons and the production of secondary particles in the MLC.

Finally, the MC simulation of the helical mode is performed by rotating and translating the initial coordinates and directions of the particles in the phase-space file according to the instantaneous position of the machine head, transporting the particles through the MLC with the TF technique (in the instantaneous configuration defined by the sinogram), and computing the dose distribution in the CT structure. As in the treatment planning system (TPS) of Tomotherapy, TomoPen can simulate either 51 projections per rotation or a virtually continuous helical motion by dividing each projection into an arbitrary number of sub-projections, without any appreciable loss of calculation efficiency. The dose values delivered by TomoPen are converted into Gy units using the conversion procedure described by Sterpin *et al* (2008b)[0]. With the adopted simulation strategy, TomoPen is able to compute the dose distribution in a typical clinical procedure in about 6 hours on a single CPU (2.5 GHz).

To allow comparisons between C/S and TomoPen in clinical cases, in the dose calculations with TomoPen we use the same spatial grid as in the TPS, namely, the CT scan grid with an under-sampling factor chosen by the user. After simulation, the dose distribution generated by TomoPen was imported into the TPS, and all the subsequent DVH calculations and comparisons were performed on the same TPS station.

The conversion of the CT scan into mass density and material was performed using the same hounsfield unit (HU)-density conversion curve as in the TPS, calibrated for the CT scan actually used for treatment planning, which is in agreement with the major recommendations by Verhaegen and Devic[27]. This curve was obtained by scanning a phantom with 12 inserts of different tissue-equivalent materials (lung, adipose, bone …) with known density. Material information was also extracted from the HU number by sub-dividing the HU curve into 12 intervals. Each of those intervals was associated to the corresponding material among the 12 provided with the phantom.

The presence of air cavities in the target volume may introduce artificial deviations in the comparison between TomoPen and C/S. Indeed, as already reported by other authors[17,28], it is not possible, in a MC algorithm, to reach an acceptable statistical noise in air in a reasonable computational time because of the low density of air. Therefore, in this study, the air cavities were excluded from the volumes for the evaluation and comparison of the DVHs.

Finally, as all the MC codes, TomoPen computes dose to medium, whereas the C/S algorithm of HT computes dose to water. For unbiased comparisons, the dose values delivered by TomoPen were converted into dose to water following the general guidelines of Siebers *et al* (2000)[29].

In summary, the methodology described above for comparisons of clinical cases, which mainly consisted of using identical dose grids, DVH computation engine and HU calibration curve as well as a dose to water conversion and removing air cavities, ensure a "fair" comparison between C/S and TomoPen. Therefore, potential differences between the two calculation modalities could only be due to differences in the beam modeling or in the description of the transport of particles in the patient geometry.

2.4. Phantom experiments

Initially, we wished to compare calculation results from TomoPen and C/S with measurements using EBT. However, it appeared that differences between TomoPen and C/S occurred for relatively extreme configurations where the presence of the film significantly perturbed the dose distribution. Since it is possible to simulate the film in TomoPen but not in the TPS, it was decided to perform a preliminary experiment where TomoPen was validated in a heterogeneous phantom with film measurements, to eliminate doubt about its reliability. Even though the accuracy of the MC algorithm (PENELOPE) itself is not *a priori* a matter of concern, one cannot exclude completely that slight errors in the beam model of HT may have an influence on the accuracy of the dose distribution for very small fields in inhomogeneities, even though they could not be observed in the various previous tests with homogeneous phantoms[14,16].

After assessing the accuracy of TomoPen by comparison with experiment, TomoPen can be used as a reference with confidence for a second "virtual" experiment where C/S and TomoPen were compared in a similar phantom geometry, but without measurements.

2.4.1. Comparison measurements-TomoPen

Measurements and calculations with TomoPen were performed for a 1.25x2.5 cm² field, with two leaves opened, in a phantom consisting of two slabs of polystyrene separated by Styrofoam (density 0.04 g/cm³) with dimensions of 20x25x20 cm³, as shown in Fig. 1 (a). EBT Gafchromic films were placed parallel to the beam 2 mm off-axis in the longitudinal direction (where the field size equaled 2.5 cm) to limit self-

attenuation in the film. The sides of the phantom were tightened to reduce the air gap between the film and the phantom. The source-surface distance (SSD) equaled 75 cm.

During the phantom experiment, around 500 monitor units were given. Depth-dose distributions and profiles could then be acquired using EBTfilms analyzed with a VIDAR VXR-16 densitometer. The resulting pixel values were then converted into dose values with a calibration curve determined for the employed batch of films. The calibration was performed in a white polystyrene homogeneous phantom. For each scan during the calibration and the experiment, films were read in the same orientation.

EBT films were chosen because of their energy-independent sensitivity for keV to MeV photons[30,31]. van Battum *et al*[32] stated that a global uncertainty of 1.8% (1 standard deviation (SD)) could be achieved for measurements in water. In our experiment, the uncertainty is reduced since only relative data are acquired and since films are scanned always in the same small area of the scanner (determined by the field width, *i.e.* 1.25x2.5 cm²). However, VIDAR scanners are somewhat less adapted than flatbed scanners[33]. For our system (EBT film+VIDAR), the uncertainty due to reproducibility and uniformity was measured and estimated to be about 1%. Taking into account other sources of uncertainties relevant to our experiment, as listed by van Battum *et al*[32], a 2-3% global uncertainty was considered as a realistic value. Of course, the experimental setup itself introduced uncertainties, but these are hard to estimate.

In TomoPen, the geometry was defined to reproduce accurately the conditions of the measurements. The phantom was simulated using the composition of the materials (polystyrene and Styrofoam™). The EBT film was simulated as a 0.04 mm thick sheet of polystyrene with a density of 1.115 g/cm³ (active layer) between two sheets of polystyrene of 0.1 mm with a density of 1.38 g/cm³. The densities of the external sheets are taken from literature[34], whereas the density of the central sheets is the average density of the three different central layers of the EBT film[34]. In the other directions, voxel sizes equaled 1mm and the dimensions were defined as in Fig. 1 (a). Polystyrene was chosen because it is tissue equivalent, as are the EBT films. The differences between the simulated film and the "real" film regarding the composition are expected to have a negligible impact compared to the other sources of uncertainties. The MC parameters of TomoPen were chosen as in Sterpin *et al* (2008b)[17] (namely, $C_1 = C_2 = 0.05$ and $W_{cc} = W_{cr} = 10$ keV), but with the absorption energies of electrons and positrons set to 10 keV because of the smaller dimensions of the voxels.

2.4.2. Comparison C/S-TomoPen

The configuration chosen is similar to that used in the measurements and is shown in Fig. 1 (b). Two slabs of water-like density material (5cm and 3 cm thicknesses) were separated with one slab of water-like material (10 cm) but with two possible densities (ρ = 0.1 or 0.25 g/cm³). These two densities were chosen to evaluate the impact of lateral electronic disequilibrium conditions in conditions usually encountered in lung tumors (ρ = 0.25 g/cm³) and in more extreme cases (ρ = 0.1 g/cm³). The phantom was irradiated using static fields with sizes of 1.25x2.5 cm² , 2.5x2.5 cm² and 10x5 cm², which correspond to two leaves, 4 leaves and 16 leaves open, respectively. Central-axis depth dose distributions and lateral profiles taken at 1.5 cm depth and in the middle of the heterogeneity (8cm depth) were calculated with C/S and TomoPen and compared. SSD equaled 75 cm and the voxels sizes were determined by the TPS and equaled 0.17x0.17x0.25 cm³ were 0.25 refers to the direction along the couch (perpendicular to the plane of the phantom illustrated in Fig. 1.

2.5. Clinical study

The clinical study was divided into three categories:

- Head and neck tumors.
- Lung tumors.
- Ewing tumor surrounding a prosthesis of the leg.

According to previous studies and observations made by other authors[12-13, 17-23], deviations between TomoPen and C/S are more likely to occur for target volumes including or having in their neighborhood air cavities or low density tissues. Therefore, the two first categories were selected because it was possible to find there cases which tested the C/S algorithm to its limits.

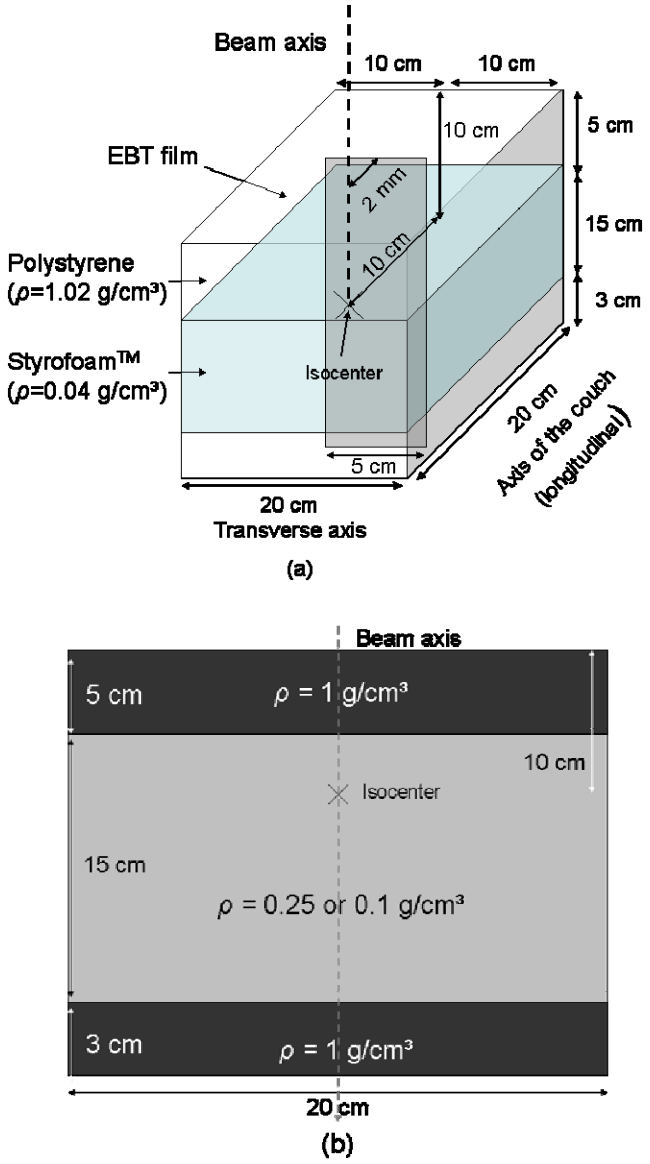


Fig. 1. Geometry of the phantoms used in this study: (a) phantom used to compare TomoPen and measurements on phantoms consisting of one slab of Styrofoam™ between two slabs of polystyrene; (b) phantom used in the comparisons of TomoPen and C/S, composed of three slabs of water material, a central slab with varying density between two slabs with the density of water.

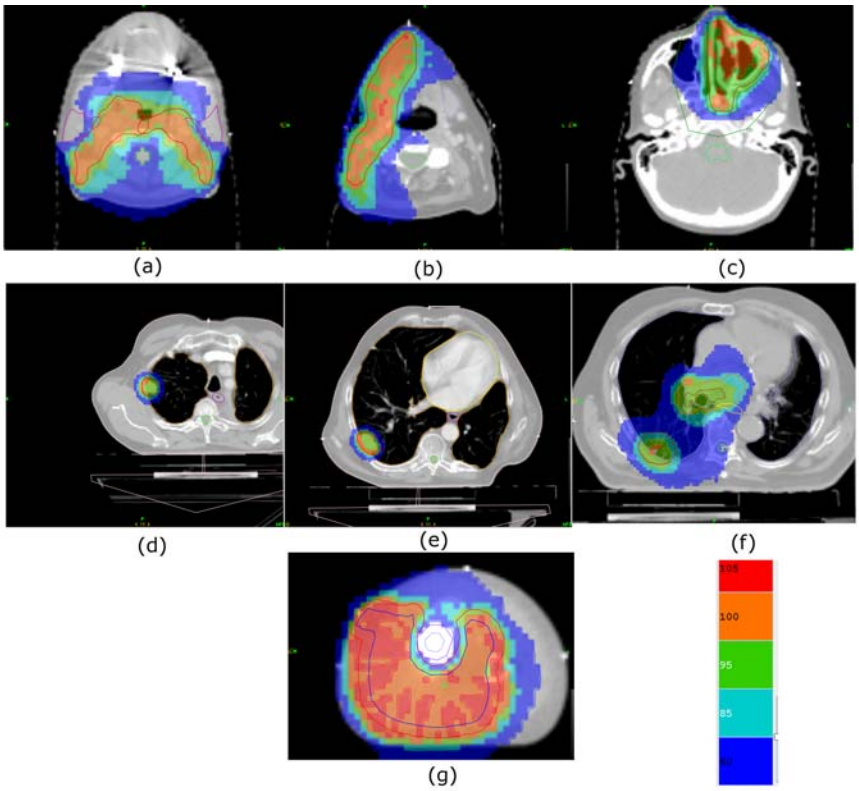


Fig. 2. Images of the target locations of the clinical cases studied listed hereafter with the prescribed dose in the parenthesis: two oropharynx tumors (a, 70 Gy) and (b, 60 Gy), an ethmoid tumor (c, 50.4 Gy), small lung tumors (diameter < 3 cm) (d, 60 Gy) et (e, 60 Gy), tumor with simultaneous treatment of two locations (mediastinal and lateral) (f, 60 Gy) and a special treatment with a tumor surrounding a leg prosthesis (g, 44 Gy). This last case was planned on a MVCT image. Isodose curves obtained with TomoPen are shown. Isodoses are given in terms of percentage of prescribed dose according to the legend shown on the figure.

For all the cases, optimizations constraints were set to reach a "reasonable" level of modulation and meet the clinical requirements of our radiation oncologists. Fig. 2 shows an overview of the various target locations studied in this work. In the results section, each result reported will be referred to by the corresponding letter in Fig. 2. For each case, clinically relevant numerical values of the DVHs were compared. For instance, for the DVH of the PTV, the mean dose and the dose received by 2 and 95 % of the prescribed dose (D_{mean}, D_2 and D_{95}, respectively) are chosen for the comparison. For organs at risk, D_2 was used for the spinal cord, whereas V_{20Gy} and V_{25Gy} were calculated for the lungs, which are percentages of volumes receiving, 20 and 25 Gy, respectively. Those values are reported in tables for each category.

The last case (g) was chosen because it used many specific capabilities of the HT system. Moreover, the presence of the prosthesis close to the target volume reduced the confidence of our radiation oncologists and physicists regarding the accuracy of the calculated dose distribution, according to the concerns of the radiotherapy community[35]. The target was a Ewing tumor at the level of the leg, surrounding a high-density prosthesis, made with cobalt (27%), chromium (5%) and molybdenum (68%). In this case, treatment planning was performed on a MVCT (megavoltage computed tomography) image acquired using the imaging mode of the HT device. This was of course required since a classic KVCT image (kilovoltage computed tomography) would have resulted in a poor quality image with huge artifacts impossible to use for treatment planning.

Another special feature of the TPS was also used. Indeed, the prosthesis was completely blocked during the optimization process to avoid that any primary photon trajectory crossed the prosthesis. It is worth mentioning that the HU calibration curve used in both C/S and TomoPen for this particular case was acquired using the same methodology as described above, but with the MVCT imager of our HT device. However, the exact composition and mass density of the prosthesis were defined in the MC simulation for this particular case, instead of extracting the information from the HU number.

For the sake of space economy, we present only the DVHs of cases where significant deviations were more likely to occur.

3. Results

3.1. Phantom experiment

3.1.1. Comparison TomoPen-measurements

Depth dose distributions from the measurements and simulations described in Section II.D.1 are compared in Fig. 3. The overall agreement between measurements and TomoPen is good, with deviations within 3% (of maximum dose) and 2 mm. The dose drop due to the loss of lateral electronic equilibrium was severe, which was expected because of the field size chosen (1.25x2.5 cm²) and the low density of Styrofoam™.

Measured and calculated transverse dose profiles are compared in Fig. 4. The agreement is again very good, with deviations within 2%/1mm.

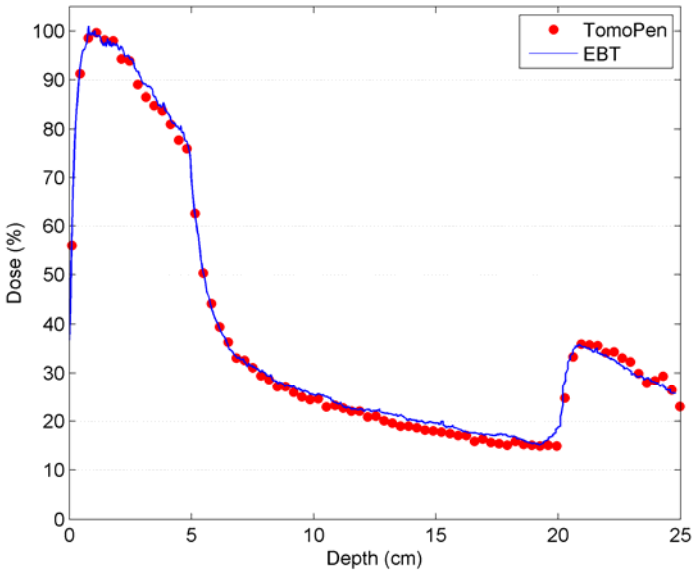


Fig. 3. Comparison of dose distributions calculated with TomoPen (red solid points) and measured with EBT (blue solid line) for a 1.25x2.5 cm² field.

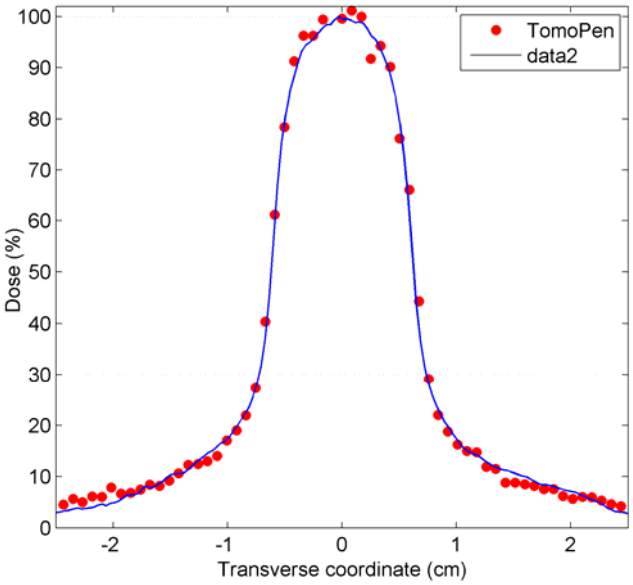


Fig. 4. Comparison of transverse profiles computed with TomoPen (red solid points) and measured with EBT (blue solid line) for a 1.25x2.5 cm² field.

3.1.2. Comparison TomoPen-C/S

Depth dose distributions calculated with TomoPen and CS for the configuration described in Section II.D.2 are compared in Fig. 5. The agreement is good for the cases shown in Fig. 5 (c), (e) and (f), with deviations within 2%/2mm in the slabs with water density, and within 4%/2mm in the low-density central slab. In Fig. 5 (b), the agreement is similar except just underneath the first interface water density - low density, where deviations are up to 8% of the maximum dose or 5 mm in the dose gradient. In Fig. 5 (a) and (c), similar deviations are observed in the dose gradient at the first interface, but significant deviations also occur in the bulk of the low-density slab with deviations up to 5% of maximum dose. In Fig. 5 (a)-(e), very good agreement is obtained between TomoPen and C/S in the "rebuild up" region after the second density interface with deviation well within 2%/2 mm. It is interesting to note that C/S seems to account correctly even for the loss of backscattered radiation before the first interface.

Transverse dose profiles at the isocenter (10 cm depth) are also compared for ρ = 0.1 and ρ = 0.25 g/cm³ in Fig. 6 (a) and (b), respectively. The differences are within 2%/2mm for all the cases except for ρ = 0.1 g/cm³ and a field size of 1.25x1.25 cm², where differences up to 8% of the maximum dose are found.

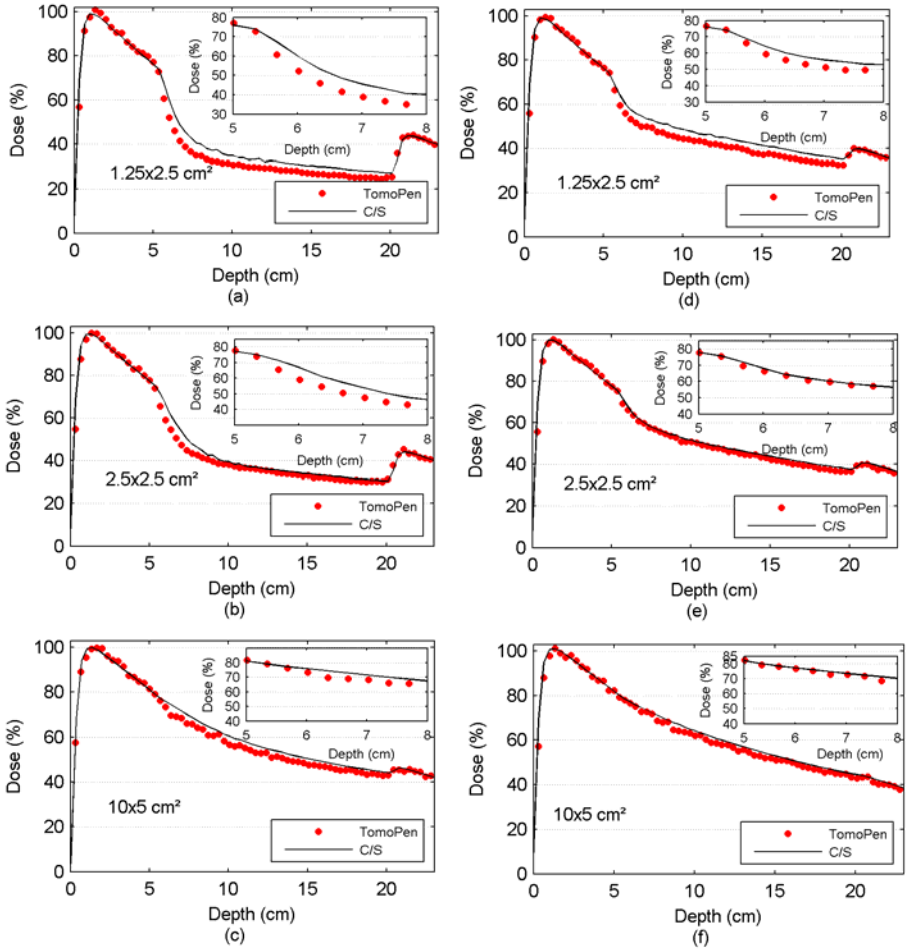


Fig. 5. Comparison of depth-dose distribution calculated with TomoPen (red solid points) and C/S (black lines) for the configuration shown in Fig. 1b, with central slabs of density ρ = 0.1 g/cm³ (a, b, c) and ρ = 0.25 g/cm³ (d, e, f). The corresponding field sizes are indicated on each figure. Insets are zooms over the first centimeters under the upper surface of the central slab.

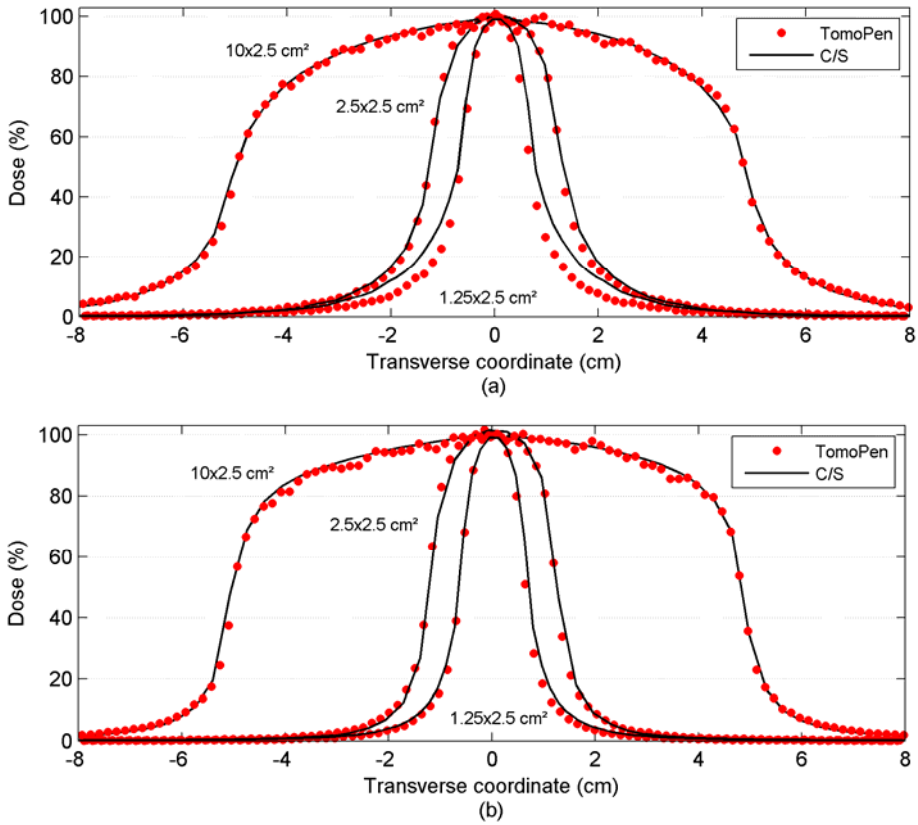


Fig. 6. Comparison of dose profiles calculated with TomoPen (red solid points) and C/S (black lines) for the configuration shown in Fig. 1b, with central slabs of density ρ = 0.1 g/cm³ (a) and ρ = 0.25 g/cm³ (b). The corresponding field sizes are indicated on each figure.

3.2. Clinical studies

3.2.1. Head and neck tumors

Three cases are discussed here: bilateral and unilateral oropharynx tumors (cases (a) and (b)) and one ethmoid tumor (case (c)). For cases (a) and (b), characteristic values are compared in Table 1. Very good agreement between TomoPen and C/S is obtained for all the values with a maximum deviation occurring for D_2 in case (a) for the PTV of around 1.4%. For case (c), values are reported in Table 2. The overall agreement for organs at risk is good, with a maximum deviation for optical chiasm of 2% of dose constraint (50 Gy). Good agreement is also obtained for the mean dose and D_2 for the PTV. However, D_{95} is significantly higher for C/S

(around 2.8% of prescribed dose), which indicates that PTV coverage is overestimated by C/S. The DVHs shown in

Fig. 7 confirms the values reported in Table 2, especially for PTV coverage which is clearly overestimated by C/S.

		Case (a)		Case (b)	
		C/S	TomoPen	C/S	TomoPen
PTV	D_{mean} (Gy)	69.5	70.0	59.6	59.6
(without air)	D_{95} (Gy)	68.7	68.1	57.6	56.9
	D_2 (Gy)	72.1	73.1	62.1	62.3
Spinal cord	D_2 (Gy)	39.2	38.9	22.4	22.2
Left Parotid	D_{mean} (Gy)	22.1	22.3	3.1	3.0
Right Parotid	D_{mean} (Gy)	27.4	27.2	57.0	57.3

Table 1. Characteristic values of the DVHs obtained for the head and neck cases (a) and (b): mean dose (D_{mean}), dose received by 95% of the volume (D_{95}) and dose received by 2% of the volume (D_2) for the PTV, D_{mean} for the parotids and D_2 for the spinal cord.

		Case (c)	
		C/S	TomoPen
PTV	D_{mean} (Gy)	50.3	50.1
(without air)	D_{95} (Gy)	49.2	47.8
	D_2 (Gy)	51.2	51.2
Optic chiasm	D_2 (Gy)	39.5	38.5
Left optic nerve	D_2 (Gy)	51.3	51.5
Right optic nerve	D_2 (Gy)	48.6	48.3

Table 2. Characteristic values of the DVHs obtained for the ethmoid case (c) mean dose (D_{mean}), dose received by 95% of the volume (D_{95}) and dose received by 2% of the volume (D_2) for the PTV, D_{mean} for the parotids and D_2 for the spinal cord.

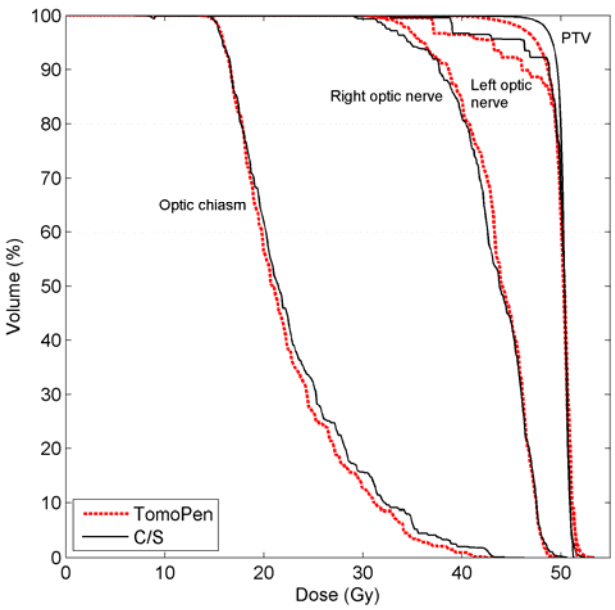


Fig. 7. Ethmoid tumor (case (c)). Comparison of DVHs obtained from calculations with TomoPen and C/S for the PTV, the optic nerves and the optic chiasm.

3.2.2. Lung tumors

The results for cases (d)-(f) are reported in Table 4. For the mean dose, agreement is within 2.2 %. For D_{95}, the maximum difference occurs for case (e) (4 %). These results are confirmed in the DVHs shown in Fig. 8 where C/S clearly predicts higher dose coverage of the target volume than TomoPen, as clearly reflected in Table 3 and Fig. 8 On the other hand, very good agreement is obtained between the DVHs of the lungs as shown in Table 3 and Fig. 8.

		Case (d)		Case (e)		Case (f)	
		C/S	TomoPen	C/S	TomoPen	C/S	TomoPen
PTV	D_{mean} (Gy)	59.2	58.6	59.2	58.0	59.4	58.1
	D_{95} (Gy)	55.4	53.4	57.0	54.6	56.6	55.0
	D_2 (Gy)	61.4	61.3	60.5	60.4	61.1	60.8
Left	V_{20Gy} (%)	0.0	0.0	0.0	0.0	3.8	3.3
	V_{25Gy} (%)	0.0	0.0	0.0	0.0	0.0	0.0
Right	V_{20Gy} (%)	3.9	3.7	4.0	3.8	61.4	61.3
	V_{25Gy} (%)	2.9	2.7	2.7	2.6	61.3	61.2

Table 3. Characteristic values of the DVHs obtained for the three lung tumors cases (d), (e) and (f): mean dose (D_{mean}), dose received by 95% of the volume (D_{95}) and dose received by 2% of the volume (D_2) for the PTV and volumes receiving 20 and 25 Gy for the lungs (V_{20Gy}, V_{25Gy}, respectively).

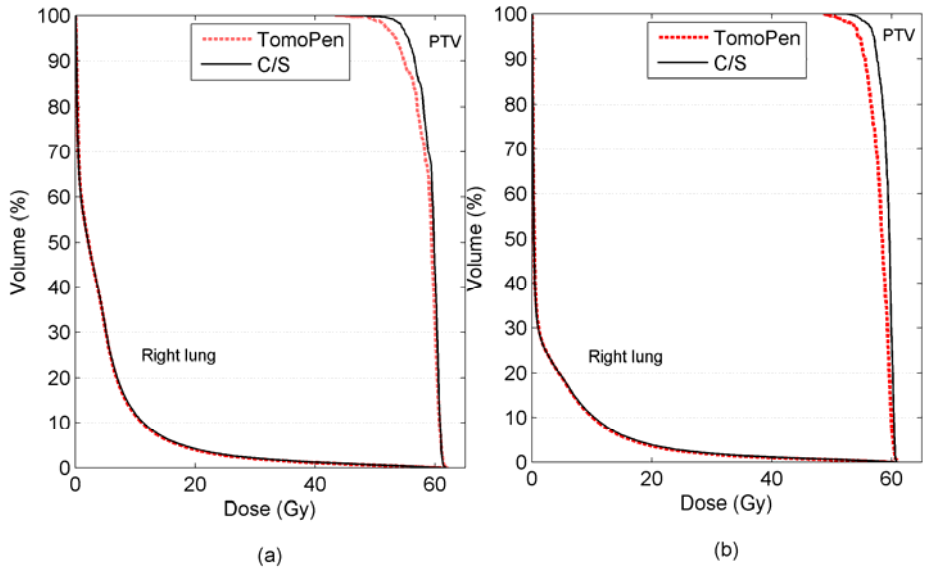


Fig. 8. Small lung tumors cases (d) (left side) and (e) (right side). Comparison of DVHs obtained from calculations with TomoPen and C/S for the PTV and the right lung.

3.2.3. Leg tumor

Numerical values characterizing the DVH of the PTV for the case (g) are reported in Table 4, and the DVHs are displayed in Table 4. Excellent agreement is obtained with deviation within 0.5% for D_{mean} and D_{95} within 1.2% for, D_2. For the prosthesis, dose is kept small as clearly seen in Table 4, despite the proximity of the structure of the target volume, proving the efficiency of our optimization strategy to avoid direct irradiation of the prosthesis.

		Case (g)	
		C/S	TomoPen
PTV	D_{mean} (Gy)	43.8	44.0
	D_{95} (Gy)	29.4	29.3
	D_2 (Gy)	47.9	48.4

Table 4. Characteristic values of the DVHs obtained for the leg tumor study (g): mean dose (D_{mean}), dose received by 95% of the volume (D_{95}) for the PTV and dose received by 2% of the volume (D_2)

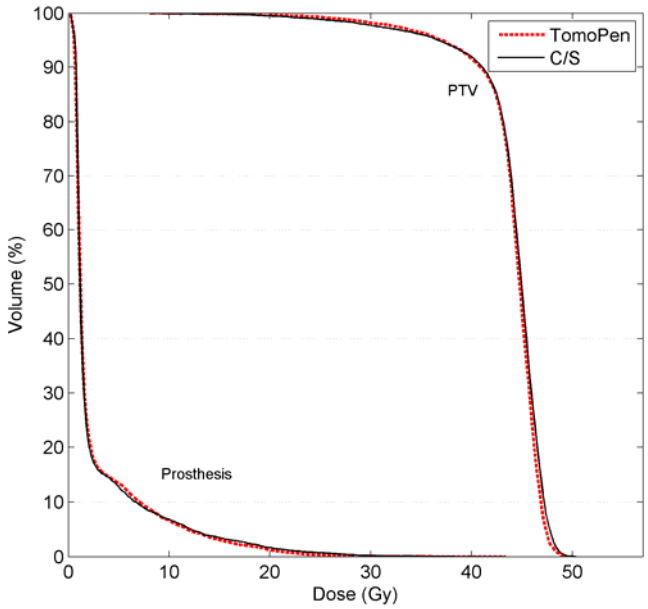


Fig. 9 Leg tumor case (g). Comparison of DVHs obtained from calculations with TomoPen and C/S for the PTV and the prosthesis

3.3. Discussion

3.3.1. Phantom experiments

The phantom experiments provided useful information to analyze and interpret the results for the clinical cases.

First, the agreement between the results from TomoPen and the measurements shown in Fig. 3 and Fig. 4, which represent an extreme situation (very small field and density), provides compelling evidence that TomoPen can be used as a reference for the other parts of this study.

Second, the comparison of TomoPen and C/S for the composite phantom shown in Figs. 5 clearly indicates that C/S does account for the loss of lateral electronic equilibrium effects, as expected for a collapsed-cone algorithm[4,5,[6]-10,20]. The "re-build up" effect is also predicted accurately for all the configurations. Moreover, density scaling of the kernels further allowed C/S for predicting penumbra widening effects as clearly seen in Fig. 6, except for the smallest field width and density, where C/S overestimated the effect. However, for relatively extreme cases, C/S deviated from TomoPen. In Fig. 5 (a), (b) and (d), the dose drop is steeper for TomoPen than for C/S, which may result in an overestimation of the dose to PTVs encompassing lung tissues and/or air cavities. This overestimation has been noted by other authors[[8],10] for collapsed-cone algorithms and a physical explanation was proposed by Arnfield *et al*[8]. In the bulk of the inhomogeneity, deviations are also visible in Fig. 5 (a) and (d), but the overall good agreement obtained for the other cases indicates that no significant differences between TomoPen and C/S should be expected for the DVHs of the lungs in the vast majority of clinical situations.

3.3.2. Clinical cases

In the clinical cases, minor deviations were found between TomoPen and C/S for cases without a significant amount of low density inhomogeneities (cases (a) and (b)). Similar agreement was also obtained for other cases with similar complexity, which are not presented in this paper for the sake of conciseness. Even in the extreme situation of the Ewing tumor (case (g)) with the problematic presence of the metallic prosthesis, C/S was able to accurately compute the dose. Therefore, the beam modeling and the C/S calculation provide accurate dose distributions in water and dense tissues/bone, at least for the cases considered in this study. Thus, additional studies are needed to demonstrate a significant clinical impact, if any, of the *a priori* improved beam modeling in TomoPen compared to C/S.

However, when a great amount of air cavities or lung tissue were encompassed within the target volume and/or tumors were small as in cases (c)-(f), significant deviations between TomoPen and C/S were found, especially in case (e) with a 4% deviation for the D_{95} of the PTV that indicates an overestimation of PTV coverage by C/S. This is consistent with the phantom study which showed potential problems for C/S close to water density – low density interfaces. Those problems could moreover be magnified because of the geometry of the patients and target volumes which are relatively far from the slab geometry used in the phantom study. Finally, the presence of air cavities may also have a clinical impact on the accuracy of the dose distributions, since a deviation of around 2.8% was found for D_{95} in case (c).

Despite those differences, which are significant only for extreme cases, the overall performance of C/S can be considered as very satisfactory, and similar to the other most powerful analytical dose calculation algorithms available, like TMS (Nucletron) and Pinnacle (Philips Medical Systems)[19,21,22].

4. Conclusions

This study is the first evaluation of the accuracy of the C/S algorithm of Tomotherapy Inc. using a benchmarked MC model (TomoPen). As expected for a collapsed-cone algorithm, C/S demonstrated an overall good behavior in inhomogeneities but was also promising regarding beam modeling. However, in relatively extreme phantom configurations and clinical cases, such as small lung tumors, differences between TomoPen and C/S were found. These deviations are attributed to the difference in particle transport in low density inhomogeneities. It is worth insisting on the fact that differences only appeared for very challenging cases (small lung and ethmoid tumors, for instance), which gives good confidence on the accuracy of C/S for the majority of tumor locations.

Finally, it has been shown that TomoPen is ready to be used for clinical applications. The differences between TomoPen and C/S observed for the lung tumors and the ethmoid case demonstrate also the potential of introducing TomoPen into clinical practice to improve the accuracy of complex treatments.

Acknowledgements

This work was supported by a Grant from the Belgian 'Fonds National pour la Recherche Scientifique' (FC 73512). Francesc Salvat acknowledges financial support from the Spanish Ministerio de Educación y Ciencia (project no.\ FPA2006-12066) and FEDER.

1. T. R. Mackie, T. W. Holmes, S. Swerdloff, P. J. Reckwerdt, J. O. Deasy, J. Yang, B. R. Paliwal and T. J. Kinsella, "Tomotherapy: a new concept in the delivery of dynamic conformal radiotherapy," Med. Phys. **20** 1709-19
2. T. R. Mackie, "History of tomotherapy," Phys. Med. Biol. **51**, R427-R453 (2006)
3. A. W. Beavis, "Is tomotherapy the future of IMRT," Br. J. Radiol. **77** 285-295 (2004)
4. A Ahnesjö and M M Aspradakis, "Dose calculations for external photon beams in radiotherapy," Phys. Med. Biol. **44**, R99-R155 (1999).
5. A Ahnesjö, "Collapsed cone convolution of radiant energy for photon dose calculation in heterogeneous media," Med. Phys. **16**, 577-592, (1989).
6. W. Lu, G. H. Olivera, M. Chen, P. J. Reckwerdt and T. R. Mackie, "Accurate convolution/superposition for mutli-resolution dose calculation using cumulative tabulated kernels," Phys. Med. Biol. **50**, 655-680 (2005).
7. P. Carrasco, N. Jornet, M. A. Duch, L. Weber, M. Ginjaume, T. Eudaldo, D. Jurado, A. Ruiz and M Ribas, " Comparison of dose calculation algorithms in phantoms with lung equivalent heterogeneities under conditions of lateral electronic disequilibrium," Med. Phys. **31**, 2899-2911 (2004).
8. A. O. Jones and I. J. Das, "Comparison of inhomogeneity correction algorithms in small photon fields," Med. Phys. **32**, 766-776 (2005).
9. M. R. Arnfield, C. H. Siantar, J. Siebers, P. Garmon, L. Cox and R. Mohan, "The impact of electron transport on the accuracy of computed dose," Med. Phys. **27**, 1266-1274 (2000).
10. A. Fogliata, E. Vanetti, D. Albers, C. Brink, A. Clivi, T. Knöös, G. Nicolini and L. Cozzi, "On the dosimetric behaviour of photon dose calculation algorithms in the presence of simple geometric heterogeneities: comparison with Monte Carlo calculations," Phys. Med. Biol. **52**, 1363-1385 (2007).
11. F Verhaegen, J Seuntjens, "Monte Carlo modeling of external radiotherapy photon beams," Phys. Med. Biol. **48**, R107-R164 (2003).
12. N. Reynaert, S. C. van der Marck, D. R. Schaart, W. Van der Zee, C. Van Vliet-Vroegindeweij, M. Tomsej, J. Jansen, B. Heijmen, M. Coghe, and C. De Wagter, "Monte Carlo treatment planning for photon and electron beams," Radiation Phys. and Chem. **76**, 643-86
13. I. J. Chetty, B. Curran, J. E. Cygler, J. J. DeMarco, G. Ezzell, B. A. Faddegon, I. Kawrakow, P. J. Keall, H. Liu, C.-M. Ma, D.W.O. Rogers, J. Seuntjens, D. Sheikh-Bagheri, and J. V. Siebers, "Report of the AAPM Task Group No. 105: Issues associated with clinical implementation of Monte Carlo-based photon and electron external beam treatment planning," Med. Phys. **34**, 4818-4853 (2007).
14. E. Sterpin, M. Tomsej, R. Cravens, F. Salvat, K. Ruchala, G.H. Olivera and S. Vynckier, "Monte Carlo simulation of the Tomotherapy treatment unit in the static mode using MC HAMMER, a Monte Carlo tool dedicated to Tomotherapy," JPCS **74**, 021019
15. E. Sterpin, F. Salvat, G. H. Olivera and S. Vynckier, "Analytical model of the binary multileaf collimator of Tomotherapy for Monte Carlo simulations," J. Phys.: Confer. Ser. **102,** 012022 (2008)

16. E. Sterpin, F. Salvat, R. Cravens, K. Ruchala, G. H. Olivera and S. Vynckier, "Monte Carlo simulation of helical Tomotherapy with PENELOPE," Phys. Med. Biol. **53,** 2161-2180 (2008)
17. E. Sterpin, M. Tomsej, B. De Smedt, N. Reynaert and S. Vynckier, "Monte Carlo evaluation of the AAA treatment planning algorithm in a heterogeneous multiplayer phantom and IMRT clinical treatments for an Elekta SL25 linear accelerator," Med. Phys. **34**, 1665-1677 (2007).
18. I. Madani, B. Vanderstraeten, S. Bral, M. Coghe, W. De Gersem, C. De Wagter, H. Thierens and W. De Neve, "Comparison of 6MV and 18MV photons for IMRT treatment of lung cancer," Radioth. and Oncol. **82**, 63-69 (2007).
19. L. Paelinck, B. De Smedt, N. Reynaert, M. Coghe, W. De Gersem, C. De Wagter, B. Vanderstraeten, H. Thierens and W. De Neve, "Comparison of dose-volume histograms of IMRT treatment plans for ethmoïd sinus cancer computed by advanced treatment planning systems including Monte Carlo," Radioth. Oncol. **81**, 250-256 (2006).
20. C. Martens, N. Reynaert, C. De Wagter, P. Nilsson, M. Coghe, H. Palmans, H. Thierens and W. De Neve, "Underdosage of the upper-airway mucosa for small fields as used in intensity-modulated radiation therapy: A comparison between radiochromic films measurements, Monte Carlo simulations, and collapsed cone convolution calculations," Med. Phys. **29**, 1528-1535 (2002).
21. T. Knöös, E Wieslander, L. Cozzi, C. Brink, A. Fogliata, D. Albers, H. Nyström and S. Lassen, "Comparison of dose calculation algorithms for treatment planning in external photon beam therapy for clinical situation," Phys. Med. Biol. 51 5785-5807 (2006).
22. B. Vanderstraeten, N. Reynaert, L. Paelinck, I. Madani, C. De Wagter, W. De Gersem, W. De Neve and H. Thierens, "Accuracy of patient dose calculation for lung IMRT: a comparison of Monte Carlo, convolution/superposition and pencil beam computations," Med. Phys. **33**, 3149-3157 (2006).
23. P. Francescon, C. Cavedon, S. Reccanello and S. Cora, "Photon dose calculation of a three-dimensional treatment planning system compared to the Monte Carlo code BEAM," Med. Phys. **27**, 1579-1587 (2000).
24. R. Mohan, C. Chui and L. Lidofsky, "Differential pencil beam dose computation model for photons," Med. Phys. **13,** 64-73 (1986).
25. M. K. Woo and J. R. Cunningham, "The validity of the density scaling method in primary electron transport for photon and electron beams," Med. Phys. **17** 187-194 (1990).
26. F. Salvat, J. M. Fernandez-Varea and J. Sempau, "PENELOPE-2006: A Code System for Monte Carlo simulation of Electron and Photon Transport," OECD Nuclear Energy Agency, Issy-les-Moulineaux, France (2006).
27. F. Verhaegen, and S. Devic, "Sensitivity study for CT image use in Monte Carlo treatment planning," Phys. Med. Biol. **50,** 937-946 (2005).
28. B. De Smedt, B. Vanderstraeten, N. Reynaert, W. De Neve, and H. Thierens, "Investigation of geometrical and scoring grid resolution for Monte Carlo dose calculations for IMRT," Phys. Med. Biol. **50**, 4005-4019 (2005).

29. J.V. Siebers, P. J. Keall, A. E. Nahum, and R. Mohan, "Converting absorbed dose to medium to absorbed dose to water for Monte Carlo based photon beam dose calculations," Phys. Med. Biol. **45**, 983-995 (2000).
30. E. Wilcox, G. Daskalov, and L. Nedialkova, "Comparison of the Epson Expression 1680 flatbed and the Vidar VXR-16 Dosimetry PRO™ film scanners for use in IMRT dosimetry using Gafchromic and radiographic film," Med. Phys. **34**, 41-48 (2007).
31. S. T. Chiu-Tsao, Y. Ho, R. Shankar, L. Wang, and L. B. Harrison, "Energy dependence of response of new high sensitivity radiochromic films for megavoltage and kilovoltage radiation energies," Med. Phys. **32**, 3350–3354 (2005).
32. L. J. van Battum, D. Hoffmans, H. Piersma, and S. Heukelom, "Accurate dosimetry with Gafchromic™ EBT film of a 6MV photon beam in water: What level is achievable?," Med. Phys. **35**, 704-716 (2008).
33. E. Wilcox, G. Daskalov, and L. Nedialkova, "Comparison of the Epson Expression 1680 flatbed and the Vidar VXR-16 Dosimetry PRO™ film scanners for use in IMRT dosimetry using Gafchromic and radiographic film," Med. Phys. 34 41-48
34. S. Devic et al., "Accurate skin dose measurements using radiochromic film in clinical applications," Med. Phys. 33, 1116–1124 (2006).
35. C. Reft, R. Alecu, I. J. Das, B. J. Gerbi, P. Keall, E. Lief, B. J. Mijnheer, N. Papanikolaou, C. Sibat,a and J. Van Dyk, "Dosimetric considerations for patients with HIP prostheses undergoing irradiation. Report on the AAPM Radiation Therapy Committeee Task Group 63," Med. Phys. **30**, 1162-1182 (2003).

Chapter 8: Discussion

In the different papers, several points were discussed. In chapter 3, the differences between AAA and MC in extreme phantom experiments and clinical cases were estimated. In chapter 6 the MC model of tomotherapy from the static mode and the helical mode was described. In chapter 7 comparisons between the collapsed-cone C/S algorithm of tomotherapy and TomoPen were performed following a similar methodology as in the AAA paper.

Although the main results were already discussed in the papers, some additional points deserve developments:

1. Since the publication of the paper presented in chapter 3, many other studies were published on AAA and its behavior in inhomogeneities (Bragg *et al* 2008, Hasenbalg *et al* 2007, Tillikainen *et al* 2008, Ding *et al* 2007, Fogliata *et al* 2007). AAA's ability to model Elekta linacs was also confirmed by another research group (Cozzi *et al* 2008). In general, their observations agree with the results presented in chapter 3, but the comparison of their results and methods with ours certainly needs additional discussion.

2. The MC model of the Elekta SL25 presented in the AAA paper is based on BEAM/EGSnrc and well known MC modeling methods (Verhaegen and Seunjens 2002, Reynaert *et al* 2007, Chetty *et al* 2008). Moreover, the MC calculator used in clinical cases (MCDE) is also well benchmarked and was already used in many other studies (Reynaert *et al* 2005, Vanderstraeten *et al* 2006, Madani *et al* 2007). On the other hand, TomoPen is a MC model based on original simulation techniques. For instance, the TF method and the dose calibration procedure of TomoPen (section 2.6.5 in the chapter 6) are specific to TomoPen and differ significantly from the modeling techniques used in conservative MC models. Concerns about the accuracy of TomoPen may arise and, therefore, it is worth extending the brief discussion of section 4 in chapter 6 to justify our choices with respect to accuracy and the dose calibration procedure.

3. TomoPen is designed to be implemented in the clinical TPS of the HT system. One section in this chapter will be dedicated to explain the additional issues that may remain for the implementation of TomoPen.

4. The main purpose of TomoPen is to be used as a final dose calculator to check the validity of the tomotherapy C/S algorithm. However, the simplicity and speed of TomoPen may open other areas of investigation or clinical applications.

5. MC in clinical cases was compared to advanced analytical algorithms, like the Varian AAA or the tomotherapy collapsed-cone C/S. To evaluate the added-value of MC, it is worth making a link between those two papers to have more examples to discuss this important subject, which is the main point of this thesis.

1. Overview of the last studies on the performance of AAA

1.1. Phantom studies

At the time of the publication of Sterpin *et al* (2007a) (Chapter 3), there was a lack of information regarding the functioning of the AAA algorithm. Originally based on the paper of Ulmer *et al* (2005), the AAA algorithm was substantially modified until the commercial version of AAA used in Chapter 3. The paper had to be written without the detailed explanations of the algorithm's physics, except the ones taken from the user manual. This lack of information was amended by the recent publication of Tillikainen *et al* (2007) but, above all, Tillikainen *et al* (2008) who extensively explained the heterogeneity correction method in AAA. However, it is important to mention that despite the simplicity of the description of AAA in chapter 3, the explanations are coherent with Tillikainen *et al* (2008).

In Tillikainen *et al* (2008), phantom configurations were comparable to the one in chapter 3 used to evaluate the performance of AAA. This study was also performed by several groups (Fogliata *et al* 2007, Ding *et al* 2007). In general, the conclusions were similar (for the 6 MV beams in low density inhomogeneities):

- AAA predicts overall accurately lack of lateral electronic equilibrium effects in low density media (<0.3 g/cm³) for small field sizes (*i.e.* < 5x5 cm²). For very light materials (<0.1 g/cm³), significant deviations may however occur (Fogliata *et al* 2007). In that extreme case, collapsed-cone algorithms perform better.

- For larger field sizes, AAA has a tendency to slightly underestimate the dose within the low density inhomogeneity and overestimate the dose in the first centimeters beyond the low density-water density interface (deviations generally within 3% of maximum dose). This is clearly shown in Tillikainen *et al* (2008) (Figure 8. 1) and was attributed to the build-up kernel correction method.

Finally, the results presented in this recent literature and the one cited in chapter 3 clearly demonstrated that AAA can be assumed as being an advanced algorithm (type "b") with performances close to collapsed-cone based algorithms.

1.2. Clinical studies

Despite the wide interest of the scientific community in AAA, only a fraction of the publications included a clinical study (Knöös *et al* 2006, Bragg *et al* 2008, Ding *et al* 2007, Hasenbalg *et al* 2007). All of them confirmed the superiority of AAA compared to older algorithms (like PB convolution with MB heterogeneity correction). In Ding *et al* (2007), it is surprising that, in the cases selected in the publication, PB convolution performed better in the absence heterogeneity corrections than with MB. This gives argument to some physicists working in clinical routine claiming that it is sometimes better to make no correction rather than making a wrong correction. On the other hand, Bragg *et al* (2008) focused on the difference between old PB convolution and AAA in IMRT treatments and concluded to the superiority of the latter in lung tumors, whereas differences observed for tumors in the head and neck region were of similar order of magnitude as in chapter 3.

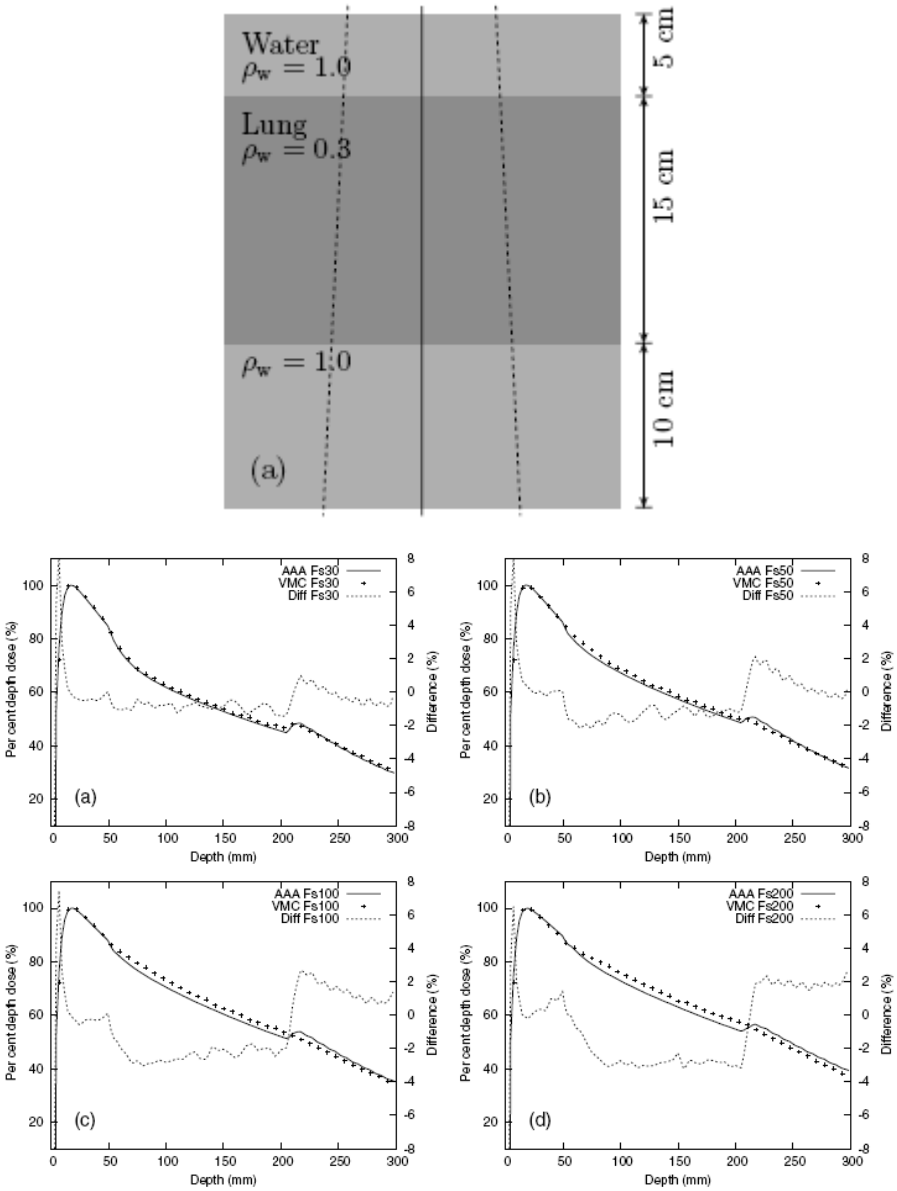


Figure 8. 1. Comparison of depth-dose distributions calculated for a 6 MV beam with AAA and VMC (fast Monte Carlo code, Kawrakow and Fippel (2000)). The dose distributions are calculated in the phantom configuration displayed above (figure taken from Tillikainen *et al* (2008)). The field sizes are given in mm and correspond to the length of a side of each square field calculated.

Among the publications, only a few included MC simulations (Hasenbalg *et al* 2007 and Knöös *et al* 2006). None of those studies included small lung tumors or ethmoid cases, which are more problematic to handle for AAA, *a priori*. However, in less critical lung and head and neck tumors, the results were comparable to the ones presented in chapter 3 (sections 3.3.2 and 3.3.3), with deviations generally within 2%.

It is worth insisting on the fact that most of the studies focused on cases commonly encountered in clinic, that is, relatively large lung, head and neck and breast tumors treated with 3D-CRT. By opposition to our approach, the cases were not selected to test AAA to its limits with complex treatments (IMRT) in critical clinical situations and evaluate its performance by an independent and very accurate calculation tool (MCDE). Therefore, even though the added-value of AAA is certainly demonstrated compared to older algorithms, there are still wide possibilities of research to bring more data to support the work presented in chapter 3.

1.3. Ability of AAA to model Elekta linacs

As mentioned in chapter 3, the configuration of the AAA algorithm depends on the physical properties of the linac (flattening filter material…). Since AAA was designed by Varian, there was a clear interest to evaluate the capability of AAA to model a linac from another company.

In chapter 3, AAA was configured only for a 6 MV beam collimated with jaws and MLC (open fields). The algorithm was not tested for wedged beams or other energies. Cozzi *et al* (2008) performed a more systematic study of AAA for Elekta linacs and concluded that AAA is appropriate for Elekta linacs as well.

2. Specific issues of the MC modeling (TomoPen) of the tomotherapy treatment unit

2.1. Impact of simplifications in the simulation on accuracy

The modeling of HT was a big challenge. First, HT has never been modeled with all the details of the machine released by the manufacturer, as it is the case in the present thesis. It thus required a new approach because of its unique design. Fortunately, the flexibility of the geometry construction package of PENELOPE allowed for modeling the various parts of the treatment head of HT without having to program new component modules as it would have been the case with BEAMnrc.

Moreover, the speed of the simulation was an important aspect since the main objective was to finally implement TomoPen into the system of the TPS of Tomotherapy Inc. for clinical routine.

Speed improvements may be achieved through conservative approaches using variance reduction techniques, but only for limited improvements. When speed becomes critical, the physics of the transport needs to be simplified to obtain large gains in speed.

Of course, one can argue that the main objective of a MC simulation is to be as accurate as possible to maximize the added-value of MC compared to analytical C/S based algorithms. Therefore, a minimum of approximations in the physics should be accepted since the potential advantage of MC is lost when beam modeling is not optimal (Reynaert *et al* 2005, Chetty *et al* 2005).

However, the objective of a MC model is to provide more accurate results from a clinical point of view. Losses in accuracy which have no clinical impact may be accepted. From this important consideration, the idea of the TF method, which is *a priori* a strong approximation compared to MC, was justified in the beginning of the project.

Because of the simplicity of the TF method, it was expected that some compromises regarding accuracy would have been necessary. Surprisingly, the architecture of the HT machine allows for the approximations explained in chapters 5 and 6 without *any* significant loss of accuracy, even for phenomenon like electron contamination or scattering from the MLC which are completely neglected in the TF method. In classic linac configurations, such an agreement could probably not have been achieved because of the presence of contaminating elements (like a flattening filter, for instance) and a general configuration with shielding items less designed for IMRT.

Therefore, in TomoPen, the beam modeling may be considered as accurate as a pure MC approach. This does not mean that potential problems regarding accuracy do not remain in TomoPen. One major issue is the transcription of the actually given treatment to a comprehensible input for TomoPen. TomoPen uses the sinogram and not the exact position of each leaf with time as in other MC models of conventional linacs, which may cause deviations from reality. Those deviations are small (Kapatoes *et al* 2001) and are taken into account in the sinogram in an approximate way. But it may be interesting to quantify from MC simulations the difference between a “perfect” modeling of the exact dynamics of the MLC and a simulation only based on the sinogram. Such a model is of course very complex, because it must account for the delay between the signal of aperture or closure and the effective corresponding movement of the leaf as well as their finite speed. Moreover, the TF method is not

applicable "as such" in this approach (the TF method inherently assumes a perfect binary MLC). Finally, the clinical interest of introducing so many details is not obvious since a good agreement between C/S, which is also sinogram based, and measurements is already observed on our HT system for QA procedures in homogeneous phantoms (Tondeur *et al* 2006). It is worth mentioning that other potential problems may originate from slight variations in the machine performance along the treatment (variation of output or response of the leaves with gantry angle …)

As a conclusion to this section, we emphasize once again on the fact that concerns regarding accuracy in TomoPen are not mainly due to the various approximations in the transport of photons through the MLC, but more from the difficulty, inherent to the design of the machine, to have a simple but perfectly detailed description of beam delivery. Moreover, those effects are potential very minor regarding the accuracy of our model. It may also be mentioned that the very good collaboration with the designers of the HT system led to a very well controlled MC model from the treatment head modeling to patient dose calculations, which is not always the case when modeling classic systems where information can be sparse. This may perhaps explain the very good agreement obtained between TomoPen, measurements and C/S for static fields, QA procedures or clinical cases in homogeneous media in the various papers presented in chapters 4-7.

2.2. Dose calibration procedure

The dose calibration protocol described in section 2.6.5 in the TomoPen paper is somewhat unusual compared to other MC simulations. As illustrated in Figure 8. 2, classic MC models are calibrated in dose by converting the MC units (Gy/primary particle) into the more practical Gy/MUs (where MUs are the monitor units) according to the definition of the MUs[7].

In this thesis, TomoPen was calibrated from a specific IMRT procedure. However, it is possible to calibrate TomoPen following the definition of the MUs in the static mode in a conventional approach. Following this process, the dose calibration factor is very close (within 0.5%) to the one obtained from the protocol described in Sterpin *et al* (2008b). Now, the question is why we choose an IMRT plan to calibrate the model. Classic linear accelerators ususally have a very stable behavior, and beam parameters influencing output are normally kept untouched. Tomotherapy is

[7] For the Elekta machine in Saint-Luc, 1 MU corresponds to a dose of 1cGy for a 10x10 cm² field at a source-surface distance of 100 cm and at the depth of maximum dose.

less stable and output needs to be checked and adjusted frequently. One of the reasons is the relatively quick deterioration of the target (the target is replaced approximately every 6 months) which sligthly modifies the dosimetric properties of the machine (Jeraj *et al* 2004). The consistence of the treatment delivered by the machine is verified through two main tests. First, the output of the machine is verified by measuring the dose in the static mode. Second, an additional check is performed by comparing the calculated (with the C/S algorithm of the TPS) and measured dose for one IMRT procedure (the same as the one chosen for the dose calibration of TomoPen). If the machine does not pass this second test, then it is not authorized to treat. In this logic, the calculated plan becomes the reference (the "Tomo reference plan") and not measurements. This observation leads to the conclusion that it may be better that TomoPen matches the reference results delivered by the TPS, since the latter will anyway be used as a reference and compared to measurements on a regular QA basis.

3. Introducing TomoPen into clinical practice

Each step of the development of TomoPen was thought for a future implementation in clinical routine. The mechanics of the simulation in TomoPen are very simple and universal for all HT machines. However, some adaptations of the model might be needed to optimize calculation time or to account for the differences from one tomotherapy treatment unit to another.

3.1. Considerations on speed

TomoPen is able to calculate a bilateral head and neck plan on a single processor (2.5 GHz Intel Centrino Duo) in around 6 hours with a very good statistic (dose profiles are very smooth with statistical variations of less than 1 % (1SD)). The calculation time scales with the volume treated but not the complexity (for instance, a low value of the pitch). If TomoPen is implemented in the cluster delivered with each tomotherapy system, then 32 processors are available which might reduce the calculation time to less than 10 minutes per plan. Of course, the user can reduce substantially the calculation time by reducing the number of particles simulated.

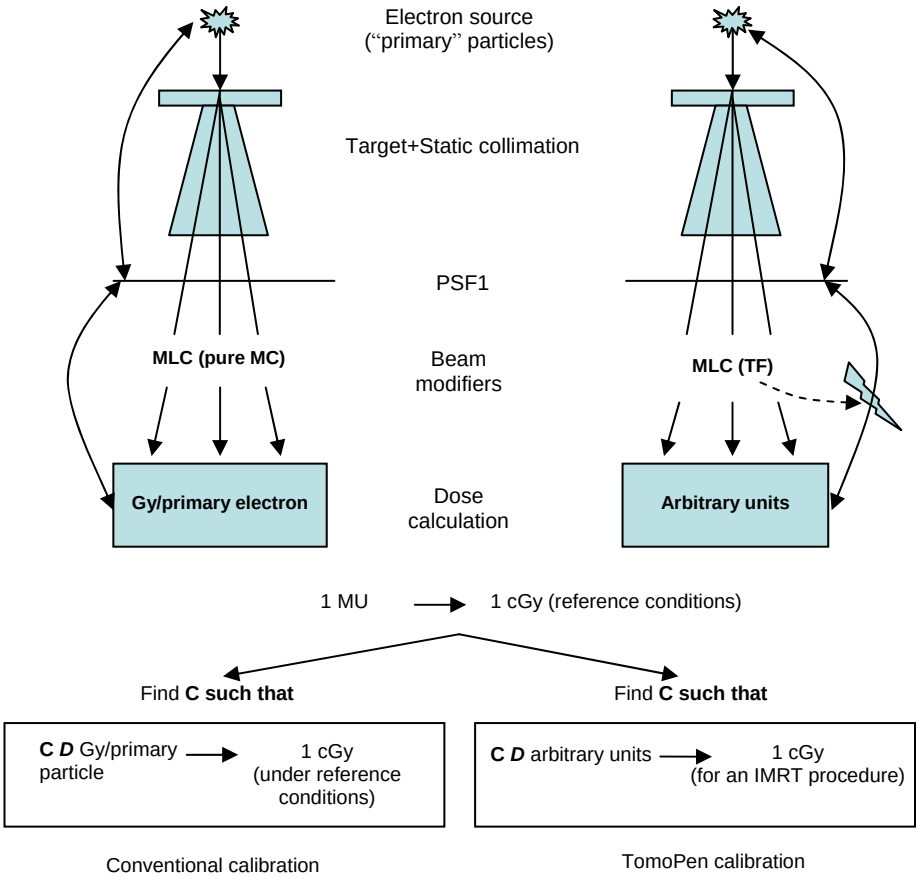


Figure 8. 2. Comparison of the dose calibration process of a MC dose calculator in the classic and pure MC approach (left) and TomoPen (right). The action of the TF on the first PSF destroys the link between the dose deposited and the number of primary electrons simulated. The factor C must be determined once to convert the results obtained with the MC codes (*D* in the figure) in cGy. By definition, C equals 1/*D* in reference conditions.

With experience gained from additional studies over a large number of patients, some guidelines could be defined to choose an optimum number of particles to simulate and find an optimum simulation time. Another possibility is to follow the approach of Vanderstraeten *et al* (2007), but this requires simulating the sinogram of the treatment randomly instead of sequentially, as it is now the case[8]. Finally,

[8] In TomoPen, the beam simulated following the sequence defined by the sinogram, projection after projection. To implement an uncertainty-based stopping criteria, the sinogram should be randomly sampled.

denoising techniques could be applied and reduce the calculation time by a factor of ten, but this may have an impact on accuracy (Naqa *et al* 2005, De Smedt *et al* 2006, Fippel and Nüsslin 2002, Deasy *et al* 2002, Jiang *et al* 2000, Sempau and Bielajew 2000, Miao *et al* 2003).

Those considerations may lead to a computation time which may vary from much less than a minute to 10 minutes. This is fast enough for TomoPen to be used for final dose calculation as well as during inverse treatment planning. Many authors already studied the importance of using an accurate dose calculation algorithm during IMRT optimization (Jeraj *et al* 2002, Jeraj and Keall 1999 and 2000, Bogner *et* al 1999, Laub *et al* 2000). If TomoPen is introduced in the optimization process, inaccuracies of the C/S algorithms may be corrected online, which is not possible if TomoPen is used as a final dose calculator tool. Indeed, in this scenario, TomoPen will only check the validity of the C/S plan but it will be impossible or very difficult for the user to use the information to correct the plan as he desires. Of course, the choice of using TomoPen during optimization depends on the needs of Tomotherapy Inc and its customers.

3.2. Tuning of TomoPen for other tomotherapy treatment units

In this thesis, TomoPen was calibrated to match the "gold standard" (GS) (see chapter 4). Only a few modifications were necessary also to match our machine in Saint-Luc (the longitudinal field widths, actually). Except for the dose calibration factor, the helical mode does not involve any tuning of the MC model. Therefore, TomoPen needs to be tuned for the static mode only. Since all tomotherapy units have very similar dosimetric properties when they are released by Tomotherapy Inc. (the matching criteria for a gold standard machine is defined in Sterpin *et al* 2007b), TomoPen could be implemented and tuned in almost all the worldwide tomotherapy treatment units with a minimum of configuration steps. In a first approximation, almost no tuning should be necessary, since differences between two machines are of order of the matching criteria used to match TomoPen and the gold standard as well as our machine in Saint-Luc. The parameters that should be tuned in priority for each machine are given here below:

- Dose calibration factor: always should be recomputed.
- Longitudinal profiles widths: only if the profiles widths are not within 1% of FWHM (acceptance criteria for a GS machine (chapter 4 and 6)).

If the longitudinal field width does not perfectly match the gold standard, no significant deviations should be introduced by keeping the phase-space files of the gold standard machine and adjusting the field width in the input file of TomoPen. The induced modification of the dose calibration factor will then account for most of the deviation (see paragraph 2.6.5 of chapter 7). Of course, it is more elegant to perfectly match calculated and measured FWHMs, but the phase-space files then needs to be recomputed. If the machine does not match the gold standard for transverse profiles and depth dose curves, then other parameters must be tuned:

- Energy.
- Electron source spot size.
- MLC geometry (global tilt or rotation).
- Head geometry (very unlikely).

When tuning those values, maximum caution is required since any error in those values will result in systematic differences in the calculated dose distributions for the clinical cases. The various test and experiments described in Sterpin *et al* 2007b and in the TomoPen paper may be used as guidelines for the tuning of a particular machine.

4. Additional applications of TomoPen

Besides its final dose calculator functionality, TomoPen could be used for other applications. From those discussed in literature and conferences as well as our personal experience, we highlight five of them we believe are important. These are summarized hereafter and will be developed in the following subsections:

1. When analyzing some specific treatments, TomoPen can provide accurate dose distributions for cases where C/S computations are not reliable and accurate measurements difficult. This was performed during the thesis in a more global study where the ability of the TPS of tomotherapy to spare the skin in head and neck treatment was quantified

(Delor *et al* 2008). A good quantification requires accurate dose distributions, and, therefore, TomoPen may bring important information.

2. Because of its flexibility, TomoPen could easily be adapted for new mechanics of treatment delivery with the tomotherapy machine. The most known technique is "Topotherapy", where gantry is kept static whereas the leaves and the couch are moving simultaneously.

3. MC is often proposed as a commissioning and verification tool of TPS, especially for routine verification of IMRT treatments (Leal *et al* 2003, Spezi *et al* 2004, Reynaert *et al* 2004 and Seco *et al* 2005). In the TomoPen paper, the potential of TomoPen for verification was illustrated in section 3.4. However, the choice of using MC for QA instead of measurements is not a trivial step and requires a deep understanding of the risks. Finally, TomoPen is so flexible than one can imagine using it for other applications for QA.

4. Performing measurements of dose distributions obtained with IMRT fields is a complex task (Bouchard and Seuntjens 2003). Moreover, the fact that HT is unable to deliver reference fields without modulation brings one additional difficulty. Since accurate MC models are often required to calculate correction factors for measurements in IMRT fields, TomoPen is an obvious candidate.

5. Since MC computation time does not scale with treatment complexity (Reynaert *et al* 2007), TomoPen has a high potential to be used for 4D treatment planning (see chapter 1, section 1.3), where dose distributions have to be averaged on several sets of CT images corresponding to organ movement during irradiation (intra-fraction motion) or between fractions (inter-fraction motion).

4.1. TomoPen for evalutating skin sparing capabilities of the tomotherapy system

Delor *et al* (2008) performed a phantom study where the optimizer of the TPS of tomotherapy was forced to spare the skin. The objective was to simulate a situation commonly encountered in treatments of the head and neck region. This was done by

delineating an OAR (3mm thick) between the PTV and the interface between the Cheese phantom and the surrounding air, as illustrated in Figure 8. 3. By adding dose-constraints on this OAR during optimization, the dose to the OAR (which models the "skin") could be reduced compared to the plan without optimization on the OAR. The objective of the work was to quantifiy this reduction with the dose distributions delivered by the TPS, *i.e.* the C/S algorithm. However, the accuracy of C/S is not guaranteed so close to an air-water interface. Therefore, the dose distributions calculated with C/S and TomoPen were compared to have a reliable estimation of the dose reduction to the skin at points difficultly accessible to measurements. As illustrated in Figure 8. 4, the dose reduction can reach 10 Gy, which is confirmed by TomoPen. Figure 8. 4 shows that C/S and TomoPen provide apparently similar results. To quantify possible differences between TomoPen and C/S, dose points were compared in Table 8. 1 along a line drawn from the edge of the phantom, horizontally through the center of the phantom, as shown in Figure 8. 3. Except for the first pixel, results are comparable.

Measurements were also performed in this study using MOSFET (Metal Oxide Semiconductor Field Effect Transistor) and EBT Gafchromic detectors. The measurements confirmed the dose reduction to the skin predicted by the C/S algorithm. Therefore, the main conclusion of the work of Delor *et al* was that optimization can actually be performed with the skin as an OAR with a significant reduction of the dose to the skin and with good confidence on the results delivered by the C/S algorithm.

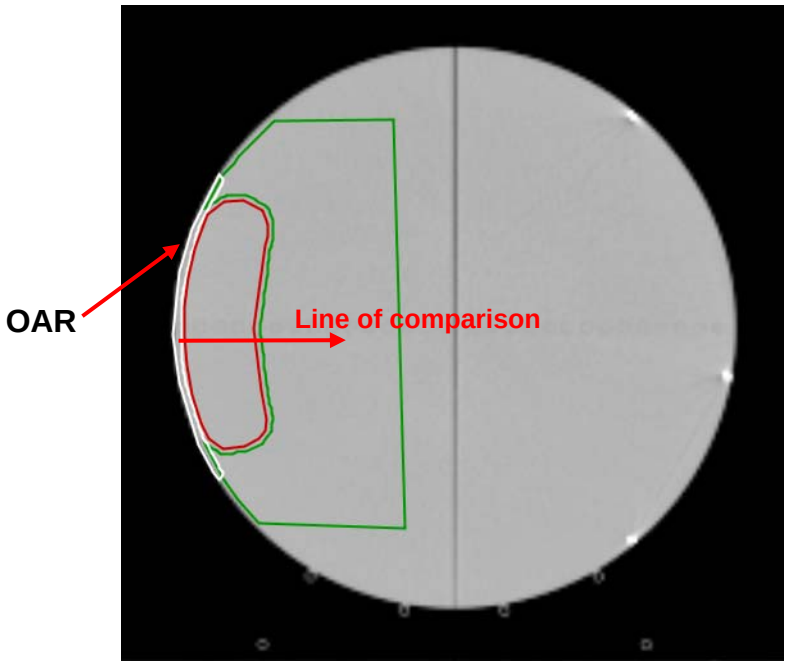


Figure 8. 3. Definition of the target volume (PTV in red) and the OAR ("skin" in white) for the optimization in the study Delor *et al* (2008)

Pixel number from the edge of the phantom	C/S (Gy)	TomoPen (Gy)	Difference C/S-TomoPen (Gy, %)
1	19.5	24.2	-4.5 (-23.8)
2	40.0	38.7	1.4 (2.5)
3	47.2	49.0	-1.8 (-3.8)
4	52.5	51.8	0.7 (1.3)
5	50.8	50.5	0.3 (0.6)
6	51.0	50.8	0.2 (0.3)

Table 8. 1. Dose differences between C/S and TomoPen for the pixels along the line drawn in Figure 8. 3.

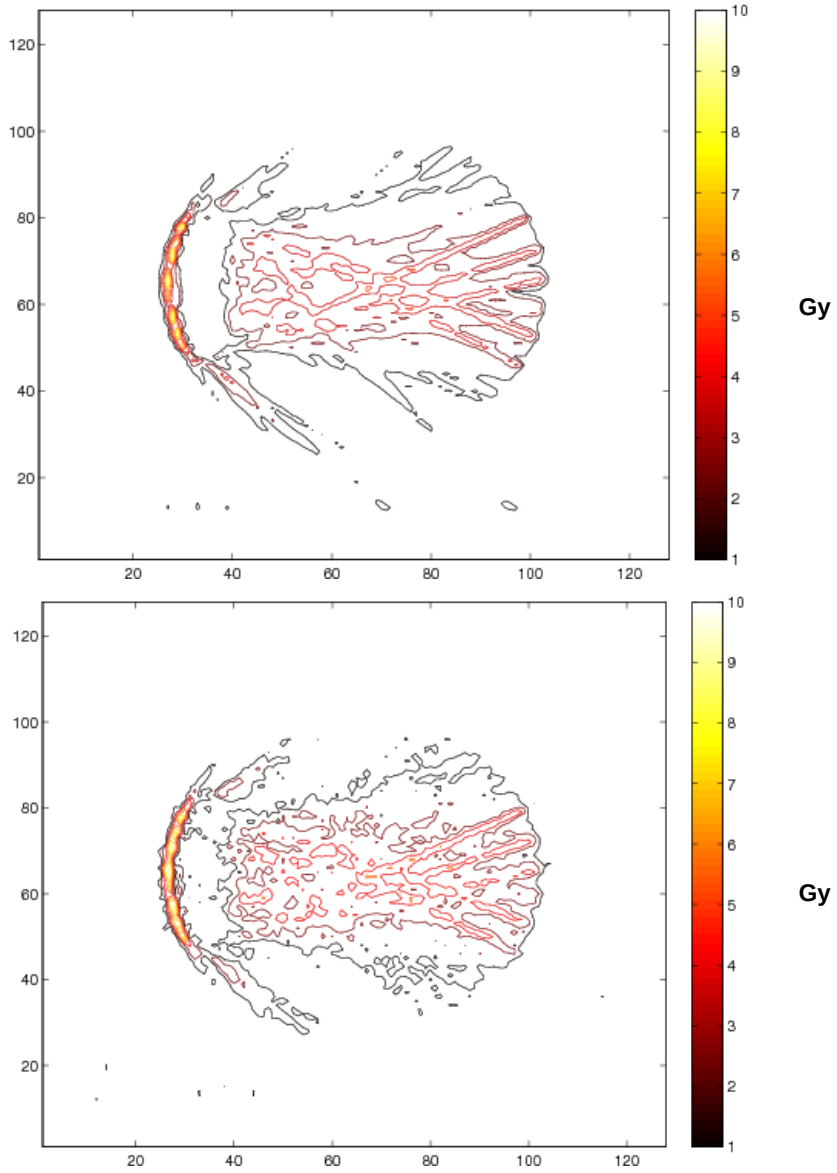


Figure 8. 4. Dose maps of the differences between the dose distributions calculated without optimization on the OAR and with optimization. The top and the bottom figures correspond to dose distributions calculated with C/S and TomoPen, respectively. Differences are given in Gy (the prescribed dose is 50 Gy). The *x*- and *y*- axis corresponds to pixel number in the transverse and vertical directions, respectively

4.2. TomoPen for Topotherapy

In tomotherapy treatment deliveries, high conformal dose distributions are achieved by the means of the simultaneous movement of the treatment couch, the MLC and the gantry. However, for some tumor localizations, like breast tumor or some palliative treatments, the use of many gantry angles will not impact treatment quality. For those cases, Tomotherapy Inc. developed a new technique where the gantry takes a few static positions, for instance two for treatment of the breast with tangential treatments, whereas the MLC and the treatment couch are still in movement (Gonzalez *et* al 2005, Olivera *et al* 2005, Lu *et al* 2007). Since breast treatments may be problematic with respect to dose calculation accuracy because of the presence of lung tissue, there could be a strong interest to adapt TomoPen for topotherapy, especially if it becomes the first choice for such treatments.

As illustrated in Figure 8. 5, the two techniques differ essentially in the shape of the sinogram and in that the gantry angle does not have to be modified for each projection (which is the case in TomoPen).

The MC modeling of topotherapy should be possible with minor modifications of the code. In its present configuration, the simulation routines are controlled through a main program which calculates the coordinates of each projection. By modifying a few lines of this main program, one can force the gantry to remain static which would allow for TomoPen to simulate a topotherapy treatment. Another possibility is to take advantage of the generality of the inner code (which transports the particles through the MLC and computes the dose in the CT structure). The coordinates could be defined directly in the input file for each projection along with the time aperture of the leaves, and not calculated in the main program. In that case, the code could simulate either tomotherapy or topotherapy treatments.

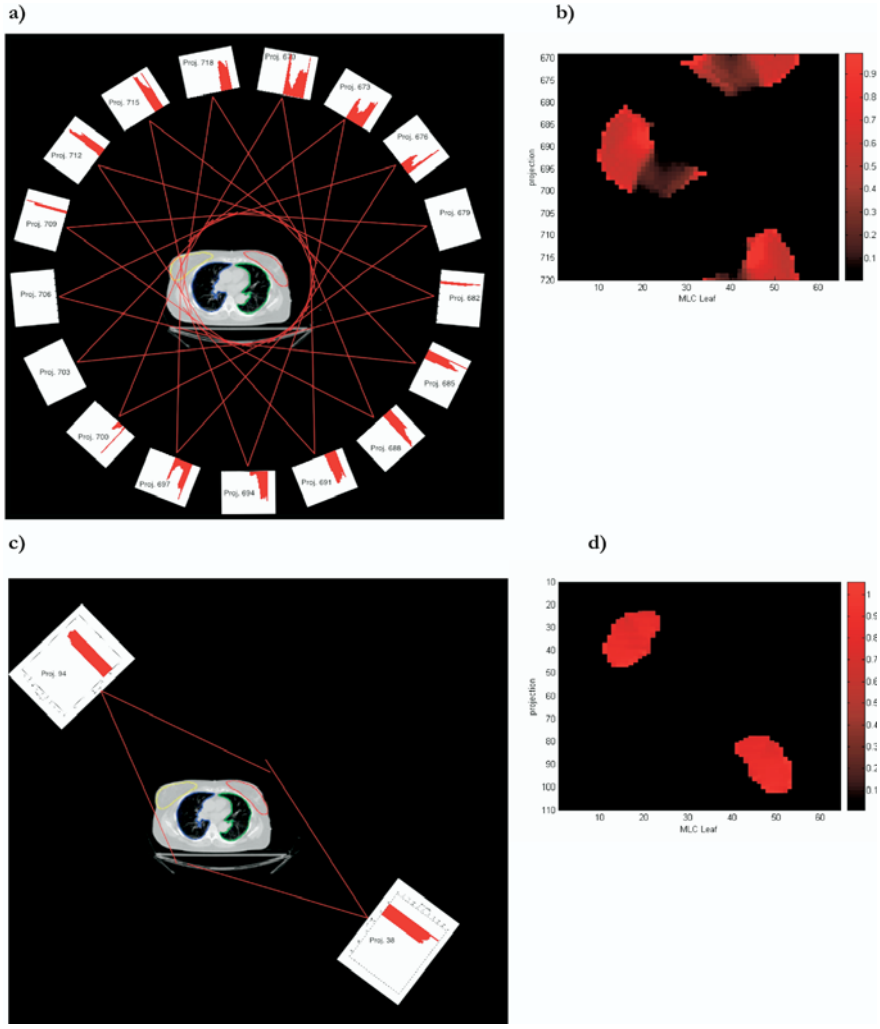


Figure 8. 5. Comparison of tomotherapy (a) and topotherapy (c) treatments deliveries. The corresponding sinograms are represented in (b) and (d), respectively. The sinogram represents the fraction of projection each leaf remains open for each projection. The main difference in the sinograms is that for tomotherapy, at each projection corresponds a different position of the gantry, which is not the case in topotherapy (figure from Gonzalez *et al* (2005)).

4.3. TomoPen as a QA tool

TomoPen could be implemented in the QA system of tomotherapy. As described by Thomas *et al* (2005a), the current system allows to calculate the

treatment plan of a given patient in a homogeneous cylindrical phantom (the "cheese" phantom, see also chapter 6) and to compare the calculation with point and film measurements. This procedure is known as the delivery quality assurance procedure (DQA). Acquiring the measurements takes, of course, more time and work than performing a MC simulation, and a full 3D verification is impossible with only a few ion chambers and films. TomoPen allows for a 3D verification and a significant reduction of work. However, TomoPen only checks dose calculation and the mechanics of the treatment assuming that the machine has a perfectly predictable behavior, which is not the case in reality. Only measurements can detect machine variations and/or unexpected response of the machine to the procedures delivered by the TPS. Therefore, the choice of using TomoPen or not as a QA tool is difficult and each medical/physicist staff should be very cautious before modifying their QA program and reducing the number of measurements.

It is relatively easy to find other applications, perhaps less obvious, for QA. The current HT systems need more maintenance than conventional treatment units. Changes in pieces of equipment having a direct influence on beam delivery occur relatively frequently. For instance, the target, the acceleration section of the linac or the MLC are often replaced. Besides the QA measurements listed in the program of Tomotherapy to check the consistency of the machine with time after the modifications, TomoPen could be used for some other specific tests, like the MLC alignment or the jaw and target positioning. It is also possible to simulate and isolate various effects, like target displacement or target burning, and quantify them on static and helical dose distributions, which is more difficult with measurements due to the inherent uncertainty of the measurement.

4.4. TomoPen for dosimetry

As for all radiotherapy machines, the delivered beam of HT must be calibrated in terms of absorbed dose to water. This is usually performed using an ion chamber calibrated in reference conditions according to well-known dose calibration protocols (AAPM TG-51, IAEA TRS-398), *i.e.* a 10 cm x 10 cm field at 100 cm SDD and a 10 cm depth in water. Since the Hi-Art^{TM} system only provides IMRT or non-homogeneous static fields (due to the absence of a flattening filter), it is impossible with HT to establish the reference field without involving beam modulation which complicates and compromises the accuracy of the measurements (Bouchard and Seuntjens 2003, Schulz and Kagan 2002, Dong *et al* 2003, Sanchez-Doblado *et al* 2003). Therefore, the reference beam used to calibrate the ion chamber is delivered by

a classic linac (Varian, Elekta …). Using this reference ion chamber, HT is then calibrated using the 40x5 cm² field. The main drawback of this method is, of course, that the conditions for calibrating HT (inhomogeneous field) are relatively far from the reference conditions for calibrating the ion chamber.

Several authors already devised dose calibration protocols for tomotherapy accounting for some specificities of the machine in the static mode (Jeraj *et al* 2005, Thomas *et al* 2005b). Dose calibration protocols often involve Monte Carlo simulations to derive accurate correction factors for ion chambers which require accurate modeling of the simulated geometry. However, in Jeraj *et al* (2005), the MC model is based on the HT prototype instead of the clinical Hi-Art^{TM} whereas in Thomas *et al* (2005b), the MC model is not based on detailed technical drawings. Moreover, TomoPen is able to simulate accurately helical delivery.

There is, therefore, a clear interest to use TomoPen to derive correction factors specific to HT for beam configurations more representative of the clinical reality. Actually, TomoPen was already used in the static mode to derive ion recombination (p_{ion} or k_{sat} depending on the formalism) correction factors for ion chamber dosimetry (paper in preparation by Palmans *et al* 2008). Ion chamber recombination correction factors are needed in ion chamber dosimetry because the charge produced in an ion chamber differ from the charge that is actually collected (IAEA 2005) due to the loss of ions that recombine or due to charge multiplication. The difference between charges produced and charges collected depends on the voltage applied to the ion chamber. Precise knowledge of the dose distribution within ion chamber cavities may provide important information and can be accurately computed with MC, which was one of the contributions of our group to the study Palmans *et al* (2008).

The MC simulation consisted in modeling a cylindrical ion chamber NE-2571 in a cylindrical water phantom, with dimensions displayed in Figure 8. 6. Dose distributions in the cavity were computed for several off-sets (0, 0.6, 0.9 and 1.2 cm) of the air-cavity with respect to the photon source and are shown in Figure 8. 7. For the simulation with no off-set, the center of the cavity is of course at the isocenter of the machine. It is assumed that the initial charge produced in the cavity is proportional the local dose computed with the simulation, which is necessary to calculate p_{ion}. From the dose distributions obtained with the various off-sets, it can be observed in Figure 8. 7 that the dose is enhanced close to the cavity edge for 9 mm and 12 mm off-sets. This phenomenon is due to the scatter coming from outside the cavity and may influence slightly volume recombination and, hence, p_{ion}.

We do not provide here detailed results and discussion since the paper is still in preparation and the subject is beyond the scope of this thesis. However, this study

provides a good example of how an accurate MC model can be used besides treatment planning purposes.

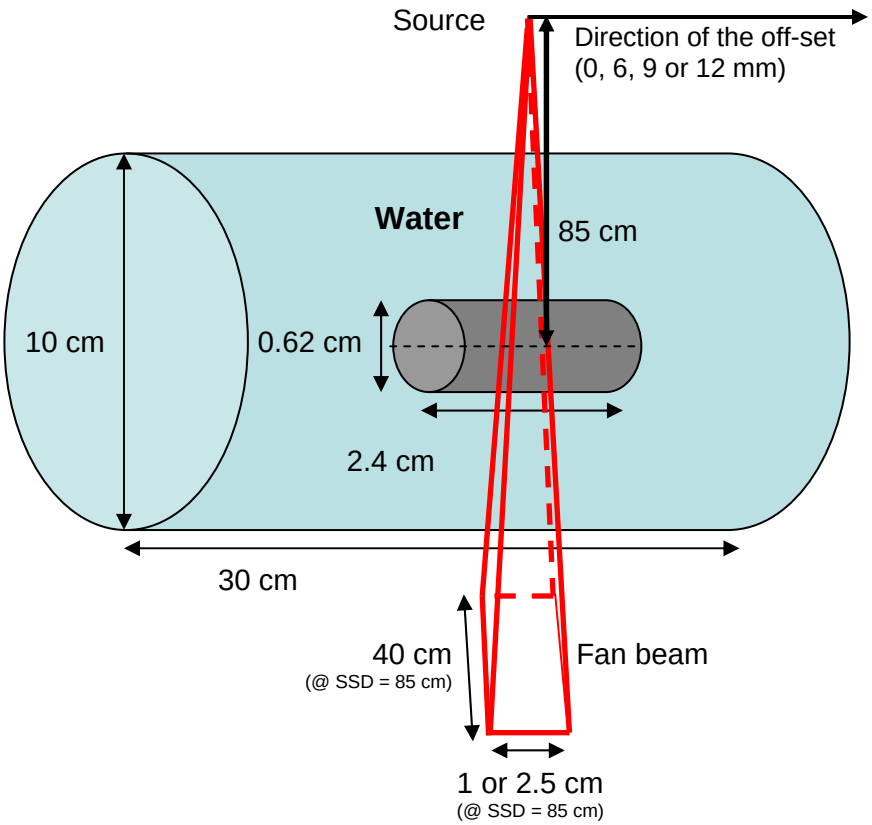


Figure 8. 6. Description of the geometry of the MC simulation performed to compute p_{ion} ion recombination correction factor. The cylindrical cavity is centered in a cylindrical water phantom and placed at SSD=85 cm. The dimensions of the air-cavity (in grey) simulated correspond approximately to the ones of the ion chamber NE-2571. The simulated beams are the 40x5 and 40x2.5 cm² field.

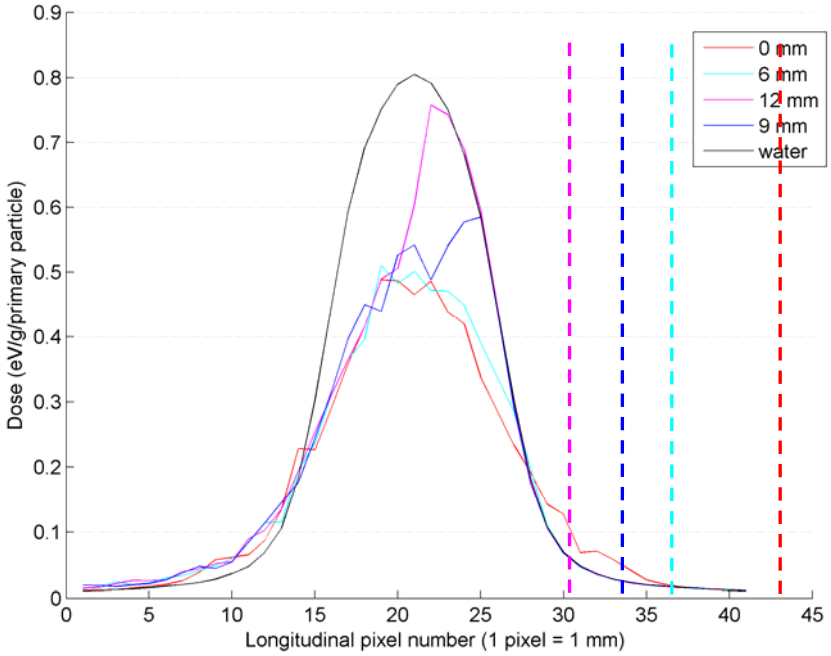


Figure 8. 7. Dose profiles obtained within the air-cavity for various values of the off-set and the field 40x1 cm². The "water" profile corresponds to the same experiment but with air-cavity filled with water. The dashed-line displays one of the edges of the cavity for each off-set. The colors of the dashed-line are consistent with the colors of the profiles.

4.5. TomoPen for 4D treatment planning

4.5.1. TomoPen for intra-fraction motion

To account for intra-fraction motion during irradiation, several patient CT data sets must be acquired throughout the entire breathing cycle. From those images, the physician may decide during which part of the breathing cycle the treatment should be delivered, as illustrated in Figure 8. 8 (gated radiotherapy). Treatment may also be delivered in such a way that tumor movement is tracked during the complete breathing cycle (real-time target tracking).

In either technique, dose distributions need to be computed on several CT data sets. To evaluate the average dose distribution received by the patient, dose distributions on the CT data sets have to be summed in an appropriate way. Techniques to incorporate organ motion into dose calculation were already proposed

(Ding *et al* 2003, Keall *et al* 2004) and including for tomotherapy (Lu *et al* 2006) but these are out of the scope of this thesis. However, it is interesting to note that, whereas analytical algorithms need to perform a full calculation on each CT data set, computation time for MC will only depend on the desired statistical uncertainty on the final averaged dose distribution. In other words, MC calculation time does not scale with the number of CT data sets whereas analytical algorithms do.

Moreover, TomoPen is very flexible since almost every movement of the leaves may be simulated by only modifying the sinogram and the CT images, which are independent of the code of TomoPen. Therefore, if tumor tracking or gating is performed by adapting dynamically the sinogram and the CT data set according to breathing cycle, TomoPen will be able to compute dose without any adaptations of the code and probably at a faster rate than the C/S algorithm.

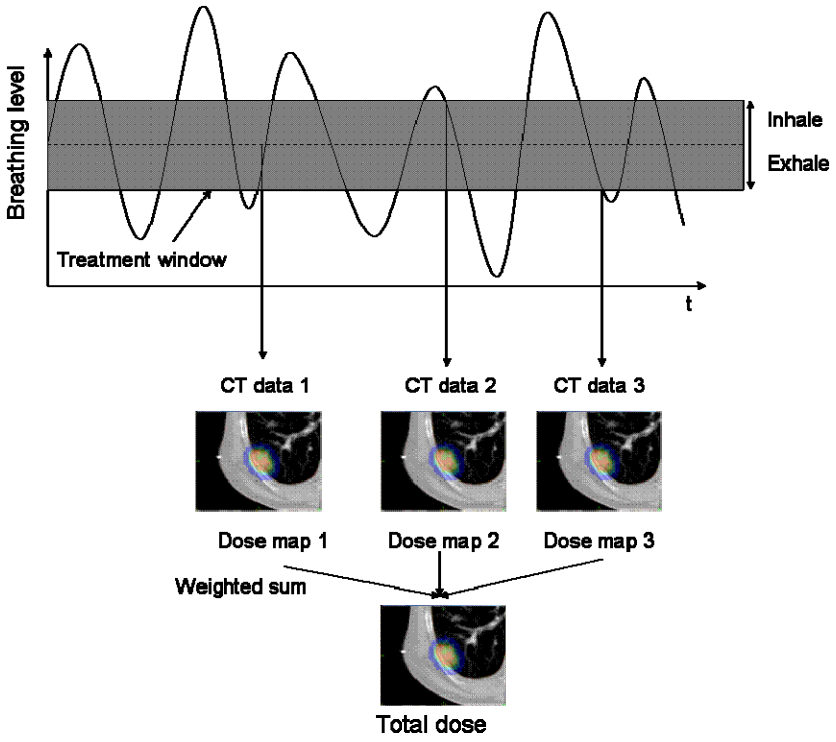


Figure 8. 8. Illustration of the total dose reconstruction in 4D treatment delivered during a defined interval of the breathing cycle (gated radiotherapy). In real-time target tracking, the treatment window can be extended over the complete breathing cycle.

4.5.2. TomoPen for inter-fraction motion

An important feature of HT is its ability to acquire MVCT images at the position of treatment. In a similar way as for intra-fraction motion, dose could be computed with TomoPen for several MVCT data sets acquired at several stages of the treatment. The different dose maps may then be averaged and DVHs computed to estimate the dose actually received by the patient, with the modifications of its anatomy during treatment precisely accounted for (Lee *et al* 2008). Treatment accounting for such anatomy modifications is often called "adaptive" radiotherapy. The advantages of using TomoPen are similar to the ones depicted in the previous sections: simplicity of use and speed. Moreover, TomoPen could easily calculate dose distributions simulating actual machine parameters, recorded on the machine the day of the treatment using the detectors mounted on the gantry ring or any other on-line measuring device. Again, this is possible because of the large freedom given to the user to simulate various situations through the input files of TomoPen.

5. Added-value of MC

Evaluating the added-value of MC is a complex task. Even though several commercial systems including MC algorithms already exist, some discussion is still needed about the relevance of introducing MC into clinic. The best approach to close the debate is to perform a retrospective study where the differences observed in treatment planning between MC and the analytical algorithms are correlated with the clinical outcome of the patients. Tumor recurrence or side effects could be linked to local differences in the dose distributions. Of course, such a study is very complicated and has not yet been realized. Moreover, this approach is almost impossible for the relatively recent techniques and dose calculation algorithms used throughout this thesis.

In this study, a methodology was used, more conventionally, to compare analytical algorithms with MC for various localizations, and evaluate differences for parameters with a clinical outcome *a priori*. It is worth insisting on the fact that comparison between MC and analytical algorithms must be performed with the most modern analytical algorithms available (collapsed-cone C/S or AAA). Therefore, algorithms based on broad beam data or pencil beam should be completely disregarded when evaluating the added-value of MC. There is no doubt that MC is superior to pencil-beam algorithms but there is also no doubt that collapsed-cone algorithms or AAA (also a pencil-beam algorithm, but much more sophisticated) are also superior to

those algorithms (Reynaert *et al* 2007, Fogliatta *et al* 2007, Knöös *et al* 2006, Vanderstraeten *et al* 2007, Carrasco *et al* 2004, Jones and Das 2005). Then, using the data from comparison between MC and older algorithms is completely irrelevant and should be avoided. The scope of the discussion will therefore be restricted to the comparison between MC and advanced algorithms (AAA or collapsed-cone C/S).

The added-value of MC compared to advanced algorithms in phantoms experiments is relatively clear regarding the literature and the results presented in chapters 3 and 7, especially in cases of severe lateral electronic disequilibrium. However, it is difficult to extrapolate the observations in phantoms to clinical cases. Generally, clinical comparisons do not lead, *on average*, to important deviations (higher than 5%) (Madani *et al* 2007, Vanderstraeten *et al* 2007). However, some authors (Vanderstraeten *et al* 2007) concluded in their work that even though C/S and MC were in agreement on average, there are some cases where C/S failed to provide accurate dose distributions and could be attributed to the presence of the inhomogeneities. A strong argument then arises: if one can show a significant deviation from reality for C/S-based algorithms for a few cases, then the added-value of MC is proven. We agree with this opinion, but showing smaller differences may also be enough to assess the added-value of MC since one of the final objectives of MC is to reduce dose calculation uncertainty to less than 2% to meet a global uncertainty requirement of less than 3% as stated in chapter one (section 2). In this approach, deviations of order of 1-2% become important.

The clinical cases shown in this paper may contribute significantly to the debate. In chapter 3 (AAA), differences could be observed in the small lung tumor case. Part of the deviations was attributed to beam modeling while inhomogeneities also played a significant role. In chapter 7 (C/S) paper demonstrated that the presence of low density inhomogeneities does influence the accuracy of the results delivered by the tomotherapy algorithm even though no “dramatic” differences could be observed (differences were all within 5%). However, in those cases, C/S seems to systematically overestimate PTV coverage, which may have a clinical outcome and influence on the decision made by a physician or a physicist during treatment planning.

From the observations made on those clinical examples, it is difficult to determine definitively whether MC should be introduced as soon as possible into clinical routine. However, the differences shown for the cases demonstrated the potential of MC and the fact that it will be difficult to reduce the overall uncertainty on the delivered dose below 3% without MC-based TPS, especially in extreme cases.

To conclude, the magnitude of the differences observed in this study indicate that no revolution should be expected from introducing MC into clinical practice, as already claimed by Ahnesjö and Aspradakis (1999). However, the observations and

tools developed during the thesis may be used to outline some propositions in *favor* of introducing MC in clinical practice:

- Overall improved accuracy, more specifically for complex treatments when low density inhomogeneities are present.
- Increased confidence of the medical and physicist staffs in the results delivered due to the proximity of the model to the physical reality.
- Complementary QA tool.
- Accurate information in cases or studies where measurements are difficult or unfeasible.

6. References

Ahnesjö A and Aspradakis M M 1999 Dose calculations for external photon beams in radiotherapy *Phys. Med. Biol.* **44** R99-155

Almond P R, Biggs P J, Coursey B M, Hanson W F, Huq M S, Nath R and Rogers D W O 1999 AAPM's TG-51 protocol for clinical reference dosimetry of high-energy photon and electron beams *Med. Phys.* **26** 1847-70

Andreo P, Burns D T , Hohlfeld K, Huq M S, Kanai T, Laitano F, Smyth V G and Vynckier S 2000 Abssorbed dose determination in external radiotherapy: An international code of practice for dosimetry based on standards of absorbed dose to water *Report No. 398*

Bogner L, Scherer J and Herbst M 1999 An inverse Monte Carlo optimization algorithm for conformal radiotherapy Phys. Medica 111-19

Bouchard H and Seuntjens J 2004 Ionization chamber-based reference dosimetry of intensity modulated radiation beams *Med. Phys.* **31** 2454-65

Bragg C M, Wingate K and Conway J 2008 Clinical implications of the anisotropic analytical algorithm for IMRT treatment planning and verification *Radiother. Oncol.* **86** 276-84

Carrasco P, Jornet N, Duch M A, Weber L, Ginjaume M, Eudaldo T, Jurado, D, Ruiz A and Ribas M 2004 Comparison of dose calculation algorithms in phantoms with lung equivalent heterogeneities under conditions of lateral electronic disequilibrium *Med. Phys.* **31** 2899-911

Chetty I J, Rosu M, McShan D L, Fraass B A and Ten Haken R K 2005 The influence of beam model differences in the comparison of dose caluculation algoirhtms for lung cancer treatment planning *Phys. Med. Biol.* **50** 802-15

Chetty I J, Curran B, Cygler J E, DeMarco J J, Ezzell G, Faddegon B A, Kawrakow I, Keall P J, Liu H, Ma C M, Rogers D W O, Seuntjens J, Sheikh-Bagheri D and Siebers J V 2007 Report of the AAPM Task Group No. 105: Issues associated with clinical implementation of Monte Carlo-based photon and electron external beam treatment planning *Med. Phys.* **34** 4818-53

Cozzi L, Nicolini G, Vanetti E, Clivio A, Glashorster M, Schiefer H and Fogliata A 2008 Basic dosimetric verification in water of the anisotropic analytical algorithm for Varian, Elekta and Siemens linacs *Phys. Med. Biol.* **18** 128-35

Dong L, Antolak J, Salehpour M, Forster K, O'Neill L, Kendall R and Rosen I 2003 Patient-specific point dose measurement for IMRT monitor unit verification *Int. J. Radiat. Oncol. Biol. Phys.* **56** 867-77

Deasy J O, Wickerhauser V M and Picard M 2002 Accelerating Monte Carlo simulations of radiation therapy dose distributions using wavelet threshold de-noising *Med. Phys.* **29** 2366-73

Delor A, Denis J-M, de Patoul N, Sterpin E, Vynckier S 2008 Skin sparing during tomotherapy treatment planning :Determination of the skin dose by MOSFET dosimetry and Monte Carlo calculations *Radiat. Oncol.* **88** S411-2

De Smedt B, Fippel M, Reynaert N and Thierens H 2006 Denoising of Monte Carlo dose calculations: Smoothing capabilities vs. Introduction of systematic bias *Med. Phys.* **33** 1678-87

De Smedt B, Vanderstraeten B, Reynaert N, De Gersem W, De Neve W and Thierens H 2007 The influence of air cavities within the PTV on Monte Carlo-based IMRT optimization *J. Phys.: Conf. Ser.* **73** 012003

Ding M, Li J, Deng J Froukai E and Ma C M 2003 Dose correlation for thoracic motion in radiation therapy of breast cancer *Med. Phys.* **30** 2520-9

Ding G X, Duggan D M, Lu B, Hallahan D E, Cmelak A, Malcolm A, Newton J, Deeley M and Coffey C W 2007 Impact of inhomogeneity corrections on dose coverage in the treatment of lung cancer using stereotactic body radiation therapy *Med. Phys.* **34** 2985-94

El Naqa I, Kawrakow I, Fippel M, Siebers J V, Lindsay P E, Wickerhauser M V, Vicic M, Zakarian K, Kauffmann N and Deasy J O 2005 A comparison of Monte Carlo dose calculation denoising techniques *Phys. Med. Biol.* 909-22

Fippel M and Nüsslin F 2003 Smoothing Monte Carlo calculated dose distributions *Phys. Med. Biol.* **48** 1289-304

Fogliata A, Vanetti E, Albers D, Brink C, Clivio A, Knöös T, Nicolini G and Cozzi L 2007 On the dosimetric behaviour of photon dose calculation algorithms in the presence of simple geometric heterogeneities: comparison with Monte Carlo *Phys. Med. Biol.* **52** 1363-85

Gonzalez V J, Buchholz D J, Langen K M, Olivera G H, Chauhan B; Meeks S L, Ruchala K J, Haimerl J, Lu W and Kupelian P A 2005 Evaluation of two tomotherapy-based techniques for the delivery of whole-breast intensity-modulated radiation therapy *Int. J. Radiat. Oncol. Biol. Phys*. **65** 284-90

Hasenbalg F, Neuenschwander H, Mini R and Born E J 2007 Collapsed cone convolution and analytical anisotropic algorithm dose calculations compared to VMC++ Monte Carlo simulations in clinical cases *Phys. Med. Biol.* **52** 3679-91

IAEA 2005 *Radiation Oncology Physics: a handbook for teachers and students* IAEA Vienna

Kapatoes J M, Olivera G H, Ruchala K J and Mackie T R 2001 On the verification of the incident energy fluence in tomotherapy IMRT *Phys. Med. Biol.* **46** 2953-65

Kawrakow I and Fippel M 2000 VMC++, a fast MC algorithm for Radiation Treatment planning *Proc. 13th Int. Conf. on the Use of Computers in Radiation Therapy (ICCR)* Heigelberg: Springer Verlag) pp 126-8

Keall P J, Siebesrs J V, Joshi S and Mohan R 2004 Monte Carlo as a four-dimensional radiotherapy treatment-planning tool to account for respiratory motion *Phys. Med. Biol.* **49** 3639-48

Knöös T, Wieslander E, Cozzi L, Brink C, Fogliata A, Albers D, Nyström H and Lassen S 2006 Comparison of dose calculation algorithms for treatment planning in external photon beam therapy for clinical situations *Phys. Med. Biol.* **51** 5785-807

Jeraj R and Keall P J 1999 Monte Carlo-based inverse treatment planning *Phys. Med. Biol.* **44** 1885-96

Jeraj R and Keall P J 2000 The effect of statistical uncertainty on inverse treatment planning based on Monte Carlo dose calculation *Phys. Med. Biol.* **45** 3601-13

Jeraj R, Keall P J and Siebers J V 2002 The effect of dose calculation accuracy on inverse treatment planning *Phys. Med. Biol.* **47** 391-407

Jeraj R, Mackie T R, Balog J, Olivera G, Pearson D, Kapatoes J, Ruchala K and Reckwerdt P 2004 Radiation characteristics of helical tomotherapy *Med. Phys*. **31** 396-404

Jeraj R, Mackie T R, Balog J and Olivera G 2005 Dose calibration of nonconventional treatment systems applied to helical tomotherapy *Med. Phys.* **32** 570-7

Jiang S B, Pawlicki T and Ma C M 2000 Romoving the effect of statistical uncertainty on dose-volume histograms from Monte Carlo dose calculations *Phys. Med. Biol.* **45** 2151-61

Jones A O and Das I J 2005 Comparison of inhomogeneity correction algorithms in small photon fields *Med. Phys.* **32** 766-76

Kapatoes J M, Olivera G H, Ruchala K J and Mackie T R 2001 On the verification of the incident energy fluence in tomotherapy IMRT *Phys. Med. Biol.* **46** 2953-65

Kawrakow I 2002 On the de-noising of Monte Carlo calculated dose distributions *Phys. Med. Biol.* **47** 3087-103

Knöös T, Wieslander E, Cozzi L, Brink C, Fogliata A, Albers D, Nyström H and Lassen S 2006 Comparison of dose calculation algorithms for treatment planning in external photon beam therapy for clinical situation *Phys. Med. Biol.* **51** 5785-807

Laub W, Alber M, Birkner M and Nusslin F 2000 Monte Carlo dose computation for IMRT optimization *Phys. Med. Biol.* **45** 1741-54

Leal A, Sanchez-Doblado F, Arrans R, Rosello J, Pavoin C E and Lagares J I 2003 Routine IMRT verification by means of an automated Monte Carlo simulation system *Int. J. Radiat. Oncol. Biol. Phys.* **56** 58-68

Lee C, Langen K M, Lu W, Haimerl J, Schnarr E, Ruchala K J, Olivera G H, Meeds S L, Kupelian P A, Shellenberger T D and Mañon R R 2008 Assessment of parotid gland soe changes during head and neck cancer radiotherapy using daily megavoltage computed tomography and deformable image registration *Int. J. Radiat. Oncol. Biol. Phys.* **71** 1563-71

Lu W, Chen M, Chen Q, Ruchala K and Olivera G 2007 TH-C-M100J-02: Real Time Motion Adaptive Delivery-I. Topotherapy *Med. Phys.* **34** 2624

Lu W, Ruchala K J, Chen M-L, Chen Q and Olivera G H 2006 Real-time respiration monitoring using the radiotherapy treatment beam and four-dimensional computed tomography (4DCT)-a conceptual study *Phys. Med. Biol.* **51** 4469-4495

Madani I, Vanderstraeten B, Bral S, Coghe M, De Gersem W, De Wagter C, Thierens H and De Neve W 2007 Comparison of 6MV and 18MV photons for IMRT treatment of lung cancer *Radiother. Oncol.* **82** 63-9

Miao B, Jeraj R, Bao S and Mackie T R 2003 Adaptive anisotropic diffusion filtering of Monte Carlo dose distributions *Phys. Med. Biol.* **48** 2767-81

Olivera G, Ruchala K, Lu W, Haimerl J, Schnarr E, Langen K, Kupelian P, Meeks S and Mackie T R 2005 SU-FF-T-363: Dynamic Tangents and Topotherapy: New Delivery Capabilities for Helical Tomotherapy *Med. Phys.* **32** 2034

Palmans H, Thomas R A S, Duane S, Sterpin E and Vynckier S 2008 Ion recombination for ionization chamber dosimetry in a tomtherapy unit *submitted to Med. Phys.*

Reynaert N, De Smedt B, Coghe M, Paelinck L, Van Duyse B, De Gersem W, De Wagter C and Thierens H 2004 MCDE: a new Monte Carlo dose engine for IMRT *Phys. Med. Biol.* N235-41

Reynaert N, Coghe M, De Smedt B, Paelinck L, Vanderstreten B, De Gersem W, Van Duyse B, De Wagter C, De Neve W and Thierens H 2005 The importance of accurate linear accelerator head modeling for IMRT Monte Carlo calculations *Phys. Med. Biol.* **50** 831-46

Reynaert N, van der Marck S C, Schaart D R, Van der Zee W, Van Vliet-Vroegindeweij, Tomsej M, Jansen J, Heijmen B, Coghe M, De Wagter C 2007 Monte

Carlo treatment planning for photon and electron beams *Radiation Phys. and Chem.* **76** 643-86

Rogers D W O, Faddegon B A, Ding G X, Ma C M, We J and Mackie T R 1995 BEAM: a Monte Carlo code to simulate radiotherapy treatment units *Med. Phys.* **22** 503-24

Sanchez-Doblado F, Andreo P, Capote R, Leal A, Perucha M, Arrans R, Nunez L, Mainegra E, Lagares J I and Carrasco E 2003 Ionization chamber dosimetry for small photon fields: A Monte Carlo study on stopping-power ratios for radiosurgery and IMRT beams *Phys. Med. Biol.* **48** 2081-99

Schulz R J and Kagan A R 2002 On the role of intensity modulated radiation therapy in radiation oncology *Med. Phys.* **29** 1473-82

Seco J, Adams E, Bidmead M, Partridge M and Verhaegen F 2005 Head and neck IMRT treatments assessed with a Monte Carlo dose calculation engine Phys. Med. Biol. 50 817-30

Sempau J and Bielajew A F 2000 Towards the elimination of Monte Carlo statistical fluctuation from dose volume histograms for radiotherapy treatment planning Phys. Med. Biol. 45 131-57

Spezi E, Lewis D G and Smith C W 2002 A DICOM-RT-based toolbox for the evaluation and verification of radiotherapy plans Phys. Med. Biol. 47 4223-32

Sterpin E, Tomsej M, Reynaert N, De Smedt B and Vynckier S 2007a Monte Carlo simulation of the AAA treatment planning algorithm in a heterogeneous multiplayer phantom and IMRT clinical treatments for an Elekta SL25 linear accelerator Med. Phys. 34 1665-77

Sterpin E, Tomsej M, Cravens B, Salvat F, Ruchala K, Olivera G H and S Vynckier 2007b Monte Carlo simulation of the Tomotherapy treatment unit in the static mode using MC HAMMER, a Monte Carlo tool dedicated to Tomotherapy JPCS 74 021019

Sterpin E, Salvat F, Olivera G H and Vynckier S 2008a Analytical model of the binary multileaf collimator of Tomotherapy for Monte Carlo simulations J. Phys.: Conf. Ser. 102 012022

Sterpin E, Salvat F, Cravens R, Ruchala K, Olivera G H and Vynckier S 2008b Monte Carlo simulation of helical Tomotherapy with PENELOPE Phys. Med. Biol. 53 2161-80

Thomas S D, Mackenzied M, Field G C, Syme A M and Fallone B G 2005a Patient specific treatment verifications for helical tomotherapy treatment plans Med. Phys. 32 3793-800

Thomas S D, Mackenzie M, Rogers D W O and Fallone B G 2005b A Monte Carlo derived TG-51 equivalent calibration for helical tomotherapy Med. Phys. 32 1346-53

Tillikainen L, Siljamäki S, Helminen H, Alakuijala J and Pyyry J 2007 Determination of parmeters for a multiple-source model of megavoltage photon beams using optimization methods Phys. Med. Biol. 52 1441-67

Tillikainen L, Helminen H, Torsti T, Siljamäki S, Alakuijala J, Pyyry J and Ulmer W 2008 A 3D pencil-beam-based superposition alogirthm for photon dose calculation in heterogeneous media Phys. Med. Biol. 53 3821-39

Tondeur V, Tomsej M and Vynckier S 2006 Tomothérapie Hélicoïdale: verification expérimentale de l'algorithme de calcul de dose dans le cadre de l'assurance de qualité en radiothérapie Mémoire UCL- Faculté de Médecine

Ulmer W, Pyyry J and Kaissl W 2005 A 3D photon superposition/convolution algorithm and its foundation on results of Monte Carlo calculations Phys. Med. Biol. 50 1767-90

Vanderstraeten B, Reynaert N, Paelinck L, Madani I, De Wagter C, De Gersem W, and De Neve W 2006 Accuracy fo patient dose calculation for lung IMRT: A comparison of Monte Carlo, convolution/superposition, and pencil beam computations Med. Phys. 33 3149-57

Vanderstraeten B, Olteanu A M L, Reynaert N, Leal A, De Neve W and Thierens H 2007 Evaluation of uncertainty-based stopping criteria for Monte Carlo calculations of intensity-modulated radiotherapy and arc therapy patient dose distributions Int. J. Radiat. Oncol. Biol. Phys. 69 628-37

Verhaegen F and Seuntjens J 2003 Monte Carlo modeling of external radiotherapy photon beams *Phys. Med. Biol.* **48** R107-64

Chapter 9: Conclusions

IMRT treatment with photons is a complex technique proposed everyday to a more and more important number of patients suffering a cancer disease. A better understanding of the physical and medical aspects of the technique as well as improvements in all the steps involved in an IMRT treatment, will, therefore, benefit an important number of patients.

The conclusions of the various papers published during this thesis are summarized in Table 9. 1. In chapters 3 to 6, two IMRT delivery techniques were modeled: step-and-shoot IMRT with the Elekta SL25 and helical tomotherapy. The modeling of the Elekta SL25 was based on well established methods, whereas tomotherapy required a completely new approach. Moreover, one additional difficulty for modeling tomotherapy was the additional constraint of the simulation speed. The model TomoPen was devised with all necessary details fully disclosed by the manufacturer and met the requirements in speed without compromising accuracy. The fast simulation of the MLC performed by the TF technique was a crucial step to achieve that objective. The helical mode simulation scheme also allowed for computation time saving.

Using the two models, studies in various phantom configurations were performed to evaluate the performance of two recent algorithms: AAA of Varian (chapter 3) and the C/S algorithm of Tomotherapy (chapter 7). Although AAA and C/S showed obvious improvements compared to older algorithms, deviations from MC algorithms were still observed and were attributed to the remaining simplifications in photon/electron transport.

MCDE and TomoPen were used to determine whether the observed differences in the phantom studies could have a significant impact on clinical cases. Although no “dramatic” differences could be observed, it was clear that in relatively extreme cases significant deviations existed between MC and analytical algorithms. Those “extreme” cases included small lung tumors and head and neck target volumes encompassing a great amount of air cavities.

Chapter #	Objectives	Conclusions
3	Feasibility of using AAA for Elekta SL25 linacs and MC evaluation of AAA in phantoms and clinical cases.	Good agreement of AAA with measurements in water phantom, ensuring that AAA can be used with Elekta SL25. Good overall performance of AAA in phantoms and clinical cases. More important deviations (up to 3.3% for the mean dose to PTV) for small lung tumors but only a fraction of the deviation could be attributed to the presence of inhomogeneities. AAA showed an obvious improvement compared to older correction-based algorithms
4	MC modeling of the static mode of tomotherapy	The MC model of tomotherapy (TomoPen) is fast (typical calculation time ~10 hours on a 2 GHz processor), accurate and flexible. It is ready for MCTP purposes.
5	Fast MC model of the binary MLC of tomotherapy (the transfer function (TF))	
6	Complete description of the MC model of tomotherapy in static and helical mode (TomoPen)	
7	MC evaluation of the C/S algorithm of Tomotherapy Inc. in phantoms and clinical cases	Very good behavior of the C/S algorithm in phantoms. Good agreement between C/S and MC overall, with larger deviations in small lung tumors (up to 4% for D_{95} and 2.2% for the mean dose to PTV)

Table 9. 1. Summary of the conclusions in chapters 3 to 7

During this thesis, MC simulation showed its importance as a benchmark and research tool. However, the objective was mostly to evaluate the added-value of MC in

treatment planning. Despite that several commercial MC algorithms already exist, the scientific community still discusses about the relevance of introducing MC into clinical practice. This thesis is certainly not sufficient to close the debate. However, the clinical studies demonstrated the potential of MC for some specific cases. The future improvements in computers will also naturally reduce the cost of introducing MC into treatment planning. Of course, because of its simulation strategy, TomoPen is already fast enough and might be used immediately for clinical routine.

Radiotherapy with photons came to a high level of sophistication. Nowadays, all the major manufacturers provide complete solutions to deliver highly conformal IMRT with high level imaging devices to implement image-guided radiotherapy. Accuracy is improved simultaneously with the erruption of those new technologies.

The very advanced technological state implies that major improvements with high clinical impact should not be expected for photontherapy anymore. But photontherapy still concerns the vast majority of the patients treated by radiotherapy and, therefore, any development in radiation delivery and accuracy may have an impact on a high number of patients.

However, innovations with large clinical impact are expected in the near future. They will involve other types of particles than photons, like protons (or heavy ions). As stated in the introduction chapter, the cost of building protons treatment facilities is still prohibitive for most of the treatment centers. But new solutions are proposed today which may give access to more treatment centers and patients to protontherapy. As with photons, requirements in accuracy will be strict, and MC simulations will again play a significant role, on one hand, for clinical routine, but also, on the other hand, during the development of those new technologies.